# Damage, Contamination and Surface Treatment of Electrical Discharge Machined Materials

**James Murray, BSc, MSc**

**Thesis submitted to the University of Nottingham for the degree of Doctor of Philosophy**

**February 2014**

# Abstract

Electrical discharge machining (EDM) is a manufacturing process capable of machining electrically conductive materials regardless of their mechanical properties. It finds extensive usage across the aerospace, automotive, medical implant and mould/die industries, and is particularly useful for the micro-machining of precision components with complicated shapes. The surface integrity of materials machined by EDM is typically poor, and reduced service life is often expected as a result of surface properties. For example, reduced fatigue performance can result due to the presence of surface cracks as well as porosity, high surface roughness and tensile residual stress. Increased surface area due to surface cracks, porosity and surface asperities also inhibits corrosion performance.

This thesis explores from a fundamental perspective the damage and contamination occurring in the surfaces of materials machined by EDM, and investigates the use of a novel surface modification technique, pulsed electron beam irradiation, to improve the most damaging surface property; surface cracking.

A transmission electron microscopy (TEM) study was conducted on the surface of single-crystal silicon, which is a chemically and crystallographically homogenous material. For the first time, porosity, contamination and cracking were observed at a scale not visible to conventional imaging techniques such as SEM and optical imaging. The study suggested that conventional microscopic techniques such as SEM and optical microscopy are not sufficient to characterise recast layers created by EDM, and the properties of materials machined by the process are in fact determined by phenomena occurring at the nano-scale.

The mechanism behind the movement of material between electrodes was investigated in this thesis. The flushing process in EDM is used to take machined material away from the machining region, and this material is not expected to reattach to electrode surfaces. Using the observation of single discharges and elemental analysis, the mechanism of attachment was determined to be a two-stage process, whereby material ejected at the end of discharge on-time is resolidified in the discharge gap by a successive discharge, which causes its fusion into the opposite electrode surface. This information is critical to the avoidance, or the deliberate deposition of foreign material on a workpiece.

Pulsed electron beam irradiation was demonstrated as a rapid and simple method of repairing surface cracks induced by the EDM process. A 4 µm depth of surface cracks created by EDM of stainless steel could be completely eliminated in a pore-free layer. Only a small section of recast layer remained unaffected. The cathode voltage parameter was identified as key to increasing the depth of the remelted layer in future developments of the process. Roughness was at the same time reduced from 3.06 µm to 0.89 µm Sa value. A predominantly austenitic graded nanostructure with grain size down to 6 nm was characterised using TEM and XRD. Such structures have implications for improved mechanical properties via grain boundary strengthening

# Publications

## Included in thesis

## Journals

- J.W. Murray, D. Zdebski, A.T. Clare, 2012. *Workpiece debris deposition on tool electrodes and secondary discharge phenomena in micro-EDM*. Journal of Materials Processing Technology 212, 1537-1547.
- J.W. Murray, A.T. Clare, 2012. *Repair of EDM induced surface cracks by pulsed electron beam irradiation*. Journal of Materials Processing Technology 212, 2642-2651.
- J.W. Murray, M.W. Fay, M. Kunieda, A. T. Clare, 2013. *TEM Study on the Electrical Discharge Machined Surface of Single-Crystal Silicon.* Journal of Materials Processing Technology 213, 801-809
- J.W. Murray, J.C. Walker, A.T. Clare, 2014. *Nanostructures in austenitic steel after EDM and pulsed electron beam irradiation.* Surface and Coatings Technology (Under Review)

## Conferences

- J.W. Murray, A.T. Clare, *Improved Surface Properties of EDM Components After Irradiation by Pulsed Electrons.* Matador Conference, Manchester, 2012.

## Not included in thesis

## Journals

- J.W. Murray, A.T. Clare, P. Kinnell, A. Cannon, B. Bailey, 2013. *Surface finishing of intricate metal mould structures by large-area electron beam irradiation*. Precision Engineering 37, 443-450
- J.C. Walker, J.W. Murray, S. Narania, A.T. Clare, 2012. *Dry Sliding Friction and Wear Behaviour of an Electron Beam Melted Hypereutectic Al–Si Alloy*. Tribology Letters, 1-10.
- J.C. Walker, R.B. Cook, J. Murray, A.T. Clare, 2013. *Pulsed electron beam surface melting of CoCrMo alloy for biomedical applications*, Wear 301, 250-256
- C.L. Li, J.W. Murray, K.T. Voisey, A. T. Clare, D.G. McCartney. 2013 *Amorphous layer formation in Al86.0Co7.6Ce6.4 glass-forming alloy by large-area electron beam irradiation.* Applied Surface Science 280, 431-438
- P. K. Farayibi, J. W. Murray, L. Huang, F. Boud P. K. Kinnell, A. T. Clare *Performance of laser clads for waterjet abrasion resistant tooling* Journal of Materials Processing Technology
- C.L. Li, J.W. Murray, K.T. Voisey, A. T. Clare, D.G. McCartney. 2014 *Effect of prior laser microstructural refinement on the formation of amorphous layer in an Al86Co7.6Ce6.4 alloy.* Applied Surface Science 289, 230-236
- J.C. Walker, J.W. Murray, A.T. Clare *FIB-TEM investigation of a large area electron beam surface melted hypereutectic Al-Si alloy.* Journal of Alloys and compounds. (Accepted with correction)
- F. Boud, J. W. Murray, L. F. Loo, A. T. Clare, P. K. Kinnell *Soluble Abrasives for Waterjet Machining.* Materials and Manufacturing Processes (Under Review)

## Conferences

- N. Vladov, J.W Murray, A.T. Clare, J. Segal, S. Ratchev *Surface-Finishing of Focused Ion Beam Milled Features by Pulsed Electron Irradiation.* EIPBN Conference 2012. Hawaii, USA.
- C.L. Li, J.W Murray, K.T. Voisey, A. T. Clare, D. G. McCartney. *Amorphous layer formation in an Al-Co-Ce alloy using electron beam melting and laser microstructural refinement*. SMT conference 2012. Lyon, France.
- J.C. Walker, R.B. Cook, J.W Murray, A.T. Clare. *Pulsed electron beam surface melting of CoCrMo alloy for biomedical applications.* Wear of Materials Conference 2013, Portland, Oregon, USA.
- T. Kawanaka, S. Kato, M. Kunieda, J.W. Murray, A.T. Clare *Micro Textured Surfaces Created By Electrolyte Jet Machining.* ASPEN Conference 2013, Taipei, Taiwan.

# Acknowledgements

Thank you to my primary supervisor, Dr Adam Clare, without whom the progress I made during my PhD would not have been possible. Working with Adam I've had the unique opportunity to access a wide range of novel machines and technologies, as well as collaborate with various industrial and academic groups all over the world. For these reasons the PhD has been a fantastic experience. Thanks also to my second supervisor, Dr Andrew Kennedy, for his expert advice and guidance.

I am very grateful for the technical help of Dr Nigel Neate, Tom Buss, and Keith Dinsdale in the Wolfson Building. I relied on their expertise on countless occasions, and their advice and assistance were always available. Many thanks also to Dr Mike Fay in preparation of excellent TEM samples which were critical to this thesis. Thanks also to Dr John Walker at the University of Southampton for his help with indexing of TEM electron diffraction patterns, as well as for his collaborative work in research on pulsed electron beam irradiation.

Thank you to my parents for their support, financial and otherwise during the PhD. Thank you also to the Rail project and EPSRC Let Nano Fly project which have also supported me financially during the PhD process.

# Contents

# List of figures

# List of tables

# List of abbreviations

BF – Bright field

BSE – Back-scattered electrons

DF – Dark field

EB – Electron beam

EBM – Electron beam melting

EDM – Electrical discharge machining

EDX – Energy dispersive X-ray spectroscopy

FIB – Focused ion beam

HAADF – High angle annular dark field

HRTEM – High resolution transmission electron microscopy

SE – Secondary electrons

SEM – Scanning electron microscopy

STEM – Scanning transmission electron microscopy

TEM – Transmission electron microscopy

WEDG – Wire electrical discharge grinding

WLI – White light interferometry

XRD – X-ray diffraction

SAED – Selected area electron diffraction

# 1 Introduction

Electrical discharge machining (EDM) is a manufacturing process which has been used industrially since the 1950s and has been subject to substantial academic research to the present day. The key ability of the process is to machine materials regardless of mechanical properties, unlike most conventional machining processes. This advantage has resulted in its common use in the aerospace industry, where mechanically superior but difficult to machine materials are necessary. The ability of EDM to cut highly complex shapes with high aspect ratios, without imparting significant stresses on the entire component, has made it indispensable for the micro-machining of precision components for example in the medical implant industry, as well as for moulds and dies.

EDM works by the application of a pulsed voltage between two electrodes (one being the workpiece), which when at sufficiently close proximity, causes the breakdown of a dielectric into a plasma consisting of temperatures above the boiling points of most materials. The repeated application of this voltage, many thousands of times per second, results in the melting and erosion of material from the workpiece at an economically useful rate.

Two of the most critical limitations of EDM are: the erosion of the tool electrode, or wire-breakage in wire-EDM; and poor workpiece surface quality, as a result of resolidification of some of the melted but not ejected material back on the workpiece. The resolidified material is referred to as the recast layer, or white layer. This thesis focuses on the recast layer caused by EDM.

The surfaces of materials machined by EDM are significantly modified from the bulk workpiece. Due to rapid resolidification, a highly modified microstructure is

produced, typically containing tensile residual stresses. Contamination of the workpiece with carbon from the dielectric, and from tool electrode material is also known to take place, resulting in an unpredictable chemical composition in the machined surface. The morphology of the recast layer is typically poor; exhibiting high surface roughness and containing pores and cracks. These morphological features typical of EDM'd surfaces limit the fatigue performance of the component due to stress concentration effects. Surface cracking is particularly detrimental to fatigue behaviour, since the crack initiation stage of failure has already occurred. Roughness, porosity and surface cracking also limit corrosion behaviour of the machined part.

The surface features which occur as a result of EDM are not well understood. For example, porosity and surface cracking are well documented at scales visible to SEM and optical imaging, but have not been investigated at the nano-scale of materials. Contamination of the workpiece is also known to take place, but the mechanism which causes it is not well understood. The rapidity and complexity of the EDM process make it difficult to observe or model the exact phenomena occurring in the machining gap which result in these poor surface properties.

In applications where mechanical and chemical properties of the component are critical, the recast layer may be removed. This might involve a process such as etching then mechanical grinding. Such a recast removal process however is difficult for complicated shapes with tight dimensional tolerances. The dimensions of the original part are also changed. Post-processing cycle time is also an undesirable factor.

This thesis aims to understand the fundamental characteristics of surface features introduced by EDM, and demonstrate a surface treatment technique to improve the properties of the recast layer. This will allow the surface properties of EDM'd materials to be more precisely controlled and more predictable.

## 1.1 Aims of thesis

The aims of this thesis are to investigate and clarify previously unknown phenomena occurring in EDM, and propose and validate a novel surface treatment technique appropriate for the post-processing of materials cut by EDM. To reach these aims, the thesis will investigate three areas:

- Characterisation of the EDM surface at the nano-scale. A fundamental study of machining damage at the nano-scale has not yet been performed. This study aims to reveal defects and phenomena previously seen at the micro-scale under SEM and optical imaging, such as pores, cracks and contamination, at the nano-scale. To perform this, a single-crystal material machined by EDM is characterised at the nano-scale for the first time. The characterisation of such phenomena at a scale not visible to conventional imaging modes is critical to understanding if the properties of machined workpieces are determined by features not visible at the micro-scale. Such a characterisation study is particularly important given the recent drive of EDM towards micro and sub-micron scale machining.

- The mechanism of material movement between electrodes. Many authors have reported deposits of electrode material onto the workpiece and vice versa. The attachment of material back on to electrodes does not agree with the principle of EDM whereby eroded material is solidified in the gap and flushed away

from the region. The mechanism of this process is investigated in order to determine the conditions under which material transfers and how it is related to the discharge process.

- Pulsed electron beam irradiation surface treatment of EDM'd surfaces. This is a novel surface modification process capable of uniformly remelting surfaces with a short cycle time. The improvement of the critical property of surface cracking is investigated in this study. Modification of surface roughness. Fundamental material characterisation is conducted to assess material changes induced by this process. A detailed understanding of the effect of this novel surface modification technique is necessary for its adoption as a simple method for improving the properties of the poor EDM surface.

## 1.2 Outline of thesis

Research previously conducted which is relevant to this investigation is reviewed in *Chapter 2*. Topics discussed in this literature review include the fundamental process of EDM and the material removal mechanism, as well as phenomena occurring in the discharge gap such as debris dynamics and contamination. The research trend in EDM towards miniaturisation is also reviewed. The current knowledge gaps on surface properties arising in workpieces cut by EDM are also reviewed in detail, including surface morphology and metallurgy and their impact on component properties. Pulsed electron beam irradiation is also discussed, from its basic physical mechanism, to its effect on surface morphology and metallurgy. At the end of the literature review, the research gaps are identified and therefore the aims of the research work are defined.

*Chapter 3* is a detailed breakdown of all the experimental methods and materials characterisation processes used in the thesis. This includes the material processing

techniques as well as a number of microscopic and X-ray diffraction methods. The physical mechanisms of these processes are also explained.

*Chapter four* is the first of three research chapters and presents a fundamental study at the nano-scale of contamination, material structure, porosity and cracking in the EDM'd surfaces of single-crystal silicon. An experimental account of attaining the necessary parameters to machine the pure silicon workpiece is also reported. This study is presented first in the thesis as its results impact the following chapters.

The contamination which is revealed in chapter four is investigated further in *chapter five*. In this study the mechanism by which contamination occurs at electrodes during EDM is explained. Here a high-aspect ratio electrode is sunk into a workpiece in order to characterise surface layers formed, and through single discharge analysis, the mechanism of layer build-up is determined.

In *chapter six*, surface cracking, also investigated in the nano-scale study in chapter four, is studied. Surface cracking is a critical surface defect common to EDM'd materials, and its elimination is a key area of research. By application of the pulsed electron beam irradiation process to the EDM'd surface, the repair of these surface cracks is investigated. The mechanism behind this repair of surface cracks is also explained. A fundamental material analysis using transmission electron microscopy (TEM) and X-ray diffraction (XRD) is conducted on the modified surface.

Finally, *chapter seven* presents the general conclusions of the research work in this thesis and outlines future work which is proposed to extend the findings presented here.

# 2 Literature Review

This chapter presents a detailed discussion of EDM from its basic physical mechanism to its future applications. A literature review of pulsed electron beam surface treatment is also presented, along with a description of its fundamental principles. Through this discussion of literature, some research challenges are identified and in doing so the scope of the thesis will be defined.

## 2.1 Introduction to EDM

Since the invention of electrical discharge machining (EDM) in 1943, the process has become indispensable for the precision machining of parts at the micro-scale, for example for the mould and die industries [1, 2], automotive engines [3] as well as surgical components [4] and for the high speed cutting of very hard and tough materials, for example for the aerospace industry [5-7]. EDM is a machining process in the non-conventional category, i.e. not based on material removal by a shear mechanism, whereby a pulsed potential difference between an electrode and a conductive workpiece initiates an electrical discharge as a result of dielectric breakdown. In doing so, a plasma is formed which is associated with high temperatures and pressures, melting and evaporating material from both electrode surfaces, one being the workpiece. Its distinct advantage is its usage of this thermal energy to erode workpiece materials regardless of hardness. The tight tolerances and intricate shapes capable of being machined by EDM have resulted in decades of industrial usage. Some examples of EDM'd products and components with dimensions difficult to attain by other manufacturing techniques are shown in Fig. 2.1.

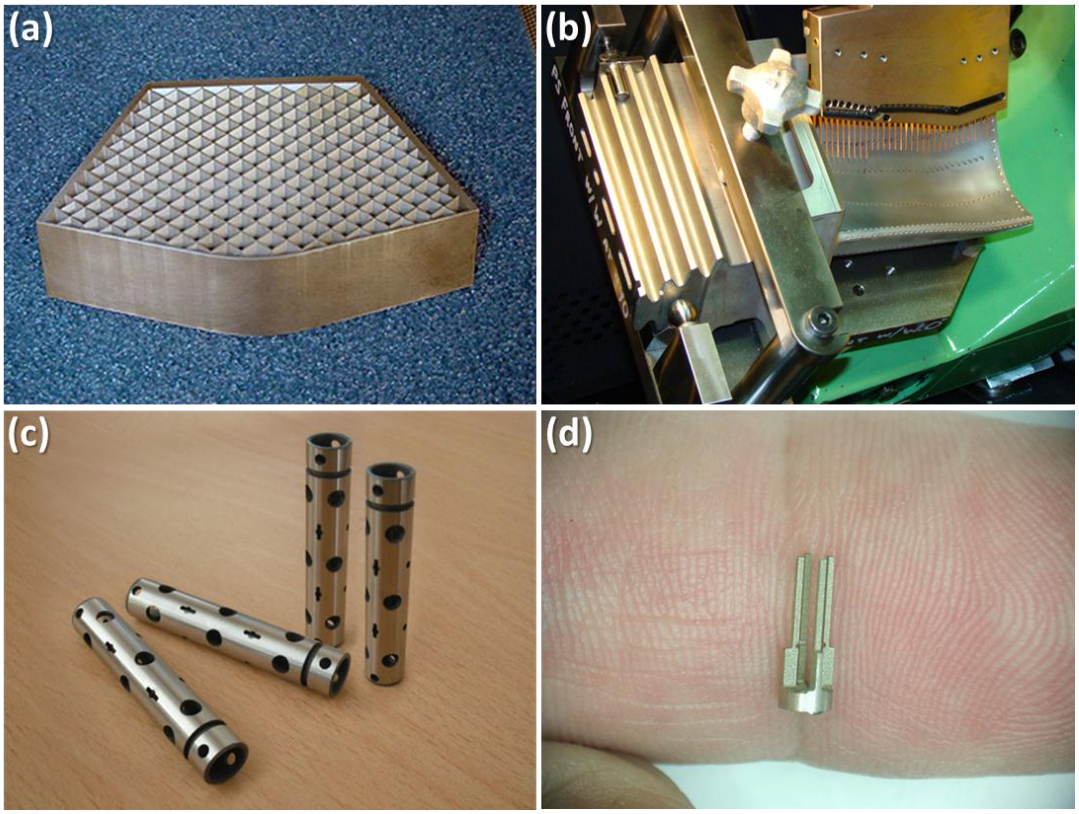


**Fig. 2.1 Example products requiring EDM to be machined - (a) Complex mould tool (sinking EDM) [8] (b) Cooling holes in turbine blades (sinking EDM) [9] (c) Precision valve parts (wire EDM) [10] (d) Surgical implant (wire EDM) [11]**

In EDM, discharges occur in the gap between the tool electrode and workpiece. This gap is filled with an insulating medium: either dielectric hydrocarbon oil such as kerosone or de-ionised water in order to avoid electrolysis effects on the electrodes but primarily to avoid short-circuiting of the machine (i.e. uncontrolled and unintended sparking). The electrode is moved toward the workpiece until the gap is small enough so that the applied electric field strength is sufficient enough to cause dielectric breakdown (ionise) the insulating fluid, thereby creating plasma [12]. This discharge ignition process occurs when the voltage overcomes the dielectric breakdown strength of the gap [13].

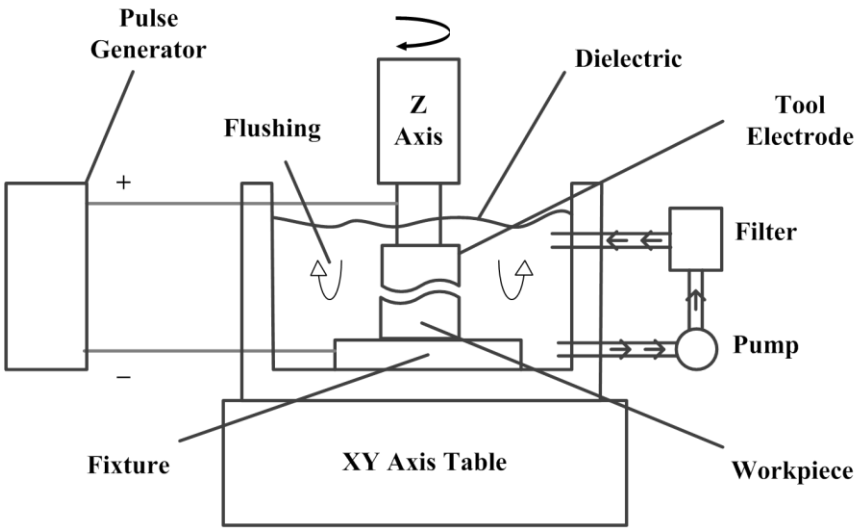


**Fig. 2.2 Sinking EDM Schematic**

Material removal per discharge is typically in the range of $10^{-6}$ – $10^{-4}$ $mm^3$ [4], and so the discharge frequency must be high ($10^3$ – $10^6$ Hz) to result in sufficient material removal rates. The temperature of the plasma channel between electrode and workpiece is also high, typically between 6,000 and 10,000 K [14, 15] but can reach up to 20,000 K [4], heating the discharge to temperatures above the boiling points of most materials. For each electrical pulse, discharge occurs at a single location on the workpiece (and the opposite tool electrode) resulting in the ejection of material in the molten phase and/or evaporation of the material. The continuous growth of gas bubbles during the discharge process creates a sharp pressure drop at the surface of the workpiece assisting in the expulsion of molten material into the dielectric at the end of spark duration [16]. The removed material is subsequently cooled and re-solidified in the insulating medium as spherical debris particles which must be flushed away by dielectric flow. When the discharge ends, the dielectric breakdown strength is recovered as the temperature of the plasma rapidly drops and the recombination of ions with electrons occurs. Plasma recombination force is large and requires high temperatures to maintain the state.

EDM is a reproductive shaping process, except in the case of EDM milling, in that the form of the electrode is mirrored in the workpiece, and so the fidelity of the part is inherently high. There are two main forms of EDM, as follows.

### 2.1.1 Die-sinking EDM

Die-sinking/Sinking EDM involves the formation of a workpiece by the replication of the tool electrode shape, or less commonly by the 3D movement of a simple electrode as in milling. EDM tool materials are typically copper, graphite, tungsten or copper-tungsten. These are chosen for their high thermal conductivities since higher heat conduction results in lower temperature at the electrode surface and therefore a lower wear ratio [13], as well as sufficient electrical conductivity in order to generate a spark [7]. Graphite and tungsten have the two highest melting points of all materials and therefore mitigate electrode wear by withstanding high temperatures.

Sinking EDM is used for the drilling of holes in diesel engine injection nozzles, where combustion efficiency achieved via the use micro-holes is required [13, 17]. It is also used to machine the high-aspect ratio cooling holes on turbine blades in aerospace engines. High quality reverse tapered holes have been achieved in sinking EDM, whereby dielectric flow through the hole is improved, suggesting there is still flexibility in a process which is typically used to produce parallel-walled holes [3, 13]. Sinking EDM is also a major method of producing dies and moulds. The products of which must be of high precision, such as injection moulding tools for lenses and automotive drive train components [18], and the accuracy of the mould production process must be higher than the accuracy required in the product of the mould.

With CNC systems and 3-axes or more of movement, conventional EDM can be applied as a 3D milling technique, whereby the electrode is rotated about the z-axis

and moved in a horizontal direction. Rotation is used to ensure homogenous electrode wear [19]. This technique has since been through some advancement in research with the development of high speed EDM milling whereby the electric arcs move rapidly within the discharge gap, i.e. the position of the discharge changes during on-time with no interval time, resulting in high removal rates and negligible electrode wear [20]. 3D milling has also been shown to give very low tool wear and high removal rates in dry-EDM [21], a process which uses only a gas as the dielectric medium.

### 2.1.2 Wire-EDM

Wire-EDM is a well-established adaptation of the conventional die-sinking EDM process whereby a spooling wire electrode is utilised. The wire is held under mechanical tension to minimise vibration and maintain a uniform kerf width, and machines material in front and at the sides of the wire, avoiding mechanical contact with the workpiece, as in standard EDM. The wire material can be copper, tungsten, or steel core with brass, but is usually brass, since the alloying of copper with zinc improves tensile strength. During machining some material of the wire electrode is eroded upon discharge and therefore the cross-sectional tensile stress on the wire temporarily increases and so the wire must have sufficient tensile strength. Diameters of wires are typically between 0.05 and 0.3 mm [22], although wires of 20 μm diameter [23] and 13 μm have been successfully used [24]. The advantage of a smaller wire diameter is the increased machining precision, good surface finish and smaller kerf width but an increased likelihood of wire breakage as well as a lower machining rate.

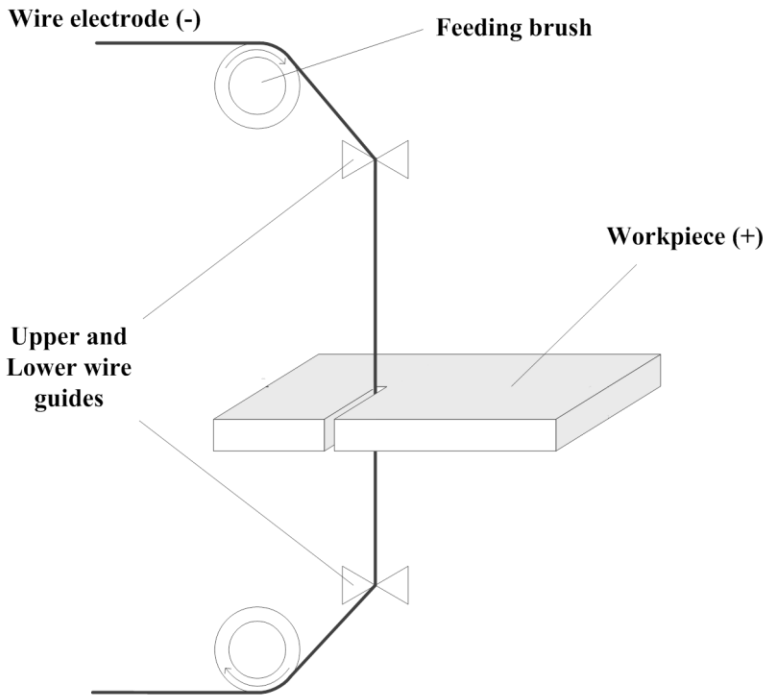


**Fig. 2.3 Wire-EDM Schematic**

The computer numerical control of the wire-EDM process allows complex, intricate parts to be cut with very high accuracy, while servo control maintains a constant gap width, typically between 0.025 and 0.05 mm [22]. This gap width is governed by the spark gap voltage. A varying degree of taper of up to 30° can also be achieved [22]. The process also eliminates the need for a complex shaped electrode, instead the wire is provided from a spool often many kilometres long. In wire-EDM overall tool wear is not a problem because fresh wire is continuously introduced via the feeding mechanism.

## 2.2 The fundamentals of material removal by EDM

### 2.2.1 The physical process of spark generation

An electrical discharge is built up by electron collisions producing fresh ions and electrons known as Townsend avalanches [25]. This occurs when an electric field accelerates and causes the collision of a small number of electrons with ions causing

an exponential increase in the number of ions. A schematic of this process can be seen in Fig. 2.4.

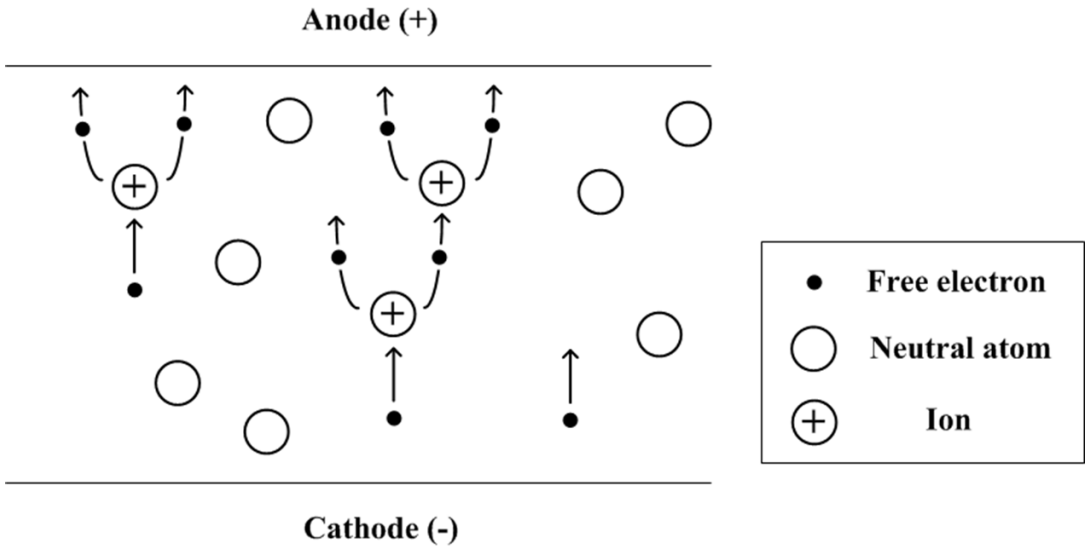


**Fig. 2.4 Schematic of first stage of discharge – the Townsend discharge process**

The Townsend discharge process requires a time lag for the generation by chance of initial (free) electrons by the random bombardment of radiation, for example cosmic, ultraviolet and X-rays with neutral atoms in the potential discharge gap [26] [13]. Under a high enough electric field, electrons are accelerated to sufficient energies to ionise atoms, producing free electrons which are again accelerated towards the anode, creating a cascading or avalanche ionisation effect. Under sufficient electric field the flow of the heavier and slower positive ions accelerating towards the cathode begins to contribute to this ionisation process by bombarding the cathode surface and releasing free, secondary electrons, which further contribute to the total current and rate of ionisation by creating more electron and ion pairs in the developing discharge gap [27]. Beyond this point in the process, a continuity mechanism must be established in order to maintain current in the developing plasma by replacing electrons lost to recombination, diffusion and attachment. At this point, after the initial dielectric breakdown process, the gate control circuit switches transistors on

supplying necessary current so that the plasma does not recombine. Here the discharge becomes independent of the external sources of irradiation supplying necessary electrons for initiation of the discharge. The transistors are switched on for a specified time according to the machine settings. This key setting is typically referred to as "on-time". After this time, the transistors are then switched off for a specified discharge interval or "off-time", during which the plasma is rapidly extinguished and dielectric breakdown strength is recovered to ensure the next discharge event is independent and does not manifest at the exact same location. The ratio of on-time to off-time is the duty factor. The discharge energy per pulse $\boldsymbol{q}$ can be calculated from the waveforms observed for an EDM process, and is expressed as follows,

$$\boldsymbol{q = I \times V \times t} \qquad \textbf{Equation (1)}$$

where $I$ is the discharge current, $V$ is the discharge voltage and $t$ is the discharge duration, or "on-time". The key stages of this discharge process are represented by gap voltage and current waveforms of the EDM process as shown in Fig. 2.5.

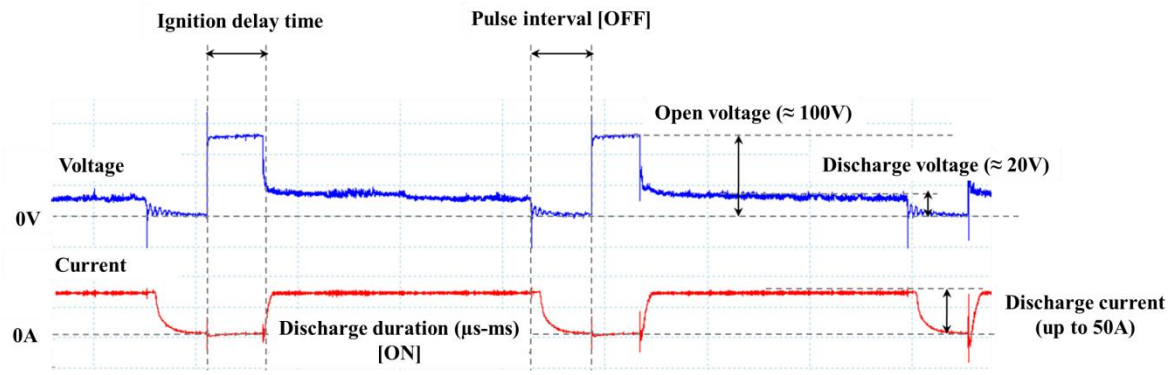


**Fig. 2.5 Typical voltage and current waveform for EDM showing the key pulse stages. Data captured from Sodick AP1L die-sinker.**

The ignition delay time comprises (1) the generation of initial electrons by bombardment of neutral species in the gap (a statistical time lag) and (2) the

acceleration of these initial electrons to cause an electron avalanche (a formal time lag). The length of the ignition delay time is dependent on the breakdown strength of the gap, and this is dependent on both gap width and density of debris particles. The presence of minute particles in insulating liquids can drastically lower the breakdown strength of the dielectric and by facilitating ignition can increase the gap size [28]. The gap size affects the precision of the process. A small gap width and/or a higher density of debris particles forming a bridge between electrodes will reduce the time required for ignition. The ignition delay time directly reflects and is determined by the conditions of the gap and is not fixed.

### 2.2.2 The plasma channel

In EDM, the effectiveness of the material removal process (further discussed in section 2.2.3) at the workpiece fundamentally relies on the distribution of energy from the heat source, which is the plasma channel that exists during on-time, and the diameter of this heat source [14]. Natsu et al. [29] observed the growth of the plasma channel with a high-speed camera, and noticed that the apparent plasma size was several times larger than the resultant discharge crater. It was also observed that plasma temperature was almost constant with time suggesting that current density stayed constant, implying that the plasma channel does not keep expanding for the length of the discharge duration. From these results a new model of EDM plasma growth was proposed called the first-stage-expansion model whereby the plasma expands completely within three micro-seconds of discharge breakdown completion. Kojima et al. [14] performed further tests to clarify these relationships and found that their measured arc plasma diameter was five times larger than the resultant discharge crater for discharge conditions of 17 A, 80 μs on-time and 0.1 mm gap width. Total

expansion of the plasma also completed within 2 μs of dielectric breakdown. Some of Kojima et al's high speed images of EDM plasma can be seen in Fig. 2.6.

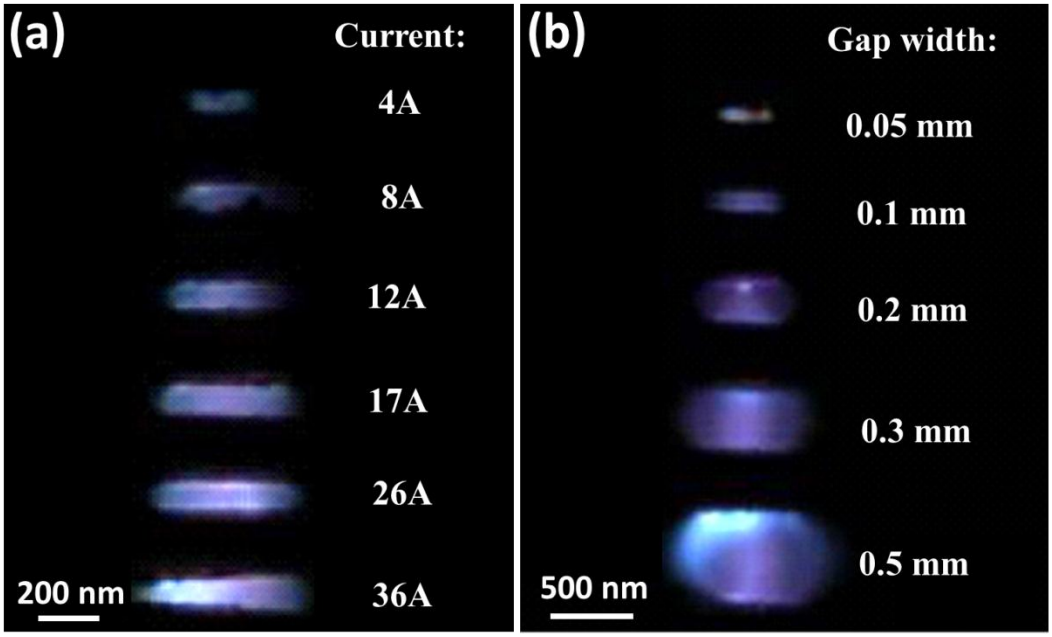


**Fig. 2.6 Direct images of EDM plasma with (a) different discharge currents and (b) different gap widths. Credit to Kojima et al. [14]**

Understanding of the physics of the plasma is particularly important in micro-EDM, where material is removed in smaller voumes. Nagahanumaiah et al. [30] further characterised the nature of EDM plasma for micro-EDM using spectroscopic measurement and made the following conclusions; larger spark gaps increase plasma temperature and density unless the gap is too large after which ions from the electrode and electrons lose their excitation status before breakdown is completed; and smaller electrodes can produce higher plasma temperatures because of higher heat resistance and smaller heat dissipation surfaces. The factors which affect plasma temperature are critical to the material removal process.

### 2.2.3 Material removal mechanism

In the literature, there is consensus on the physical principles of spark generation in EDM, however the details of the mechanism of material removal are still not entirely clear.

Ho & Newman [4] summarise the material removal process as the conversion of electrical energy into thermal energy through an electrical discharge. The channel of plasma connected between both electrodes results in substantial heating and melting at the surfaces of the electrodes. When the current supply is turned off and the plasma channel breaks down, the sudden reduction in temperature and therefore pressure facilitates material ejection after which flushing of molten debris by the dielectric fluid can occur.

Schumacher [31] also discusses the contention which still exists within EDM literature, whereby since the conception of the constructive use of metal removal by sparks by Lazarenko in 1943 [32], there has been no uniform interpretation of the description of the process occurring in the discharge gap, even though it is accepted that the primary material removal mechanism is melting and/or evaporation [4, 13, 33]. The author attempts to arrive at a new consensus on the phases of electrical discharges. Three phases in the electrical discharge procedure are discussed: the preparation phase of the ignition, the phase of discharge and the interval phase between discharges.

The preparation phase includes the physical process described in section 2.2.1: the Townsend discharge process. Here, when the generator switches the voltage on, the electric field reaches its highest strength where electrode surfaces are closest as well as where particles in the gap assist the discharge process. If debris particles are

assisting in this discharge process then this particle bridge is evaporated by the current flow across it forming the high temperature plasma associated with EDM. In Fig. 2.7 a schematic of the material removal process is shown.

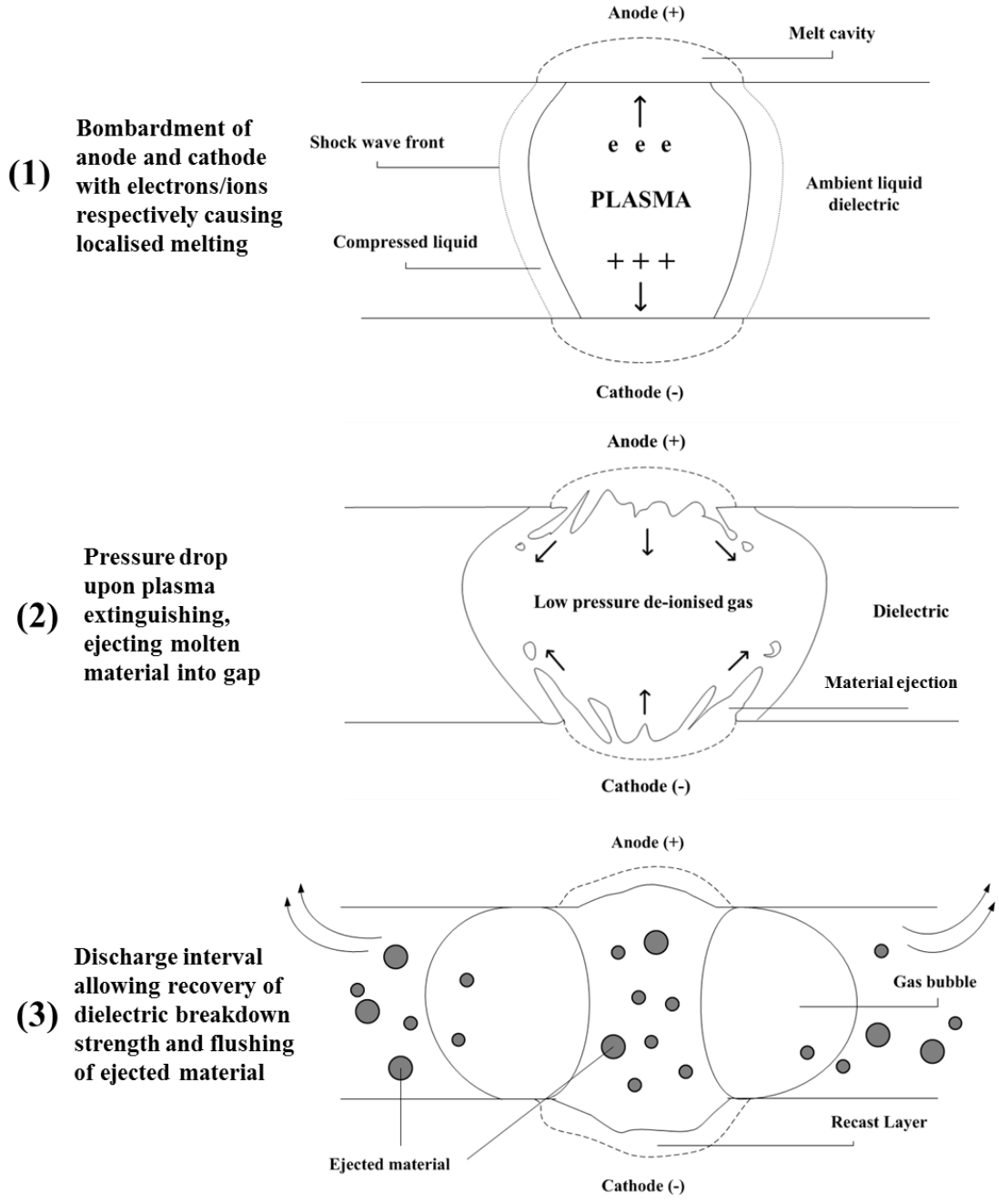


**Fig. 2.7 Schematic of material removal process in EDM**

In the discharge phase rapid development of the plasma channel occurs, resulting in high pressure in the channel as well as shock wave distribution in the liquid [31]. The

current flow in the gap creates high temperatures resulting in the melting of material at both electrode spots. This melting results from heating caused by the bombardment of electrode surfaces with electrons or ions and the conversion of their kinetic energy into thermal energy. For short on-times, material removal mainly takes place at the anode due to faster movement of electrons given their smaller mass compared to anions [31, 34], however, for longer on-times, the action of ions dominates and most energy is distributed to the cathode, resulting in less heating (and ultimately wear) at the anode. As the plasma channel continues to grow, current density and temperature decrease quickly, followed by a stabilisation of the plasma channel diameter. This happens when equilibrium is reached between energy supply from the generator and the heat flow to electrodes and further evaporation of the liquid. Schumacher also observed that particularly under roughing conditions with relatively low discharge current and long spark duration there is clear marking from the action of the gas bubble around the active area of discharge plasma, suggesting some conditioning of the discharged spot is caused the presence of this bubble [31]. Shervani-Tabar et al. [16] support this observation of the useful debris-removing effect of the bubble by showing numerically that the continuous expansion of the gas bubble results in a sharp pressure drop over the surfaces of the two electrodes, aiding the expulsion of gas dissolved in the molten material and helping this molten material escape.

In the interval phase, deionisation of the plasma channel quickly occurs once the generator is switched off, however the gas bubble remains for up to 25 times the on-time duration [31]. The de-ionisation of the plasma channel causes the pressure and temperature to decrease, resulting in the instantaneous boiling and ejection of liquid globules of molten material, previously superheated under the discharge pressure.

Their entry into the cool dielectric causes their shock hardening and shrinkage. Dielectric flow ensures this solidified material is removed from the discharge area.

### 2.2.4 Gap debris

As an inherent part of the process of machining, melted and ejected material from the workpiece needs to be removed from the machined area. The presence of debris, however, can play both a positive and negative role in the EDM process. With demands in machining for high precision and low surface roughness, small gap widths (<30 μm) become necessary to facilitate smaller discharge energies. However smaller gap sizes can be a cause for instability since debris evacuation can become blocked [28]. This is a well-known issue, as the result of a contaminated gap can be a series of sparks striking the same spot repeatedly, caused by the greater polarisability of these spheres in an electric field. This phenomenon can be seen in Fig. 2.8.

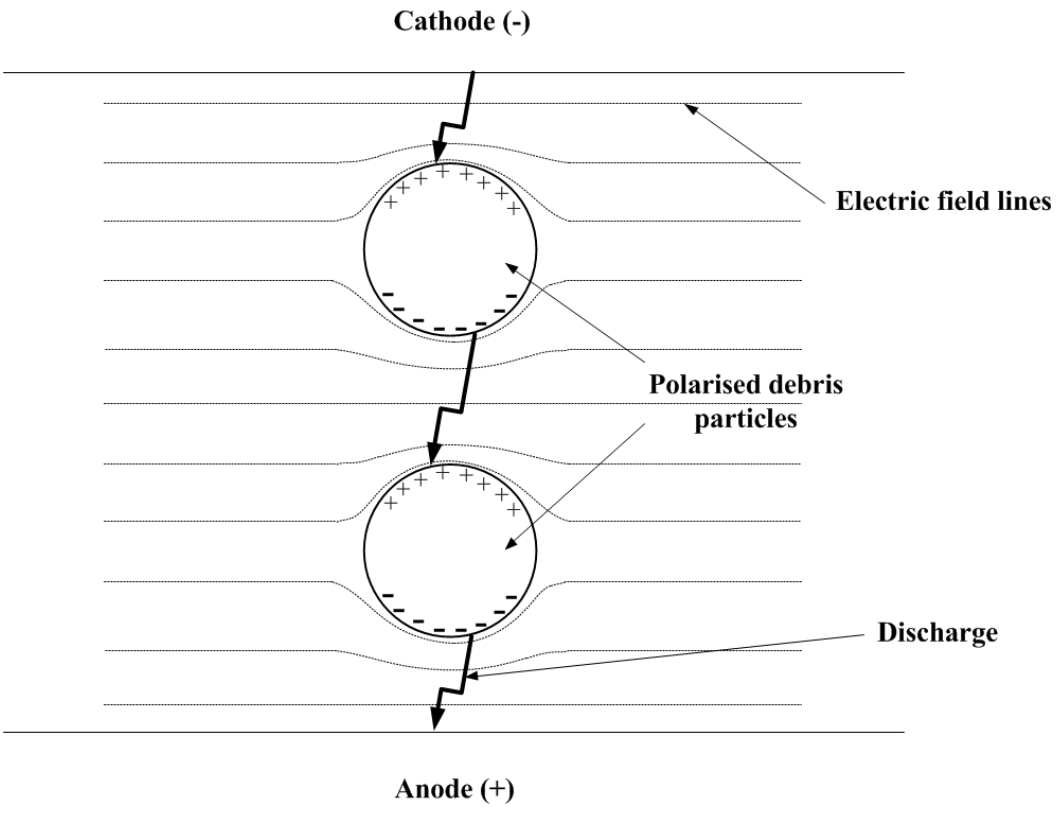

**Fig. 2.8 Principle of series discharge due to polarised particles**

This is referred to as arcing and in modern control systems is detected and responded to positively by increasing the spark gap to enhance flushing. On the other hand, Luo [28] suggests that without debris bridges in the gap, an extremely small gap width is required for dielectric breakdown – increasing the frequency of short circuits. As a result, in this situation, modern gap control systems will (over) compensate by increasing the gap width which results in unstable and inefficient machining. Gap debris therefore has an essential role in maintaining reasonable gap size. Luo also showed that less debris in the gap will cause a lower resolution of surface irregularity due to the reduced discharge transitivity, resulting in a less stable process. Discharge transitivity is the ratio of electrical field intensity, whereby a higher value of transitivity denotes an easier transfer of breakdown location and hence higher process stability. It is also suggested that the absence of debris can in fact be a cause for arcing. This work changes the role of the presence of debris in the gap as being a purely negative one to being essential from a process stability point of view.

During discharge and subsequent melting of the workpiece, the ejected matter decelerates less in the plasma and surrounding gas tunnel than in the liquid given its higher viscosity causing densification of debris [35]. This concentration of contamination can cause greater ignition readiness than in the cooling and deionising discharge tunnel. This discharge readiness is directly related to the ignition delay time as seen in the waveforms in Fig. 2.5, with a “readier” gap associated with shorter delay times. The discharge readiness of the gap refers to the ability of particles to arrange in a line and enable shorter discharge delay times although the phenomenon can be eliminated when flushing is intensive enough to occur on the order of microseconds, removing all contaminatory matter from the discharge region [35].

### 2.2.5 Discharge location

A key benefit of the EDM process is the tolerance of the final machined shape to the tool electrode. This level of accuracy is possible because under gap conditions which are not contaminated, in principle the next individual discharge event will occur at the location of smallest gap width. This principle behind the discharge location in EDM is shown in Fig. 2.9. The first discharge between the electrodes will occur at the point where the gap is smallest, assuming a uniform electric field. The material removal at this point will leave another pair of points on the electrodes as having the shortest distance, and therefore discharge will occur here. This process results in a machining of the workpiece to a replicated shape of the tool electrode.

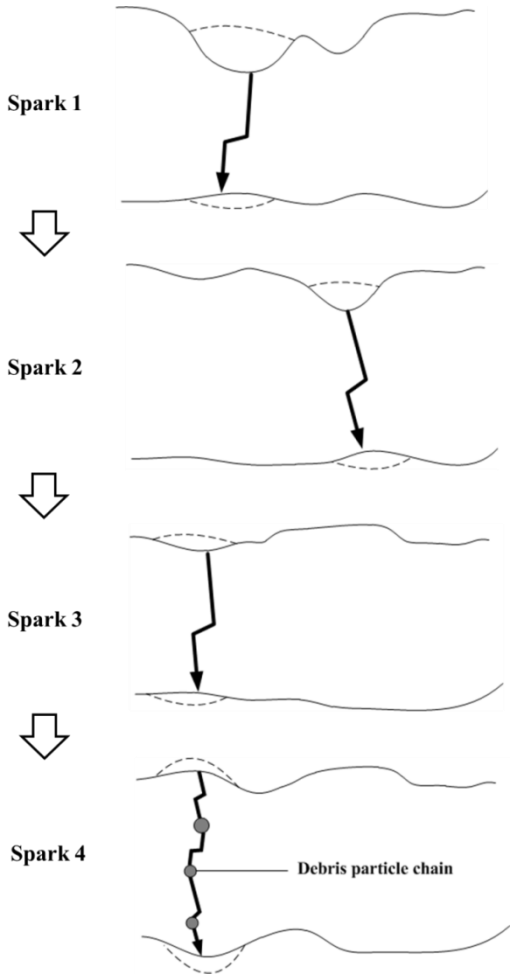


**Fig. 2.9 Principle of discharge location in EDM**

It is now established that the presence of debris particles, despite their contribution to the likelihood of arcing when unevenly distributed, does enhance the process of EDM allowing the gap width to be larger than it otherwise would be with clean dielectric. This extension of the gap width makes gap control via the servo easier [13] allowing a more even spread of discharge locations. This principle of creating a more uniform spread of discharge locations has been exploited using a polymer composite electrode to continuously provide nano-scale conductive carbon particles into the discharge gap, and thereby stabilising the ignition process and yielding a fine workpiece finish [36].

Kunieda & Nakashima [37] investigated the influence of gap width, debris concentration, surface area and degree of plasma deionisation on discharge location. It

was found that discharge does not always occur at the point the gap is narrowest due to the effect of surface area. The probability of discharge is determined by the product of discharge per unit area and its surface area, and the presence of a debris particle despite occupying a significant height in the gap still has a negligible surface area compared to typical electrode surface areas [13, 37]. This suggests that discharge location is determined in a probabilistic way and not deterministic given a section of smaller gap width e.g. a debris particle will only slightly increase the probability of discharge at that point. It was also found that for a series of pulsed discharges, the growth of numerous chains of debris particles over the working surface becomes a more dominant influence than gap width distribution. These experiments also concluded that as long as plasma is extinguished before the following discharge, the location of the preceding discharge has no effect on the next.

### 2.2.6 Removal/reattachment of machined material

Although debris plays an important role in the discharge process, the principle of EDM is such that removed material is eventually removed from the discharge region at a rate consistent with the amount of material being continuously ejected due to discharge. Despite this the attachment of machined debris to both workpiece and tool electrode surfaces has been subject to little investigation despite the phenomenon being observed by several authors.

It is now well understood that a carbon layer produced by thermal dissociation of carbon-based EDM oil on the surface of the tool electrode can improve its wear resistance in EDM. This was discussed by Mohri et al. [38] whereby in the machining of carbon steel, wear of the copper electrode was reduced due to the attachment of carbon to the electrode surface. Marafona [39] also investigated the carbon based

layer attached to the electrode, and noted a reduction in electrode wear rate when this layer was formed on it. The contribution of surface carbon to lower electrode wear rates was clarified by Kunieda and Kobayashi [40] through spectroscopic measurement of copper vapour density for different electrode wear rates. The attachment of workpiece elements onto the electrode during machining however is less well understood.

In the theory as stated by Kunieda et al. [13], the rapid cooling of melted and ejected material causes its rapid solidification into spherical debris particles upon entering the dielectric fluid and these are not reattached to the electrode surfaces. Soni and Chakraverti [41] investigated the migration of material in EDM with a rotating electrode and noted an appreciable amount of iron and chromium from the steel workpiece material was observed to bind with the tool electrode, although the mechanism of this attachment was not investigated. It has also been suggested by Mohri et al. [38] that attached metal elements from the workpiece observed to attach to the electrode can act as catalysts for the production of turbostratic carbon, which protects the electrode from wear, although they suggest that workpiece material moves to the tool electrode while molten, despite this not agreeing with the theory of EDM whereby ejected material is rapidly solidified in the dielectric. Marafona [39] also noted other elements from the metallic workpiece can form in the carbon-based black layer, although again the mechanism of attachment is not presented. Shue et al. [42] also observed the attachment of workpiece material on the electrode surface during dry EDM. They concluded that attachment of iron on the surface for discharge currents below 25 A created a protective layer resulting in a lower electrode wear rate which is more commonly associated with dry EDM. This does not necessarily

disagree with the theory of EDM since during machining in gas the ejected material is not solidified until it hits the electrode surface [13].

Bulk accretion of material onto the workpiece from a green compacted electrode by Wang et al. [43] as well as from powder suspended in the dielectric by Furutani et al. [44] has also been investigated and proposed as a surface alloying method. Despite this the method of accretion in either case was not explained.

Yang et al. [45] simulated the movement of atoms from both electrodes at the end of discharge, and found that both single atoms and clusters of atoms can settle on the top surfaces of the opposite electrodes. So in this model the expulsion of material created by the machining process causes the attachment to opposite electrodes, although the locations of attachment are randomly dispersed and not correlated with the opposite discharge spot. It is not clear if this mechanism is responsible for bulk attachment of material from opposite electrodes however.

It is known that the material composition of the electrode in EDM has a significant effect on the wear of the electrode and ultimately the shape of the intended part [46-48]. Similarly, the electrode material properties influence the surface finish of the opposite workpiece electrode [49]. It is thought that electrode materials with higher electrical conductivity better facilitate dielectric breakdown and promote uniform and predictable sparking, with less unintended short circuiting or “arcing”. So although the importance of initial electrode material choice is understood, the attachment of foreign materials originating from the workpiece is not well known, nor is the mechanism understood.

### 2.2.7 Miniaturisation of EDM

The precision and good surface quality of the EDM process as well as the development of new CNC systems and advanced spark generators have made EDM ideal for the fabrication of micro-parts and micro-features.

Recent research in EDM has had an increasing focus on the reduction of the size of electrodes with the aim to reduce feature resolution. Han et al. [50] investigated the machining of a tungsten rod to less than 5 μm diameter using the wire electro-discharge grinding (WEDG) method. A diameter of about 4 μm was obtainable although the diameter was not repeatable. The experimental results showed that sub-micron machining was not possible, with the conclusion that positional accuracy, machined shape error and the limit of the smallest discharge energy of the EDM machine were the main restrictions on sub-micron machining.

Egashira et al. [51] succeeded in the EDM of submicron holes by fabricating tungsten electrodes with a diameter as low as 0.3 μm. A combination of WEDG and electro-chemical machining was used to fabricate straight sub-micron diameter electrodes, as shown in Fig. 2.10. A 2 μm diameter and 5 μm deep hole was drilled in brass with a 1 μm diameter tungsten electrode, and less than 1 μm diameter holes were drilled in brass and zinc with tungsten electrodes. Holes of 0.5 μm were successfully drilled in zinc with silicon electrodes. These are the smallest holes currently reported to have been drilled by EDM [51].

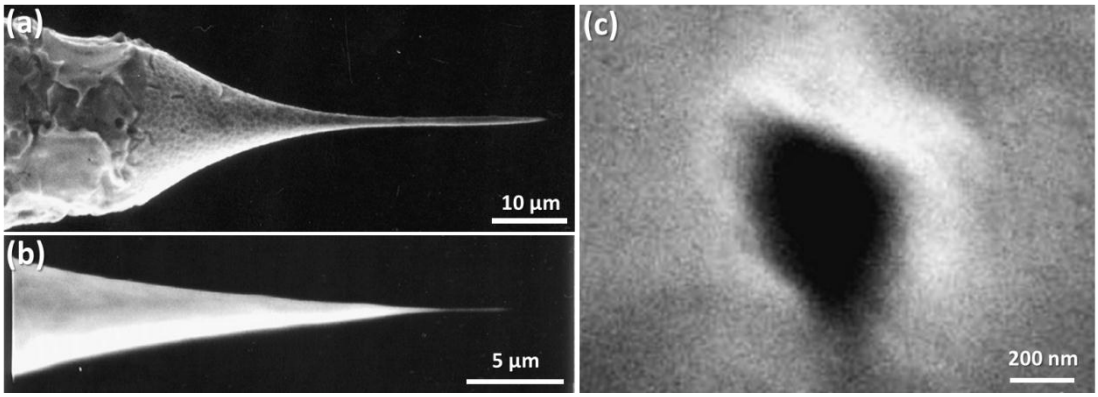


**Fig. 2.10 Fabricated electrodes using WEDG, of (a) 1 µm diameter (b) 0.3 µm diameter and (c) 500 nm diameter hole EDM drilled using WEDG fabricated electrode [51]**

Wire-EDM has also been the subject of miniaturisation efforts. Chen et al. [24] successfully cut micro-slits of 14.5 µm width with 13 µm diameter wire. This was achieved using a capacitance of 500 pF and a feed rate of 0.05 mm $min^{-1}$, with magnetic repulsive force employed to control the tension of the wire. A 13 µm wire is the smallest diameter cut with in wire-EDM according to the literature.

Kawakami & Kunieda [52] investigated the factors which limit the minimum machinable size in micro-EDM, in particular the influence of residual stress already present in the workpiece and caused by EDM, as well as the micro-structure of the workpiece. Tungsten and cemented tungsten carbide micro-rods of 20 µm diameter were machined with WEDG and it was found the residual stress present before machining caused significant bending, and the tensile stress generated by the EDM process caused bending to the side where EDM took place. It was however found that annealing to release the residual stress prior to machining was effective in reducing the bending of slender features.

The influence of crystal orientation in mono-crystal tungsten workpiece on its EDM was also examined [52]. With a roughing micro-EDM process with a depth of cut 10 µm, cracks were generated with a pattern parallel with the (100) planes. Under

finishing conditions with a depth of cut 2 µm, orientation of the cracks and the lattice interval were almost equal. The paper however also states that cracks were not found at all on polycrystalline tungsten, suggesting mono-crystal should not always be preferred for miniaturisation of EDM. Other work on the micro-EDM of single-crystal silicon supports the dependency of crack formation on crystal orientation. Song et al. [53] observed that if a spark occurred on the {110} orientation surface, the majority of heat will flow in the direction perpendicular {100} orientation. Surface tensile stress is generated in the direction of the local temperature gradient. However fewer micro-cracks were generated on the {100} orientation surface compared to the {110} under the same conditions, which can be explained by the higher fracture toughness of the {100} orientation – a $K_{IC}$ of between 1.19 to 1.23 compared to between 1.05 and 1.07 for the {110} surface.

With the continuing miniaturisation of EDM and ease of fabricating smaller EDM electrodes, the process can potentially compete with the resolution of conventional semi-conductor processing techniques, such as lithography and chemical etching. The minimum feature size obtainable by lithography is fundamentally limited by the wavelength of the incident energy according to the Rayleigh criterion, whereas in EDM feature size is limited by the stray charge remaining on the discharge circuit. The high accuracy and absence of mechanical contact between tool and workpiece when cutting extremely brittle materials also give the process advantages over mechanical based cutting processes.

Slicing of single-crystal silicon by wire-EDM has been the subject of research in recent years. For example Takino et al. [54] successfully cut low-resistivity silicon wafers, although some cracks and a rough surface were observed. They further improved upon this by using a finishing operation to produce a crack-free surface,

although in both cases cutting with oil produced a better finish than using a water dielectric [55]. Kunieda & Ojima [56] also improved the machining rate of sinking EDM for normal resistivity (8.3 Ω.cm n-type and 354 Ω.cm p-type) single crystal silicon by reducing the contact resistance between the workpiece and the metal clamping system by vacuum evaporation plating the contact surface with Al and Au-Sb for p and n-type wafers respectively.

Despite such interest in improving the machinability of silicon wafers by EDM, microstructural changes at the machined surface as well as any sub-surface defects induced by the process have not been investigated. This is of particular importance since defects such as cracks or pores, as well as amorphisation/re-crystallisation will influence the optical, electronic and mechanical performance of the wafers. Precision diamond machining, a potentially competing technology for the cutting of silicon, has been the subject of sub-surface characterisation. Yan et al used TEM and Raman spectroscopy to characterise the surface damage of silicon after precision diamond machining [57]. An amorphous layer with fluctuating thickness was formed, with a dislocation rich region below this. The mechanical cutting regime in diamond-turning of single crystal silicon has also been investigated and despite the extreme brittleness of the material, a ductile cutting regime, producing spiral-like chips can be achieved under careful machining parameter selection [58]. The EDM process however involves a distinct material removal mechanism which does not depend upon sheer mechanics to remove material and the resulting surface damage is neither predictable nor understood.

### 2.2.8 Summary of literature review of EDM mechanism

- An EDM spark is created by the Townsend avalanche effect whereby the acceleration of electrons under sufficient gap voltage will result in ionisation of neutral species in the gap, and the exponential increase in the number of ions and electrons. The bombardment of electrons and ions with the anode and cathode respectively result in a significant localised temperature rise, typically above the melting and often boiling points of all materials.

- The general consensus on the material removal mechanism is that the pressure drop upon extinguishing of the spark plasma at the end of spark on-time is responsible for the ejection of super-heated material into the dielectric from the discharge locations on both electrodes.

- It is thought that polarisable debris particles in the gap play a significant role in the breakdown of the dielectric into a spark, by providing a favourable path for discharge by the effective localised increase in gap voltage in the location of these particles.

- Despite the functional role of gap debris, excessive gap contamination is notoriously harmful to machining conditions and will eventually cause machining deformity through uncontrolled, non-randomised sparking. For this reason, flushing of the dielectric, either externally applied or created by the action of a rotating or reciprocating electrode, is used to eject machined debris from the spark gap.

- Upon extinguishing of the EDM spark and ejection of molten material into the discharge gap, this machined debris is rapidly solidified and expected not to reattach to opposite electrode surfaces.

- Material has however been observed on opposite electrode surfaces, both on the workpiece and tool electrode. This has been demonstrated as a novel coating method. By using a powder sintered electrode, or using powder-form material in the dielectric, a layer can be built up on the workpiece.

- By limiting the capacitance of the discharge circuit, nano-scale EDM is possible. This includes techniques such as electrostatic induction feeding to remove stray capacitance from the circuit. Holes have been machined with diameter of 0.5μm, using electrodes of diameter 0.3μm, also fabricated using EDM. With continued miniaturisation efforts, EDM is a possible competitor to lithographic techniques for the processing of semiconductors and other brittle materials, given the absence of significant stress during machining. Despite this, the presence surface cracks and roughness remains an issue.

## 2.3 EDM surface properties

Up to this point, the contribution of debris to the sparking process in EDM, and the attachment of debris to electrode and workpiece surfaces have been examined. The contamination of these surfaces ties in with the most well recognised disadvantage of EDM – poor surface quality.

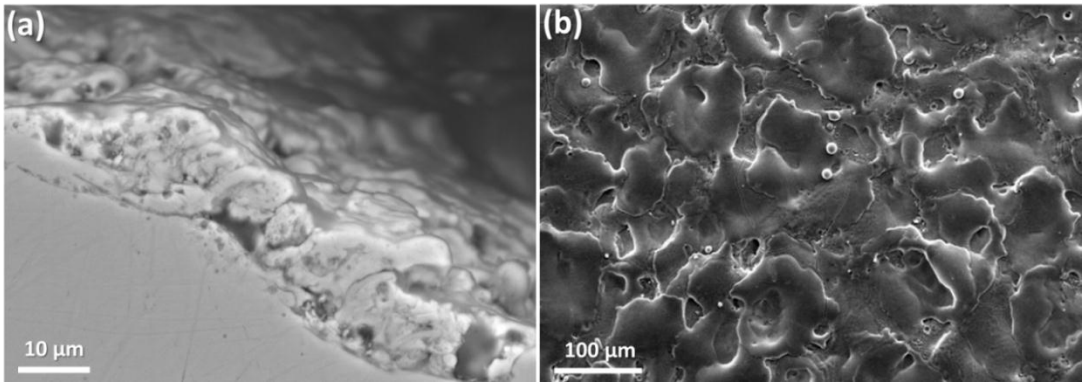


**Fig. 2.11 Recast layer on steel post-EDM**

Although the pressure drop at the end of on-time results in the ejection of much of the melted material, some of this region which is molten during discharge is not ejected but resolidified as a recast layer. This is because the viscous forces binding the melt-pool to the underlying solid bulk are too large for the force of ejection due to the pressure drop. The result is a resolidified, and modified region of material remaining on the surface of the workpiece (and tool electrode), known as the "recast layer", or "white layer" due to its white appearance under optical microscopy. This layer is typically rough, brittle, and will often contain cracks, properties usually undesirable in engineering applications where good surface integrity is required. Reducing the size and improving the properties of this layer is a continued goal of EDM research, particularly since EDM parameters associated with faster machining rates (i.e. higher

spark energies) will usually yield a larger recast layer, and hence a lower quality surface layer.

Much research has been done to simply characterise the properties of the recast layer such as thickness both experimentally [59] and theoretically [60] with changing parameters and electrode/workpiece materials, such is the importance and influence of this layer on the final properties of the EDM'd component. The layer is known to be typically fine-grained, brittle and hard due to rapid cooling rates [61], with good adherence to the bulk material [62]. It is often characterised by globules of debris, craters and voids. It has been observed that the average thickness of the recast layer decreases with lower energy sparks [61]. The thickness of the recast layer is dependent on the thermal conductivity of the workpiece, with more efficient thermal diffusion resulting in larger layers [63]. Softening of the layer via chemical etching and then removal by steel brush or mechanical grinding has been demonstrated [64] although this is a two stage process and mechanical removal is not possible for deep or complex shaped cavities or for when high precision is required; scenarios for which EDM is commonly utilised. More practical and repeatable methods are therefore required for the finishing of complex shaped EDM surfaces.

### 2.3.1 Cracks

In terms of surface defects, cracking is significant since it leads to a reduction in the material's corrosion and fatigue resistance [63]. Fatigue resistance is reduced more under tensile loading conditions [65]. Fig. 2.12 shows cracks on EDM'd steels after EDM, in both cross-section and on the surface.

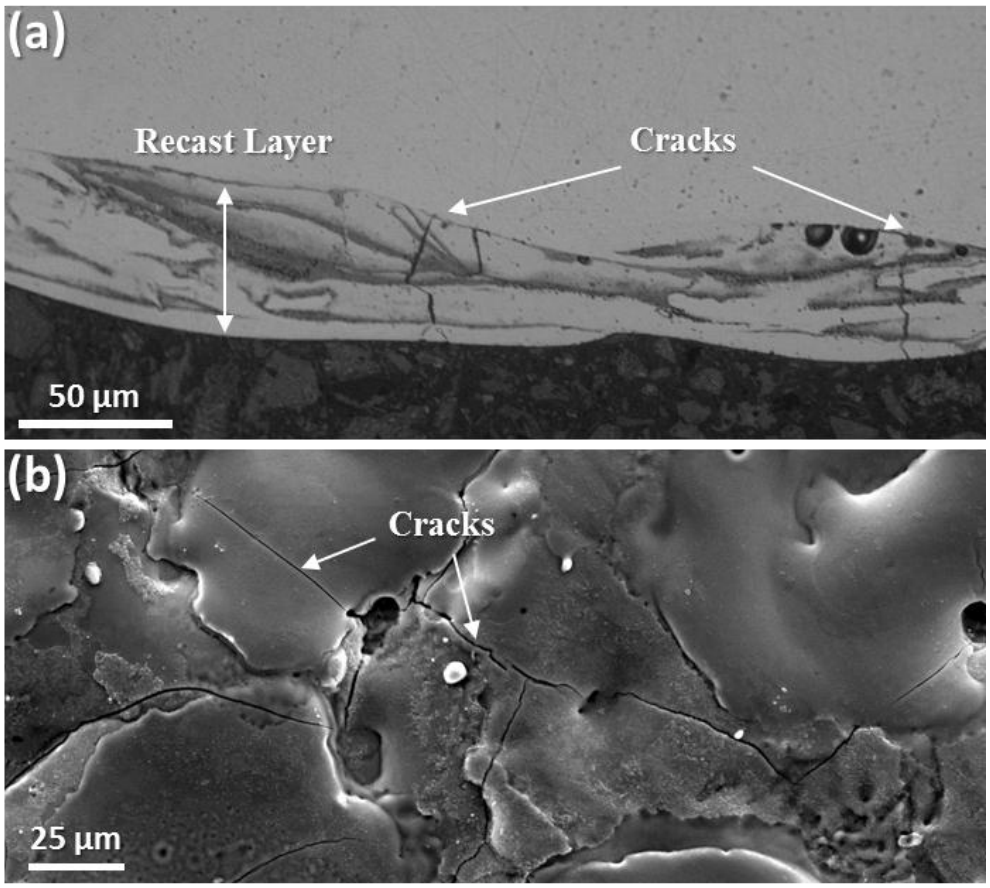


**Fig. 2.12 EDM'd steels (a) in cross-section showing a large recast layer with cracks penetrating perpendicularly and terminating at the bulk interface and (b) showing surface cracks**

Surface cracks induced by EDM typically do not penetrate to the bulk material but usually remain in the recast layer, perpendicular to the surface, terminating at the interface between parent material and recast layer [63]. An example of this can be seen in Fig. 2.12.

It has been shown by Zeid [66] that EDM has an adverse effect on the fatigue life of tool steel. Tai and Lu also [67] have shown that the presence of these surface cracks contribute to the reduced fatigue life of EDM'd tool steel. This is because the presence of micro-cracks combined with tensile residual stress at the surface shortens the two stage process of fatigue failure – crack formation then crack propagation [66]. Crack tips themselves can also act as stress concentrators. Therefore the elimination

of EDM surface cracks is desirable for improving the service life of stamping dies and other EDM'd components subject to cyclical loads.

Crack formation can be attributed to the application of tensile stresses in the machined component. Tensile stress is generated when the melted material contracts more than the unaffected parent material during the cooling process. When the stress in the surface exceeds the material's ultimate tensile strength, cracks are formed. Lee et al. [63] investigated the relationship between EDM parameters and crack formation and made several conclusions. A thicker recast layer and higher induced stress promote cracking, although the density of cracks remains similar for thick and thin recast layers. The tendency for crack formation is greater for materials with lower thermal conductivities and increases with both pulse on-time and discharge current, although on-time has been observed as the most significant contributor [63, 68]. Patel et al.'s study [68] confirms this relationship and the contribution of thermal shock to crack formation, adding that low fracture toughness and low thermal shock resistance contribute to cracking.

### 2.3.2 Surface roughness

EDM and micro-EDM are widely used in the field of mould and die making as well as for complex cavity structures [69]. The principle of EDM to maintain a constant gap width allows a high precision of machining required for such industries. However the surface finish of components such as mould tools machined by EDM will be directly reflected in the moulded part. It is also known that surfaces with higher surface roughness parameters generally exhibit higher wear rates under fretting [70] and sliding [71] regimes.

The lifetime of moulds and dies can be severely limited under the processing of certain materials. For example the plastic injection of glass and ceramic fiber reinforced plastics for automotive components can be highly abrasive for the mould cavity [72, 73]. The stress patterns associated with polymer injection pressure and thermal gradients can also be enhanced by notch effects on the mould cavity surface and accelerate the wear and ultimately failure of the mould [74]. For this reason surface finishing [75, 76] of mould surfaces as well as protective coatings for polymer moulds [72] and die castings [77] have been investigated such is the severity of the wear process and its potential economic impact.

Fatigue failure of materials for polymer moulds has also been subject to research efforts to predict and model fatigue behaviour for different microstructures and material properties [78, 79]. It is known that the presence of surface cracks, such as those introduced by EDM has an adverse effect on fatigue life [67, 80]. Combined with the contribution of surface cracks, fatigue life also has a strong dependence on geometrical surface characteristics. For example Andrews and Sehitoglu [81] showed via computer simulation and experimental verification that average asperity heights have a strong influence on fatigue life. Rohklin and Kim [82] also demonstrated that surface cavities act as preferential sites for fatigue crack initiation. Therefore, improvement to the surface finish and suppression of stress concentration sites in the surface of an EDM'd component is important for extending a component's fatigue life.

For an improved surface finish under EDM, the discharge craters should generally be of a smaller size and their distribution more uniform. This can be achieved by removing a smaller unit of material per pulse by using a low discharge energy with shorter pulse duration [49]. It is also known that an RC-type pulse generator is

preferred for producing very low discharge energies with short pulse duration via the usage of smaller capacitance and lower voltage [49]. Recently, a stochastic orbiting strategy has been applied by Maradia et al. [83], whereby the typical "planetary" movement strategy of the electrode was replaced by a more stochastic model, in order to bring random microscopic regions of the electrodes in machining proximity. In combination with this strategy a circuit using only stray capacitance (3 nF) was used to generate pulses with duration below 50 ns. The resulting surface exhibited an Ra roughness below 0.06 μm. A relatively thin recast layer was formed – less than 1 μm thick. Cracking however was still significant, and larger cracks were observed when machining for the lowest surface roughness.

### 2.3.3 Metallurgy and morphology of EDM'd materials

The surfaces of EDM'd workpieces consist of a recast layer made of material resolidified at a rate typically faster and in different compositional environments than when the bulk workpiece was formed. For this reason, new grain structures are expected. Since the final mechanical properties of the component's surface are dependent on the microstructures in this layer, its metallurgical characterisation is important.

The small size of expected phases and structures in this EDM recast layer has made detailed investigation of the contamination, either elemental or of porous and morphological structures, as well as phase structures and sizes, limited to high resolution TEM interrogation or X-ray diffraction. For example, pores of several to tens of microns diameter and observable under SEM and optical microscopy are often expected in EDM recast layers [84, 85]. Some pores can also be seen in Fig. 2.12 (a). The porosity of the recast layer at scales smaller than this has yet to be investigated,

despite the potential implications for surface integrity of such nano-scaled pores unresolvable under SEM. Similarly, while deposits of tool electrode material have been observed to form as part of the workpiece recast layer, the micro-structures of these have not been investigated.

Ekmecki investigated steel recast layer characteristics with different dielectric media and tool electrode materials [86]. The formation of retained austenite is correlated with the uptake of carbon in the workpiece surface. Since retained austenite exists outside its normal temperature range, i.e. it is metastable, it is liable to change form in service, for example under thermal cycles or deformation. Under carbon-based dielectrics, the amount of retained austenite is independent of tool electrode material, since its absorption is predominantly from the dielectric. In de-ionised water, carbon uptake and subsequently retained austenite formation is dependent entirely on using a carbon based electrode, e.g. graphite.

It has also been noted that the EDM'd surface can consist of two or three single layer-type recast layers which overlap on one another, formed from the expulsion of molten metal onto an existing recast surface [86]. This can be seen in the cross-sectioned sample in Fig. 2.12 (a).

Cusanelli et al. [62] used transmission and scanning electron microscopy to observe the complicated nano-structure of the EDM'd surface of a ferritic steel. The recast layer was shown to consist mainly of residual austenite, with martensitic needles and an austenitic layer at the interface between the recast and the heat-affected zone. Cementite was identified at the very top surface, and was attributed to carbon from the dielectric measured by Auger spectroscopy.

Ghanem et al. [87] analysed the effect of EDM on the formation of the recast layer and heat affected zones on a range of steels. They observed that the metallurgy of the surface layers depends on the hardenability of the steel. For example, hardenable steels such as martensitic steels tend to form three distinct layers. Firstly, at the top surface, a recast layer is formed containing dendritic structures, although the exact phases were not identified in this study. The size of this layer can vary between 5 μm for low discharge currents of 2 A and 80 μm for a high current of 50 A. Beneath this layer is a quenched layer, containing a martensitic structure, and the thickness of this layer depends on the type of steel as well as machining conditions. Beneath this martensitic layer is a transition layer much smaller than the other layers, where the microstructure of the raw material begins to change to that in the rest of the heat affected zone. In the case of steels more stable at high temperatures such as ferritic and austenitic stainless steels, a recast layer containing a more uniform dendritic structure is expected, beneath which a transition layer or heat-affected zone is barely visible. Therefore in the case of the more high temperature stable steels, effectively a single recast layer characterises the EDM'd surface. In the same study, surface hardening was observed in all materials after EDM, although the increase depends on carbon content, and therefore steels with an initial FCC structure containing more carbon are hardened more easily by the EDM process. Volume changes in the materials due to chemical and structural modification caused by carbon uptake and rapid heating and cooling cycles, result in plastic deformation explaining tensile residual stresses measured up to 750 MPa in the case of hardenable steels, and 500 MPa for non-hardenable steels.

Non-uniform heat flow and the resulting metallurgical transformations caused by the EDM process generate residual stresses. These stresses have been shown to be mostly

tensile in nature, with increasing magnitude with pulse energy [88]. In steel the formation of retained austenite plus distorted martensite has a strong correlation with residual stress [86]. Tensile residual stress is a critical detrimental surface integrity factor of the EDM recast layer and it can induce crack propagation and ultimate failure of the material [89].

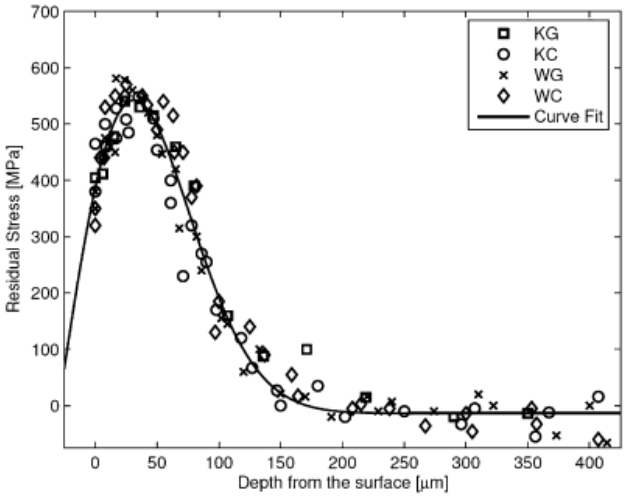


**Fig. 2.13 Residual stresses as measured by Ekmekci using XRD [86]. Experiments were with kerosene and de-ionised water as dielectrics, and electrodes were graphite and copper. The abbreviations denote the combination.**

Ekmekci et al. [86, 88] used an electro-chemical polishing technique combined with X-ray diffraction measurement according to simple elastic theory to measure the change of residual stress with depth into the machined surface of various steels. Residual stresses were found to increase rapidly to a maximum tensile stress, close to the material's ultimate tensile strength near to the surface, then sharply decreasing to a relatively small compressive stress beneath the white layer [86], and after which stress converges back to a zero value. Das et al. [89] support this trend of rapid increase at the surface and quick dissipation with depth into the workpiece with their residual stress simulation model and experimental data. Residual stresses are of particular concern for the fabrication of micro-parts by EDM where the recast layer assumes a

significant portion of the part. Soo et al. [90] showed through fatigue tests using a Ti-Al based aerospace alloy that tensile residual stress states were likely to be responsible for a slight difference in fatigue life for the WEDM'd sample compared to a conventionally milled sample. This was because in the EDM'd samples, there was no apparent surface cracking.

The recast layer has been and is still subject to much research to reduce its thickness and roughness, and these two parameters have been subject to substantial statistical analysis given its typically undesirable properties in engineering applications [61, 91-93].

### 2.3.4 Minimising, removal and surface treatment of the EDM recast layer

Although EDM has been used for decades for its efficient machining of components such as aerospace engine parts which are difficult to machine by conventional methods, surface integrity of these components has remained under scrutiny given the nature of this thermal process and the layer remaining on the surface. This has resulted in secondary operations such as grinding or chemical processing being used for the total removal of this recast layer [60].

Some adaptations of the conventional EDM process have been investigated to reduce the extent and impact of the typical expected recast layer. Yan et al. [94] used an electrode with a ball burnishing attachment to EDM and surface finish in a single operation, with a much improved finish compared to the EDM process alone. This process however is limited to round electrodes. In wire-EDM, a novel adaptation of using a wire with a diamond abrasive coating to simultaneously electrically and

mechanically machine was proven to yield a surface with minimal remaining recast, although this modification is only relevant to wire-EDM [95].

As a secondary finishing operation, abrasive micro-blasting has also been used with 4-20 µm size SiC abrasive particles in order to completely remove the EDM induced recast layer [96]. This finishing process may be desirable as it is known to induce more desirable compressive residual stresses, particularly advantageous for the inhibition of crack initiation [97, 98]. Despite this, complex shapes as well as internal cavities and highly delicate micro components machined by EDM present a problem for such a mechanical abrasive technique. A significant reduction of the initial machined precision occurs when removal of the EDM recast layer occurs in this process, since the layer can be over 50 µm thick, and therefore prediction of recast layer thickness must be accounted for in precision machining. Etching and mechanical grinding has also been demonstrated to remove the EDM recast layer [64], however a flat surface is required, and therefore it is limited against complex sinking EDM processes.

### 2.3.5 Electrical discharge coating

Modification of the workpiece by introduction of electrode material into its surface was first demonstrated by Mohri et al. [99] using sintered composite electrodes. Since this observation there has been considerable investigation into the attachment of material in sufficient quantities to replace the machined material with a coating of a preferred material. Wang et al. [43] observed a 20 µm thick layer of TiC ceramic could be produced on a steel workpiece in a few minutes under specific machining conditions. They reported a hardness of the coating three times that of the base material. Furutani et al. [44] also demonstrated a method to produce a TiC layer on a

workpiece by using titanium powder suspended in the dielectric, thereby avoiding the need to use a green compacted electrode, which by the nature of the process is required to wear. Once again, hardness in the deposited surface several times higher than that of the steel workpiece was achieved. The phenomenon of electrical discharge coating has been proposed as a practical method of introducing coatings onto tools such as drills [100], and under certain drilling parameters, extended tool life was achieved, although the life of tools treated with ED coatings is limited by their surface roughness. Other example of coatings for hard layers on workpieces include using powder sintered sacrificial titanium/graphite [101], TiC/WC/Co [102] WC/Co electrodes [5] and from titanium powder [103] as well as tungsten powder [104] suspended in the dielectric. As a result of funding much of this promising research into this practical coating technology, Mitsubishi Electric (Japan) now manufactures an electrical discharge surface treatment machine to produce functional coatings for improved durability of parts.

Despite much research into the necessary parameters required to produce a significant layer of a preferred material on a workpiece, the mechanism of this attachment process is still not clear. Wang et al. [43] suggests that a chemical reaction may occur between worn electrode material and carbon particles decomposed in the dielectric due to high temperature, after which a hard ceramic layer is built-up on the workpiece. This however is just a hypothesis and does not explain how many hundreds of microns of material can be built up within minutes. Furutani et al. [44] repeat this theory by suggesting that the heat caused by discharge is responsible for metal powder particles reacting with cracked carbon, and the resultant powder adheres on the workpiece. Although it is acknowledged that discharge is required in order for

material to attach to the workpiece, it is not understood whether attachment occurs during and at the location of discharges.

Yang et al. [45] simulated the movement of atoms from both electrodes at the end of discharge, and found that both single atoms and clusters of atoms can attach to the top surfaces of the opposite electrodes. So in this model the expulsion of material created by the machining process causes the attachment to opposite electrodes.

### 2.3.6 Summary of literature review of EDM surface properties

- Surface cracking is a problem for EDM'd components, given its contribution to reduced fatigue life and corrosion properties. The rapid cooling cycles involved in EDM results in the presence of cracks on a component surface. These cracks are difficult to avoid without the use of low energy machining parameters, associated with reduced machining rates. Using discharge circuits designed to minimise discharge energy as much as possible, to enable super-finishing using EDM, cracks have still been observed [83].

- It is known that high surface roughnesses and large surface asperities contribute negatively to the fatigue and wear behaviour of EDM'd components such as moulds and ultimately their failure, due to notch effects exacerbating stress. Using ultra low capacitance discharge circuits, a roughness of 0.06μm has been achieved.

- Carbon is known to be present in the surface of an EDM'd component after machining when using a carbon-based dielectric. This affects the microstructures formed in the remelted surface given the altered elemental composition. It has been found that carbon uptake is correlated with the

formation of a metastable retained austenite in the surface in steels. This metastability means that under changing service conditions, i.e. thermal cycles or deformation, form change and therefore volume change may occur, and consequently induced internal stresses may be relieved by the formation of cracks. When using a carbon-absent dielectric – deionised water, carbon uptake relies on the presence of a graphite (or other carbon based) electrode.

- In microstructural analysis of the recast layer which has been performed in steel it has been found that martensite and retained austenite are formed in the surface of steel, despite an originally ferritic workpiece. These structures are known to contribute to tensile residual stress, which would explain the tensile stress measurements made by Ecmecki [86, 88]. Residual tensile stress measured in recast layers of approximately 20 μm thickness, which is typical for many EDM'd components, measured at a maximum of 580 MPa, and up to 750 MPa for a recast layer of 80 μm thickness.

- A number of techniques for removing and surface finishing the EDM surface have been investigated. These include chemical etching then grinding, as well as micro abrasive blasting, both of which involve total layer removal. A novel method of using a ball burnishing electrode to EDM then surface finish has also been demonstrated, although electrode shape is limited to being round.

- Contrarily, as well as removal of the recast layer being pursued, a deliberate coating of tens of microns thickness has been demonstrated by the EDM process. This is performed either using a powder sintered electrode, or a powder mixed dielectric. In producing a TiC based coating, improved wear properties have been demonstrated for potential use as a drill coating.

## 2.4 Surface treatment by pulsed electron beam irradiation

Pulsed electron beam irradiation is a relatively new addition to the wide range of already available surface modification techniques. The process uses short (μs) pulses, or shots, of high current electrons to rapidly remelt surfaces to improve their surface finish as well as some mechanical and chemical properties. The process has been used to modify the surface properties of several engineering alloys, such as titanium alloys and steels. Mould steel subject to EDM has also been treated by Uno et al. [75, 105], whereby Rz surface roughness was successfully reduced and evidence of improved corrosion behaviour was shown.

The key advantage of this surface modification process over laser techniques is the beam application and uniformity over approximately 60 mm diameter [75]. This is combined with the ability of the beam to modify surfaces with equal effect at angles highly acute to the direction of the beam [75], therefore allowing complex shaped structures to be treated. Since remelting of the surface with uniform energy density across the area of irradiation occurs during pulsed electron beam treatment, the process is considered in this thesis for its potential to improve surface morphology of electrical discharge machined surfaces, and in particular the property of surface cracking. These characteristics of the process therefore make the process particularly suited to components machined by EDM.

### 2.4.1 The physical process of pulsed electron beam generation

The pulsed electron beam process used in this thesis falls under the category of low energy (20-40 keV), high current (10-30 kA) electrons beams [106]. It is also often described as large-area or wide-aperture given the cross-sectional area of the beam is greater than 10 $cm^2$ [106]. The process was developed by a research group at the

Institute of High-Current Electronics of Siberian Branch of the Russian Academy of Sciences under Prof Dmitry Proskurovsky. Low-energy, high-current electron beams, like other high-energy beams were conventionally produced using vacuum diodes with explosive emission cathodes [107]. The beam duration using such diodes is approximately ~$10^{-7}$ s. Such beams are characterised by local non-uniformities in current density distribution [108]. To be able to apply such low-energy, high-current electron beams to the surface modification of materials, a homogenous beam is required. A beam (shot) duration of ~$10^{-6}$ s allows a substantial improvement in cross-sectional homogeneity of energy density distribution [107]. Beam duration and beam homogeneity can be increased by using plasma-filled diodes [109]. Pulsed electron beam systems for surface modification of materials are therefore now based on a plasma-filled diode system, whereby the electron beam incident on the workpiece travels through a plasma.

The irradiation process is carried out in an air-tight chamber into which argon gas at a pressure of 0.05 Pa is supplied, after an initial 10 minute vacuum cycle time. Argon gas is used as the medium for plasma build up required for electron beam propagation. The diameter of the beam is 60 mm; with a pulse-time of 2-3 μs, pulse interval of 11 seconds and energy density 1<20 J/cm2. The beam has been shown to extend further than its 60 mm diameter although the energy density is significantly diminished beyond this point. Within the 60 mm diameter, energy density is thought to be uniform [75]. A schematic of the irradiation process is shown in Fig. 2.14.

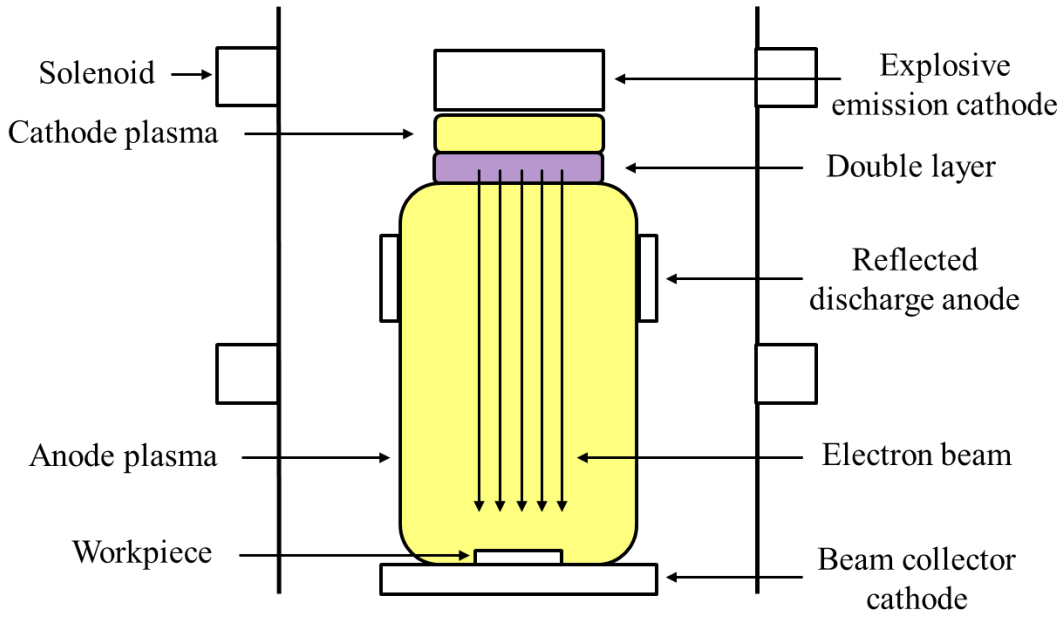


**Fig. 2.14 Schematic of pulsed electron beam irradiation process. Adapted from paper by Batrakov et al. [110].**

The following principle of the process was provided from private communication with Dr Grigory Ozur at the Institute of High-Current Electronics. Firstly a solenoid coil produces a magnetic field, at the maximum intensity of which a pulsed voltage of 5 kV is applied to the anode and Penning discharge is initiated. After a duration of 50-100 μs, the current of the Penning discharge reaches 150-170 A and a plasma column is formed near the anode. After a delay time of 10-30 μs, an accelerating voltage of up to 40 kV (on the Sodick AP1L) with a rise time of 20-100 ns is applied to the cathode. The electric field is concentrated in a near-cathode ion layer and reaches values of up to 400 kV/cm. Explosive emission takes place on the cathode causing a number of cathode spots (dense plasma clouds) to appear and emit electrons. The applied voltage is concentrated in a double-layer, between the cathode plasma and the anode plasma, in which electrons are accelerated and the beam is formed. The electron beam accelerated in the double layer is transported through the anode plasma to a collector cathode where the workpiece is placed.

### 2.4.2 Metallurgy and morphology of electron beam treated materials

The bombardment of low energy, high current electrons upon a workpiece surface causes it to rapidly heat and quench resulting in a significantly altered microstructure. Heating is normally sufficient to cause melting. The preferential melting of asperities on a rough surface results in a smoothing effect on most materials subject to this process. Rapid cooling rates are caused by the irradiation process and as a result, novel microstructures can be rapidly produced on large surfaces. This ability of producing microstructural changes over a large area in a short time is a key advantage compared with other techniques, and as a result, many recent publications regarding pulsed electron beam irradiation focus on metallurgical changes occurring in the remelted layer of the irradiated surface and the resulting changes in mechanical and corrosive properties.

For example, with the surface treatment of iron by pulsed electron beam irradiation with energies of 20-30 kV, depending on parameters, a molten layer with a melt lifetime of $\sim 10^{-6}$ s expected. Maximum cooling rate from the melt and maximum velocity of the crystallisation front both occur at the surface, and are approximately $\sim 10^{9}$ $Ks^{-1}$ and 5 $ms^{-1}$, respectively [111]. Due to the rapid cooling rate from the melt, nano-scale grain sizes and metastable phases such as retained austenite are expected to form.

Markov & Rotshstein [112] observed a hardened surface zone which could be produced using short pulse (10 μs) electron beams. It was observed that this hardening effect could occur from solidification from the liquid state as well as from the solid state by quench hardening. Ivanov et al. [111] applied this improvement in surface hardness to the treatment of WC-TiC-Co cutting tools. Again, increased

hardness was measured up to depths of about 10 μm and relative wear during cutting tests was also reduced at high cutting speeds. These improved mechanical properties were explained by TEM observation of a fine grain structure in the remelted layer, thereby improving grain boundary strengthening as well as the segregation of nanosized carbide particles, resulting in solid solution strengthening. Rotshtein et al. [113] also used TEM to show that significant grain size reduction can occur at the surface of alloys subject to electron beam irradiation. Zuo et al. [114] have also reported austenite grains as small as 50 nm, and carbides down to 20 nm forming after irradiation of AISI D2 steel, contributing to improved mechanical properties at the surface. Despite hardening of the surface being widely reported, it has also been shown that a slight softening of the workpiece can occur at the very top surface of 316L stainless steel [115]. Below this the hardness is increased up to 100 μm below the surface. The hardening of the sub-surface layers is consistent with the reported improvement in wear behaviour under both dry [116] and lubricated conditions [117].

Improved mechanical performance has been shown to occur after pulsed electron beam treatment of a number of materials. These include WC/Co cutting tools whereby the wear rate was reduced by up to 1/8 of the raw material after treatment due to nano-scale grain refinement [118, 119]. Al-Si alloys have also shown improved wear and hardness properties after treatment in a number of research papers [120-122], with significant impact given their use in engine block cylinders in internal combustion engines. The surface of Hadfield steel used for long service-life die-inserts subject to pulsed electron irradiation has also shown increased micro-hardness as well as enhanced wear resistance owing to the formation of a nano-scale grain structure [116]. The presence of residual stress in both the ferrite and austenite phases of AISI D2 steel has been confirmed by Zhang et al. [123], whereby after 25 pulses the

austenite phase has a tensile stress value of 700 MPa, and the ferrite has a similar value of 730 MPa. Despite the softening effect observed at the top surface of 316L steel after irradiation, an increase in hardness and an improvement in wear behaviour were seen, which is thought to be due to work-hardening of the heat-affected zone beneath the remelted layer [115].

Achieving nanostructured layers at the surfaces of metals is a research goal in its own right with significant implications for mechanical properties. Therefore the ability to achieve a uniform layer of nanostructures on large and complex shaped surface is highly desirable.

There are a few processes which may compete in producing very fine grain structures. It has been shown that a nanostructured layer produced by surface mechanical attrition treatment (SMAT) at the surface of carbon steel can improve its surface hardness and fatigue strength [124]. In this study, the treatment process utilised the vibration of steel balls, typically 1-10 mm diameter [125], larger than those used in shot peening, to induce significant plastic deformation and grain sub-division. Similarly, a nanocrystallised surface on 316L stainless steel, yielded by fast multiple rolling rotation, was shown to improve its surface hardness by almost three times [126]. Fast multiple rolling rotation (FMRR) is a plastic deformation process using static pressure to introduce a nanocrystalline surface on a large sample. Both of these processes are limited from application on components with a small surface or with delicate surface structures. This is because SMAT requires the use of balls usually above 1 mm diameter, and FMRR requires linear movement. Both processes are effective due to the application of mechanical forces. Pulsed electron beam irradiation is an ideal competing process for the surface treatment and modification of highly intricate surfaces.

Pulsed electron beam irradiation is also of interest from the perspective of surface modification due to its proven enhancements to corrosion behaviour. For example, pure titanium has been shown to exhibit an enhanced corrosion resistance after surface treatment, which may be due to the redistribution of impurities segregating at grain boundaries, resulting in an improved ability to form a passive film [127]. A similarly improved corrosion performance was demonstrated on M50, Cr4Mo4V and 316 L steel after pulsed electron beam treatment, which can be explained by the gradual dissolving of carbides and other alloying elements, with irradiation number, becoming more uniform in the surface layer. The improvement is also explained by an increase in retained austenite content [115, 128, 129]. It has also been observed that cratering, which can occur after pulsed electron beam irradiation due to preferential melting and eruption of carbides and other precipitates, reduces corrosion performance due to the occurrence of pitting corrosion. However homogenising a surface containing many craters, by treatment with further pulses to reduce the number of craters, can inhibit further pitting corrosion [115].

As well as improvements to mechanical and corrosion properties through metallurgical modification, pulsed electron irradiation has been used to modify the surface morphology of a range of materials.

Surface treatment of thermal barrier coatings has been demonstrated by the irradiation process by Mei et al. [130] and combined with an improvement in oxidation resistance and thermal insulation, a significant reduction in surface porosity and surface asperities was achieved. Undesirable surface features from cutting such as milled lines in Ti6Al4V can also be eliminated by the process [131], and surface roughness can generally be significantly reduced in a large number of other materials

to Rz values below 1 μm from above 6 μm in cemented tungsten carbide [132], martensitic orthopaedic stainless steel [133] and mould steel [75].

As well as the improved surface finish generally expected after finishing with electron beam irradiation, hydrophobic properties have been demonstrated as a combined result of the induced surface features as well as chemical properties of the surface layer. A consistent increase in water repellency contact angle of more than 20° was demonstrated in cemented carbide [132], and similarly an increased contact angle for blood has been demonstrated for surface treated orthopaedic stainless steel [133]. In this same study, a reduction in force required for mould releasibility for a moulded resin was also demonstrated, which is likely influenced by both surface roughness characteristics and hydrophobic surface properties.

### 2.4.3 Surface treatment of EDM'd components

The use of large-area EB irradiation for the post-processing of EDM'd surfaces is potentially one of the most useful applications of such a process given the combined necessity of this machining process for the production of complex shapes in the hardest materials, and its notoriously undesirable surface characteristics.

EB irradiation has been subject to preliminary investigation for the surface finishing of electrical discharge machined surfaces, with reductions in Rz surface roughness from above 6 μm to below 1μm demonstrated [75]. Despite this the change in thickness of the EDM recast layer with irradiation parameters has not been investigated, nor have the poor morphological characteristics of the EDM'd surface such as presence of voids and particularly the presence of surface cracks. The uniformity of the electron beam over a large area and therefore the uniform energy

density applied to the surface is of interest for resolving issues created by the rapid heating and cooling generated during EDM, such as cracks.

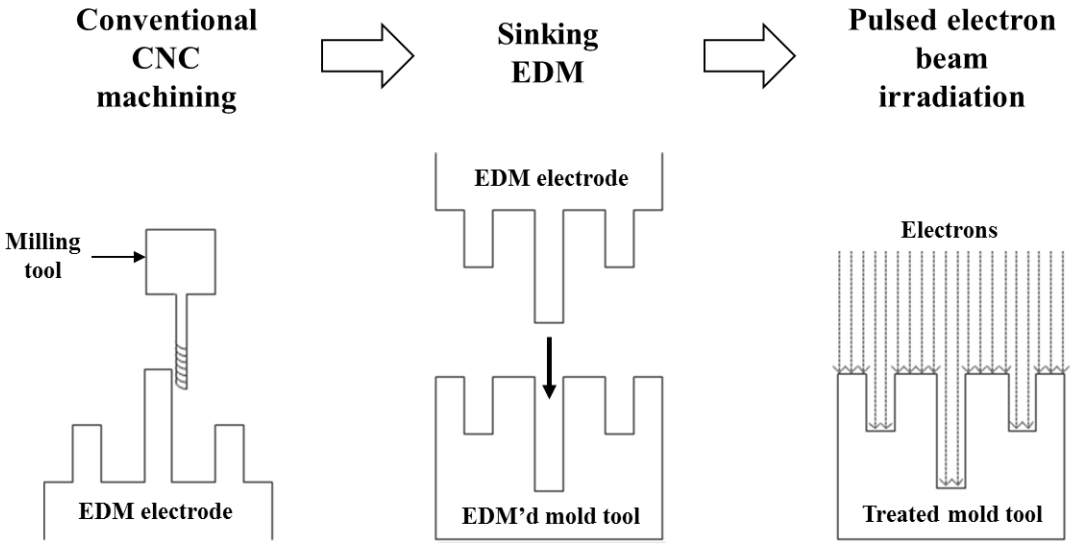


**Fig. 2.15 Proposed process chain for EDM involving electron beam surface treatment**

The widespread use of EDM for the processing of highly complex components, cavities, blind and through holes, for example the products seen in Fig. 2.1, increases the relevance of investigating the effect of the EB irradiation process on the EDM surface. A process chain featuring both an EDM-produced mould tool and post-machining EB surface treatment is shown in Fig. 2.15. With increasing demands for higher form accuracy and lower surface roughness of produced parts, technologies for the finishing of tools have been the subject of much research [134]. A rapid and predictable ejection mechanism during mechanical separation at the end of the moulding process is also vital to the repeatability of the operation and the quality of the finished part and it is known that higher surface roughness increases friction coefficients and the required de-moulding forces between tool and moulded part [135]. Murray et al. [136] have used pulsed electron irradiation to demonstrate the intricacy of the surface treatment process for mould tools, showing that the bottoms of

holes 20μm diameter as well as the tops of intricate micro-rods can be successfully polished, with under 20 nm Ra roughness achievable. The polishing of surfaces close to parallel to the beam direction was also elucidated, showing that the process is ideal for surface treatment and modification of complex and delicate structures. This accompanies the direction of miniaturisation of EDM components, and suggests that EB irradiation is well suited as a post-processing technique for EDM.

### 2.4.4 Summary of literature review of pulsed electron beam irradiation

- Pulsed electron beam irradiation is a novel surface modification technique, not yet industrially widespread, which is able to heat and remelt surfaces over a large area in single pulses. An argon gas medium is used for the provision of initial electrons which are then accelerated by a pulsed voltage difference into a workpiece. The high current ($10^2 – 10^3$ A) created by this acceleration results in significant heating and usually melting of metallic surfaces.

- Resultant surfaces have typically a greatly reduced surface roughness. Other properties which have been widely tested are increased hardness and improved wear behaviour across a range of materials, including steels, Ti-6Al-4V, Al-Si alloys and WC. Hydrophobic surfaces have also been created by EB irradiation.

- Rapid thermal cycles invoked in the workpiece surface by the process have resulted in a number of TEM studies and fundamental materials characterisation analyses to identify the material structures responsible for the improved mechanical properties of workpiece surfaces. It is understood that an ultrafine grain structure, for example 50 nm austenite grains and 20 nm

carbides in steel, is mainly responsible for mechanical property improvement via grain boundary strengthening. This is despite tensile residual stresses of up to 730 MPa being measured in a steel surface subject to irradiation.

- The process has been used to improve surface roughness and corrosion properties of an EDM'd surface, although changes to surface cracks caused by EDM have not been investigated.

## 2.5 Summary of research gaps

This chapter has introduced the EDM process from its general usage and applications, to its fundamental physical mechanism. The concept of surface integrity as a result of EDM was identified as one of the key challenges facing the process, and was discussed further in detail. A developing surface modification process – pulsed electron beam irradiation was also identified as an appropriate and novel method of solving some problems which face the EDM recast layer, and recent developments in the technique as well as its mechanism were described in detail.

The precise phenomena occurring during the EDM process have remained unclear as acknowledged by experts in EDM such as Kunieda et al. [13] and Schumacher [31]. The lack of understanding of the mechanism of material removal and the complex nature of energy distribution between electrodes means that composition, material structure and morphology of the surface of the machined component are difficult to predict, and experimental investigation of these factors is ongoing. The complexity of the recast layer on the workpiece surface has resulted in its generally being considered undesirable, and particularly for high value components, removal of this layer is usually performed, despite the inherent change in dimensions of the part.

Using new pulse generation technologies to limit discharge energies, there has been a drive in EDM towards miniaturisation, since the absence of mechanical force allows delicate and brittle components to be machined. Miniaturisation of the process has been demonstrated by sub-micron diameter holes being drilled by EDM. In such precision machining operations, control of the negative properties of the EDM recast layer is particularly important, particularly where the recast layer is thick compared to feature size.

In order to tackle the gaps in understanding of the EDM process, the research problems identified and summarised in the literature review are grouped into three main areas, as described below.

- Nano-scale characterisation of the EDM surface has not been performed. Phenomena such as contamination, cracks and pores previously observed at the micro-scale have not been investigated at the nano-scale. TEM analysis of a single element or single crystal material machined by EDM, which could reveal clearly these phenomena, has not been performed.

- Transfer of material between electrodes is known to occur in EDM, whether as an unintended contamination, or potentially for the development of coatings. Despite this the mechanism of attachment is unknown and disagrees with the conventional idea of EDM whereby material is solidified in the discharge gap and flushed from the region. EDX analysis has not been performed on discharge craters to help reveal the role of discharges in deposition

- Surface cracking, complex surface morphology and surface roughness remain inherent negative characteristics of an EDM'd surface. Removal of the recast layer is often performed, requiring additional process steps, and dimensional loss from the part. Recast layer removal is typically performed by grinding/polishing or a combination of chemical etching and grinding. A research gap has been identified for the application of a novel method of uniform heating and remelting via an electron beam, rapidly and over a large area to tackle these typical EDM characteristics of surface cracking and high roughness.

# 3 Experimental

## 3.1 Introduction

In this chapter, the choice of materials, the EDM and electron beam irradiation equipment used, as well as the materials characterisation techniques utilised throughout the thesis, are detailed. The principles and practical methods of electron microscopy, X-ray diffraction and Raman spectroscopy are explained. For clear interpretation of the results in this thesis, an understanding of these methods as well as their capabilities and limitations is required.

## 3.2 Machining and surface modification equipment

### 3.2.1 EDM

Two EDM machines were used for the work in this thesis. The machine used for experiments in Chapter 4 was a Panasonic "MG-ED72" sinking EDM machine, with an "MG-NC72" numerical controller. Rotation of the tool electrode was used for flushing of machined debris. In Chapters 5 and 6, a Sodick AP1L sinking EDM machine was used. Reciprocating movement of the tool electrode in this case was used to flush machined debris. A kerosene dielectric oil was used in all machining experiments. Parameters chosen are explained in the experimental sections of the relevant chapters.

### 3.2.2 Pulsed electron beam irradiation

A Sodick "PF32A EBM" machine was used for all pulsed electron beam irradiation experiments. The machine is a commercialisation of technology developed by the Institute of High Current Electronics (IHCE) of the Russian Academy of Sciences in

Russia under Professor Proskurovsky [107]. Table 1 shows the parameters used under all experiments. The main variables used in pulsed electron irradiation experiments are accelerating voltage, which yields a certain energy density at the workpiece surface, and the number of irradiation cycles (shots). The principle of the process is described in section 2.4.1.

**Table 1 Sodick "EBM" machine settings**

| | |
|---|---|
| Cathode (accelerating) voltage | 15-40 kV |
| Number of shots | 1-20 |
| Solenoid voltage | 1.5 kV |
| Anode voltage | 5 kV |
| Argon pressure | 0.05 MPa |
| Beam diameter | 60 mm |

## 3.3 Electron microscopy

Since much of the work in this thesis requires characterisation at the micron and sub-micron scale, electron microscopy techniques are pervasive throughout. For this reason, here, the principles of electron interaction with solids and the different forms of information which can be gathered from it are discussed. Williams and Carter [137] have been referred to in this section, as their textbook discusses TEM and electron microscopy in great detail.

There are several advantages to using electrons for materials characterisation, in terms of identifying both chemical and structural properties. Firstly the interaction of electrons with energy in the order of 10s and 100s of kV generates a number of different signals, each of which contains information about the sample. An illustration of this process is shown in Fig. 3.1.

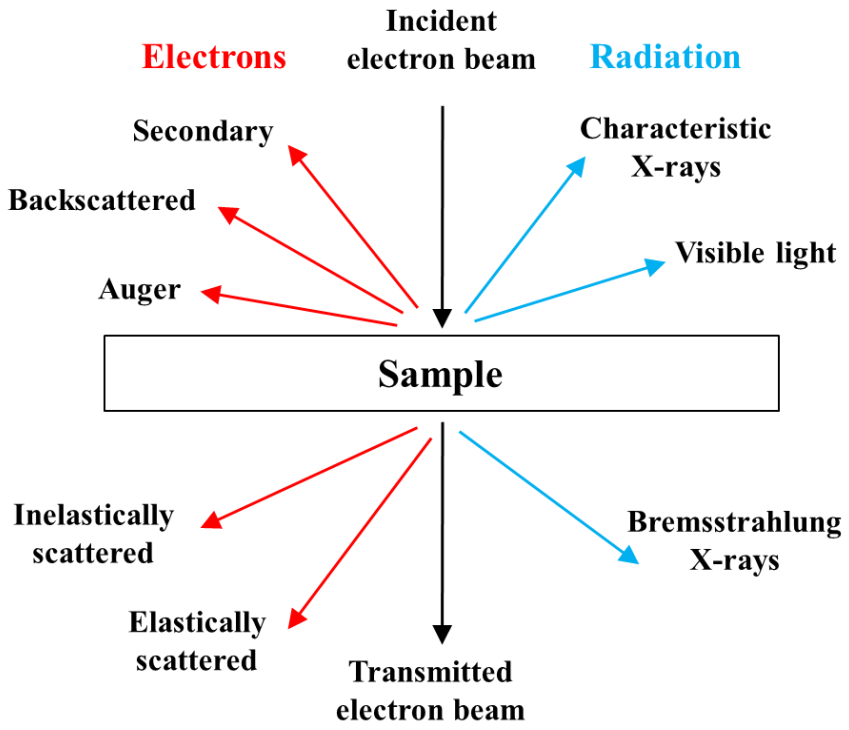


**Fig. 3.1 Illustration of signals produced via the interaction between electrons and a material. Adapted from Williams and Carter [137].**

Secondly the spatial resolution of electron imaging is much higher than that of optical microscopy. The spatial resolution of optical microscopy is fundamentally limited by its wavelength according to the Rayleigh criterion. The wavelength of visible light is in the order of 100s of nanometres, whereas that of electrons is in the order of several picometres, using acceleration voltages typical of scanning and transmission electron microscopes. For this reason, the spatial resolution achievable with electrons is limited by the system's equipment as well as scattering by the sample, and not by its wavelength.

Finally, the depth of field exhibited by electron microscopy can be much greater than that of optical microscopy, allowing more useful imaging of complex surfaces and morphologies. This is because the depth of field becomes greater when the distance to the object is much larger than the diameter of the limiting aperture of the lens, and

therefore since for optical microscopes to achieve higher resolutions, a larger lens must be used, the depth of field is typically poor. In electron microscopy, the limiting aperture lens must be made relatively small, and therefore the depth of field is relatively large.

### 3.3.1 Scanning electron microscopy

Scanning electron microscopy (SEM) is widely used in this thesis, in terms of both amount and variety of information gathered. The SEM uses electron energies typically between 10-40 kV to produce and detect secondary electrons and often back-scattered electrons (BSE) from the surface of the sample. Secondary electrons are created when incident electrons on the surface of a sample pass near enough to an atom to impart some energy onto a low-energy state electron, causing it to be ejected with some kinetic energy, and causing a path change to the incident electron. The ejected electron is a secondary electron. Secondary electron imaging is heavily topography dependent, since the ejected electrons are low energy and the population emitted comes from very near the surface. Back-scattered electrons are caused by the elastic reflection of incident electrons with atoms which are normal to their path, resulting in 180° scattering back of the electrons. Because of this mechanism BSE imaging is dependent on atomic number, given more electrons will be reflected by larger nuclei, resulting in higher contrast for heavier elements. Many SEMs are equipped also with an Energy-dispersive X-ray spectroscopy (EDX) detector to perform compositional analysis of the sample surface. In this thesis, EDX analysis using the SEM was performed using a Philips XL30 SEM at 20kV with attached Oxford Instruments EDX detector and INCA X-ray microanalysis software. All other SEM work was performed using a Hitachi S-2000N equipped with back-scattered detector for qualitative compositional analysis.

### 3.3.2 Transmission electron microscopy

When a sufficiently thin sample is used (~100 nm), electrons at higher voltages (80-300 kV) can pass through a material allowing a variety of useful information to be gathered. Despite the usefulness of TEM techniques, the extent of its usage is limited due to the difficulty and expense involved in preparation of electron transparent samples. In this thesis, Focused Ion Beam (FIB) machining with an FEI Quanta 200 3D FIBSEM was used to prepare one sample of single-crystal silicon and two samples of stainless steel. The FIB lift-out technique for TEM sample preparation allows excellent spatial control and precise measurement of sample thickness. FIB machining to approximately 80 nm thickness was attempted in certain regions of each sample to ensure excellent electron transparency and clear observation of structures under TEM analysis.

Since the characterisation techniques involved in TEM are more complicated than in SEM imaging, this introduction is used to explain the principles of the many forms of imaging using a TEM for proper interpretation of the results.

Imaging in TEM occurs due to three unique mechanisms: diffraction contrast, mass-thickness contrast and phase contrast. Diffraction contrast is particularly useful in this thesis and is the most frequently used technique as it can resolve grains at different orientations, and therefore gives clear information of the size, and variety of orientations, of grains within the sample. Diffraction contrast arises due to scattering at specific angles for which the incident electron beam satisfies the Bragg condition for that crystal (ordered atomic lattice planes) and therefore small changes in lattice orientation relative to the incident beam can yield large changes in imaging contrast. Mass-thickness contrast arises due to incoherent elastic scattering of electrons, also

known as Rutherford scattering. Given the ability of electrons to penetrate the atom (compared to the original alpha particle experiment), the scattering of the electron beam is highly sensitive to mass i.e. atomic number and thickness of the sample. This information is most useful at high scattering angles, whereby the influence of atomic number on the extent of scattering is maximised. Finally, phase contrast arises due to shifting of the phase of the electron beam as it passes through the sample, and the subsequent interference of the directly transmitted beam and the diffracted beam allows direct imaging of the lattice planes. This is often referred to as High-resolution TEM (HRTEM). All three of these mechanisms are exploited in this thesis.

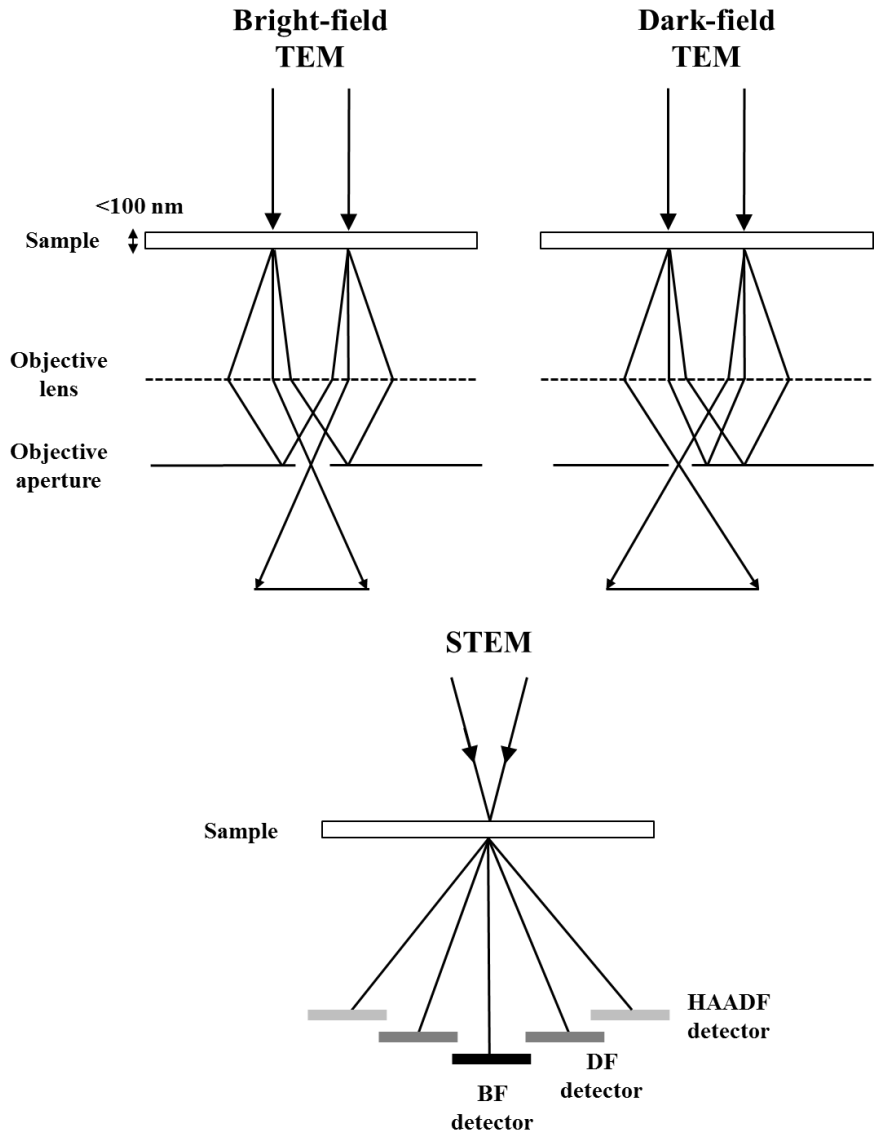


**Fig. 3.2 Schematic of TEM bright and dark-field modes, as well as the different detectors in STEM. The primary difference of the convergent incident beam in STEM as opposed to parallel incident beams in TEM should be noted.**

In conventional TEM mode, Bright-Field TEM (BF-TEM) exhibits high contrast from diffraction, since the aperture directly behind the sample is open, the detected directly transmitted beam is used to produce the "bright" parts of the image. Dark-Field TEM (DF-TEM) blocks the central parts of the detector directly behind the sample and instead uses the strongly diffracted beams to produce "bright" contrast in the image. In a sense, DF-TEM is the "reverse" image of that produced by BF-TEM. Choice between these imaging modes depends on emphasis required of different parts of the

sample as well as initial positioning of the sample. Correct usage of BF and DF-TEM can produce very different images depending on the extent of certain lattice orientations present in the sample. Conventional TEM also allows the collection of selected area electron diffraction patterns (SAED). Before the recombination of the transmitted diffraction patterns in order to create an image on the image plane, the diffracted electrons are first collected in the back focal plane. These patterns of electrons can be collected as an image (SAED) which reveals information on the crystal structure, orientation of the crystal, as well amorphicity and polycrystallinity. The ability of TEM to produce SAED patterns which correspond to exact areas on a conventional TEM image is a powerful advantage and is utilised in this thesis.

Whereas in conventional TEM a parallel electron beam is incident on the sample, Scanning TEM (STEM) uses a convergent beam which is scanned across the surface, much like in an SEM. In STEM, detectors positioned at different angles from the directly transmitted beam can be switched on to give different information about the samples. These detectors are BF-STEM, DF-STEM and High-Angle Annular Dark-Field STEM (HAADF-STEM). The BF-STEM detector includes the non-diffracted beam and the beam diffracted to very small angles. This means both mass-contrast and diffraction-contrast phenomena contribute to the image. DF-STEM includes beams collected due to a greater extent from mass-contrast and a small contribution from diffraction contrast, and HAADF-STEM imaging arises purely from mass-contrast i.e. is effectively chemical imaging, as it only collects beams at very large angles.

TEM and (STEM) were performed with a JEOL 2100F at 200kV. Bright field (BF), Dark Field (DF), and High Angle Annular Dark Field (HAADF) STEM were performed using a JEOL Digital STEM System. Energy dispersive X-ray

spectroscopy (EDX) mapping was performed in STEM mode using an Oxford Instruments INCA X-Ray Microanalysis System.

### 3.3.3 Energy-dispersive X-ray spectroscopy

As shown in Fig. 3.1, characteristic X-rays are produced when electrons of sufficient energy are incident upon as a sample, and this is independent on its being electron transparent. These X-rays can be used in order to quantitatively analyse the chemical composition of a sample. Fig. 3.3 is a schematic of this process. An electron incident on an atom is capable of ejecting a core electron from its orbital. An electron from a higher orbital will relax to fill this core hole created and this difference in energy is emitted in the form of an X-ray photon with energy characteristic of that element. Since the energy levels of core electrons are dependent on proton number and hence the element of the atom, the energy and intensity of a characteristic X-ray can be interpreted and quantified by an EDX detector and software. This thesis uses EDX as a tool in both SEM and STEM techniques. Despite the usefulness of the technique, when detecting low atomic number elements ($Z<11$) the ratio of Auger electrons to X-ray photons yielded becomes significant enough that quantification is difficult, this ratio of X-rays to Auger electrons is known as fluorescence yield. Qualitative analysis of lower atomic numbers however is still valid. EDX in chapter 4 was performed using the JEOL 2100F TEM in STEM mode at 200 kV. EDX in chapter 5 was performed using a Philips XL 30 SEM at 20 kV.

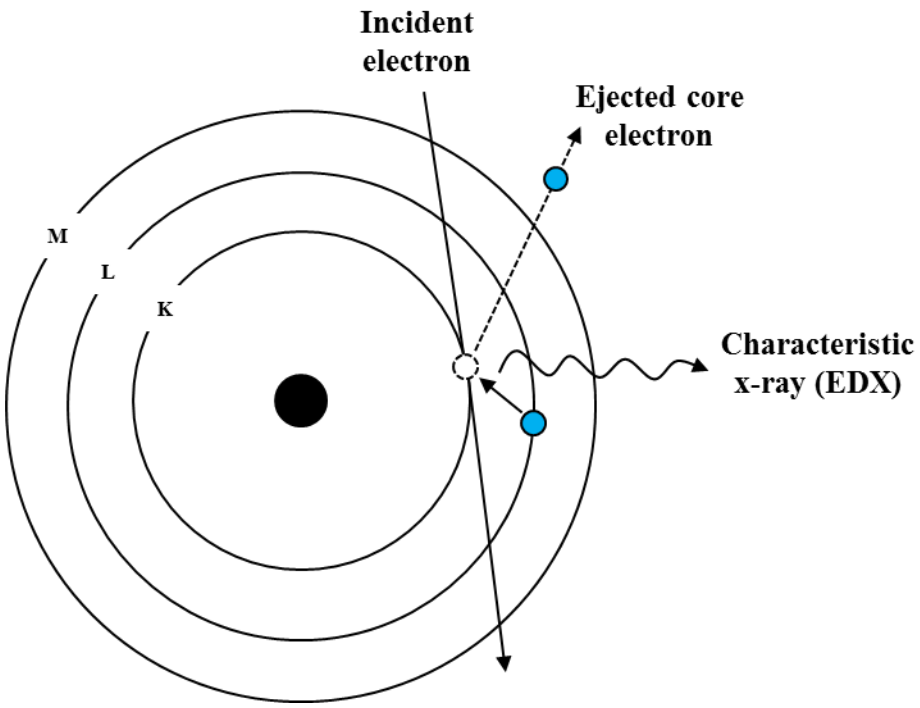


**Fig. 3.3 Schematic of electron-atom interaction process to produce characteristic X-rays for use in EDX analysis**

## 3.4 X-ray diffraction

X-ray diffraction (XRD) is a powerful materials characterisation technique for determining the crystal structure of typically polycrystalline materials. It can be used also used to detect changes in overall orientation (texture) of the grains in a polycrystalline sample.

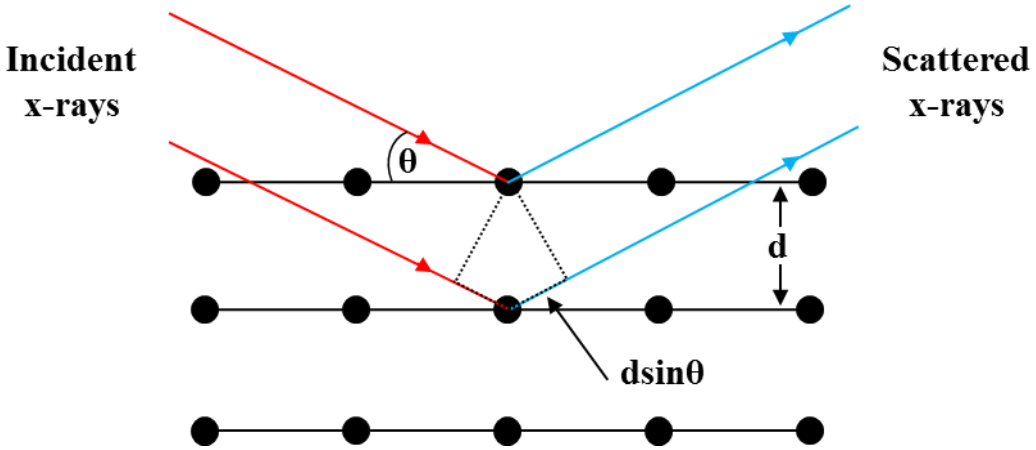


**Fig. 3.4 Illustration of the X-ray diffraction process in a crystal.**

X-rays incident on a sample with either be transmitted with direction unchanged, or scattered (diffracted) by the electrons of the atoms in the sample. X-rays are chosen for the diffraction process since their wavelengths are of the same order of magnitude as the d-spacings in a crystal lattice. The constructive interference of scattered X-rays is used in XRD analysis, and Fig. 3.4 gives an illustration of this diffraction process. If the scattering atoms are arranged symmetrically, such as in a crystal lattice, with separation **d,** the scattered waves will add constructively in directions where their path-length difference **2dsinθ** equals an integer number of wavelengths of the X-ray. The resulting reflection spots at multiple angles of **2θ** yield a diffraction pattern unique to specific crystals. From this information, the phases present in an alloy can be easily identified, and the ratios between their amounts can be compared.

In this thesis, a Bruker-AXS D8 Advance XRD system was used with Cu k-α radiation. Copper X-ray radiation has a wavelength of 0.154 nm, close to the lattice spacings of many materials and therefore typically yields a high count.

## 3.5 Raman spectroscopy

Raman spectroscopy exploits the phenomenon of inelastic scattering of monochromatic light by phonons in a molecular system. The impingement of a photon of laser light on a molecule results in the excitement and subsequent relaxation of the molecule to a different energy state. The energy difference between these states is conserved in the energy shift between the photon re-emitted from the molecule and the incident photon.

In this thesis, Raman spectroscopy is used to characterise the structure of single crystal silicon machined by EDM. Silicon is easily analysed using Raman spectroscopy as the intensity of the Raman spectra is relatively high, and the signal positions of the amorphous and different crystal structures are distinct and do not overlap. For this reason, single crystal silicon is typically used to calibrate Raman systems. In this work, Raman is used simply to clarify the presence of the amorphous phase, characterised by a broad hump, with peak at 480 $cm^{-1}$ wavenumbers. A Horiba "LabRAM HR" confocal Raman microscope with a green 532 nm wavelength laser was used for Raman experiments.

## 3.6 Surface roughness measurement

White-light interferometry (WLI) was used to yield surface profiles and provide Ra, Sa and Sz roughness values. Interferometry exploits the principle of wave superposition whereby 2 waves interfering will combine to produce a resulting pattern determined by the phase difference between the waves – i.e. constructive interference if in phase and destructive if half a wavelength out of phase. A Fogale nanotech "Photomap 3D" WLI was used for all roughness measurements. Two parameters were used for assessing surface roughness; Sa and Sz. The Sa parameter is the arithmetic

mean of the absolute values of the surface departures from the mean plane, and Sz is the ten point average of the five highest peaks and five deepest valleys.

## 3.7 Materials and sample preparation for microscopy

Cross-sections of samples imaged by SEM were mounted in a conductive polymer resin before polishing on six different polishing wheels down to the finest polish using 1 µm size diamond paste. Etching of steel samples was achieved using a five second swab of Kalling's solution to reveal grain boundaries. Kalling's solution contains copper chloride, hydrochloric acid, methanol and water in a 1:20:20:20 ratio, respectively.

Workpiece materials as well as EDM tool electrode materials used in the thesis and their chemical compositions are shown in Table 2 and Table 3 respectively. The choice behind each material is explained in the relevant research chapter.

**Table 2 Workpiece materials**

| Material | Chemical Composition (weight %) |
|---|---|
| 304 Steel | Fe – Balance, Cr – 18.5, Ni - 8.5, Mn – 1.5, Si – 0.5, C – 0.06 |
| 310 Steel | Fe – Balance, Cr – 25.6, Ni– 19.2, Mn – 0.9, Si – 0.6, C – 0.05 |
| Co-Cr-Mo | Co – 65, Cr – 28, Mo - 7 |
| Inconel 718 | Ni – 53, Cr – 19, Fe – 18, Nb – 5, Mo – 3, Ti – 0.9, Al – 0.5, C- 0.08 |
| Single crystal silicon | 99.999% pure Si |

**Table 3 Tool electrode materials**

| Material | Chemical Composition (weight %) |
|---|---|
| Tungsten | 99.95% pure W |
| Copper-tungsten | W – 85, Cu - 15 |
| Copper | 99.9% pure Cu |

# 4 Contamination and material structure of the EDM'd surface at the nano-scale

## 4.1 Introduction

The aim of this chapter is to perform a nano-scale characterisation of the EDM'd surface. This involves the TEM analysis of a successfully electrical discharge machined feature in single-crystal silicon. The use of TEM analysis reveals electrode material contamination, the presence of pores and cracks, microstructural changes of silicon in the recast layer and the depth of such phenomena. The use of single-crystal silicon allows clear observation of such phenomena since the material is chemically homogenous and has a single crystal orientation. This study will give a fundamental insight into how EDM damages surfaces of materials machined by the process, and is necessary research to accompany the direction of EDM towards micro scale and sub-micron scale machining. The research is also particularly relevant as recast layers become smaller through new technologies from machine tool manufacturers, and hence the unobserved defects become more dominant.

Contamination of both the recast layer and electrodes is known to occur during EDM [38, 39, 43]. The presence of pores, craters and cracks in the recast layer is also well documented at scales visible when using SEM and optical imaging techniques. There has however been little research into these phenomena at the nano-scale, i.e. below what is visible to SEM imaging. This is because the preparation of samples for TEM imaging is time consuming and expensive. The surface integrity of components machined by EDM is critical to their overall mechanical and chemical performance, and it is dependent on the presence of the aforementioned morphological and

metallurgical features in the machined surface. For this reason, a fundamental understanding of the recast layer introduced by EDM at the nano-scale is necessary.

There are a number of reasons for the choice of single-crystal silicon as a workpiece material to perform a sub-micron scale characterisation study:

- Firstly and most importantly, using single-crystal silicon, observation of modifications to its crystal and morphological structure is simple, and in this respect the material is highly characterisable under TEM imaging. This is because the presence of a single element and a single crystallographic orientation gives the material homogenous contrast under all imaging modes, and so contamination and modification is much easier to resolve. The single element also enhances the effectiveness of EDX elemental analysis. The single-crystal structure also allows easy identification of interruptions to the lattice.

- Secondly, the material can be relatively easily machined using focused ion beam in order to prepare a TEM sample. This is because it is electrically conductive and therefore dissipates charge created by both the electron and ion sources, which would otherwise cause unpredictable ion beam paths due to electrostatic repulsion/attraction. The absence of inclusions, grains and precipitates in the material also improves the predictability of the milling process particularly when thinning the TEM lamella down to 100 nm for high electron transparency, since different phases are machined at different rates under FIB.

- Thirdly, as it continues to miniaturise, EDM is a potentially competing technology for the processing of semiconductors. Silicon ingot slicing in

particular is a developing area. Information gathered regarding surface damage will accompany other research into the machinability of single-crystal silicon for example by Okada et al. [138] Qian et al [139] and Kunieda et al. [56]. Detailed analysis of the damage mechanism of single-crystal silicon under EDM has not been performed.

## 4.2 Methodology and experimental setup

### 4.2.1 Research methodology

In order for the observations made in this chapter to be relevant to a range of EDM machining setups, the silicon feature from which the TEM lamella was extracted had to be created under stable machining conditions representative of a normal machining process, whereby debris build up is avoided. To achieve this, an experimental investigation of machining parameters, machining rate and hole quality and accuracy was conducted. Given that single-crystal silicon has a number of material variables including orientation, p- or n-type, and dopant element, an array of experiments was performed to determine the exact experimental setup with the most stable machining results. This initial study began with drilling through-holes to determine the point at, if at all, unstable machining were to occur. Based on this initial machining, a stable machining depth was chosen for further machining trials to establish the most stable machining regime.

After these tests were performed, the most successful machined hole was identified in terms of fidelity to intended shape, surface and edge damage, as well as machining speed and stability. This sample was used to prepare a TEM lamella using FIB of approximately 100 nm thickness for full electron transparency.

To fully characterise the TEM sample, the following were done. Firstly, a sequence of selected area electron diffraction patterns was then taken from the edge of the sample inwards. Low magnification inspection for any larger scale structures such as voids and cracks, as well as contamination was then performed. EDX analysis was then conducted to determine the elemental composition of contamination observed in the sample. High magnification imaging of the lattice and contamination was then conducted in order to identify the presence of defects and new structures introduced by the EDM process.

Finally, Raman spectroscopy was also used on the rest of the original EDM'd feature to confirm that the material structure of silicon determined by TEM analysis was created by the EDM process and was not a by-product of the FIB milling technique.

### 4.2.2 EDM and materials

Machining was performed using a Panasonic sinking-EDM with a rotating electrode for flushing of machined debris. A schematic of the setup is shown in Fig. 4.1. A polycrystalline tungsten electrode with diameter 150 ± 5 μm was prepared using wire electrical discharge grinding (WEDG) [140] before being sunk into the workpiece. These dimensions were chosen to be representative of a micro-EDM setup, and not intended to push the limits of miniaturisation. The dimensions of the machined feature themselves are not expected to have any influence on the phenomena taking place in the machined surface. The workpiece materials for this study were low resistivity, n-type (antimony doped) and p-type (boron doped) single-crystal silicon wafers, with orientation types both [100] and [111]. Properties are shown in Table 4. Open circuit voltage and capacitance of the relaxation type pulse generator remained constant at

90V and 1000pF respectively, and a kerosene oil dielectric was used. An Olympus OLS3000 confocal laser microscope was used to produce images of holes after EDM.

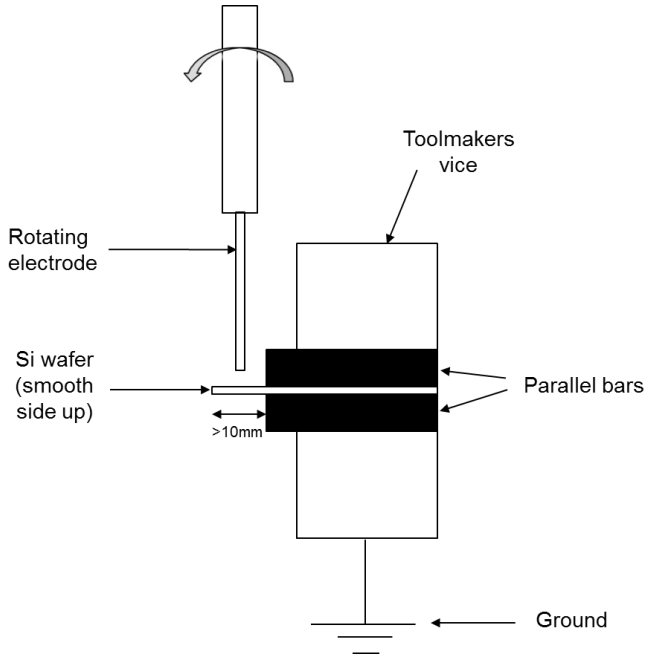


**Fig. 4.1 Schematic of final clamping arrangement**

**Table 4 Properties of single-crystal silicon workpieces**

| Type | Dopant | Orientation | Resistivity (Ω.cm) | Thickness (μm) |
|---|---|---|---|---|
| n | Antimony | [100] | ≤0.02 | 500 |
| n | Antimony | [111] | ≤0.02 | 500 |
| p | Boron | [100] | ≤0.02 | 500 |
| p | Boron | [111] | ≤0.02 | 500 |

### 4.2.3 TEM and Raman spectroscopy

Focused Ion Beam (FIB) machining using an FEI Quanta 200 3D FIBSEM was performed to prepare a lamella from one of the machined holes. Given that it was not possible to perform a lift out from the bottom surface of the hole due to the restricted manipulator entry angle, an “L” shaped lamella was prepared from the top edge of the hole. A micrograph of one of the machined holes, along with the site of lift-out and a TEM image of the lamella attached to the copper grid are shown in Fig. 4.2.

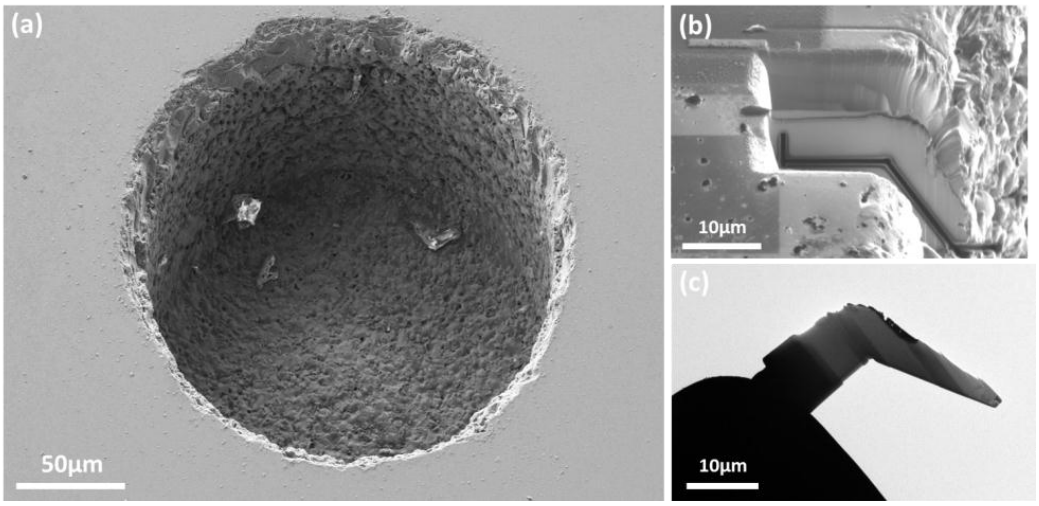


**Fig. 4.2 (a) Machined hole on n [100] type Si wafer, machined with positive electrode, (b) TEM lamella position on edge of hole, (c) Thinned Lamella attached to a Cu lift-out grid**

Raman spectroscopy was performed using a LabRAM HR (Horiba) confocal Raman microscope with green 532 nm wavelength laser. An exposure time of 5 s was used for all measurements. The process is particularly useful for the rapid evaluation of the state of pure materials such as single-crystal silicon. The maximum penetration depth for 532 nm laser light in Silicon is 927 nm [141]. This is important for qualifying the depth assessed by Raman spectroscopy and therefore whether its results represent the machining induced recast layer or a combination of it and the bulk beneath. The use of Raman spectroscopy is also a demonstrator for quality control in EDM processing of silicon and electrical ceramics.

## 4.3 Results

### 4.3.1 Achieving stable machining conditions

It is well understood that during EDM a build-up of machined detritus can occur if there is insufficient flushing of the machining region, for example when producing high aspect ratio features where the distance for machined chips to exit the machined feature is large. This build-up of conductive debris can cause sparking and therefore

machining in unintended areas (short-circuiting), such as the sides instead of the end of the electrode. For this reason, initial experiments involved drilling through-holes through the silicon wafers (500 μm) in order to determine the depth beyond which unstable machining would occur. Fig. 4.3 shows the three repeat tests for each variant of silicon, whereby unstable machining occurred in all tests, beginning at between 750 seconds and 2000 seconds depending on material type and orientation. Unstable machining can be identified in the graphs by sudden changes in z-translation rate. Gap voltage of 90 V and capacitance of 1000 pF were determined as effective for simple sinking EDM experiments according to preliminary tests in single-crystal silicon.

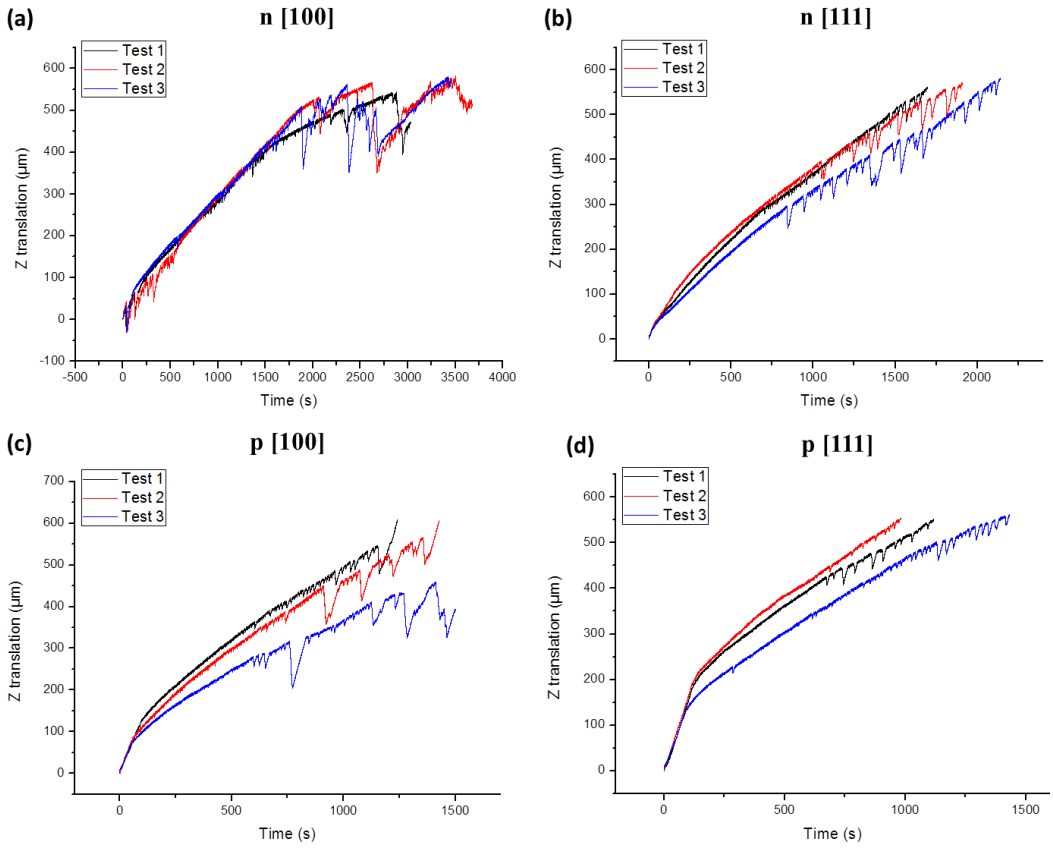


**Fig. 4.3 Z-translation against time during EDM sinking of through-holes in all silicon wafers.**

The increasing instability of z translation rate and interruption of machining with time for all materials was assumed to be caused by a combination of two factors. First

debris build up due to insufficient evacuation of machined detritus is known to cause randomised machining conditions from unintended sparking. It was also proposed that clamping of the workpiece to the earthed block was a factor. Since small clamping forces are necessary given the brittleness of the material, proper earthing contact and therefore the intended machining voltage across the electrodes was not properly maintained. The holes exhibiting poor roundness, particularly at the outlet, can be seen in Fig. 4.4.

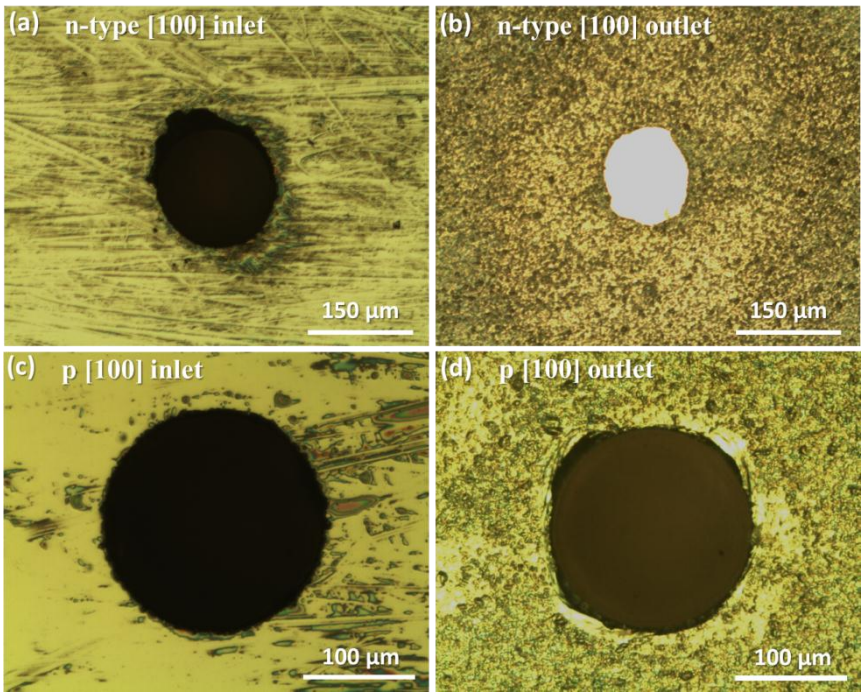


**Fig. 4.4 Example inlet and outlet holes of drilled through-holes in n-type and p-type [100] silicon. Poor roundness can be observed, particularly for outlet holes.**

The smaller diameter at the outlet end of the through-holes compared to the entry hole is caused by excessive electrode wear. The poorer roundness seen at the outlet holes can be explained by the more erratic machining conditions present for all tests after a z translation of 500 µm. For all variants of silicon, after approximately 100 µm of machining depth, z translation rates of the tests for each material showed increase divergence. After 300-400 µm, unstable machining was seen for almost all tests, with

significant interruptions to the machining regimes. In light of this information, a set of experiments was undertaken to produce blind holes of 100 µm sinking depth, which was in the most as stable and repeatable machining region. Other machining parameters remained the same in this new set of machining trials, except that swapping the polarity of the workpiece and electrode, an important parameter in EDM, was also investigated.

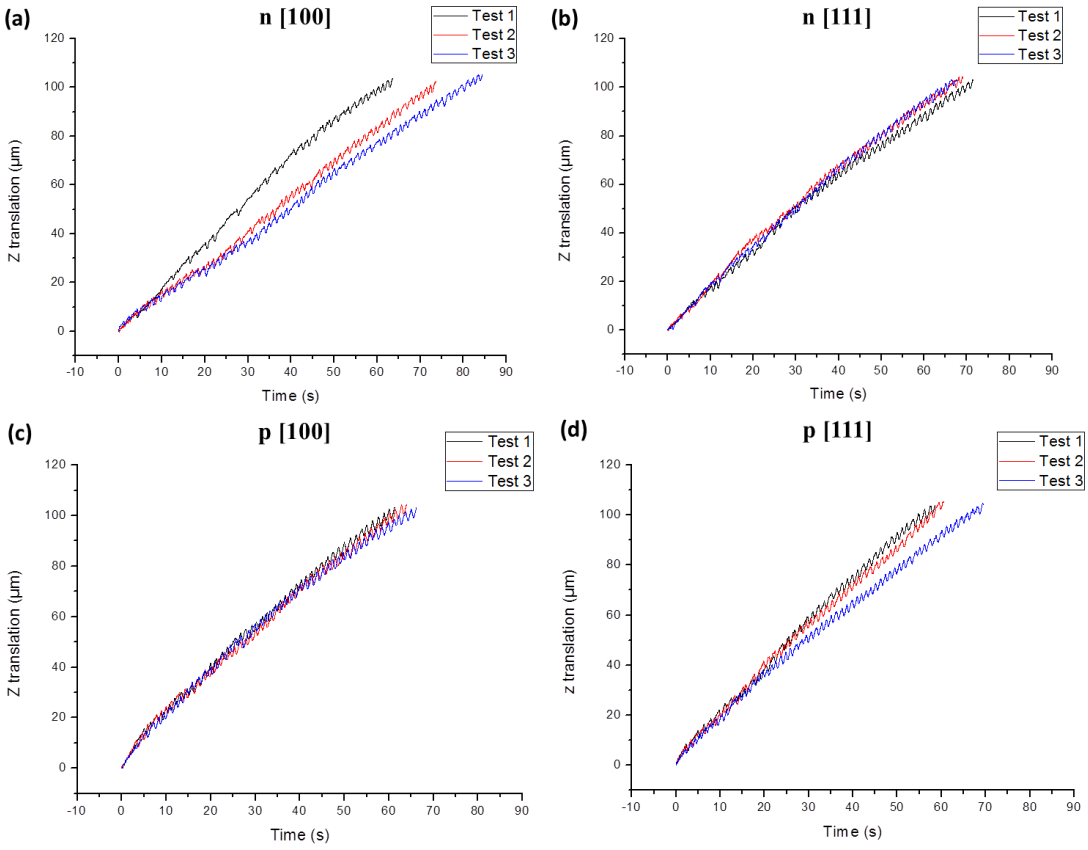


**Fig. 4.5 Z-translation against time for machining of blind holes using parallel bar clamping and a negative tool electrode polarity**

Fig. 4.5 shows electrode z translation against machining time for workpieces machined using negative tool electrode polarity. None of the setups resulted in unstable machining, such as that seen when machining through holes (Fig. 4.3). Good repeatability was shown, and under all setups 100 µm depth was achieved between 60 and 80 seconds. Mean completion time was highest for the n [100] workpiece at 74 s,

and lowest for the p [111] workpiece at 62.9 s, translation rates of 1.41 and 1.66 µ/s respectively. On all tests, curvature in the z-translation graphs was observed, with gradient decreasing with time, indicating decreasing of machining rate. The three tests performed under negative tool polarity and on the n [100] and p [111] workpieces showed scatter more scatter in terms of translation rates compared to the other experiments, specifically, one test during the n [100] machining was 23% quicker than the average of the other two, and a test during p [111] machining was 15% slower than the average of the other two. Since EDM is fundamentally a stochastic process, and machining is dependent to some extent on debris movement and effectiveness of flushing, different gap conditions in each test may explain the scatter among machining rate results.

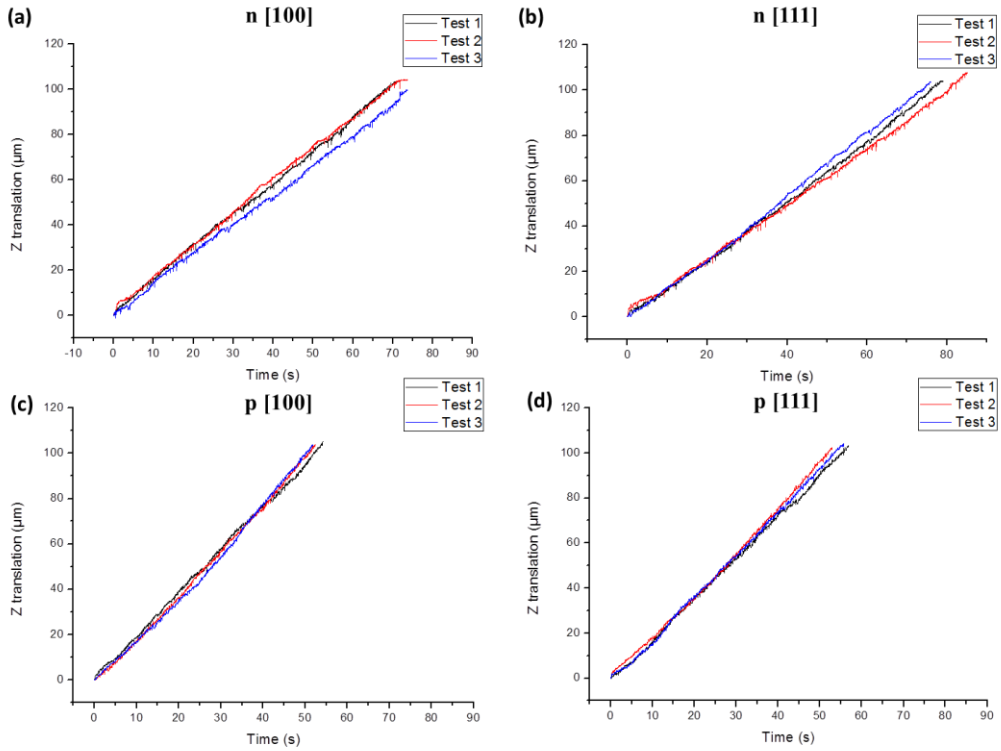


**Fig. 4.6 Z-translation against time for machining of blind holes using parallel bar clamping and a positive tool electrode polarity**

The testing was repeated with reversed electrode polarity; now using a positive tool electrode. For all tests and types of silicon, the gradients of z-translation against time, as seen in Fig. 4.6, were more constant compared to that under negative tool polarity, indicating machining was stable for the entire duration of sinking. In Table 5 the overall translation rates, i.e. the final depth of cut divided by the time taken, are shown.

**Table 5 Overall translation rates for blind holes machined using both polarities**

| **Positive electrode translation rates (µ/s)** | | **Negative electrode translation rates (µ/s)** | |
|---|---|---|---|
| n [100] - 1 | 1.43 | n [100] - 1 | 1.62 |
| n [100] - 2 | 1.41 | n [100] - 2 | 1.38 |
| n [100] - 3 | 1.35 | n [100] - 3 | 1.24 |
| n [111] - 1 | 1.31 | n [111] - 1 | 1.44 |
| n [111] - 2 | 1.26 | n [111] - 2 | 1.5 |
| n [111] - 3 | 1.36 | n [111] - 3 | 1.52 |
| p [100] - 1 | 1.93 | p [100] - 1 | 1.68 |
| p [100] - 2 | 1.98 | p [100] - 2 | 1.62 |
| p [100] - 3 | 2 | p [100] - 3 | 1.55 |
| p [111] - 1 | 1.78 | p [111] - 1 | 1.77 |
| p [111] - 2 | 1.93 | p [111] - 2 | 1.73 |
| p [111] - 3 | 1.87 | p [111] - 3 | 1.49 |

The p [100] and [111] workpieces machined quicker in 52.3 and 55.2 s mean completion time, or 1.97 µ/s and 1.86 µ/s respectively, whereas the n [100] and [111] variants yielded translation rates of 1.40 µ/s and 1.31 µ/s respectively. The saw-tooth pattern seen in Fig. 4.5 for negative tool polarity was not seen in this case, indicating generally more stable machining and possibly avoidance of debris build-up. After these machining tests, the resultant features were imaged.

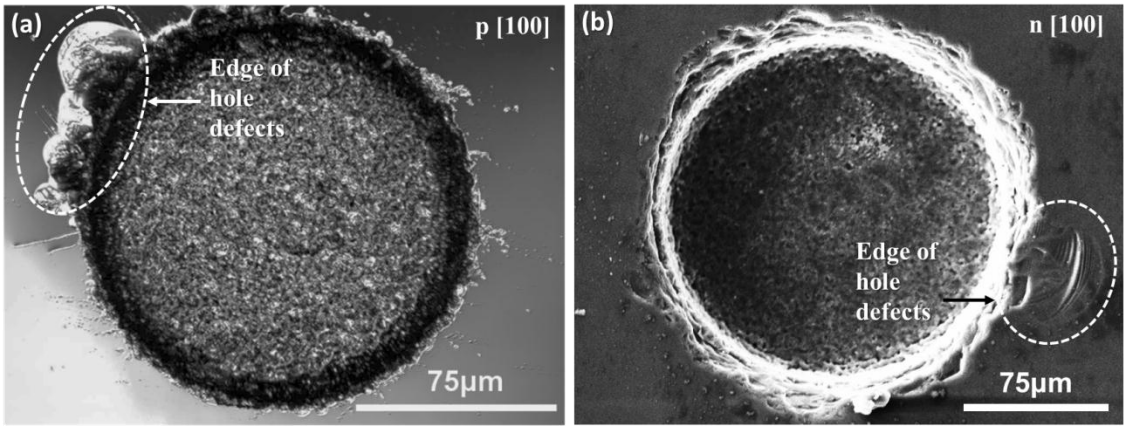


**Fig. 4.7 Comparison of holes machined using positive tool polarity - (a) p [100] silicon and (b) n [100] silicon. Hole-edge defects appeared more frequent on the p type workpieces.**

Fig. 4.7 shows example holes machined using what was determined as the more stable and faster in the case of the p type, (positive) tool electrode polarity. Both p and n-type silicon exhibited some defects at the edges of machined holes.

For use of a workpiece for TEM lamella preparation, the n [100] type workpiece from the positive tool electrode experiments exhibited the fewest machining defects, compared to others, and this material was chosen. This study is interested in the nano-scale features present in the surface of workpiece which may otherwise be considered defect free under SEM imaging. Therefore the characterisation of a feature which would normally be considered to have few defects is of particular interest. A hole with no edge defects from this same workpiece, and the feature used to prepare the TEM lamella is shown in Fig. 4.2.

### 4.3.2 TEM lamella preparation

Preparation of a TEM lamella from the bottom of the machined hole presented difficulties, since after successful cutting of a lamella, a manipulator must be moved to this location. However with this hole aspect ratio, entry of the manipulator to the bottom of the hole was not possible. Therefore a lamella was prepared from the top

edge of the hole to enable successful attachment to the copper TEM grid. An L-shaped lamella was prepared, which effectively curved down approximately 15 µm depth into the hole. In Fig. 4.8 different surface characteristics at the very edge and top of the hole can also be seen, such as a fracture, possibly caused by mechanical contact before machining between tool and workpiece, whereas the sides of the hole exhibit a more typical EDM surface.

### 4.3.3 Micro-damage observation

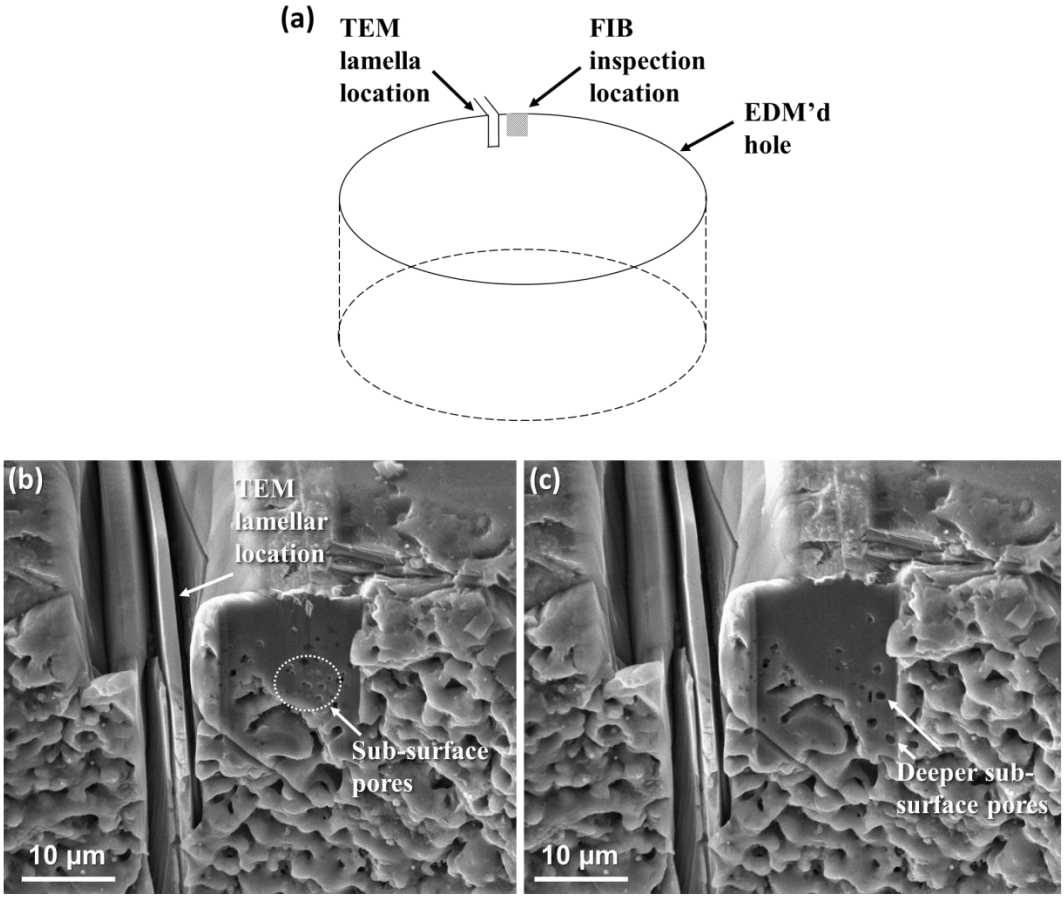


**Fig. 4.8 FIB milling of EDM surface near lamella, of approximately (b) 1 µm depth and (c) 2 µm depth. Sub-surface pores are revealed at different depths into the surface. A schematic showing the location of the lamella extraction location and area of FIB inspection is shown in (a)**

The FIB technique used to prepare the TEM lamella can also be used to perform sub-surface characterisation of cross-sections. Fig. 4.8 shows the use of this technique

next to the region of lamella lift-out. FIB milling was performed in incremental distances of 100 nm into the surface, to reveal micro-level sub-surface damage. Pores between 500 nm and 1 μm were seen after cutting to 1 μm depth, as seen in Fig. 4.8 (a), and slightly larger pores between 1 and 2 μm diameter were seen only after milling to 2 μm depth, where smaller pores previously seen were no longer present.

### 4.3.4 Nano-structure

Under bright-field TEM imaging, locations at the bottom of the L-shaped lamella seen in Fig. 4.2 were observed for overall identification of material structure and damage and for obtaining diffraction patterns.

#### 4.3.4.1 Diffraction patterns

A sequence of SAED patterns in a direction perpendicular to the machined surface and in intervals of approximately 250 nm was used to determine microstructural changes induced by the EDM process (Fig. 4.9). Close to the surface, in pattern 1, a combined amorphous structure with some possible polycrystalline signal, as well as the single crystal pattern was identified. The amorphous structure may have been caused by the FIB process [83]. In locations 2 and 3, an amorphous signal was no longer present, and a combination of single crystal and a twinned pattern was observed, this phenomenon is further discussed around Fig. 4.19. In locations 4, 5 and 6 a solely single crystal pattern, the same as that of a non-EDM'd region of the lamella (see Fig. 4.19 (a)) can be seen.

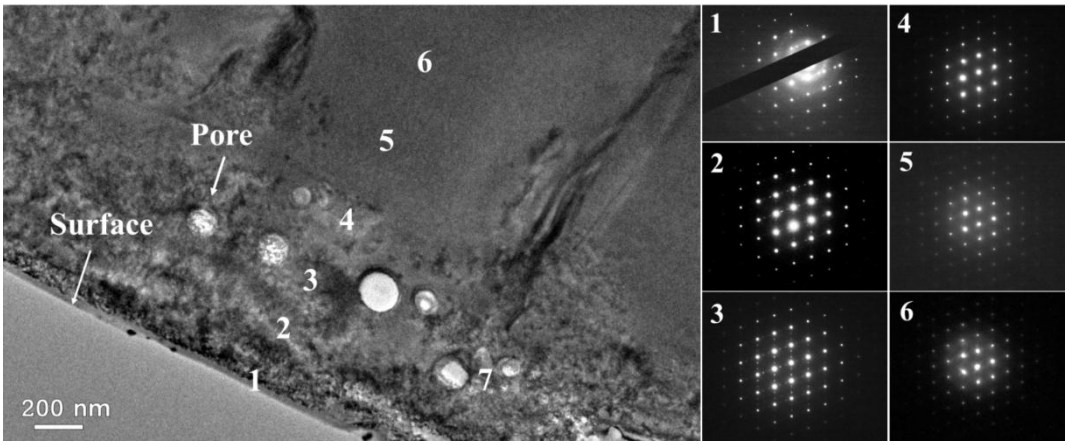


**Fig. 4.9 Bright field TEM image of recast layer. Sub-surface bubbles are revealed. Diffraction patterns indicate some amorphicity in location 1, a twinned region in 2 and 3, and purely single crystal in locations 4, 5 and 6**

Fig. 4.10 shows larger versions of the diffraction patterns at location 1, 3 and 4. A single-crystal pattern is clear and consistent on all diffraction patterns, indicating the beam is well aligned to a zone axis. Fig. 4.10 (a) exhibits a dominant single crystal pattern, with thick and unclear rings present indicating the presence of an amorphous structure, although this signal is not clear. The single crystal pattern in the image is the same as that from deeper into the lamella, i.e. pattern 6. Fig. 4.10 (b) reveals a distinctive twinning pattern, i.e. offset spots with the same structure. Fig. 4.10 (c) shows a purely single-crystal pattern seen in locations 4, 5 and 6.

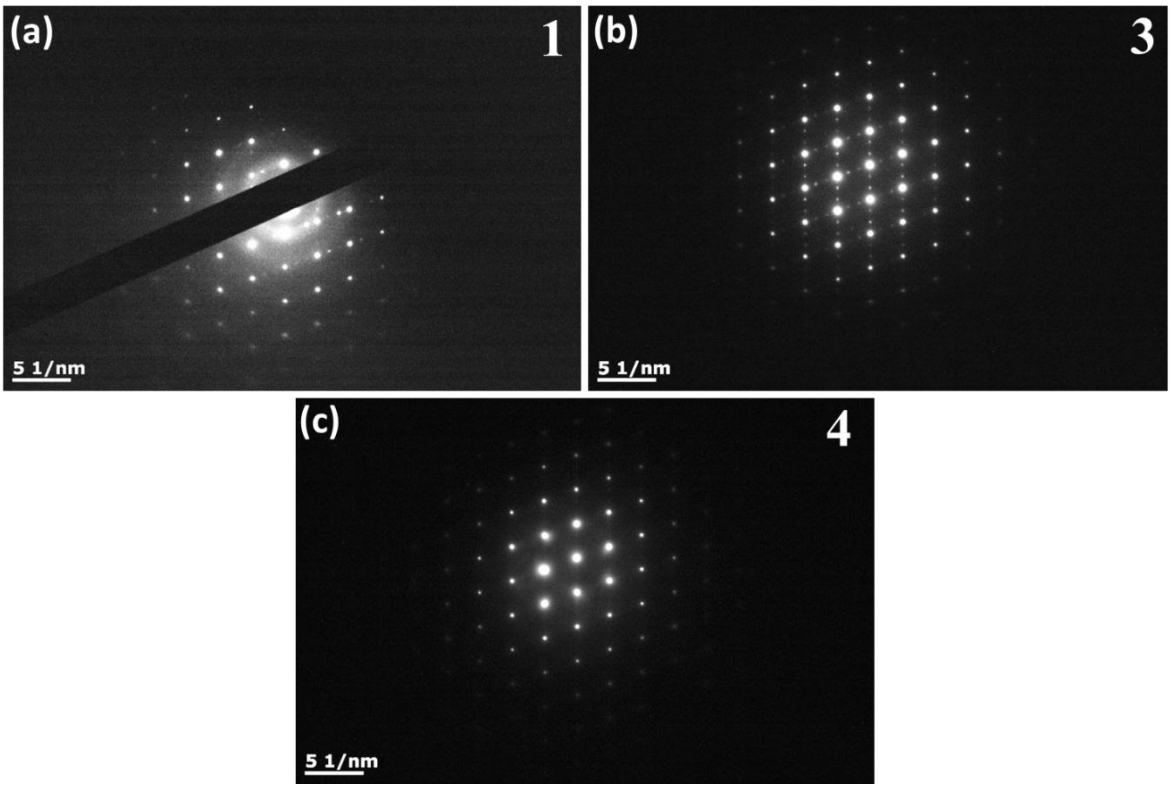


**Fig. 4.10 SAED patterns from Fig. 4.9 showing (a) Amorphous + single-crystal/single orientation in location 1 (b) Twinned structure in location 3 and (c) single crystal/single orientation in location 4**

Although tilting the sample relative to the beam direction so that it is parallel to a zone axis is required for clearest identification of single-crystal patterns, these strong signals may disguise underlying amorphous or polycrystalline structures. The lamella was therefore then tilted relative to the electron beam so that the direction of the beam was no longer in the direction of a zone axis, thereby exposing any underlying amorphous or polycrystalline structure otherwise hidden against the dominant crystalline pattern. An SAED pattern from location 2 after this process can be seen in Fig. 4.11. A combination of an amorphous structure (broad rings) and a fine polycrystalline signal (small points in fine rings) can be seen in this new pattern. This suggests that despite a strong crystalline pattern previously detected, the surface is also composed of a finer crystalline structure, since the diameter of the pattern region was about 150 nm. An amorphous matrix was also apparent. Since the nano-

crystalline structure has no preferential orientation, higher resolution imaging and EDX analysis is required to determine which features contribute to this structure.

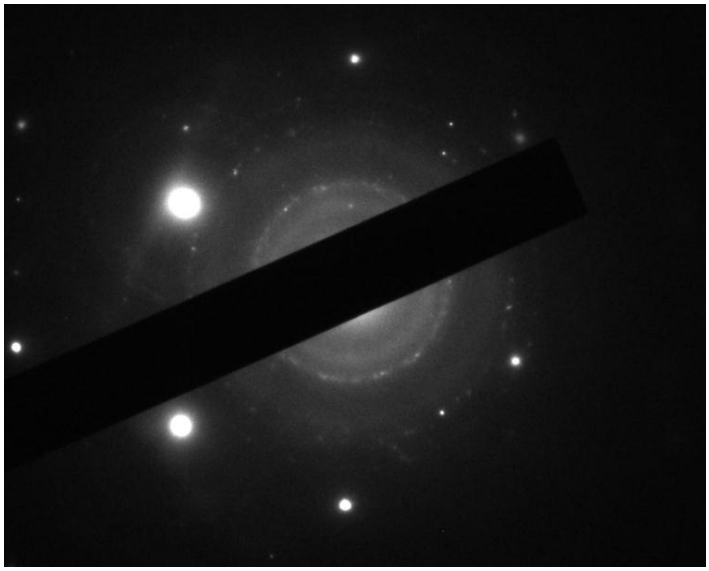

**Fig. 4.11 Electron diffraction pattern from location 2 in Fig. 4.9 when beam is tilted away from the zone axis. A polycrystalline signal is observed**

#### 4.3.4.2 Raman spectroscopy

In order to confirm the presence of the amorphous layer after EDM, Raman spectroscopy was performed on the as-received silicon wafer as well as the surface of the original machined hole. This was particularly important because it is known that FIB machining can create a thin region of amorphisation on a crystalline sample, and therefore this factor should be removed.

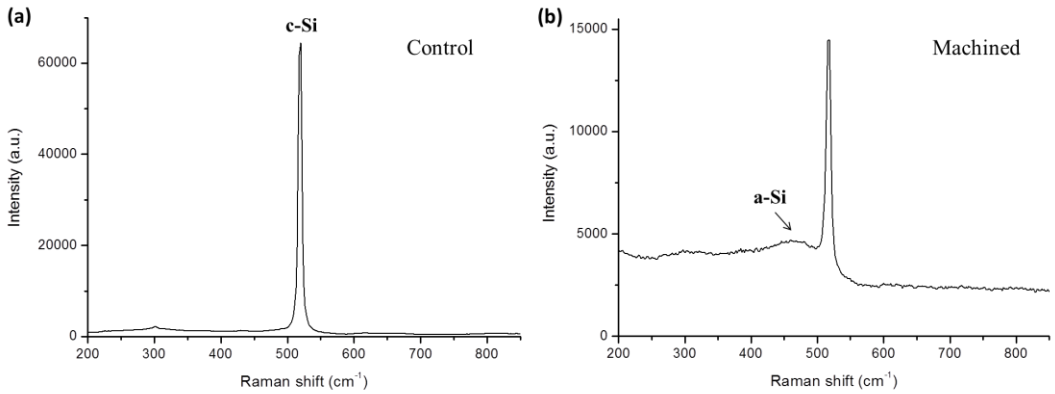


**Fig. 4.12 Typical Raman spectra of (a) as-received silicon wafer and (b) bottom of machined hole**

Example Raman spectra from both the as-received single-crystal material and the machined surface can be seen in Fig. 4.12. A solitary sharp peak is observed for the single crystal material at 520 $cm^{-1}$, consistent with that for c-Si [142]. A hump was observed on all spectra taken from the machined surface at approximately 470 $cm^{-1}$ Raman shift, consistent with amorphous Si [143]. Despite this, a large peak for c-Si still remained for all spectra taken from the machined surface. This supports the SAED patterns indicating crystalline silicon is the dominant structure with some amorphisation at the near surface.

#### 4.3.4.3 Lattice imaging

The principle of phase contrast occurring in a TEM, interference between the electron beam phase shifted by the atomic lattice, and non-phase shifted beams (explained in section 3.3.2) can be exploited to provide lattice images (HRTEM). This imaging mode was used to reveal the depth in the surface at which amorphous, crystalline and twinned structures begin to appear.

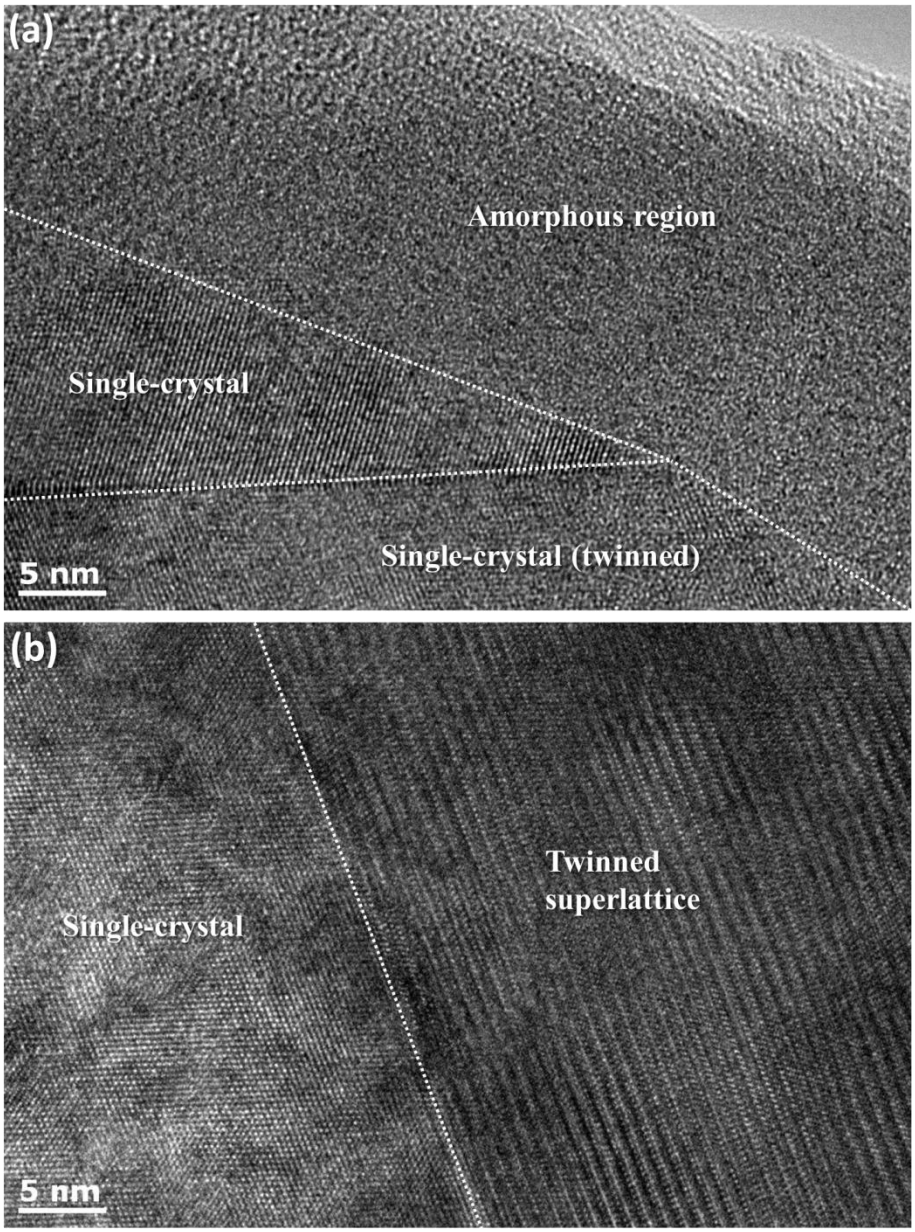


**Fig. 4.13 HRTEM images showing (a) near surface amorphisation and beginning of crystalline zone and (b) 500 nm depth revealing a twinned super-lattice next to a single crystal**

The amorphous structure identified in the diffraction patterns, and by Raman spectroscopy can be seen in Fig. 4.13 (a). The region of atoms with no apparent structure can be clearly seen. Two crystalline regions beneath this 30 nm amorphous layer can also be seen. Although they both have lattice structure, they are reflections of each other about a mirror plane, i.e. twins. In Fig. 4.13 (b), at 500 nm from the

edge of the lamella, a complex twinned super-lattice structure can be seen. This is a repeating pattern of alternating twins, of only several atoms width.

#### 4.3.4.4 Porosity

Pores at 400 nm below the surface and terminating after 1.1 μm were observed (see Fig. 4.14). The pores were observed up to the very edge of the observed recast layer. The diameters of pores exhibited a large variety, with the smallest approximately 10 nm and the largest with a diameter of 200 nm.

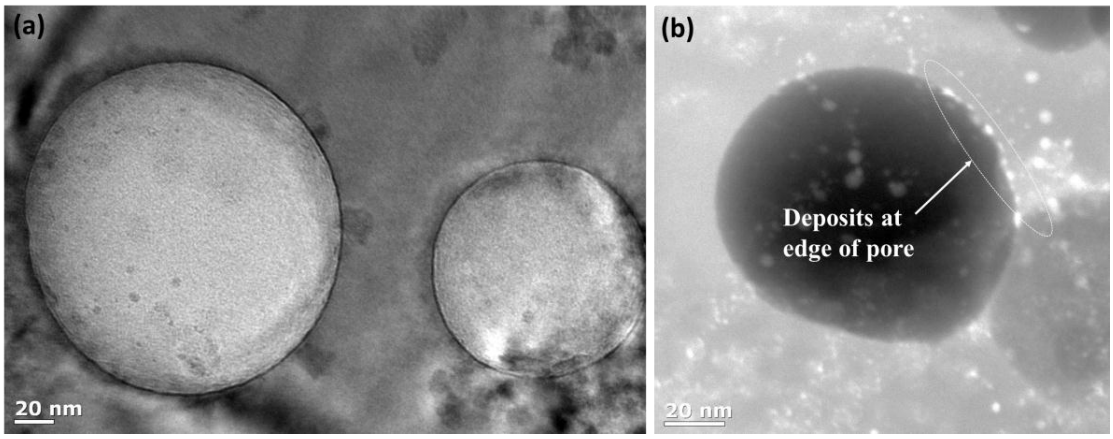


**Fig. 4.14 Pores imaged in (a) Bright field TEM and (b) Dark field STEM. High electron transparency is observed.**

The highly spherical shape seen at higher magnification suggests they are formed by either the expansion or contraction of gas trapped in the recast layer. Gas may have moved into the recast layer during discharge when the surface is molten, after which solidification of the surrounding silicon occurs. A concentration of deposits was also observed at the outer rim of many of the pores, which could be explained by the agglomeration of particles at their edges as the molten recast layer containing particles flows around the trapped gas. If the circular nature of the pores is explained by the expansion of gas, then particle concentration at their edges would also be explained by gas expansion forcing the particles outwards, where their motion is subsequently

impeded by the presence of liquid matter. The high electron transparency of the pores, i.e. their brighter appearance in bright field imaging, also indicates the lamella is much thinner in these regions (see Fig. 4.14).

### 4.3.5 Material deposition

A significant compositional change was observed in the machined surface. HAADF-STEM imaging in particular revealing contrast according to atomic number indicated the presence of a heavier element in the surface (see Fig. 4.15), and this contamination was observed up to approximately 1.2 µm depth into the surface. To examine the elemental composition of the surface, and to explain the polycrystalline selected area diffraction patterns, EDX analysis was performed.

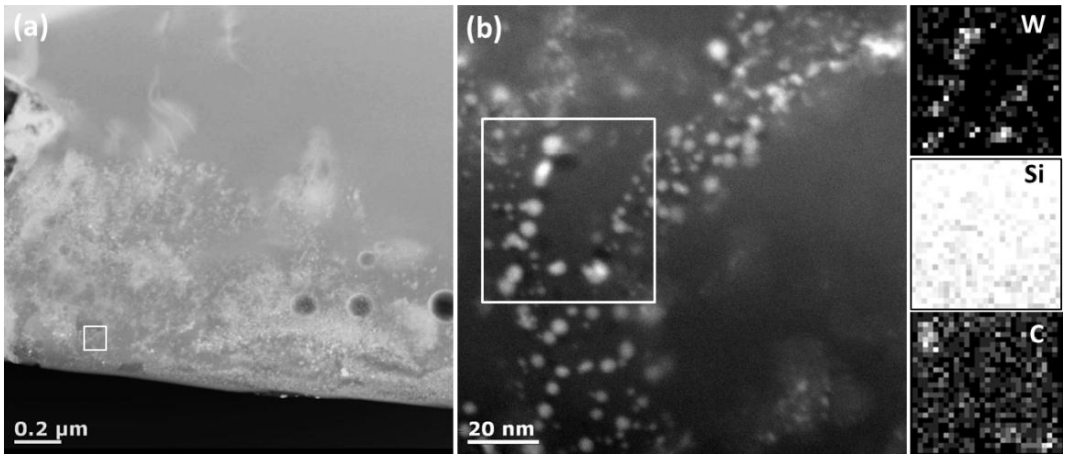


**Fig. 4.15 HAADF STEM image of deposits in recast layer with indicated EDX region with Tungsten, Silicon and Carbon EDX maps proving absorption of tool electrode material and Carbon into the silicon recast layer.**

Fig. 4.15 shows HAADF STEM images of nano-particles of a heavier element in the recast layer of the workpiece. A distinctive region of material deposits was used to allow EDX mapping to prove the presence of the element more easily. The region mapped by EDX is indicated, and the W map shows tungsten matching the positions of the particles in the micrograph. The Si map also shows the matrix is silicon. This

suggests that tool electrode material from the dielectric is mixed in with the discharge melt pool and makes a contribution to the composition of the machined surface. A carbon map is also shown, with a distribution more uniform than that of the tungsten deposits, but also with some regions of localised concentration. HRTEM imaging (see Fig. 4.16) was used to observe size, shape and crystal structure of the tungsten particles.

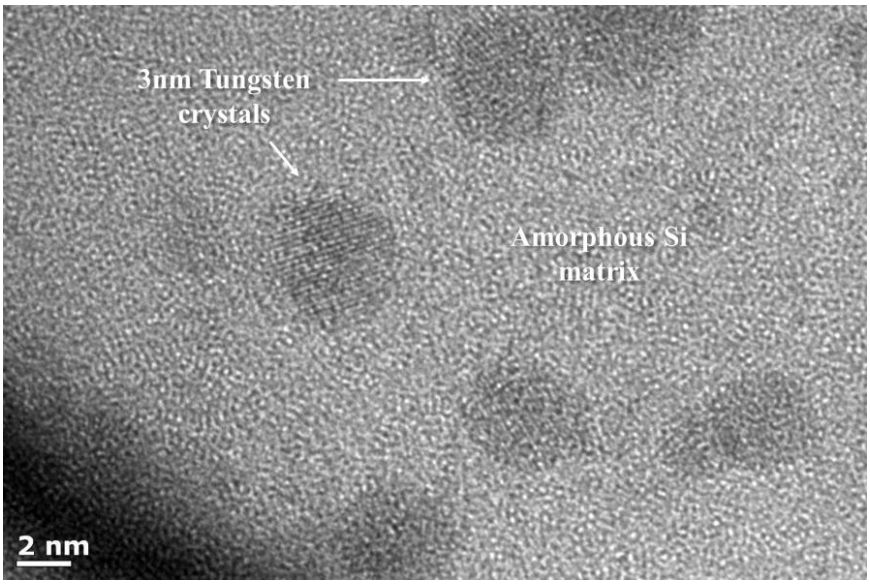


**Fig. 4.16 Tungsten crystals of approximately 3 nm diameter in an amorphous region of silicon.**

A defined crystal structure can be seen in the location of particles, whereas a distinct amorphous matrix with no lattice structure can be observed for the surrounding silicon. The crystalline lattice structure of silicon shown in Fig. 4.20 can be used for a comparison under high resolution imaging to the amorphous structure seen in Fig. 4.16. The smallest size of tungsten crystal observed was approximately 3 nm. It was also observed that the lattices of the tungsten crystals were randomly oriented, this may be explained by their movement into the surfaces as solid particles and their crystal structure is maintained, and therefore crystal growth by a directional cooling gradient was unlikely to be responsible for their formation.

### 4.3.6 Dislocations, strain and damage

Below the recast layer characterised by high tool deposition and pores, an inhomogeneous dislocation rich region was observed (Fig. 4.17 (b)). Contrast arises from dislocations in BFTEM mode since in these locations the lattice is distorted and more electrons will satisfy the specific Bragg diffraction angle here compared to the rest of the single crystal sample where the image is formed (i.e. brighter contrast regions) by the admittance of the primary (non-diffracted) beam, hence darker contrast is observed in dislocation regions. This TEM imaging principle also shows the polycrystalline regions near the surface in Fig. 4.17 (a), since a mixture of light and dark contrast is observed, suggesting no preferential orientation.

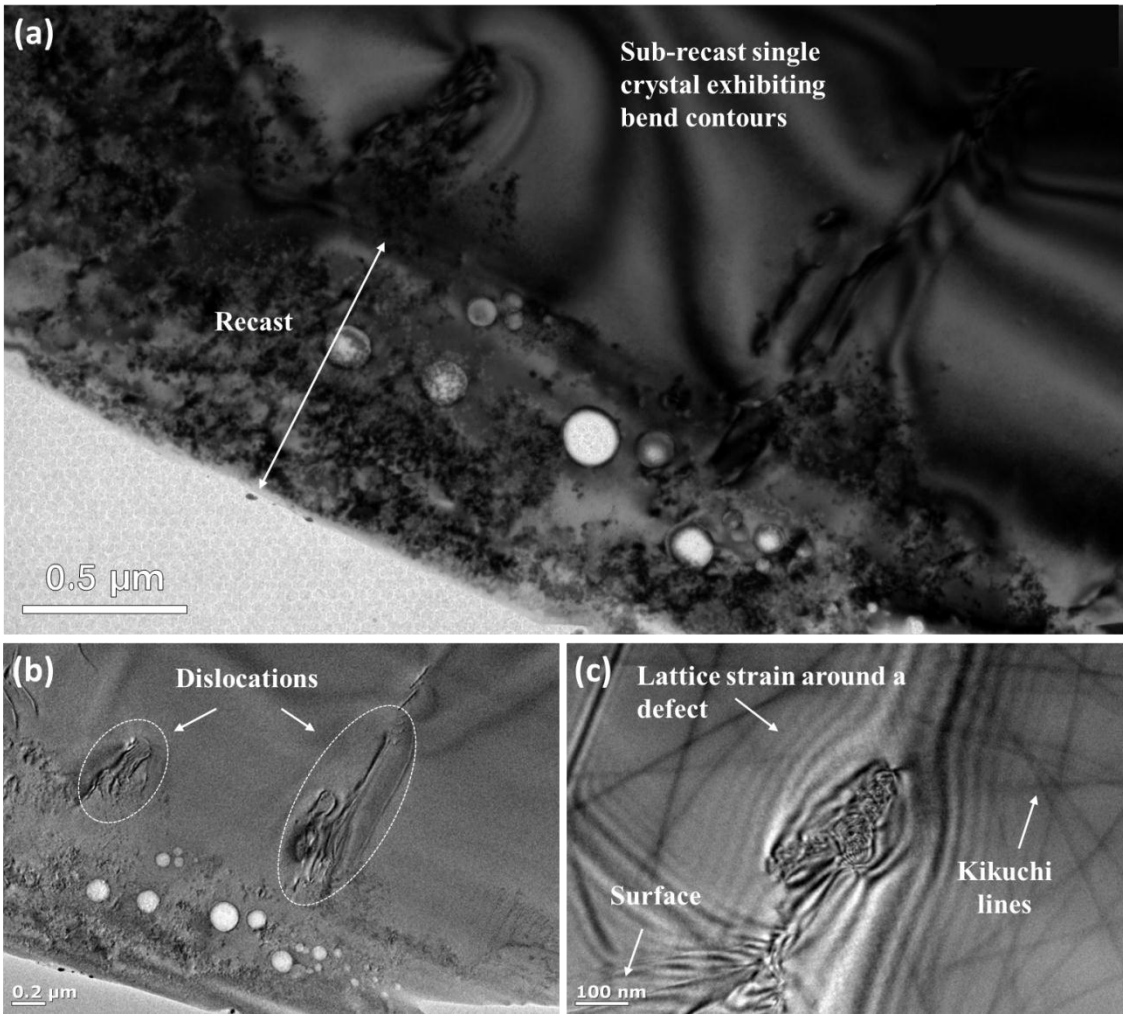


**Fig. 4.17 (a) Bright-field TEM image showing extent of recast layer and single crystal region beneath showing bend contours, (b) BFTEM image of the same area showing dislocation regions (c) BFTEM image of strain field induced by a dislocation.**

In Fig. 4.17 (a), bend contours can also be seen in the single crystal region of the lamella beneath the recast layer typical of a single crystal when the lamella is slightly buckled, whereas in the contaminated recast layer at the surface, such contours cannot be easily identified. Bend contours arise when the sample is not perfectly straight. This effect clearly distinguishes the boundary of the recast layer. Lattice strain can be inferred by the presence of contrast fringes observed in BFTEM mode. In Fig. 4.17 (c) localised contrast fringes can be seen in a region just beneath the recast layer, inferring the presence of a defect. In the vicinity of a defect such as a dislocation, it is known that the diffraction planes are distorted. This strain field around a dislocation

core is sufficient to locally tilt lattice planes into and out of the Bragg condition, thereby resulting in an oscillation of intensity of the outgoing beam, producing contrast fringes [137].

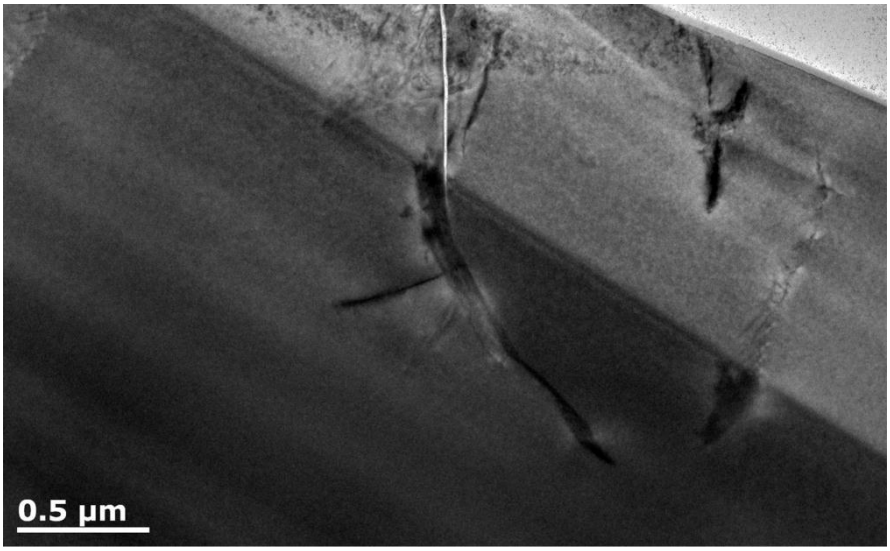


**Fig. 4.18 Crack of approximately 20 nm width from approximately 1.0 µm depth extending towards the surface.**

A single crack was observed in the TEM lamella, emanating from approximately 1.0 µm from the edge and up to the surface. The crack was approximately 20 nm in width, and therefore would not have been resolved by optical or SEM imaging. Dislocations can be seen at the base of the crack, indicating stress was applied in these regions, resulting in the creation of the crack. A crack is formed when the stress in the material exceeds the material's fracture strength – equivalent to the ultimate tensile strength. Since the crack appears to begin just beneath the recast layer, at about 1.0 µm depth, it was likely caused by the contraction of the solidifying recast layer next to the solid bulk beneath, resulting in a significant level of tensile stress at this interface.

## 4.4 Discussion

### 4.4.1 Crystal structure

#### 4.4.1.1 Amorphisation

TEM selected area electron diffraction patterns of a sequence of regions of the recast layer when the electron beam was perpendicular to the zone axis showed a clear single crystal silicon pattern was present in all regions analysed. In combination with single crystal silicon, nearest the surface an amorphous region was identified based on these patterns, and beneath this a twinned region was identified. Approximately 800 nm into the machined surface, a twinned pattern was no longer observed and a single crystal silicon pattern equal to that of the non-machined section of the lamella was seen. After the beam was tilted away from the zone axis, a polycrystalline pattern emerged on amorphous rings in location 2 in Fig. 4.9. High resolution imaging of the surface as well as Raman spectroscopy of the machined surface also confirmed that a combination of twinning and amorphisation is the damage mechanism occurring when machining single-crystal silicon with EDM. This is in contrast to a solely amorphous layer which has been shown to occur after machining single crystal silicon by mechanical means in the ductile cutting mode [144].

Under ductile mechanical cutting conditions when machining single crystal silicon, as have been achieved by several authors, a purely amorphous layer is observed, for example by Fang et al. using TEM diffraction patterns of amorphous machined chips [144], and by Yan et al. using Raman spectroscopy and direct TEM observation [57]. After EDM machining, based on the results in this chapter, the recast layer is dominated by crystalline silicon, with a weak signal, based on both SAED patterns, high-res imaging and Raman spectroscopy. In other words, the damage in silicon as a

result of the thermal based EDM process is distinct from that caused by mechanical machining processes, in that the structure of the recast layer is effectively regrown in a crystalline form. Determining and minimising the depth of amorphisation taking place in the near-surface layers has been a goal of much research in the field of precision semiconductor processing [57, 145, 146], and is important since single-crystal silicon is an essential material for solar cells, electronic devices as well as infrared optics. This study is the first time the sub-surface damage taking place due to EDM of a semi-conductor material has been performed. The ability of EDM to avoid a completely amorphous phase, and to yield a remelted layer dominated by a crystalline structure is promising for the process, particularly given the precision of the process at the micro-scale.

To eliminate the factor of the FIB amorphisation during preparation of the lamella, Raman spectroscopy confirmed the presence of the amorphous phase in the machined surface with the characteristic hump in the signal, peaking at approximately 470 $cm^{-1}$. The maximum penetration depth of 532 nm laser in silicon is 927 nm [141], although it should be noted that this value cannot be considered exact considering the contamination of the surface with tungsten. It is also important to note that the Raman shifts recorded represent an average value from the entire scattering volume between the surface and the ~927 nm maximum depth. Combined with the observation of deposition of material up to approximately 1.2 µm into the surface, it is reasonable to suggest the Raman shifts observed represent only the recast layer and not the bulk beneath. Therefore the strong Raman shift for c-Si at 520 $cm^{-1}$ as well as the amorphous hump in Fig. 4.12 (b) supports the findings from the SAED patterns that the recast layer is not a uniform region of the amorphous phase but is only partially amorphised. A polycrystalline SAED pattern was also observed 250 nm from the

surface after tilting the beam away from the zone axis, and upon EDX analysis, HAADF imaging and direct observation of the nano-crystals in the surface it was concluded that this pattern arises from the deposition of crystals into the recast layer from the tool electrode, although this was not in sufficient enough quantity to noticeably affect the Raman spectrum.

#### 4.4.1.2 Twinning

Crystal twinning is when two or more crystals are formed in a symmetrical fashion. This means that lattice points in one crystal are reflected in the twinned crystal by a twin plane (or mirror plane) in the lattice. Twinning can occur either during growth of a crystal, or if a crystal is subjected to stress. In several SAED patterns of our machined surface, a strong twinning pattern of the single crystal silicon matrix was observed. Fig. 4.19 compares an SAED pattern of a non-machined region of the single crystal lamella with a pattern from location 7 in Fig. 4.9. In (a) lattice points are identified, and in (b) the lattice planes across which the crystal twins are mirrored can be seen. Two twins were identified according to the patterns, one is a twin of the parent matrix mirrored along the $(11\bar{1})$ plane and the other is a twin of the parent matrix along the (111) plane. Lattice points and planes were identified according to previous work on twinning during semiconductor growth [147]. A schematic is also shown to illustrate more clearly the twin planes about which the crystal is mirrored.

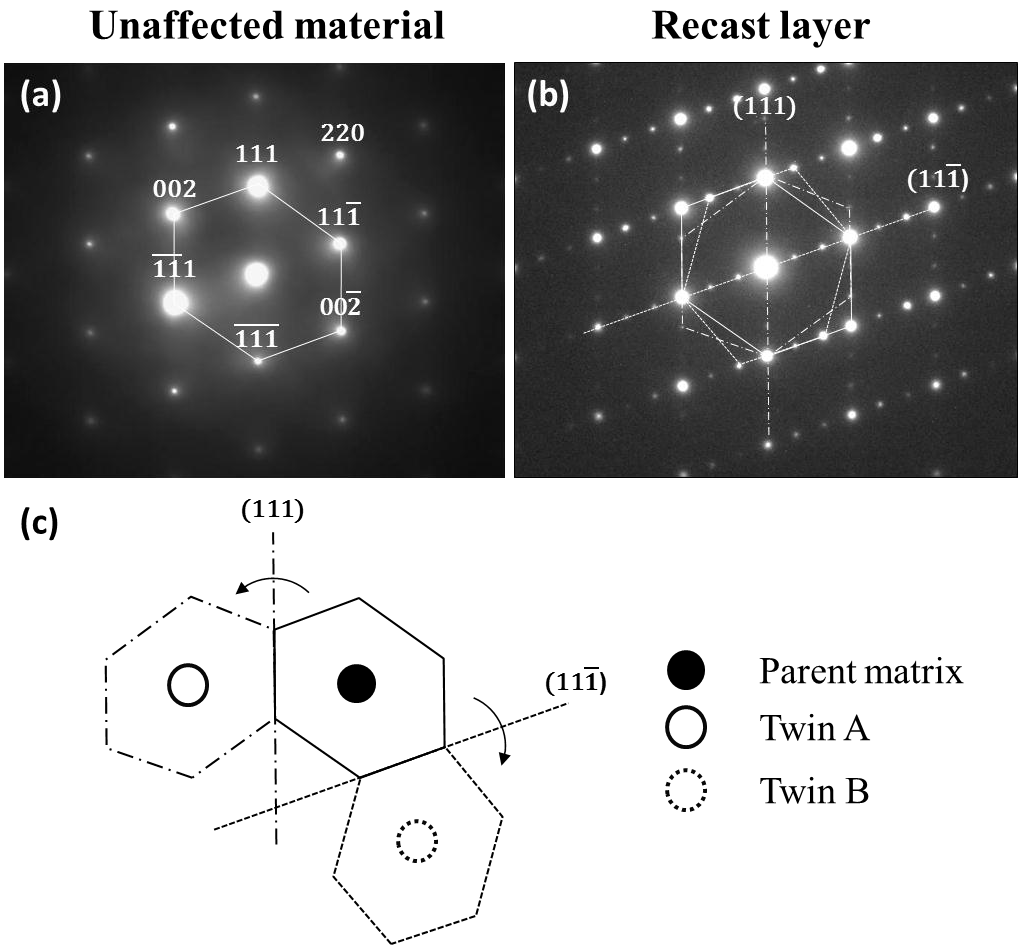


**Fig. 4.19 Diffraction patterns from (a) location on lamella not subject to machining, revealing single crystal silicon structure (b) location "7" on Fig. 4.9 revealing twin structure (c) schematic of twinning planes**

There is evidence that impurities, especially carbon promote twinning during growth of crystalline silicon [148]. Since it is understood that the machined surface is molten during spark on-time, and the observation of pores in our results supports this, it can be concluded that twin formation in this study likely occurred as a result of crystal growth during resolidification, and since carbon as well as tungsten contamination has been detected in our EDX results, the presence of these contaminants may explain the interruption of crystal growth and the subsequent formation of twins. Given the primary lattice structure (i.e. the brightest spots) of the recast layer seen in the diffraction pattern in Fig. 4.19 (b) is the same as that of the unaffected, single crystal structure of the lamella in Fig. 4.19 (a), this would suggest that epitaxial growth of

silicon is occurring, whereby a crystalline structure in the recast layer is grown beginning at the liquid-solid interface and is a continuation of the bulk crystal structure. However, in this case twinning was observed to occur during crystal growth. Treatment of the mechanically machined surface of single-crystal silicon has been the subject of research in order to eliminate the amorphous damaged structure and recreate the crystalline structure beneath by epitaxial growth. For example Yan et al. successfully reconstructed the bulk single crystal structure in the surface of a machining-damaged silicon wafer by the use of nanosecond (3-4 ns) pulsed laser irradiation surface treatment [149].

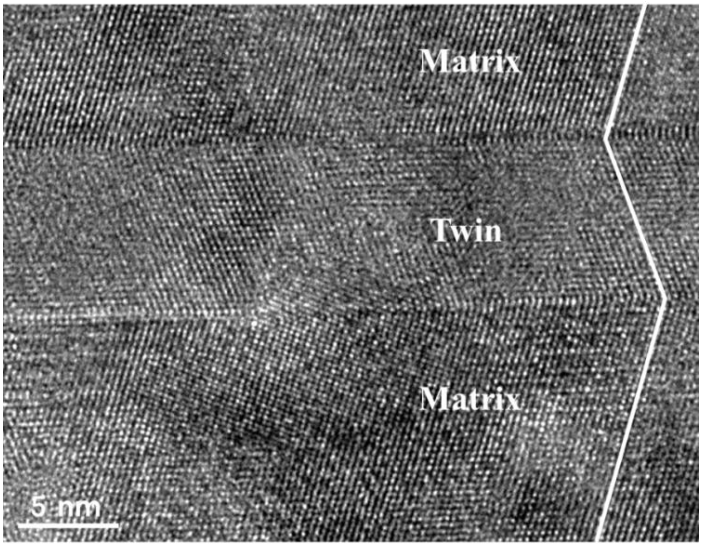


**Fig. 4.20 Twin observed approximately 100nm from the surface of the sample**

The presence of twins in the recast layer was also confirmed by direct BFTEM imaging of the lattice. Fig. 4.20 shows a TEM image of a twin in the parent silicon matrix, with twin boundaries clearly visible.

### 4.4.2 Contamination

EDM is fundamentally different from mechanical machining techniques in that the mechanism of material removal depends on the superheating of the molten workpiece

and the subsequent pressure drop at the end of spark duration expelling some of the melt pool into the dielectric. Despite the use of a flowing dielectric to remove this resolidified debris from the machined region and maintain predictable electrical conditions in the spark gap, carbon from oil based dielectrics is known to move during machining into the surface of the workpiece [62] and the tool electrode [40]. This is thought to occur due to thermal dissociation or "cracking" of the carbon based oil [38]. In EDX results in order to identify the foreign particles, carbon was also detected in the recast layer, in a more uniform distribution than the tungsten deposits.

In machining of materials where chemical composition of the original material must be maintained, as well as for machining where the precise properties of the surface of the workpiece should be known, understanding and predicting the movement of material into the workpiece surface is critical. In this study, tungsten crystals were observed down to 1 µm depth from the surface; the same depth at which porosity and amorphisation were also seen. Contamination was therefore not present as a separate layer created on the workpiece, but an inherent part of the recast layer induced by EDM. This suggests that EDM is not only a process which induced porosity and surface cracking in machined components, but should also be considered a chemical modification process dependent on the composition of the tool electrode.

Addition of the tool electrode material onto the workpiece during EDM has also been considered as a beneficial phenomenon, and has been achieved by several researchers, such as Mohri et al. using a composite structured electrode onto a steel workpiece [99], as well as by Ho et al. onto Ti-6Al-4V [150] and proposed as a practical method of introducing coatings onto tools such as drills [100]. The nano-scale diameter of embedded tool electrode (tungsten) crystals observed in the recast layer is of particular interest from the perspective of EDM coatings, since a nano-structured

layer of deposited material would have significant benefits for the mechanical properties of the coating. For example increased hardness has been measured through deposition of a nano-crystalline layer of Fe-Si by cold-spraying compared to a cold-sprayed micro-crystalline layer [151]. Fe-Ni coatings with improved hardness have also been demonstrated through electrodeposition [152]. Recent work on electrical discharge coating (EDC) has shown that titanium deposition from powder suspension onto a tungsten carbide substrate can increase surface hardness to 1750 HV from 990 HV in the substrate [103].

### 4.4.3 Deformation, cracks and porosity

Dislocation regions were observed just beneath the recast layer, where pores and tool electrode contamination were no longer observed. These regions of dislocations were not homogenous but concentrated to smaller regions. It is proposed that the stress induced at the interface between the solidifying recast layer and unaffected bulk beneath results is compensated by the nucleation of dislocations, and in one case in this sample, the stress was large enough to overcome the fracture strength of the material, causing a crack to initiate. The damage observed in this study in single-crystal silicon is similar to that observed by Yan et al. [57] in precision diamond machining of the same material, in the sense that a dislocation-rich region was produced beneath the damaged region, which in their case was an entirely amorphous layer.

The presence of cracks as well as pores in the recast layer is considered critical to the surface integrity of the component machined by EDM, and as a result there has been a substantial research effort in characterising and determining parameters which result in the fewest pores or cracks. For example Zhang et al. [153] have investigated the

characteristics of recast layers produced using different dielectric types. It was observed through cross-sectional and surface SEM/optical imaging that many more were observed when using a water-in-oil emulsion dielectric compared to a kerosene and a water dielectric. This was explained by the larger volume of gas generated in water-in-oil dielectric during machining, which was measured in the paper. In terms of surface cracks, the water dielectric produced the shallowest cracks compared to the other two dielectrics. The results in this chapter however reveal that pores with a diameter as small as 10 nm, and a crack of 20 nm width can be produced in a surface machined by EDM. This effectively nullifies the conclusions which are made based on SEM and optical imaging regarding the surface integrity of EDM'd surfaces. It is therefore suggested that only fundamental, TEM imaging can properly reveal the structure of materials machined by EDM.

## 4.5 Conclusions

For the first time, a nano-scale characterisation study of a single-crystal material machined by EDM has been performed. This study has revealed a number of material phenomena on the EDM'd surface previously unseen at the nano-scale. The work has indicated that more conventional and convenient imaging techniques such as SEM and optical microscopy are not sufficient to properly explain the surface integrity of EDM'd surfaces. In reality, the presence of porosity, contamination and cracking occurs at the nanometre scale, and therefore TEM analysis is required for full characterisation of surface features of EDM'd components. The existence of such phenomena at this scale has implications for the surface integrity of all EDM'd workpieces, and is particularly important for the furthering of EDM as a micro-machining process. It also impacts the requirements for the post-processing of EDM'd workpieces, for example surface treatment techniques.

Based on TEM imaging as well as diffraction patterns, the machined surface of single crystal silicon is modified significantly from that of the bulk crystal. Pores of a range of sizes from 10 nm to 200 nm comprise the recast layer. Since little TEM work has been done on the analysis of the recast layer of EDM'd materials, this is the first observation of sub-micron sized pores in the machined surface. Diffraction patterns and direct imaging of the lattice have exposed that the surface is mainly composed of crystalline silicon with some twinned crystalline and amorphous structure. Since there are a number of phenomena which have been characterised in this chapter, they are summarised in the schematic in Fig. 4.21.

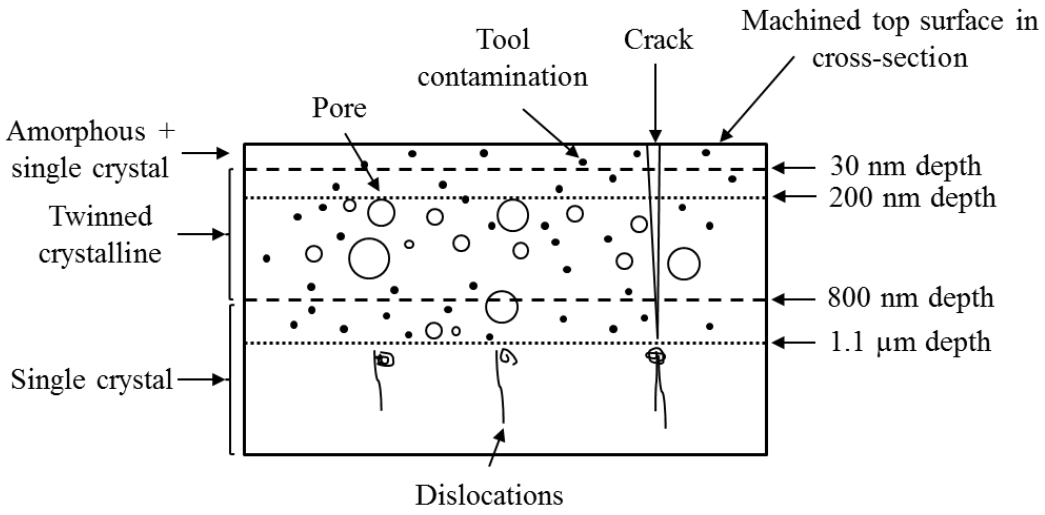


**Fig. 4.21 Schematic of phenomena and corresponding depths in cross-section observed in cross-section in EDM'd single crystal silicon**

The conclusions made in this chapter can be summarised as follows:

- Three phenomena at the nano-scale created by the EDM process not discussed before in literature have been observed: nano-scale pores, nano-scale crystals of embedded tool material, and a nano-scale crack. Porosity and cracking are critical phenomena associated with EDM'd surfaces which inhibit the fatigue performance of components due to stress concentration effects. These

phenomena also have implications for the creation of coatings by ED processes.

- Spherical pores of varying diameters between 10 nm and 200 nm were observed in the machined surface, at depths of up to 1.1 µm. It is thought these pores are created from the absorption of gas in the surface when molten.
- A 20 nm wide crack was observed, originating just beneath the recast layer, at approximately 1 µm depth. The presence of a crack in the small TEM sample suggests it is likely for nano-scale cracks to be prevalent in the remainder of the surface of the machined feature.
- Selected-area electron diffraction patterns and Raman spectroscopy were used to show that the surface microstructure is primarily crystalline silicon with some twinned crystalline and amorphous silicon. The twinned-crystalline structure is formed due to epitaxial growth during resolidification of the molten surface. A complex repeating twinned super-lattice was also observed.
- Movement of tool electrode material (tungsten), as well as carbon from the dielectric into the machined surface occurred during machining.
- The size of embedded tungsten particles is typically several nm with the smallest particles approximately 3 nm in diameter. The particles appeared to be single crystals, which were observed in random orientations in the recast layer.
- These new structures observed at the nano-scale of an EDM'd workpiece have implications for the integrity of components subject to the machining process, and TEM analysis should be considered for future analysis of EDM recast layers.

# 5 The mechanism of material transfer between electrodes

## 5.1 Introduction

The aim of this chapter is to explain how material transfers between tool electrode and workpiece during EDM. Based on the results in chapter 4, it is now understood that a number of material phenomena are introduced to the surface of materials after EDM at the nano-scale. These include pores, cracks, as well as opposite electrode deposits. This chapter focuses on contamination of opposing electrodes which is known to occur in EDM, yet the mechanism of which has not been explained. The motivation of this chapter is to understand how foreign material moves between electrodes, and explain how this fits with the principle of EDM whereby removed material is expected to solidify upon ejection into the dielectric, and then is flushed away and not reattached to the tool or workpiece surface [13]. A full understanding of the relationship between the discharge process and the attachment of material during EDM is not just essential for understanding how unintended contamination of chemically homogenous materials such as semiconductors occurs, but it is also important for the deliberate avoidance or introduction of species to a surface during EDM.

Since the 1990s, EDM has been investigated as a coating process. For example, a titanium coating has been successfully deposited using both powder suspension in the dielectric [103] as well as from a sacrificial electrode [43], and TiC has been deposited using a sacrificial layered electrode of graphite and titanium [101]. Mitsubishi Electric Corporation now manufactures an EDM machine designed to coat workpieces with a wear resistant or corrosion resistance layer. Observation of this

process, according to the literature in the subject, has focused only on the resultant layers produced under certain conditions, and no fundamental study has been performed to demonstrate the mechanism of material deposition. Determining how deposition relates to the discharge process and the resultant discharge spot, as well as the conditions which cause it, is critical to both the avoidance and creation of layers of contaminating material on workpiece and electrode surfaces in EDM.

The high frequency of discharges necessary in EDM – many thousand times per second – means that direct observation of the material removal process is difficult. Therefore in this chapter, the discharge process will be characterised by the inspection of individual discharge craters and the cross-sections of electrode surfaces. This work includes an investigation on the machining of high-aspect ratio slots, followed by metallurgical analysis of the surfaces of the tool electrodes as well as the workpiece. Low magnification microscopy and elemental mapping was first conducted to explain the movement of machined debris and subsequent deposition onto the electrodes. Cross-sectional analysis was then performed on the tool electrodes to quantify the thickness and composition of the deposited layer. To determine the mechanism of attachment of material during the process, elemental analysis of individual primary and secondary discharge craters was performed.

## 5.2 Methodology and experimental setup

### 5.2.1 Research methodology

This study required the analysis of individual discharges spots. For this reason a large surface area of electrode was required for an increased probability of distinguishing individual discharge spots. Since in the normal machining region of an electrode, the surface is affected by many successive discharges, the sides of a sinking electrode

undergoing much less frequent sparking are more useful for identifying individual discharges. For this reason deeper sinking EDM was required to leave some regions of the electrode free of discharge craters. The sinking experiments investigated the primary EDM parameters of discharge current, on-time and off-time to establish the dependence of material deposition on these variables. A factorial design of experiments was used for this investigation.

After machining, the resultant holes were cross-sectioned, and observed to confirm successful machining had occurred, before examining the surface for a contaminant layer. The used tool electrodes were subject to EDX mapping to determine the extent of workpiece material contamination in relation to machining parameters.

The thickness of contaminating layers on both tool and workpiece was then measured, and their dependence on machining parameters was determined. Individual discharge spots on the electrode were finally analysed using EDX mapping and SEM imaging to determine if specific regions of the discharge spot were responsible for material deposition.

### 5.2.2 EDM, EDX and materials

A Sodick AP1L die-sinking EDM machine was used for all EDM experiments in this chapter, using “Steel fluid W95-SE” kerosene as a dielectric. The selected workpiece material was a cobalt-chrome-molybdenum based alloy. It is a hard and wear resistant material used in hip replacements and in functional prototypes. Cobalt-chrome based alloys also have applications in the hot pressing and extrusion die industries given their high wear resistance at elevated temperatures. Its application in the medical implant industry means that contamination of the workpiece surface is of particular importance. Given its high hardness and good wear properties, future work regarding

electrical discharge coating for hard wearing layers may consider this material. For these reasons the material is a sensible choice of workpiece material in this study.

Copper-tungsten composites are attractive materials for use as EDM electrodes given the combination of high electrical and thermal conductivity of the copper with the high melting temperature of tungsten, resulting in low electrode wear rates. It is also easily machinable by conventional milling; an essential property for the cutting of electrodes into specific shapes. It is fabricated by powder metallurgy since the lower melting point of copper means alloying it with tungsten is difficult. This fabrication process means the material is a composite of tungsten particles with a copper binder matrix. This material structure is also interesting in terms of its EDM wear properties since it is made of 2 distinct components with differing thermal properties.

The electrodes were conventionally milled from a copper-tungsten block into a high-aspect ratio of 0.2 x 2 mm cross sectional shape with 5 mm length. The AP1L machine used interval z-axis reciprocation to enable flushing from the workpiece area. Fig. 5.1 shows a cross-section of a typical machined slot, with inserted optical images of the tool electrode to present the aspect ratio of the operation. Slots were machined into a single cuboid workpiece of 20x10x8 mm.

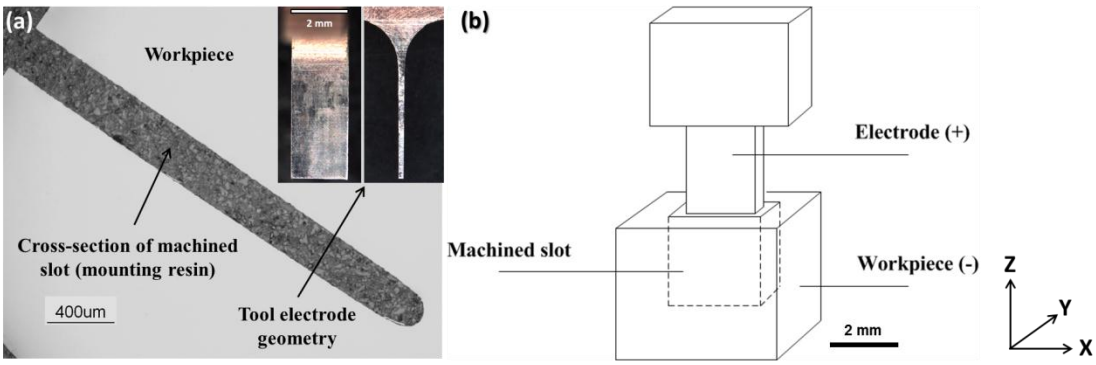


**Fig. 5.1 (a) Cross-section of typical machined micro-slot with insert of electrode images and (b) schematic of operation**

Since the core of this study involves the migration of material during machining, elemental analysis was a key aspect. Energy dispersive X-ray spectroscopy (EDX) was employed for this, using a Philips XL 30 SEM at 20 kV. Since the deposited layer reported in the results was observed to be on the same order as typical electron penetration depths used for EDS analysis, i.e. between 1 µm and 5 µm, electron penetration ranges were calculated for the elements permitting the shallowest and deepest penetration depths. An average penetration depth based on the EDS results was not calculated given the result itself is dependent on the elemental composition. The equation used is an expression for the total penetration depth in a straight line of a single electron [154]. $\rho$ is density, A is atomic mass, Z is atomic number, $E_0$ is accelerating voltage.

Electron penetration range:

$$R(\mu m) = \frac{0.0276A}{Z^{0.89}\rho} {E_0}^{1.67} \qquad \textbf{Equation (2)}$$

Given the depth of electron penetration using EDX is dependent on the elemental composition of the layer being analysed, an exact figure of this depth is difficult to determine and is transient across the area mapped. However, if we consider a maximum and minimum depth based on the elements present, a reasonable window of

accuracy can be inferred. Based on Equation (1), considering an $E_0$ of 20 keV, the element permitting the highest electron penetration is chromium at 1.76 µm, while tungsten allows the least penetration at just 0.85 µm. Based on this it can be said that the depth of the elemental map represents the composition no deeper than 1.76 µm into the surface.

A Hitachi S-2000N was used for both secondary electron and back-scattered electron microscopy. “ImageJ” image processing software was used to measure distances on the electrode surfaces and in cross-section.

### 5.2.3 EDM parameter selection

Preliminary experiments were used to define the process window from which the experimental parameters were based. Preliminary trials were conducted based upon typical parameters used by authors for micro-features with similar dimensions. For example Diver et al. investigated on-times between 1 and 10 µs for the EDM of tapered micro-holes with 100 µm entry diameter in NiCr alloy [3]. Liu et al. also used a pulse on-time process window between 4 and 50 µs when machining with 110 µm diameter electrodes in high-nickel alloy workpiece, with good stability achieved using the lowest on-time of 4 µs [155]. Currents typically used in micro-EDM span a large range, for example currents between 2 and 15 A have been used for the fine machining of monocrystalline silicon [156], and 40 A for the drilling of micro-holes at high speeds [3], while currents of 320 mA have been used to produce fine micro-holes in polycrystalline diamond [157]. After experimental trials based on this information, conformity of holes and machining times were evaluated and a process window with currents between 2 and 5 A, and on-times between 3 and 15 µs were identified which would represent typical, representative of neither roughing or

finishing machining conditions. Limitations regarding the increments of allowed current settings on the apparatus used restricted the range over which current could be set with regular increments. With regards to off-time, a duty factor of approximately 50% is typical in EDM, i.e. using an off-time roughly equal to on-time, although using a shorter off-time can be beneficial for shorter machining times to the detriment of tool wear rate. The design of experiments was based on a mixed level factorial design with 3 levels for current and on-time, and 2 for pulse off-time, in order to investigate the influence of these key factors on the deposition observed, and to clarify if it is not dependent on off-time. Long machining times associated with the geometries produced were also a factor in minimizing the number of required machining operations. Table 6 shows the range of experimental parameters, and the resultant machining times.

**Table 6 Experimental parameters with resultant machining time**

| | **Test number** | | | | | | | | | |
|---|---|---|---|---|---|---|---|---|---|---|
| | 1 | 2 | 3 | 4 | 5 | 6 | 7 | 8 | 9 | 10 |
| **Main current (A)** | 2.3 | 3.4 | 4.5 | 4.5 | 2.3 | 4.5 | 2.3 | 2.3 | 4.5 | 2.3 |
| **Pulse on time (µs)** | 3 | 3 | 3 | 15 | 15 | 15 | 3 | 15 | 3 | 9 |
| **Pulse off time (µs)** | 2 | 2 | 2 | 2 | 2 | 10 | 10 | 10 | 10 | 2 |
| **Mach. time (mins)** | 156 | 77.2 | 57.5 | 34.3 | 62.6 | 36.7 | 515 | 74.9 | 248 | 49.1 |

Gap voltage was set to 90V and tool electrode polarity was also set to positive to best represent a typical EDM set-up given a positive polarity is associated with lower electrode wear.

## 5.3 Results

### 5.3.1 Conformity of machined slots

All machined slots were cross-sectioned in order to confirm the internal shape matched the design intent based on tool electrode geometry. In one of the machining experiments, undercutting was observed. The deformity was only revealed when the slot was cross-sectioned, as the entry to the hole was not abnormal. This can be seen in Fig. 5.2, where a cross-section of the deformed hole is shown, showing recesses at the sides of the machined slot, in a symmetrical pattern about the centre line of the intended feature.

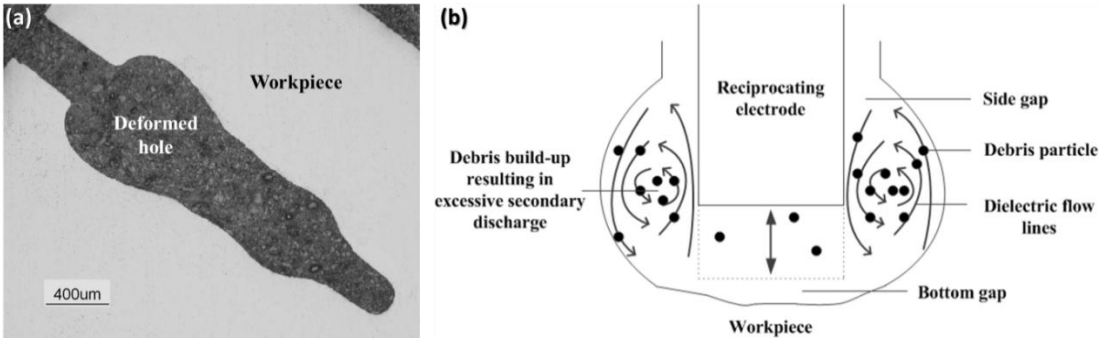


**Fig. 5.2 (a) Cross-section of deformed hole and (b) schematic of debris movement due to a reciprocation-induced vortex, resulting in the deformed hole due to excessive secondary discharge.**

Such a phenomenon occurring when machining deep holes has been observed before. Cetin et al. [158] discussed the formation of concaved walls during EDM of deep holes using linear motor jump flushing, and after experimentation and simulation concluded that the degree of wall concavity depends on the jump height – and more specifically that concavity and average machining side gap width become smaller with increasing jump height of the tool electrode. This is explained by the reduction in debris concentration when using a larger jump height. When jump height is too small, non-ejected debris particles are redistributed inside the gap and captured by the

induced vortex from the jump motion. A schematic of this phenomenon is presented in Fig. 5.2. The high concentration of debris particles induces a localised reduction in dielectric integrity resulting in favourable discharge paths and subsequent excessive secondary discharge, machining the sides of the holes. In these experiments reported in this thesis however, the jump height was unchanged for all experiments, yet this phenomenon was only observed in one operation. This suggests that the build-up of a critical amount of unejected debris, enough to begin machining the sides of the workpiece, may be a stochastic phenomenon and also dependent upon machining conditions. The creation and avoidance of such internal structures should be the subject of future work.

All other machined holes exhibited normal machining characteristics, such as straight sides with slight convergence towards the bottom of the hole, as well as a rounded bottom. These characteristics are expected due to the enhanced wearing of the corners of the electrode.

### 5.3.2 Discharge surfaces of tool electrode

All tool electrodes used during machining were then inspected using optical microscopy. Two main electrode wear regions were observed. The darker regions at the end of the electrode as seen in Fig. 5.3 and Fig. 5.4 correspond to the main working area of the electrode. It is here where the majority of sparks occur during the machining operation. The nature of the lighter, non-working regions will be investigated in section 5.3.3 to explain their formation and material composition. This primary discharge area is observed to increase with discharge current, while it decreases with increasing on-time.

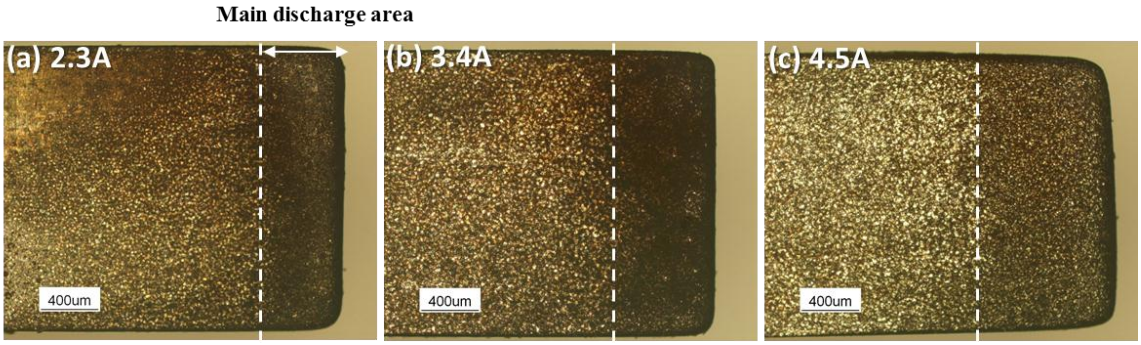


**Fig. 5.3 Main discharge working area of tool electrode increasing with current a) 2.3 A b) 3.4 A c) 4.5 A (On-time 3 µs, off-time 2 µs)**

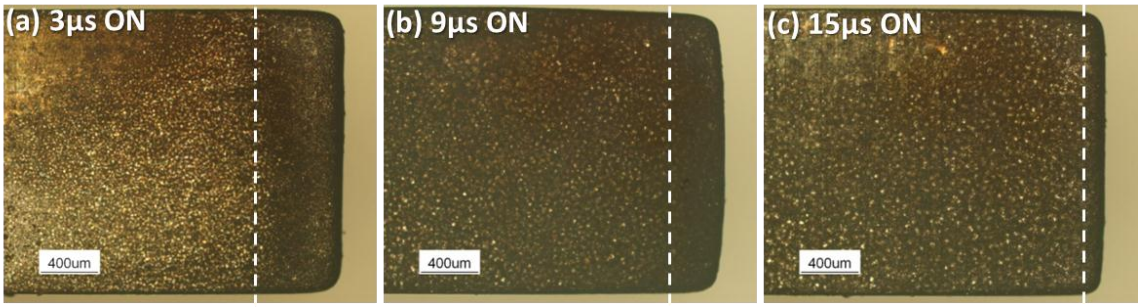


**Fig. 5.4 Main discharge working area of tool electrode decreasing with on-time a) 3 µs b) 9 µs c) 15 µs (Current 2.3 A, off-time 2 µs)**

The distance from the end of the main discharge area (fringe) to the end of the worn electrode was measured at ten points and averaged to quantify how the main working area varies with on-time and current. The volume eroded from the electrode during machining was also evaluated in terms of change of length. As shown in Fig. 5.3 and Fig. 5.4 the main discharge region increases with current and decreases with on-time. The distance was also observed not to change with off-time.

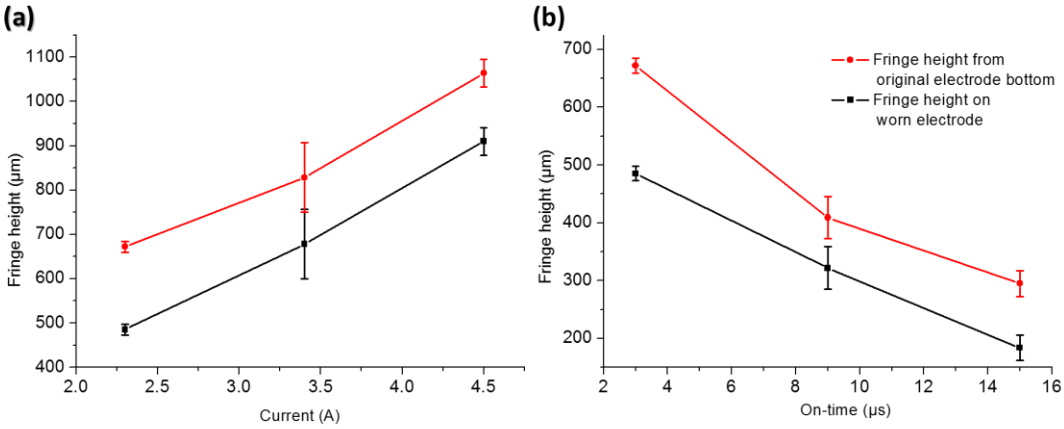


**Fig. 5.5 Average height of the main discharge region (a) increasing with Current and (b) decreasing with On-time. The distance between the lines represents the electrode wear. Error bars are the standard deviation of the distances measured to calculate the mean value.**

The distinct discharge fringe can be seen in Fig. 5.6. SEM images reveal the smooth surface to the left part of the image, with the rough primary wear surface to the right. This end section of the electrode is uneven since the copper matrix is preferentially removed due to its lower melting temperature. The surfaces can be differentiated from the unsparked surface given the characteristic flat surface after milling which displays the tungsten particles in the copper matrix.

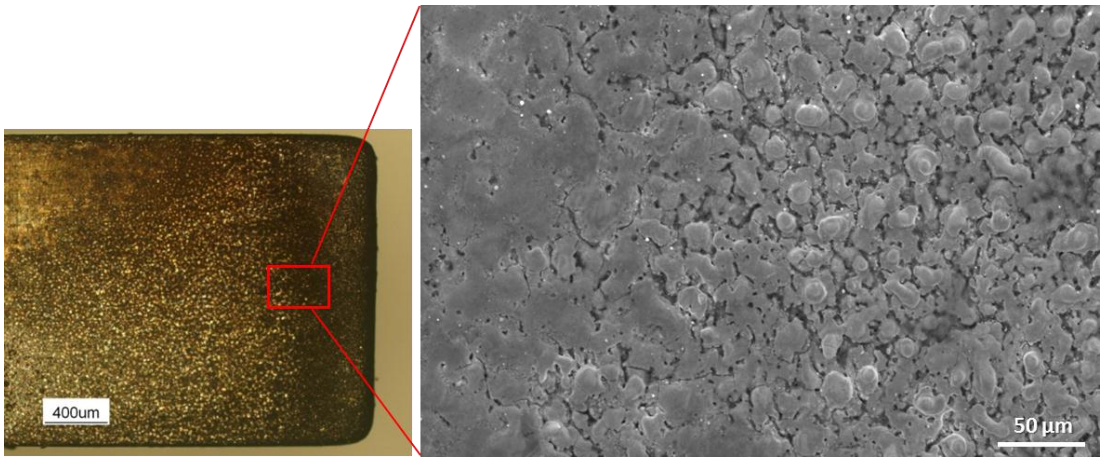


**Fig. 5.6 Secondary electron image of discharge fringe on electrode 1 (2.3 A, 3 µs ON, 2 µs OFF).**

A difference in the worn surfaces of some electrodes on one side as compared to the other was observed in some cases. This is assumed to be because of a slight tilt in sinking angle, causing preferential movement of ejected debris on one side of the electrode and significantly more sparking. This suggests that the primary working area of the electrode is significantly smaller than the total affected regions observed.

### 5.3.3 EDX mapping of electrode surfaces

To confirm the elemental composition of the electrode surfaces and any deposition on the working and non-working regions of the electrode, EDX analysis was used. The surface of the electrode used in test 1 was mapped using EDX to assess the amount of debris attachment in the different areas of the electrode. Electrode 1 was chosen to be analysed as the discharge fringe was well defined. The entire electrode was mapped, along with smaller regions from the end and middle of the electrode (see Fig. 5.7). The regions selected were chosen as they best reflected a typical worn W-Cu electrode surface (end), and a distinctive melted surface in the non-working region (middle).

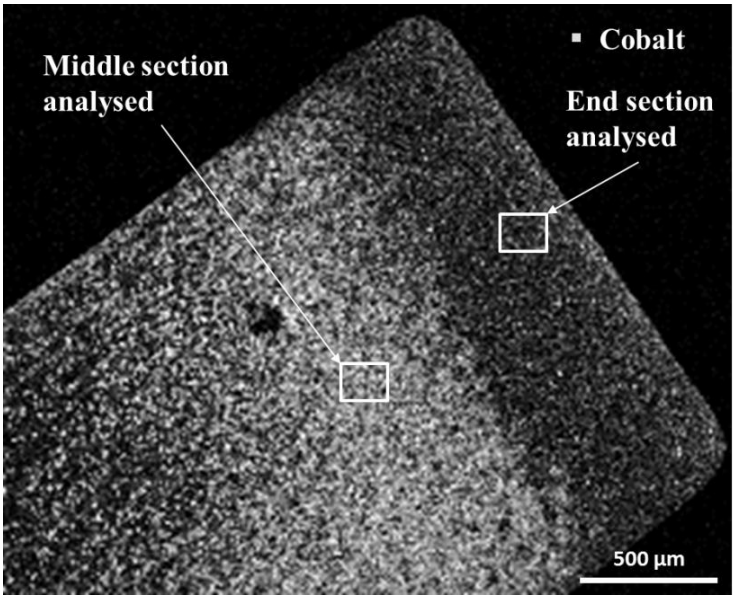


**Fig. 5.7 Large-area EDX map of cobalt (primary workpiece element) distribution on electrode (2.3 A, 3 µs ON, 2 µs OFF). There is significantly more workpiece deposition above the main discharge fringe. Sub-sections analysed quantitatively for Fig. 5.8 are highlighted.**

A higher concentration of workpiece material was present on the non-working regions of the electrode, as seen in Fig. 5.8. In the near surface regions in the middle section mapped, the EDS analysis shows there was more workpiece present than electrode elements. Additionally, the ratio of copper to tungsten increased from 20% to 50% from the end to the middle section, which could suggest preferential melting of copper from the end sections and its reattachment above the fringe.

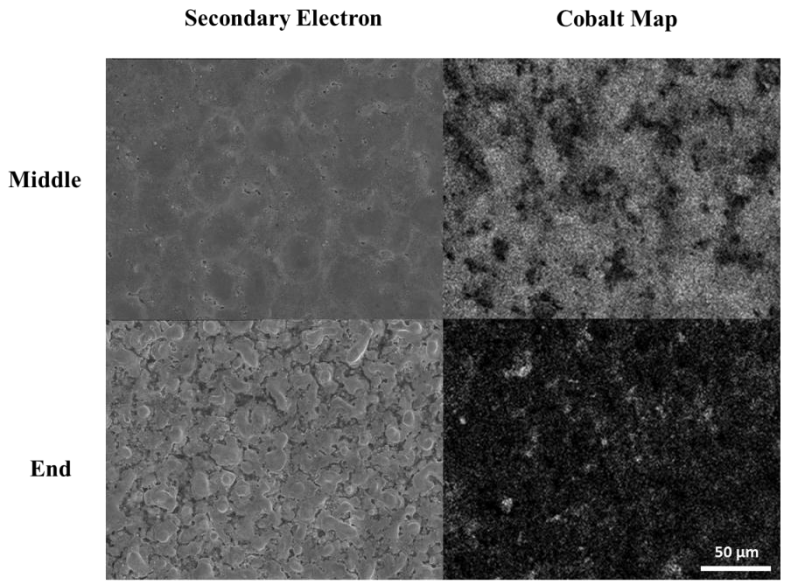


| Element | Weight % |
|---|---|
| Cr | 18.3 |
| Co | 30.9 |
| Mo | 6.5 |
| Cu | 14.4 |
| W | 29.9 |

| Element | Weight % |
|---|---|
| Cr | 3.70 |
| Co | 5.77 |
| Mo | 2.73 |
| Cu | 16.2 |
| W | 71.6 |

**Fig. 5.8 Cobalt distribution on middle and end sections of electrode by EDS. The locations mapped are defined in Fig. 5.7. There is significantly more deposition of workpiece in the middle section than the working end of the electrode.**

Levels of carbon are difficult to quantify using EDX because the C X-ray K line is of low energy and hence easily absorbed by surrounding material. Despite this, uniformity and trends can still be inferred from its measurement. Maps of the same regions analysed in Fig. 5.7 showed that carbon on the electrode is highly non-uniform, preferentially forming on the copper-rich regions, both in the primary and secondary working regions of the electrodes, while tending to avoid the tungsten and workpiece-rich areas. This suggests that the deposited workpiece regions are distinct from the carbon-based black layer associated with discharge on-times longer than 20 µs as reported by Kunieda and Kobayashi [40].

## 5.3.4 Electrode cross-section

### 5.3.4.1 Electrode surface composition

All electrodes were cross-sectioned and polished to reveal the workpiece deposition layer. A layer of between 1 µm and 3 µm thickness was observed with back-scattered electron (BSE) imaging on all samples. The layer is clearly darker than tungsten in

BSE mode but lighter than the copper matrix suggesting there is a significant amount of lighter elements in the layer, likely to be cobalt and chromium as deduced in the previous EDX analysis. This layer of darker contrast in optical imaging was only present in the middle section of the electrode and not below the fringe in the main working region.

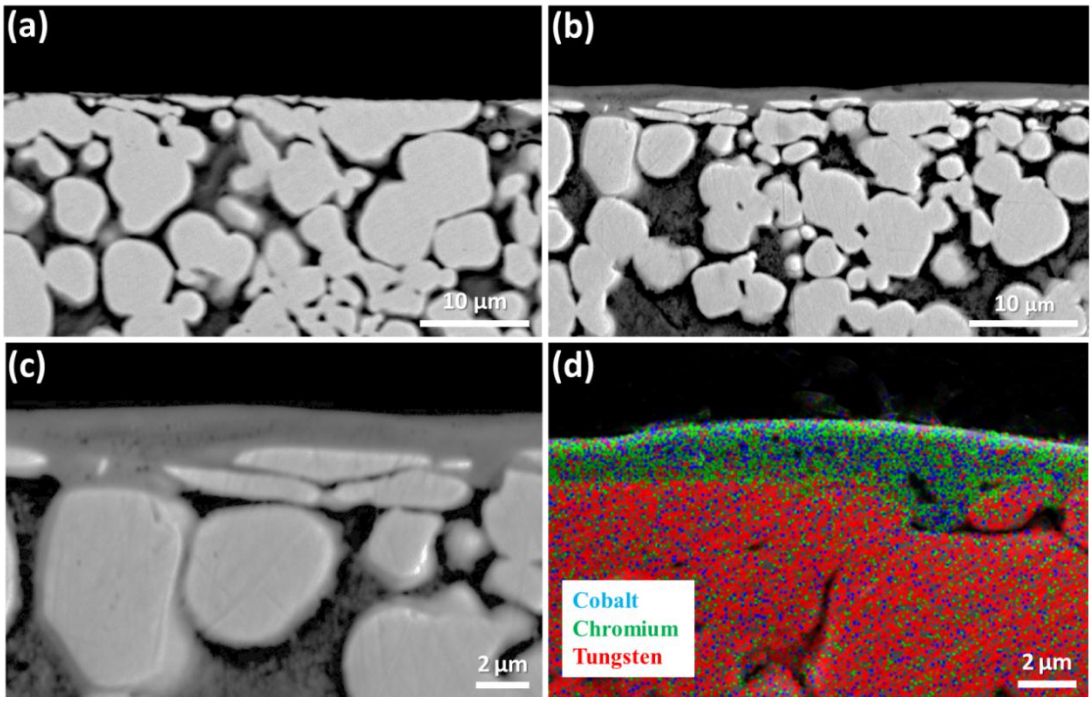


**Fig. 5.9 Cross-sectional BSE images of a) virgin electrode, b) workpiece-rich deposited layer in middle of electrode, c) bonding of the workpiece-rich layer between tungsten particles and d) EDX map of the layer proving workpiece element attachment.**

The deposited layer also bonds between the tungsten particles. The tungsten in these regions shows no evidence of melting i.e. cracks or a distinguishable recast layer, suggesting low intensity melting. This suggests the primary discharge process was unlikely to be responsible for this layer, given the working-region of the electrode shows a highly melted and deformed topography. In order to prove that the layer observed in cross-section is mainly composed of elements from the workpiece, EDX

mapping was performed. Fig. 5.9 shows the layer is distinct from the tungsten-rich bulk and is dominated by cobalt and chromium.

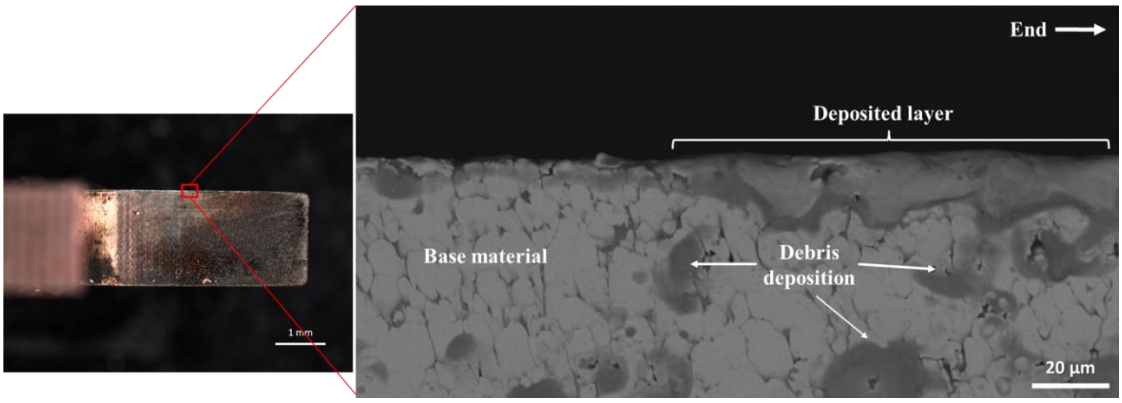


**Fig. 5.10 Non cross-sectional BSE image of deposited layer on edge of electrode. The layer can be clearly seen as a deposit on top of the electrode beneath. Individual debris deposits can be seen on the face of the electrode.**

Fig. 5.10 shows the deposited layer on the edge of the electrode. Back-scattered electrons reveal where the workpiece deposits are as dark areas. The raised topography of the layer can be clearly seen compared with the unaffected base electrode around it. Given the area analysed is near to the (non-working) top of the electrode, it is worth noting that this section of the electrode has spent only a small amount of total machining time inside the machined slot being subject to low frequency sparks and debris. On the edges of the electrode this layer is only observed in these upper regions of fewer sparks and below this the surface is worn instead of grown.

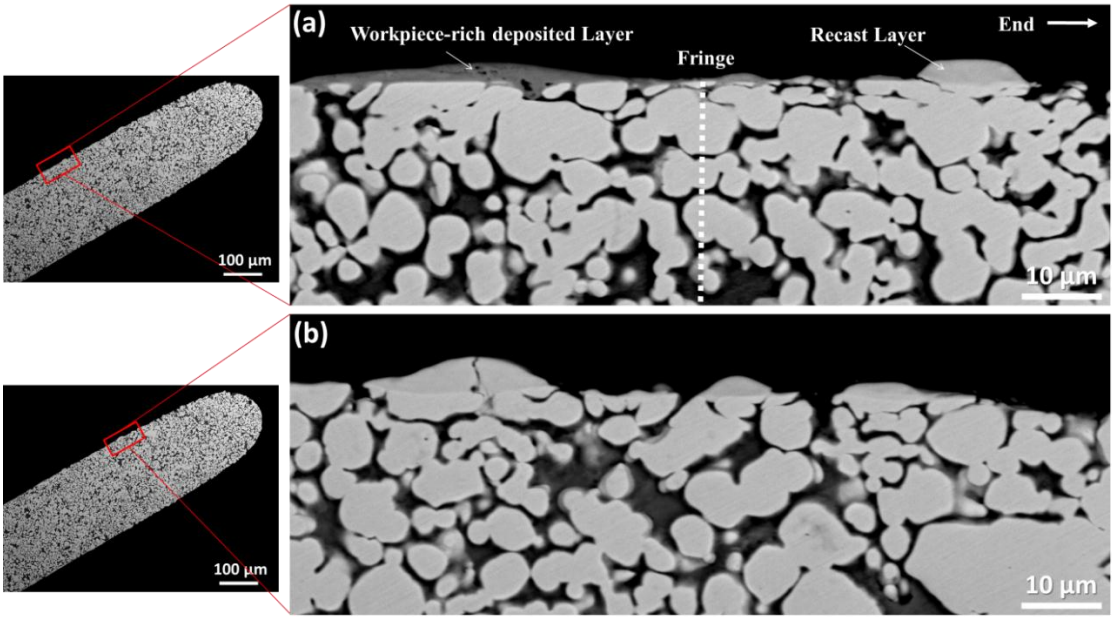


**Fig. 5.11 Cross-sectional BSE image (a) at the fringe, and (b) below the fringe. The recast layer on tungsten particles can be observed, with the lighter shades suggesting little or no workpiece deposition.**

The uneven primary discharge surface just below the fringe as seen in Fig. 5.6 can be observed in cross-section as shown in Fig. 5.11 (b). Back-scattered electrons show the recast regions on the tungsten particles, with the lighter shades indicative of tungsten dominance in this layer with little or no workpiece deposition as deduced by the EDX analysis. Cracks are characteristic of a typical EDM recast layer, and therefore suggest normal machining is taking place in these regions. A cross-section image at the discharge fringe (Fig. 5.11) shows the disappearance of the workpiece-rich layer and its flow between tunsgten particles below the fringe. A re-melted tungsten particle with a recast zone and crack can be seen to the right.

#### 5.3.4.2 Deposited layer thickness

All electrodes after machining were cross-sectioned and polished to reveal if the layer was present with all machining parameters. This workpiece-rich layer was present across all experiments, although its thickness as well as its uniformity varied depending on machining parameters. All electrodes were imaged with BSE

microscopy and the thickness was measured using "ImageJ" image processing software. 36 total points at 15 µm intervals, across approximately 500 µm of each cross-sectioned surface were used to calculate the mean layer thickness as well as the standard deviation of the values used to calculate this thickness.

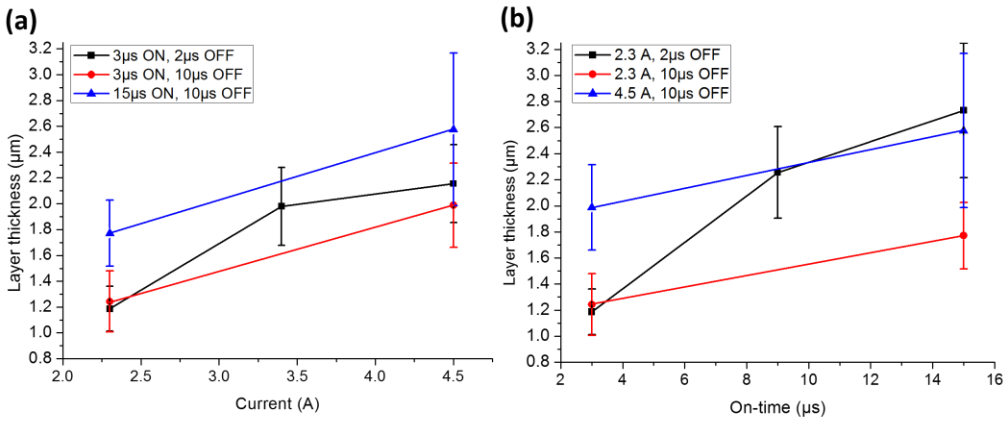


**Fig. 5.12 Average layer thickness above the discharge fringe showing an increasing trend with both current and on-time. Higher off-times produced a smaller layer on average. Error bars are the standard deviation of the measurements used to calculate the mean.**

Fig. 5.12 shows the trend of the mean layer thickness with both current and spark on-time. Standard deviations are included in the graphs since they give a good representation of the variation of the thickness of this layer on each electrode. It was found that there was a general trend upwards for the layer thickness with both increasing spark current and on-time as expected. This is consistent with higher spark energy causing more extensive melting. With higher off-times the layer was also typically smaller. The standard deviations are significant since the upper values of these also have a clear trend upwards with current and on-time, showing the maximum layer thicknesses at any point observed on the electrodes using the highest currents and on-times was significantly higher than that observed for lower spark parameters. The general trend of the thickness of the deposited layer with discharge settings suggests that this deposited layer is likely a function of discharge energy, as

well as total number of discharges, given the generally lower thickness for higher discharge off-times. This trend is consistent with the relationship between EDM recast layers and discharge conditions measured elsewhere, for example by Newton et al. [59], whereby recast layer thickness on Inconel 718 increased with both discharge current and duration.

#### 5.3.4.3 Removal of tool electrode material

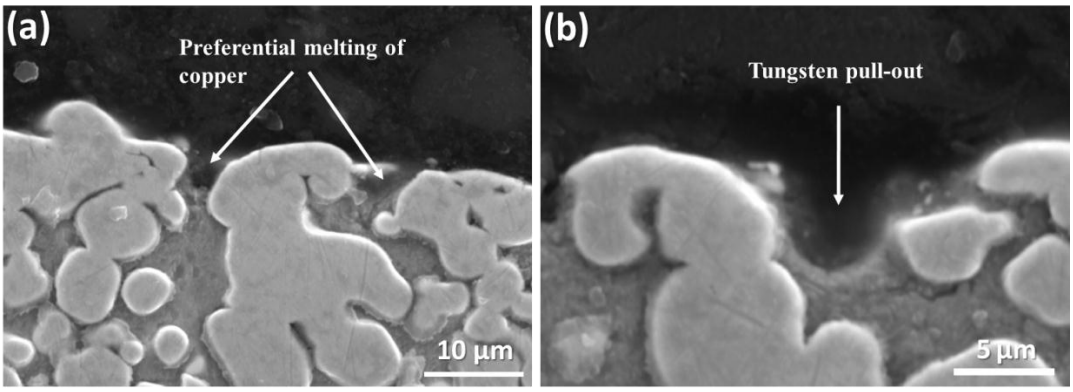


**Fig. 5.13 Evidence of wear mechanism of W-Cu due to preferential melting of copper and dislodging of tungsten particles.**

In the main discharge region, i.e. the region below the fringe there was evidence that dislodging of the tungsten occurred due to preferential melting of the copper matrix, as seen in Fig. 5.13. This is explained by the much lower melting point of copper.

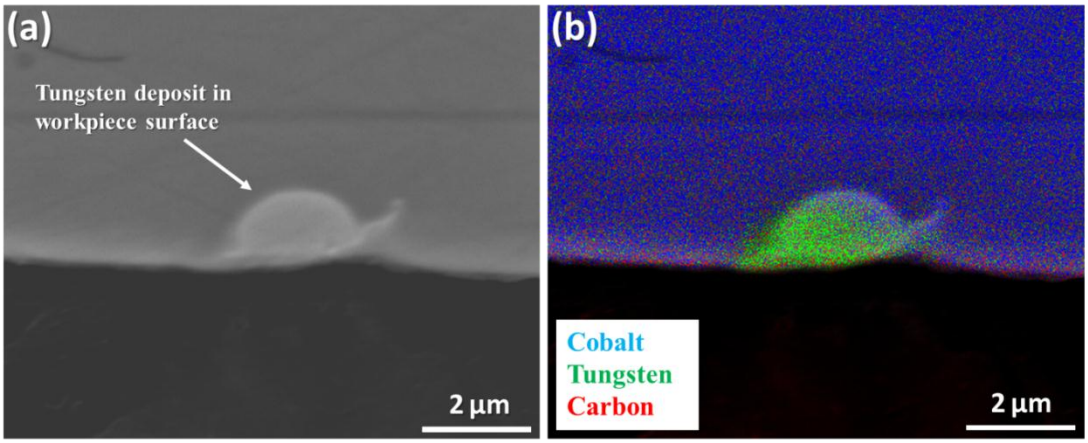


**Fig. 5.14 Deposition of tungsten particle in the workpiece surface. (3.4 A, 3 µs ON, 2 µs OFF).**

Deposition of tungsten from the tool electrode was observed in the workpiece surface. This supports the theory of total dislodging of tungsten particles due to preferential copper melting, since various deposits of whole tungsten particles were identified in one particular cross-section in the surface regions of the machined holes. EDX mapping was used to determine the elemental composition of these deposits. Fig. 5.14 reveals a particle of tungsten embedded in the workpiece surface. Much of its original round shape as it is in the electrode matrix still remains with some remelting at the surface due to sparking once embedded, suggesting it was mostly removed and deposited as a semi-solid particle. The mechanism of lodging in the surface of the workpiece is difficult to investigate since the workpiece surface is subject to machining and so discharge craters can no longer be identified. Quantitative EDX analyses of the recast layer of the workpiece were also carried out and apart from carbon as has been reported by Cusanelli et al. [62] via Auger spectroscopy, there were no foreign elements present except for the mentioned whole tungsten particles. Since the tungsten appears embedded in the workpiece as a solid particle, it is thought that its attachment occurs during the melting of the nearby surface and therefore is most likely attached during spark duration.

### 5.3.5 Analysis of deposits and discharge craters

To understand the attachment mechanism of workpiece material on the surface of the electrode, and electrode material onto the workpiece, micro-analysis of the discharge surface was required. Using secondary electron and back-scattered electron imaging of the electrode surfaces, the relationship between discharge craters and debris deposition could be understood. The distinctive gas bubble affected region has been reported upon elsewhere, for example by Schumacher [31]. This characteristic of discharge craters was used to isolate individual sparks on the electrode surface using secondary electron microscopy, and back-scattered electron microscopy was used to reveal the lighter workpiece elements as darker areas. EDX was used to prove the presence of certain elements.

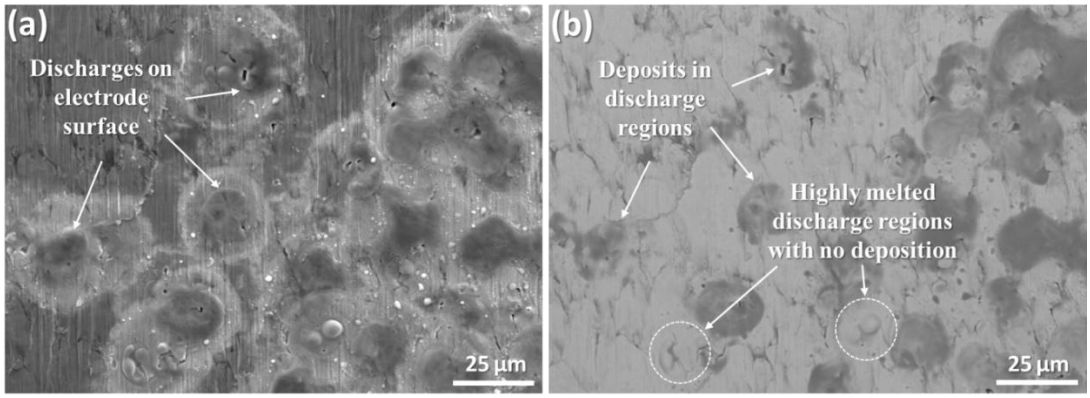


**Fig. 5.15 Discharges on electrode (2.3 A, 3 µs ON, 10 µs OFF) viewed in a) SE mode and b) BSE mode. Back-scattered electrons reveal the workpiece elements migrated to the electrode.**

In the central areas of the electrode, away from the primary discharge regions, discharge affected areas appear to have positive topography. This is consistent with the observed debris deposition. This can be seen in Fig. 5.15, where deposition occurs in discharge regions, although in some highly melted regions no deposition is observed.

The workpiece-rich layer seen in cross-section which does not appear to affect the base material fits with low energy sparking in these regions and the deposition of ejected workpiece material. It is suggested that the presence of debris particles and the favourable discharge conditions as a result are the cause for low energy secondary sparking in the central regions of the electrode. The subsequent plasma channel causes the re-melting of ejected debris in the gap and its attachment to the electrode surface in the region onto which sparking occurs. Given the uniform layer in these secondary sparking regions and the unaffected base electrode material, it appears that deposition due to secondary discharge can compensate for melting of the base material.

To prove that these discharge craters at the top of the electrode contain workpiece elements, as suggested by the BSE image, an EDX map of a single discharge crater was performed. Fig. 5.16 shows the dominance of workpiece elements in the melted region. It is also observed that small particle attachment does not occur on the melted region of the discharge, giving further evidence that deposition is caused by sparking and small particles are ejected from the melted region after discharge.

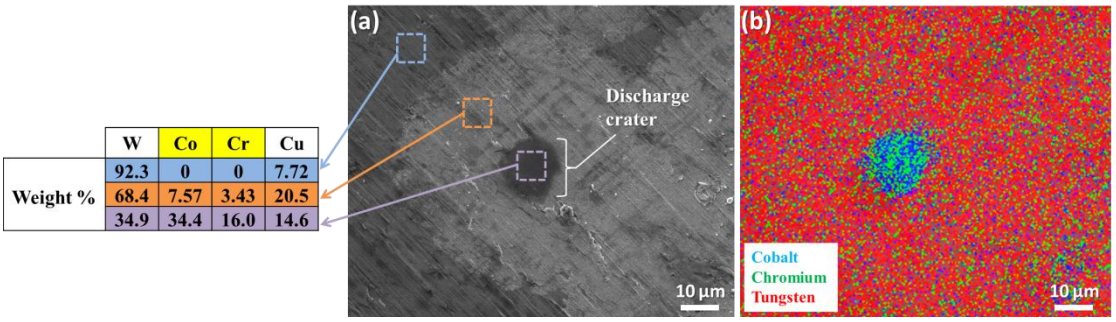


**Fig. 5.16 Quantitative elemental analysis of 3 regions of the discharge zone. Workpiece elements are highlighted in yellow. Highest workpiece concentration is in the discharge crater, with lower deposition in the gas bubble region.**

Quantitative elemental analysis with EDX of the discharge region as shown in Fig. 5.16 reveals the workpiece-rich discharge crater. It can also be seen that debris is still

deposited in the gas bubble affected region, while no workpiece elements whatsoever were detected on the base material unaffected by discharge. This suggests attachment of debris does not occur randomly from the dielectric, but is dependent on the discharge process. Although the carbon levels cannot be accurately determined in this EDX analysis, it can be noted that after EDX analysis the level of carbon was also roughly doubled both in the region of the gas bubble and the plasma channel, compared to outside of the discharge regions.

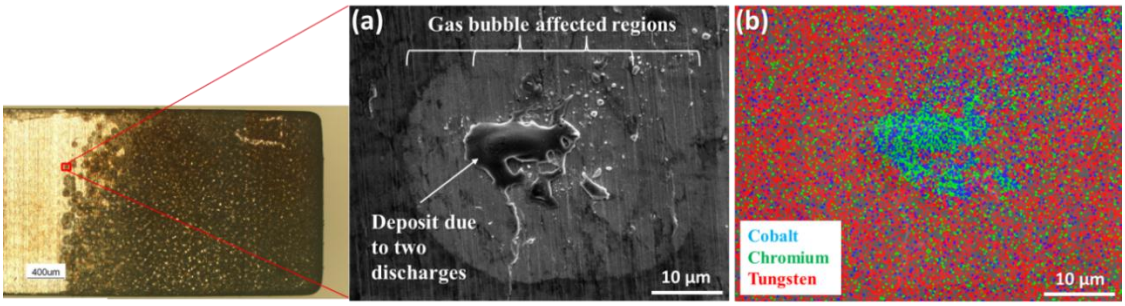


**Fig. 5.17 Large deposit at top central region of electrode 6 (2.3A, 15 µs ON, 3 µs OFF). The round gas bubble-affected areas indicate two discharges occurred here. EDX maps indicate the deposit is workpiece rich.**

On electrode 7 (2.3 A, 15 µs ON, 3 µs OFF), preferential secondary sparking and deposition was observed on one side instead of the other. This was assumed to be because of a slight tilt of the electrode. Although difficult to differentiate explicitly between primary and secondary sparks, the phenomenon of electrode tilt and preferential debris movement was exploited and the side onto which little secondary sparking occurred allowed within good reason primary discharges to be isolated and imaged. In a region of low debris deposition and near the working edge of the electrode, two primary discharge craters can be observed (Fig. 5.18), appearing to be characterised by recesses and melting of the tungsten surface. Back-scattered electrons reveal no debris deposition occurred due to the discharge. Discharge craters

exhibiting significant melting of the tungsten, with no deposition can also be seen in Fig. 5.15.

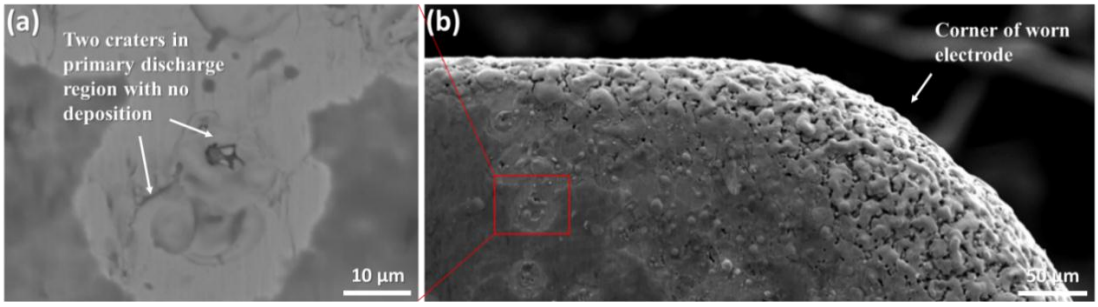


**Fig. 5.18 Two overlapping primary discharge craters with no debris deposition viewed in a) BSE mode, with b) showing the location near the working region of the electrode. Melting of the tungsten-rich surface can be clearly seen.**

This is consistent with the lower workpiece deposition in the working region of the electrode observed in Fig. 5.8 and explains why workpiece elements are not distributed evenly across the electrode surfaces.

## 5.4 Discussion

### 5.4.1 Characteristics of the deposited layer

Under the experimental conditions and materials used in this study, a uniform layer of tool electrode material could not be built up on the workpiece. This is thought to be because the rate of material removal is much greater than the rate of deposition. The observation of several whole tungsten particles in regions of the workpiece but with no copper present suggested that the rate of deposition of material was too low compared to the rate of removal of workpiece material during machining in order to leave a uniform layer. On all tool electrodes however; a uniform layer was produced, coating most of the regions of the electrodes which were submerged in the blind hole during machining.

Electrical discharge coating (EDC) has utilised the phenomenon of material deposition during electrical discharge processes to produce coatings. For example, Mohri et al. [159] produced a uniform TiC layer on a steel workpiece using opposite polarity conditions of a negative tool electrode. This layer was approximately 10 μm thick and therefore 4-5 times larger than the coating produced on the electrodes in this study, but shared a similar porous structure. Furutani et al. [44] were able to produce a much thicker TiC coating of 150 μm from powder suspended in the dielectric after experimentation revealed a negative electrode polarity was also more capable of producing the thickest coating on the positive polarity workpiece. Since other authors have established that positive polarity is preferred for the target coated electrode, this suggests that the positive tool electrode polarity used in this chapter's study may have been necessary to observe the layer generation phenomenon, and that polarity may be a significant factor. Despite this, layer generation was occurring on the negative workpiece, although since a significant amount of machining was taking place in order to produce the deep cavity, the conditions under which material removal as opposed to material attachment occurs are not clear.

In terms of understanding the conditions which result in net layer generation on a workpiece or tool electrode, further work should be conducted using powder suspended in the dielectric as well as powder sintered and normal alloy electrodes to establish when the replacement of machined material with a new layer effectively impedes machining progress, or conversely when layer generation on a tool electrode can potentially compensate for its wear. Mohri et al. [159] also observed that at some point during their electrical discharge coating experiments, layer generation was inhibited as machining rate took over the rate of deposition. No explanation was proposed for this considering the complicated phenomena in the discharge gap,

although it could be explained by alterations in flushing conditions and changes in electrical properties of the electrodes as their composition changed.

### 5.4.2 Discharges and material attachment

The aim of this study was to determine how individual discharges and deposition of material onto electrode or workpiece surfaces are related, from the analysis of individual discharge craters. Since the production and isolation of individual discharges using conventional EDM machines is not inherently possible, a solution was devised to increase the chance of isolating discharge spots on high-aspect ratio electrodes. The machining of high-aspect ratio holes also provided a large surface area for the build-up of a deposited layer.

Under both optical and electron microscopy, the primary machining region of the electrodes could be seen as distinct from the upper regions, which was expected as the primary machining region should be only near the bottom of the electrode. Despite this, above the primary machining region, significant modification of the electrode surfaces occurred which was proved to be a coating of workpiece material. In the working region of the electrodes, workpiece attachment was still observed, although to a much lesser extent. This indicated that material attachment does not necessarily directly transfer to the opposite electrode during primary discharge.

In regions on the sides of the electrodes where individual discharge craters could be isolated, using BSE microscopy and EDX analysis, it was observed that material was attached only in discrete regions, almost entirely in the centre of the discharge spot. In some regions of the main working area at the bottom of the electrodes, individual discharge affected spots could also be isolated. These spots were distinct from those identified in the non-working regions of the electrode, as material deposition was not

detected in such discharge spots. In cross-section, electrode material beneath the deposited layer appeared unaffected, with little evidence of melting, whereas at the ends of the electrodes, significant melting and deformation of the tungsten particles as well as removal of the copper matrix indicated that lower energy sparking, indicative of secondary sparking through polarised debris, may be the source of the deposited uniform layer in the upper regions of the electrodes. This was further evidence that material does not move directly from the workpiece to the opposite electrode during one single discharge, but it suggests that secondary discharges responsible for sparking in the non-machining regions of the electrode are the cause of melting of workpiece debris and attachment during discharge. The dependence of layer thickness on discharge parameters, however, is also evidence that the characteristics of each discharge have a strong influence on the volume of deposition per discharge. Mohri et al. [44] found that the thickest layer (150 µm) they could produce in the electrical discharge coating of titanium carbide was yielded under 3 A current, 2 µs on-time and 1024 µs off-time. Despite this the trend between thickness and machining parameters was not presented. The schematic in Fig. 5.19 illustrates the concept of material movement between electrodes as suggested by the information gathered in this chapter.

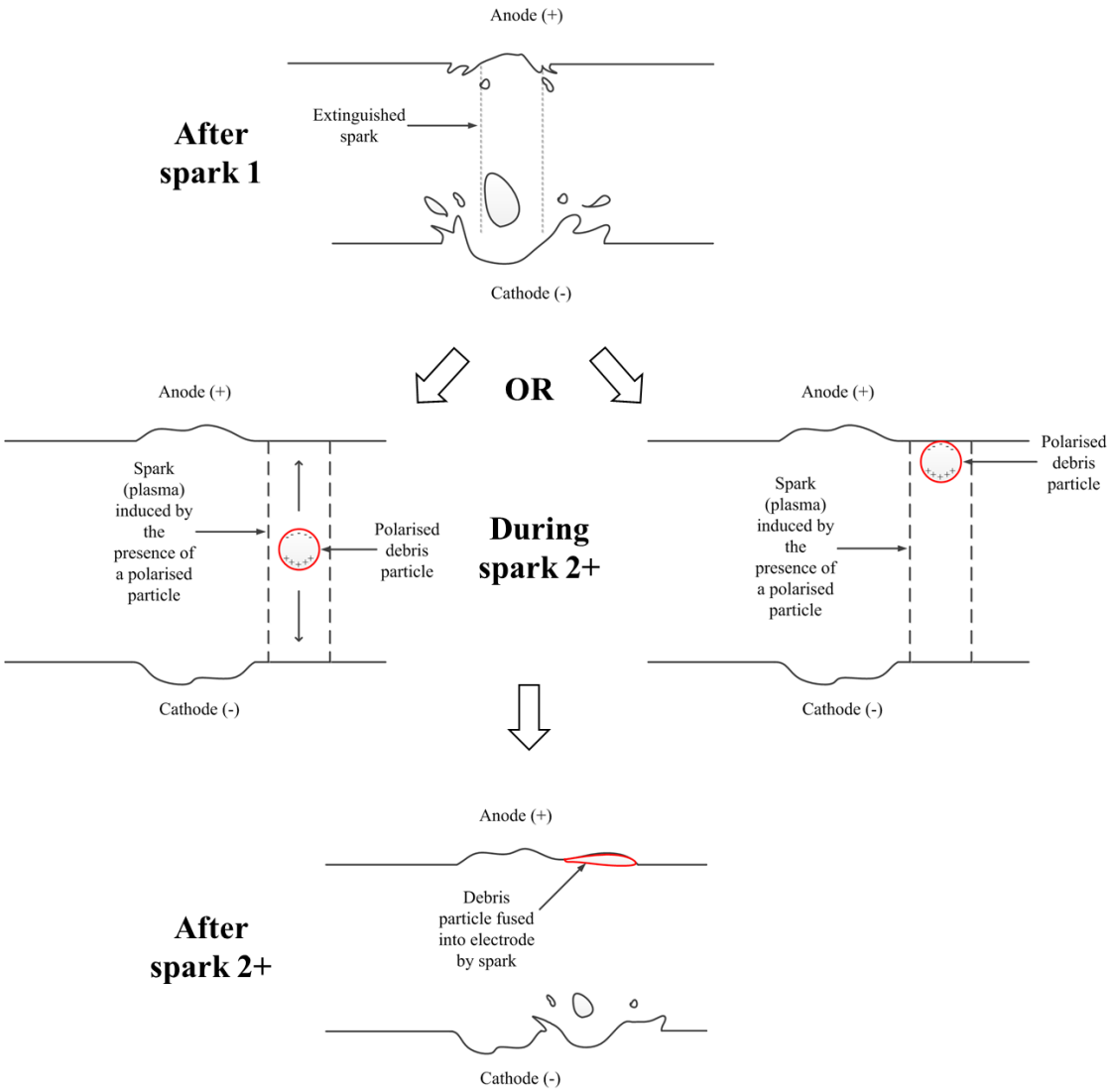


**Fig. 5.19 Schematic of process of material movement between electrodes**

The model for material attachment is that machined material which has been ejected from either electrode is not expected to attach unless it is remelted in the gap. This phenomenon is expected to occur due to discharges induced by the favourable discharge conditions due to the debris particle's presence; this is known as secondary discharge. These secondary discharges cause the melting of debris which are in transit, by the plasma channel of the spark and subsequent fusion and reattachment into the discharge's melt pool on the electrode surface, as opposed to material removal which occurs in the case of primary sparks. Since some of the energy of the spark will be consumed in the melting of the debris in the discharge gap, the effective

melting taking place at the electrodes will be reduced, explaining why a net deposition effect can occur instead of machining. Continued secondary discharges and the subsequent attachment of material into the spark's discharge region results in the build-up of a workpiece-rich layer which is larger and present mostly in the non-working regions of the electrode.

The direction of movement of material during secondary discharging may be related to the proximity of the nearest electrode, and therefore the strength of electrostatic attraction between the polarised particle and the electrode. For example if a particle in random motion is nearest the positive electrode before secondary discharge occurs, it will become increasingly strongly attracted to it the closer it becomes, and as the particle becomes increasingly polarised to stronger electric field. The same phenomenon is expected near to the negative electrode. This will cause the settling of debris onto either electrode simply by electrostatic attraction, and secondary discharges then ignite through this path. Alternatively, debris particles in random motion in the discharge gap are melted by secondary discharge, then forces acting on the material in the plasma channel cause the motion of the molten material towards either electrode.

Yang et al. [45] in their simulation work to understand the complex material removal mechanism in EDM, calculated that after each discharge, the first part of the removed material becomes debris in the gap, then the second part settles on the opposite electrode surface, and the final removed material settles back on the same electrode. Material in this simulation is ejected to random locations on both electrodes after discharge, and is not limited to solely the discharge spot as seen in the results in this chapter. In their work on electrical discharge coating using titanium powder suspension, Janmanee et al. [103] describe the mechanism of creation of a

contaminant layer on a workpiece as the capturing of metallic particles by the recast layer. Wang et al. [43] describe their method of creating a titanium carbide layer from a powder sintered electrode, as a chemical reaction between worn electrode material and carbon in the dielectric under high temperature, after which a ceramic layer can be built up under the correct parameters. These descriptions are not clear and somewhat contradictory, and have not been backed up with a fundamental study into the process. Despite a number of publications on the observed coating layer, as well as work regarding contamination in normal machining, there has been no study to link the process to fundamental discharge phenomena. This chapter adds clarity to the mechanism of material attachment, and its conclusions should be considered in further work regarding electrical discharge coating as well as machining which requires an absence of contamination.

### 5.4.3 The role of secondary discharges

In section 5.3.1 the phenomenon of vortex creation due to the jump motion of a reciprocating electrode was discussed. It has been observed that the creation of this vortex in deep hole machining can effectively inhibit the ejection of machined material from the machining area and trap large amounts of debris in the discharge gap at the sides of the electrode [158]. A clear example of this phenomenon occurred in one of the results in this study, as can be seen in Fig. 5.2. Such an extreme machining deformity indicates that a significant build-up of debris was occurring with the machine setup in this chapter's work. It has been explained that such a phenomenon of deformed machining occurs due to secondary discharge caused by favourable discharge paths through the particles. Since it is clear therefore that significant secondary discharge is taking place during machining with this machine set-up, this is further support that secondary discharges themselves are responsible for

this build-up of a deposited layer on the electrode surfaces seen in this study. Luo [28] published work which suggested that debris in the discharge gap plays a positive role in any form of machining with EDM. In Luo's model, debris particles both in the gap as well as settled on the electrode surface play a vital role in that they reduce the breakdown strength of the dielectric and supply of debris particles is necessary to achieve randomised and stable machining. Secondary discharges are therefore thought to represent a significant proportion of normal as well as abnormal sparking. This would suggest that deposition of material in either electrode caused by secondary discharge under stable machining conditions is an unavoidable side-effect of EDM. Further work and applications of this phenomenon could involve the deliberate suppression of flushing to promote gap conditions in which secondary discharges are extremely frequent, thereby increasing the effectiveness of the coating process

## 5.5 Conclusions

The results of this chapter have built upon the study performed in Chapter 4 to understand the material changes taking place at EDM'd surfaces during machining. From the perspective of surface contamination of electrode and workpiece surfaces, so far both attachment in the form of a layer as well as material deposition within the recast layer and not as a separate coating have been observed. This chapter has shown that material deposition is a two-stage process, where material ejected at the end of discharge on-time is resolidified in the discharge gap by a successive discharge, causing its fusion into the opposite electrode surface. A contaminated layer is therefore created by the gradual build-up of material through discrete concentrated deposits at the locations of discharge. The thickness of this layer increases with discharge current and on-time. This understanding is important for the avoidance, or deliberate deposition, of a contaminating layer during EDM.

The main conclusions drawn from this chapter are as follows:

- Two wear surfaces were characterised on the EDM electrode face after machining of micro-slots: the primary wear region at the ends and sides of the electrode and a secondary wear region above this. The primary wear region is uneven with little workpiece deposition after machining. The area of primary sparking on the electrode increases with increasing current and decreases with on-time. Linear motor reciprocating action of the electrode therefore does not eliminate side sparking in deep slots, with every electrode showing evidence of secondary discharge.

- A workpiece element-rich layer of between 1 µm and 3 µm thickness is observed on the electrode towards the non-working region of all electrodes. It is characterised by a high amount of workpiece material deposition and bonds between tungsten particles of a W-Cu based electrode. The base electrode beneath appears mostly unaffected from the machining process..

- The average thickness of this layer increases with both current and on-time, yet is lower with higher off-times, suggesting layer thickness is a function of spark energy and total number of sparks.

- Debris attachment to the electrode occurs in the central region of the discharge spots observed on the electrode, with a lower amount in the outer regions, and no deposition outside of these. A new model is therefore proposed for the movement of material to the opposite electrode during EDM, which suggests that attachment occurs due to re-melting by the plasma channel of debris previously ejected into the discharge gap. The secondary discharge phenomenon, also known as arcing [28, 160], which is sparking induced by

the presence of debris particles, is thought to be responsible for the melting of material settled on electrode surfaces or suspended in the dielectric. Attachment does not therefore occur randomly from the dielectric.

This chapter has explained the phenomenon of surface contamination in EDM as observed in a single-crystal material in Chapter 4. Due to the complexity as well as rapidity of the discharge process, its mechanism has until now remained unexplained. A novel method of performing elemental analysis on discharge craters was used to reveal the process.

# 6 Pulsed electron beam surface treatment of the EDM surface

## 6.1 Introduction

The aim of this chapter is to improve the properties of the EDM surface using a novel surface treatment technique – pulsed electron beam irradiation. Specifically, its effect on surface roughness, surface crack density and recast layer thickness are analysed. The metallurgical changes occurring at the surface as a result of the surface modification process are also assessed.

EDM is known to have a detrimental effect on fatigue life of a machined material compared to the raw material. This is because the recast layer remaining on the workpiece contains cracks which propagate under high and cyclic stresses due to their stress concentration effect [161], along with high roughness and tensile residual stresses. Premature fatigue failure will occur before failure predicted by the properties, as well as geometry, of the raw material. The layer is often harder and more brittle than the bulk material due to rapid quenching and for example the formation of martensite in steels, a phase formed by rapid, diffusionless transformation, whose heterogeneous needle structure results in brittle properties. For these reasons the recast layer is often deliberately completely removed after machining from components which will be subject to high stresses or cyclic loads.

For critical components used in highly stressed environments, for example in aerospace engines, the degradation as a result of the recast layer is pronounced. The size of the recast layer, and therefore the extent of its negative properties, also tends to increase with the use of parameters associated with faster machining rates.

The removal of the recast layer is an additional process step in the manufacturing chain. Its removal also results in a dimensional loss dependent on the size of the layer, undermining the accuracy of the EDM process. Preferable to this, is the transformation of the EDM recast layer into one with desirable properties, while the component still possesses the intended dimensions. In this chapter a surface treatment process is investigated for its potential to improve the properties of the EDM recast layer without its removal.

Pulsed electron beam irradiation is a surface modification process capable of remelting the surfaces of materials over a large area. In this respect the process can invoke changes which are consistent over the entire area of a workpiece. The process is known to reduce the Rz roughness of EDM'd surfaces, and has been shown to achieve this smoothing effect at very high tilt angles [105]. In this study the effect of the irradiation process on crack proliferation and surface morphology of the EDM surface is investigated. The metallurgical changes arising in the remelted surface as a result are also studied. Since rapid cooling rates are expected after surface melting by the irradiation process ($10^8$-$10^9$ K/s have been theorised for this process [162]), novel metallurgical changes such as the formation of nanostructures are also expected. TEM analysis is therefore used in this chapter to identify phases and characterise these structures.

## 6.2 Methodology and experimental setup

### 6.2.1 Research methodology

Given the aim of the chapter is to investigate the effect of pulsed electron beam surface treatment on the common negative properties of surfaces cut by EDM; such as surface cracking and surface roughness, EDM parameters firstly needed to be

established which are representative of typical machining setups and which resulted in surfaces with an exaggerated number of cracks, and exhibited typically rough morphologies. In this study, the most widely used stainless steel; 304, a stainless steel used at higher temperatures with superior corrosion resistance; 310, as well as a common superalloy used as a structural material in gas turbine engines; Inconel 718, were subject to EDM trials. It was important that the material chosen for this investigation was representative of a range of commonly used engineering materials which may be cut by EDM, so that the results of the investigation are relevant to industrial users.

Preliminary electron beam irradiation testing was then conducted on the surfaces of all three materials exhibiting significant cracking after EDM. Tests were undertaken using 30, 35 and 40 kV cathode voltage with 20 shots each. Previous experimentation on a range of materials, for example on Al-Si alloy [122] revealed that between 30 and 36 kV invoked substantial modification of the metal surface. Therefore in these preliminary tests between 30 kV and the maximum of 40 kV were used to observe any change in crack density and surface morphology on EDM'd surfaces. On the sample exhibiting the most significant reduction in crack density and surface asperities, a detailed investigation of the influence of irradiation parameters on crack density was then conducted, varying both number of irradiation shots and cathode voltage. Surface roughness was also assessed against these parameters.

Cross-sectional analysis of the treated surfaces was then performed in order to establish the mechanism behind crack repair observed on the surface, as well as determine the dependence of remelted layer thickness on irradiation parameters.

Transmission electron microscopy was then performed on a lamella prepared from the sample with completely repaired cracks, in order to characterise the effects of the irradiation process. XRD and GAXRD analysis were also performed on treated and non-treated surfaces to confirm phases identified in the TEM analysis, as well as determine if the phases detected were commonplace.

### 6.2.2 Parameter selection and equipment

Recast layer thickness is dependent on the 'pulse on-time' EDM parameter [59]. On-time is the duration for which current is flowing between the electrodes and melting of the workpiece takes place. For this experiment two on-times were chosen to induce two surfaces with differing recast layer thicknesses as well as surface characteristics such as crack frequency. The two EDM surfaces were subject to electron beam irradiation using a Sodick PF32A EBM under a varying numbers of shots and cathode voltages which determine the total energy delivered per pulse. A square copper electrode of cross-section 6 x 6 mm area was sunk 500 µm into the workpiece. Fig. 6.1 gives a schematic of this operation.

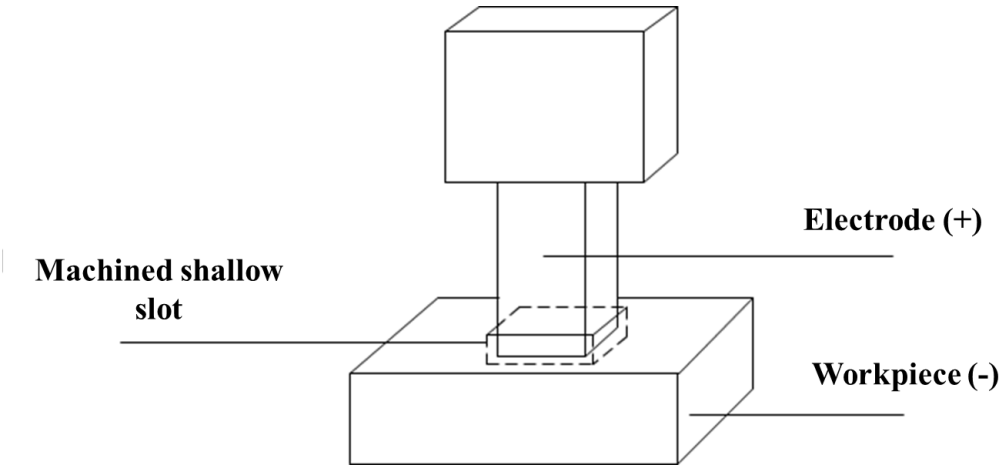


**Fig. 6.1 Schematic of machined shallow slot as performed in each EDM operation.**

X-ray diffraction was performed using a Bruker AXS "D8 Advance" diffractometer, producing Cu k-alpha monochromatic radiation. For standard XRD, the diffractometer was rotated from 40° to 100° with a step value of 0.04° and a step time of 2s. For glancing angle, the same 2 theta values, 40° to 100°, were used, but with a step value of 0.02° and a dwell time of 8s at each step. Microscopy was performed with a Hitachi S-2600 scanning electron microscope. Roughness was measured using a Fogale nanotech "Photomap 3D" white-light interferometer (WLI). Two parameters were used for assessing surface roughness; Sa and Sz. The Sa parameter is the arithmetic mean of the absolute values of the surface departures from the mean plane. This was chosen given the formation of craters was expected on surfaces treated with pulsed electrons, and therefore a linear Ra parameter may not best represent the surface characteristics. Sz is the ten point average of the five highest peaks and five deepest valleys, and was investigated since the presence of peaks and troughs on the surface is particularly detrimental to the fatigue behaviour of the part. For the identification and quantification of cracks on the surface and crack density, 4 back-scattered electron images were taken of the surface of every sample at a working distance of 30.3 mm and a magnification of 250x. This converts to a total area of 3.15

$mm^2$ of the surface of each sample evaluated for crack density. BSE mode was chosen for the high contrast produced between surface and crack. Images were then further analysed in "ImageJ" image processing software. Cracks of each image were then manually traced in the ImageJ software and the length of each individual crack was measured. This method was preferred to a thresholding method, since only the length of cracks was of interest and automatic thresholding algorithms could not sufficiently differentiate length from area.

A Sodick AP1L micro die-sink EDM machine was used to machine the initial shallow slots and induce a typical recast surface on the samples. A kerosene dielectric and positive electrode polarity were used to best represent a typical micro-EDM setup. Positive electrode polarity is usually associated with minimal electrode wear especially with copper electrodes due to carbon adhesion onto the electrode from cracking of the hydrocarbon dielectric [13], based on this the polarity was set only to positive. Observations made prior to this work also noted that on-times of 5 µs and 30 µs produced noticeably different surface characteristics, such as frequency of surface cracks and so these parameters along with a current of 4.5 A were chosen to represent typical micro-EDM parameters as well as induce different surface characteristics, such as recast layer thickness, roughness and crack proliferation. The EDM parameters are shown in Table 7.

**Table 7 EDM parameters**

| **Electrode polarity** | **On-time (µs)** | **Off-time (µs)** | **Main current (A)** | **Gap voltage (V)** | **Capacitance** |
|---|---|---|---|---|---|
| + | 5, 30 | 3 | 4.5 | 90 | Stray |

Preliminary trials were conducted to establish a process window which would best represent the range of capabilities of the EB irradiation process. Roughness and surface morphology were evaluated and 15, 25 and 35 kV cathode voltages were used with between 1 and 20 shots for each. It was observed in previous tests that shot numbers beyond 20 tended to have little further influence on the surface morphology of the sample, while 1 shot usually showed change to the surface. Similarly, between 35 kV and the maximum possible cathode voltage of 40 kV there was little change in the influence of this parameter, while 15 kV was established as a minimum value required for noticeably changing the surface of metal samples. The chosen range of parameters for this study is presented in Table 8. 12 different electron beam settings were used to investigate the effect of both the acceleration voltage and number of shots on the EDM'd surface. The EDM operation was therefore performed 26 times to prepare samples for EB irradiation; 13 times for each EDM pulse on-time setting, one of which was a control. This number of samples was used as it allowed a large range of EB parameters to be investigated.

**Table 8 Pulsed electron beam irradiation parameters**

| Cathode voltage (kV) | Number of shots | Anode voltage | Solenoid voltage (kV) | Argon pressure (Pa) |
|---|---|---|---|---|
| 15, 25, 35 | 1, 5, 10, 20 | 5 | 1.5 | 0.05 |

### 6.2.3 Lamella preparation and TEM

Focused Ion Beam (FIB) milling using an FEI Quanta 200 3D FIBSEM was performed to prepare two lamellae from the irradiated surface. Preparation of one lamella with sufficient depth into the sample as well as with sufficient thinness proved

difficult as thinning of a large area of the lamella inevitably resulted in damage to the topmost edge of the lamella. For this reason, two lamellae were prepared, one with approximately 100 nm thickness, with a depth of 3 µm into the sample, the second slightly thicker and of a depth into the sample between 1 and 6.5 µm. TEM was performed with a JEOL 2100F at 200kV using both Bright field (BF) and Dark Field (DF) imaging.

## 6.3 Results

### 6.3.1 Surface characteristics after EDM and pulsed electron beam irradiation

Machining of 304 stainless steel, 310 stainless steel and Inconel 718 using EDM with 4.5 A discharge current and 30 µs on-time, yielded surfaces containing cracks on all materials. The surfaces were then subject to pulsed electron beam irradiation with 20 shots at 30, 35 and 40 kV cathode voltage. Secondary electron images of these three materials after EDM and irradiation are shown in Fig. 6.2.

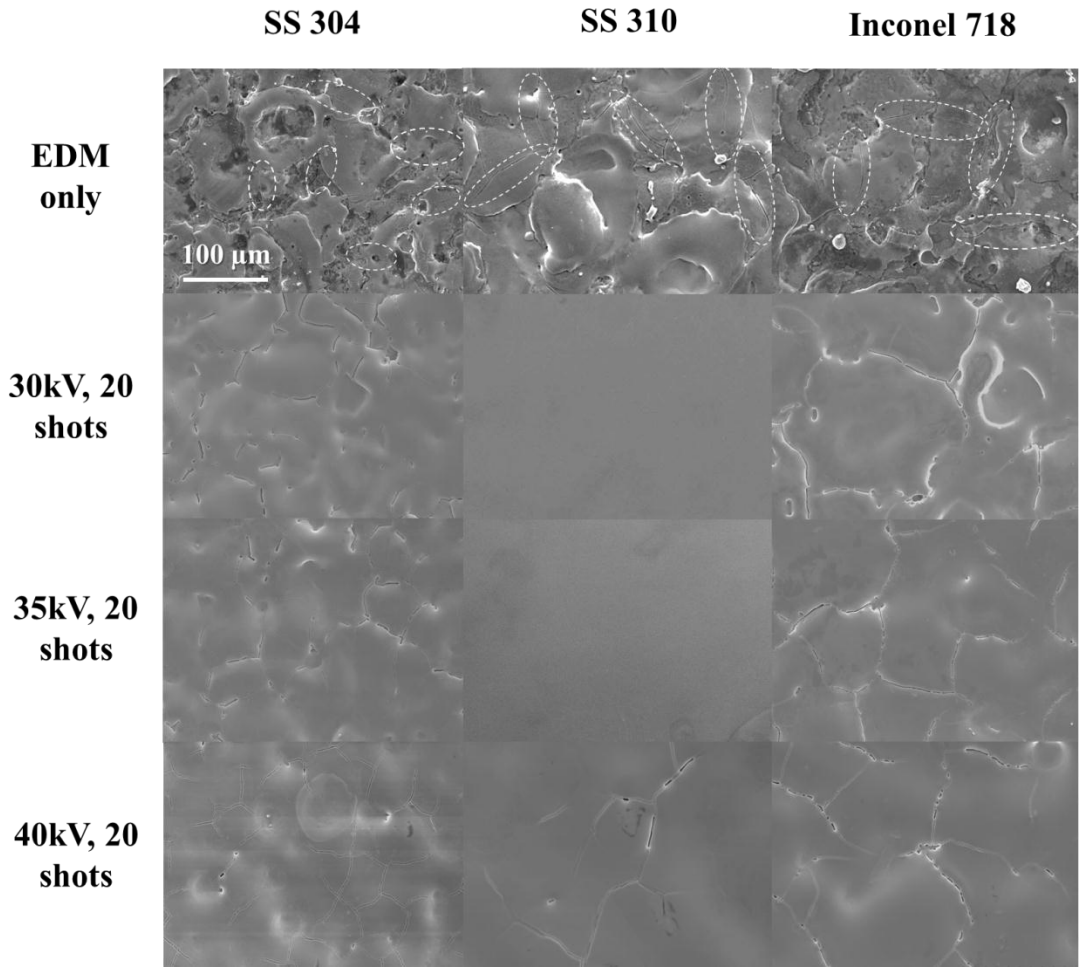


**Fig. 6.2 Steel and Inconel surface characteristics for various irradiation parameters. Cracks on the EDM'd only surfaces are labelled.**

Under this range of preliminary parameters, 310 steel obtained a crack free surface after 20 shots at both 30 and 35 kV cathode voltage. After 20 shots under higher cathode voltage of 40 kV, the same material displayed a mostly crack free surface, although a few cracks had reemerged. The 304 steel behaved quite differently to the 310, with a reduction in surface cracking only occurring in small areas on the surface after 20 shots at 35 kV and at 40 kV. The cracks present on the surface of Inconel 718 showed some evidence of repair through melting, however the majority of the cracks were still present after irradiation at 30, 35 and 40 kV.

Since 310 steel under these parameters displayed more susceptibility to crack repair and after 20 shots at 35 kV produced a completely crack free surface, surface treatment of this material was investigated in more detail.

EDM of the 310 steel with two different on-time parameters produced, as expected, different surface characteristics. The higher energy sparks caused by the 30 µs on-time parameter produced a crack dominated surface with higher Sa and Sz roughness values. Fig. 6.3 shows the different surface characteristics of the EDM'd surface caused by the on-time of 30 µs compared to that of 5 µs,

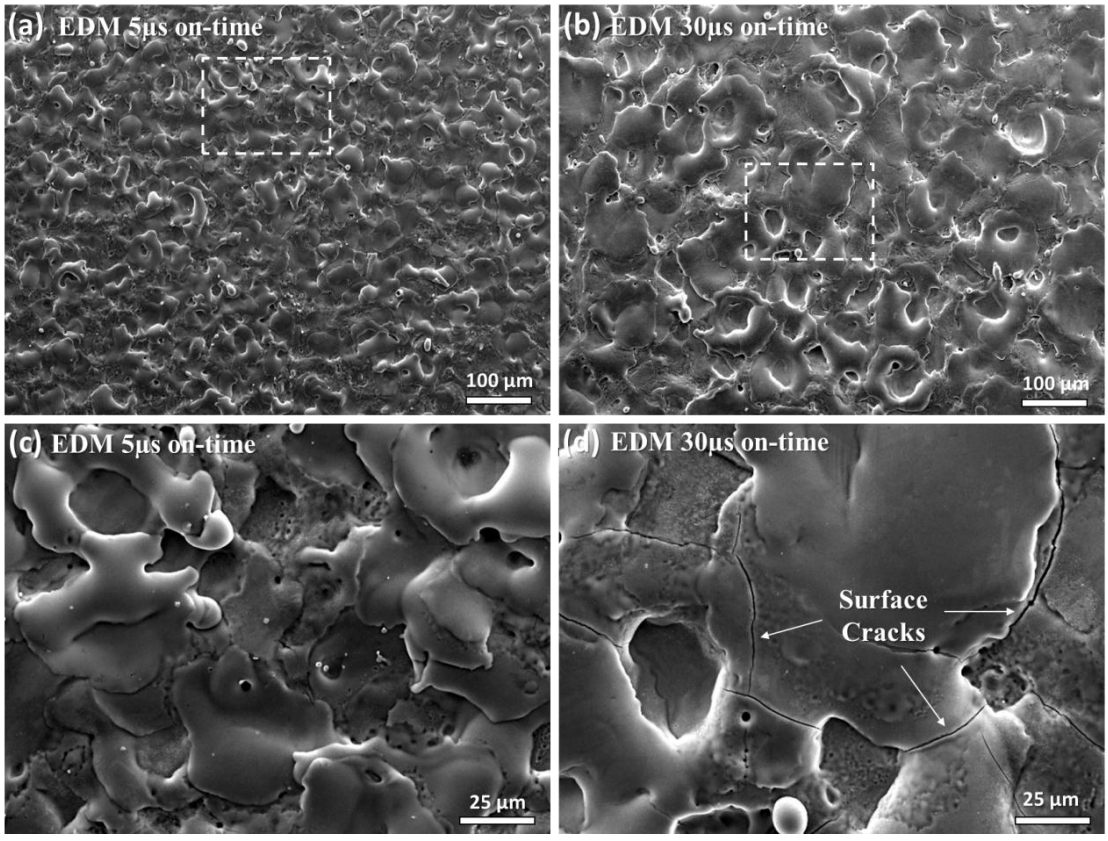


**Fig. 6.3 Secondary electron images of EDM'd surface of 310 steel using on-times of (a) 5 µs, magnified in (c) and (b) 30 µs, magnified in (d). Magnified regions are highlighted. Surface cracks induced using EDM with 30 µs on-time can be seen in (d).**

The different surface characteristics between the two surfaces are caused by the lower total number of sparks used to machine the same volume with the 30 µs parameter.

Fig. 6.3 (c) and (d) compare surface features of both initial surfaces. 5 µs on-time results in a surface with a higher frequency of micro-features but appears to have no, or very few cracks. The 30 µs on-time produced a surface with significant cracking caused by more aggressive machining conditions. The 30 µs machined samples are therefore useful for the assessment of crack repair by the electron irradiation process and surfaces machined using this EDM parameter are used throughout the rest of this chapter.

### 6.3.2 Crack proliferation and crater formation

A factorial design of experiments incorporating three cathode voltages and four different numbers of irradiation shots was used to establish the dependence of crack density and crack length on these two key parameters. 15 kV is the lowest cathode voltage setting at which electron beam generation can occur, while a small amount of surface modification of metals is still expected to take place under this setting. 25 kV was chosen as a medium acceleration voltage, and 35 kV was set as the maximum in this study, given the crack free surface produced under preliminary experiments with 35 kV, and crack re-emergence seen at the higher 40 kV setting. Irradiation parameters are shown in Table 8.

Two properties of crack proliferation (density of cracks and mean crack length) of the EDM'd surfaces were observed and measured after electron beam irradiation. The dependence of these properties on irradiation parameters is shown in Fig. 6.4.

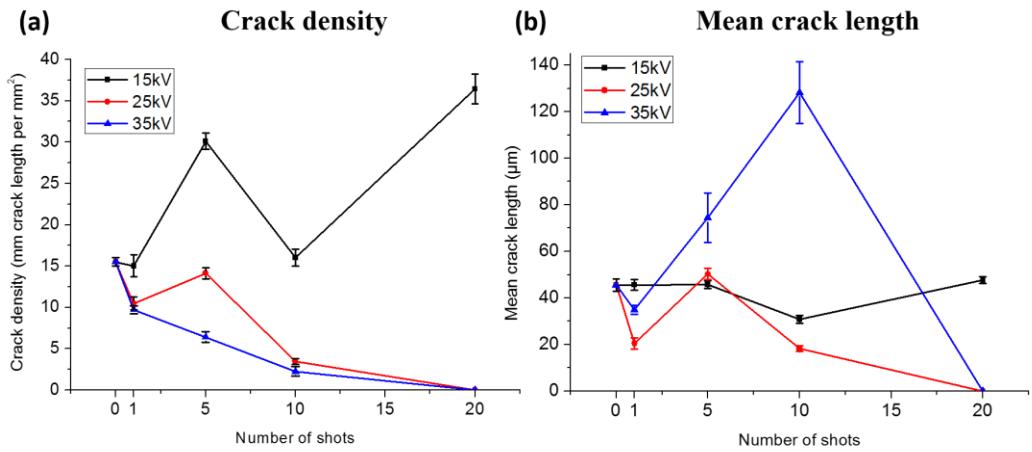


**Fig. 6.4 Variation of (a) crack density and (b) mean crack length with cathode voltage and number of shots. Error bars are the standard deviation of the data used to calculate the mean crack density and crack length.**

Fig. 6.4 (a) shows the influence of EB cathode voltage and the number of shots on the crack density at the surface. To evaluate crack proliferation at the surface, this crack density parameter was used as a metric by measuring the total length of cracks divided by the total area over which cracks were measured (3.15 $mm^2$ from images taken at an SEM magnification of 250x). Notable is the capability of the irradiation process to both decrease and increase crack density at the surface. After 1 shot at the lowest acceleration voltage, considering the error bars the crack density was unchanged, and then only worsened after further shots. After 10 shots at 15kV some crack resealing was visible. This mechanism is further investigated in 6.3.3. It is thought that this resealing effect at this parameter was sufficient enough to compensate for the further cracks created/revealed by the irradiation process, explaining why crack density returns to a similar value to that of the untreated sample. At 20 shots crack density is again worsened to more than double that of the control sample. The increased crack density caused by this parameter can be seen in the back-scattered electron images in Fig. 6.5.

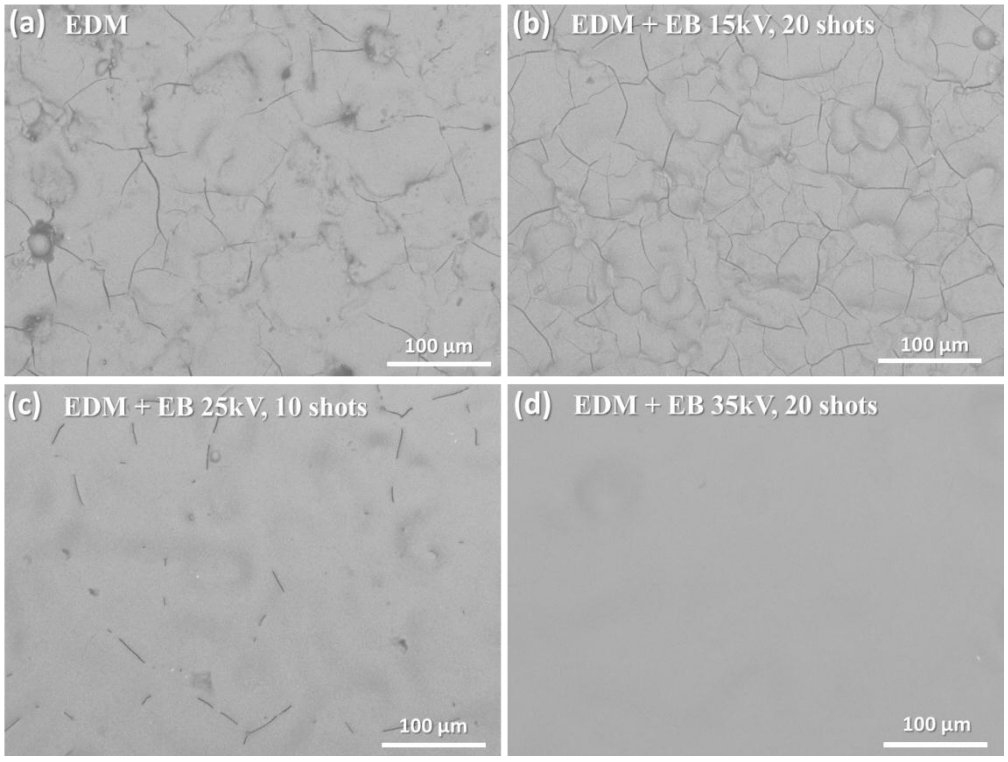


**Fig. 6.5 (a) EDM'd surfaces subject to (b) increased cracked density (c) reduced number of cracks and (d) elimination of all surface cracks. Images taken in BSE mode.**

In Fig. 6.5, the increased crack density as a result of 20 shots at 15 kV cathode voltage can be clearly seen. With 25 kV, 20 shots resulted in complete elimination of surface cracks, although with only 10 shots, a five-fold reduction in surface crack density was still produced, and this can be seen Fig. 6.5 (c). 10 shots at 35 kV also yielded a surface with a significantly reduced density of surface cracks. 20 shots at both 25 kV and 35 kV produced a crack-free surface based on surface imaging, as seen in Fig. 6.5.

Although crack density was measured via the total length of cracks per area, and this showed a clear trend downwards with the highest acceleration voltage, this did not take into account the length of the cracks themselves. Fig. 6.4 (b) plots the mean crack length for each surface against the number of shots and cathode voltage. The most noticeable discrepancy between the results for crack density and mean crack length is

that for the highest cathode voltage of 35 kV. Despite a decrease in total crack length with number of shots, the average length of cracks is increased up to 10 shots, and then at 20 shots they are eliminated completely. Again with 25 kV and 35 kV cathode voltage, after 1 then 5 shots of each, mean crack length is reduced then increased. This is explained by the partial crack healing occurring after 1 shot and the division into shorter cracks, then the elimination of this sealing effect after continued shots.

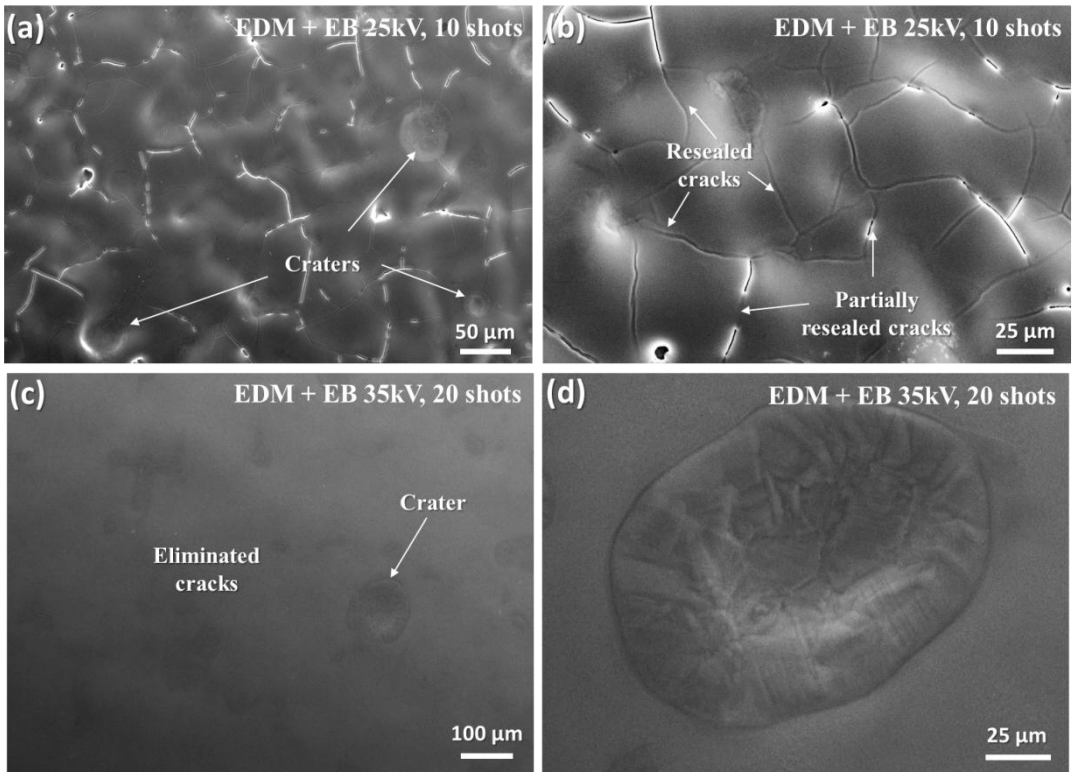


**Fig. 6.6 (a) Formation of craters and (b) resealing of cracks by 10 shots at 25kV, (c) elimination of cracks and (d) typical crater by 20 shots at 35kV.**

Craters were observed on all surfaces treated with 25 kV and 35 kV with 10 or 20 shots. The morphology of craters produced under 10 shots at 25 kV and 20 at 35 kV can be seen in Fig. 6.6. With 10 shots at 25 kV cathode voltage, obvious craters were more frequent, whereas with 20 shots at 35 kV, craters are generally less prominent, suggesting the continued melting at higher acceleration voltages causes their melting into the rest of the surface. On surfaces where cracks were not fully eliminated, and

craters had formed, no cracks were present in the location of the craters themselves. Suggesting more extensive melting had occurred in these regions compared with the rest of the surface.

### 6.3.3 Crack elimination and mechanism of crack repair

The surfaces subject to irradiation which were not completely healed of cracks were inspected in more detail to determine the mechanism by which crack repair takes place. The use of lowest cathode voltage irradiation and few shots was of particular interest in this study as it exposed the physical mechanism of crack repair and explains the trends in crack reduction and ultimately the elimination of cracks as shown for surfaces subject to 20 shots at 35 kV.

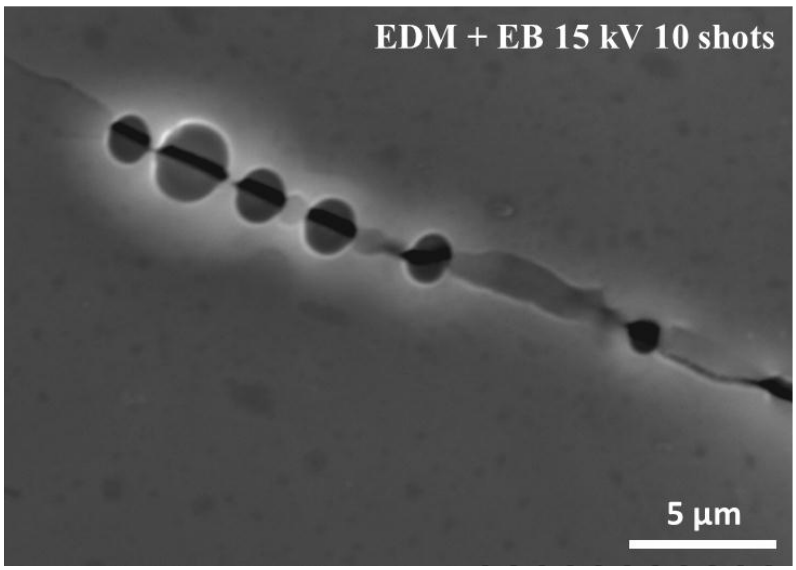


**Fig. 6.7 Surface image of resealing mechanism of EDM surface cracks by electron beam irradiation at low voltage (15 kV and 5 shots)**

Under the lowest irradiation cathode voltage of 15 kV and with 5 and 10 shots, a distinctive partial crack resealing effect was observed and is shown in Fig. 6.7. Such features seen in Fig. 6.7 were present in the locations of cracks on the entire surface of samples treated with 15 kV and 5 or 10 shots. The circular nature of the seal suggests flow occurred across the crack when the surface was molten then upon contraction

due to quenching, some joined parts remained. If the joined regions solidified more rapidly than the other regions of the crack, the rate of cooling would be expected to be lower the further away from these points, explaining the greater extent of contraction and volume reduction between the joins. Since volume of the material around the cracks must be conserved and material is not added by this process, if sealing of a crack occurs, there must be an equal extent of widening of the crack.

In cross-section the same phenomenon can also be observed. The sample seen in Fig. 6.7 was cross-sectioned to reveal the crack repair mechanism beneath the surface. The same was etched to reveal the three distinct sections; the EB remelted layer, the remaining EDM recast layer and the underlying bulk. Two cracks subject to partial resealing can be seen. The penetration of the unaffected regions of the cracks into the remaining EDM recast layer can also be seen. In cross-section, the resealing effect is clear, with a thin region at the top surface joining the sides of the cracks, and expansion of the cracks themselves inside the remelted layer.

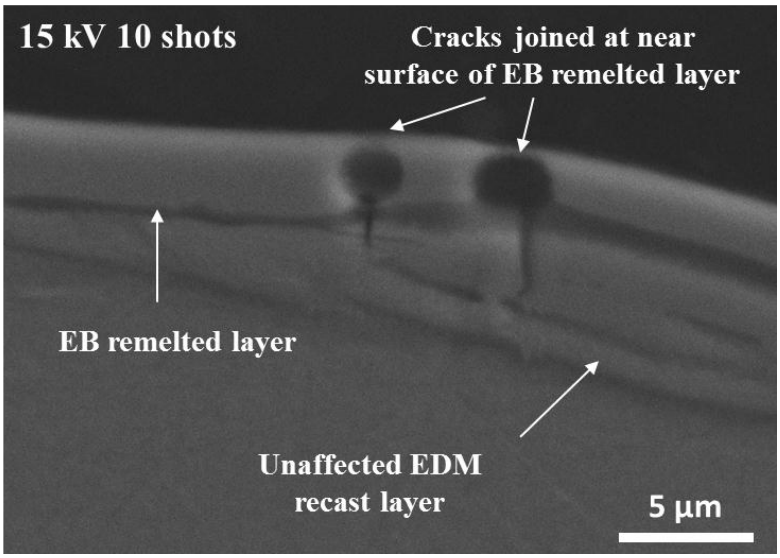


**Fig. 6.8 Crack repair mechanism in cross-section, using low cathode voltage of 15 kV and 10 shots**

After further irradiation shots (20) at 15kV, there was no evidence of the sealing effect suggesting that the continued irradiation of the seals at this cathode voltage caused their removal, thus exposing the cracks again. This may suggest a volume loss from the top surface. The mechanism of the crack repair process is discussed in section 6.4.1.

### 6.3.4 Surface roughness

Surface roughness was assessed to quantify the change in surface characteristics. Both the surface machined with 5 µs on-time with no visible surface cracks, as well as the crack dominated 30 µs machined surface were measured before and after irradiation. The surface roughness of each machined slot was measured before and after electron beam irradiation, three times for each measurement, using WLI over an area of 633 µm by 475 µm.

**Table 9 Key improvements to Sa and Sz surface roughness of both machined surfaces under electron irradiation**

| | 5 µs on-time machined surfaces | | 30 µs on-time machined surfaces | |
|---|---|---|---|---|
| | **Sa (µm)** | **Sz (µm)** | **Sa (µm)** | **Sz (µm)** |
| Pre-irradiation mean | 2.09 | 19.5 | 3.06 | 28.7 |
| Irradiated by 20 shots at 35 kV | 0.95 | 9.53 | 0.89 | 6.99 |

Table 9 presents the key improvements to surface roughness parameters at the electron beam setting of 20 shots at 35 kV, shown previously to yield a crack free surface. The machining process using 5 µs discharge on-time resulted in a surface with both Sa and Sz roughness values approximately one third lower than that of the 30 µs on-time parameter. This is expected given the lower energy per spark, but larger total number of sparks used to machine the surface, resulting in smaller discharge craters, and therefore lower average profile height (Sa) and lower peak height (Sz). The comparison between these surface features can be seen clearly in Fig. 6.3 (a) and (b), where the 5 µs yielded a surface with a higher frequency of peaks and troughs. After irradiation using the highest settings in this study, 20 shots at 35 kV, interestingly the previously rougher 30 µs surface was smoothed to a lower roughness in terms of both Sa and Sz compared to irradiation of the 5 µs surface.

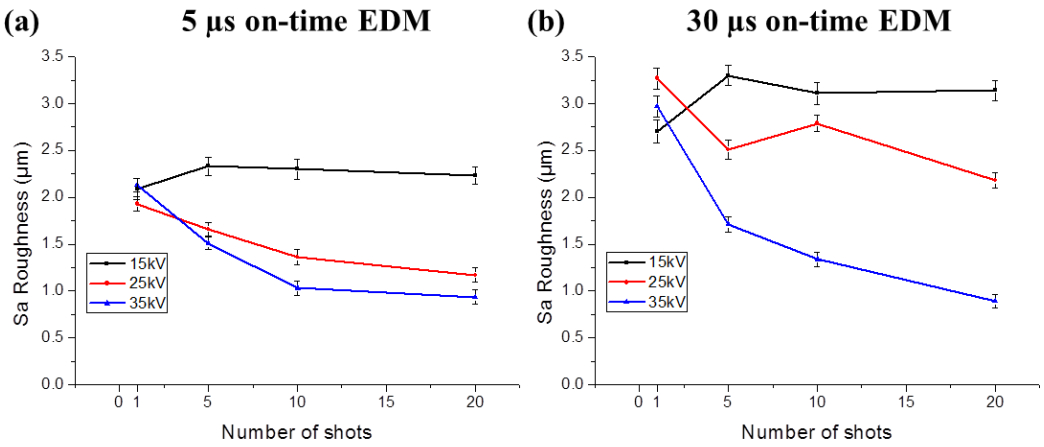


**Fig. 6.9 Variation of Sa roughness after EB irradiation using average roughness values. Error bars represent the standard deviation of the three measurements used to produce each value.**

As plotted in Fig. 6.9 the EDM'd surfaces with pre-irradiation average Sa roughness of 2.09 µm and 3.06 µm can both be reduced to below 1 µm with 35 kV cathode voltage and 20 shots. At 25 kV, the roughness showed a similar trend although the same smoothness could not be reached. The lowest possible roughness with irradiation at 25kV cathode voltage also seemed to be dependent on the initial roughness of the samples, given Sa values didn't reach below 2 µm for the 30 µs on-time sample, yet approached 1 µm for the 5 µs on-time sample. With 35kV however, after 20 shots the roughness of both surfaces was reduced to similar Sa values of 0.95 µm and 0.89 µm for the 5 µs and 30 µs on-time samples respectively. 35 kV cathode voltage was therefore more effective for treating rougher surfaces compared to 25kV. With 15 kV cathode voltage, despite the change in surface crack density measured in section 6.3.2, no significant change in surface roughness was seen. This indicates that the surface melting occurring due to irradiation at 15 kV is sufficient only to melt crack tips, and not asperities on the remaining surface. It is clear that the surface finish produced by pulsed electron irradiation was highly dependent upon surface condition at the beginning.

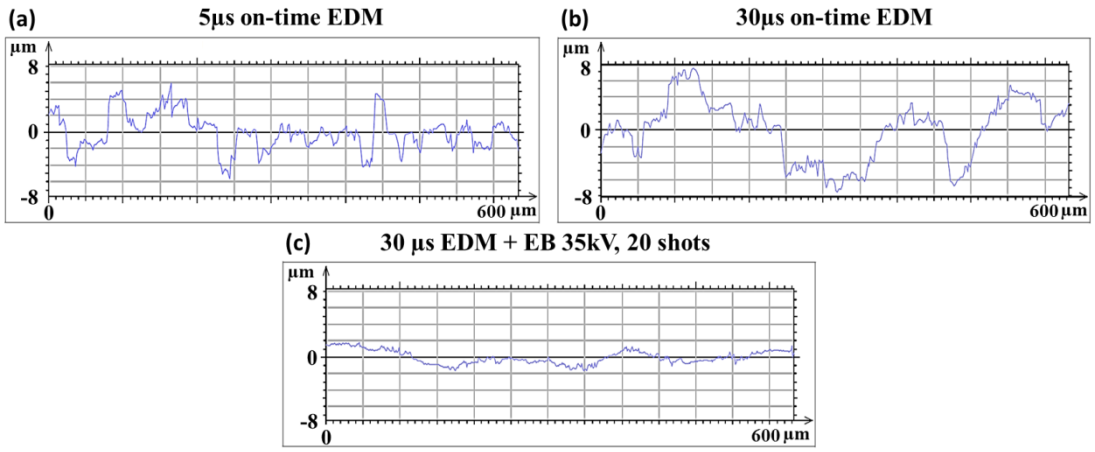


**Fig. 6.10 Typical as-machined surface profiles after EDM with (a) 5 µs and (b) 30 µs, (c) shows the 30 µs surface irradiated with 35 kV cathode voltage and 20 shots. All profiles set to the same scale.**

Although useful for determining trends, since Sa and Sz roughness values provide only limited information on the surface characteristics, surface profiles were also obtained. Fig. 6.10 gives example profiles of both initial machined surfaces and a smoothed machined surface after pulsed electron beam irradiation. The 5 µs machined surface has a higher frequency, as well as smaller amplitude of peaks and troughs, compared to the 30 µs machined surface. The maximum peak height was substantially reduced after irradiation, as was also shown by the reduction of the Sz parameter of the 30 µs on-time samples from 28.7 µm mean to 6.99 µm with 20 shots at highest voltage. In Fig. 6.10 (c) it can be seen the typical EDM'd surface profile is completely changed and much smaller peaks and troughs remain.

### 6.3.5 Cross-sectional analysis

Although it has been determined that a crack-free surface based on surface observation can be produced on 310 steel using pulsed electron beam irradiation, the depth of the repair process for parameters which result in this effect is not known, and the dependence of the depth of the crack repair process on irradiation parameters is also not understood. In this section, to determine the thickness of the remelted layer,

and the depth of the resealing effect induced by irradiation, all 310 steel samples machined with both on-time parameters were cross-sectioned and etched. After etching, the new remelted layer is distinct from any remaining EDM recast layer and the bulk microstructure, due to differential melting rates. The thickness of the layer on each sample was measured using SEM images at 36 points across the whole length of the samples. The results are presented in Fig. 6.11 along with cross-sectional SEM images.

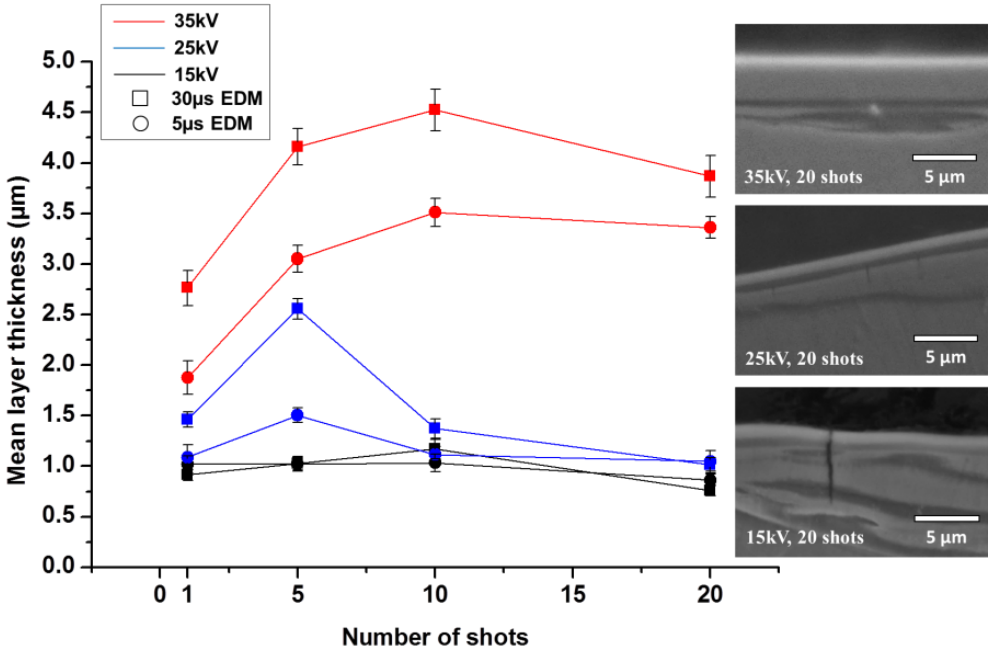


**Fig. 6.11 Mean thickness of EB remelted layer against cathode voltage and number of shots. Error bars are one standard deviation of the 36 data points used to calculate the mean value.**

Between the bulk material and the top surface, there are three distinct layers: the homogenous, high contrast EB remelted layer nearest the surface; the remaining EDM recast layer still containing cracks; and a layer exhibiting dark contrast between these which is likely a heat-affected zone induced by the EB melted layer above it. For the results in Fig. 6.11 the homogenous top layer was used for measurements of remelted layer thickness, given cracks were clearly affected in this region. Based on the results

in Fig. 6.11, the thickness of the remelted layer is highly dependent on cathode voltage, with a maximum thickness of 4.5 μm achieved using 10 shots at 35kV. Under 10 and 20 shots at 15 kV and 25 kV, cathode voltage had very little influence on layer thickness, although with 5 shots, 25 kV produced a 2.5 μm thick layer, while 15 kV yielded only a 1.0 μm thick layer.

Thickness of the remelted layer showed some dependence on number of irradiation shots. For example for both 25 kV and 35 kV, there was an increase in thickness from 1 to 5 shots for both EDM parameters. In comparison with the roughness results in Fig. 6.9, in both cases the roughness was unchanged after 1 shot but notably reduced after 5, suggesting initial roughness may be a limiting factor in the thickness of the newly remelted layer. It is also noteworthy that there was a significant drop in thickness after irradiation by 10 shots compared to 5 shots at 25 kV. This may be explained by the evaporation of surface material after continued irradiation. This drop in thickness is also seen for all voltages after 20 shots compared to 10.

Interestingly, the layer thickness was clearly dependent on the initial EDM machining conditions. Although samples of both EDM on-time parameters exhibited the same general trend of layer thickness dependent on cathode voltage, its thickness at each parameter was generally slightly larger for the 30 μs EDM parameter. This disparity was greatest for the highest cathode voltage of 35 kV, as well as for 5 shots at 25 kV - conditions under which the thickness of the EB remelted layer was greatest.

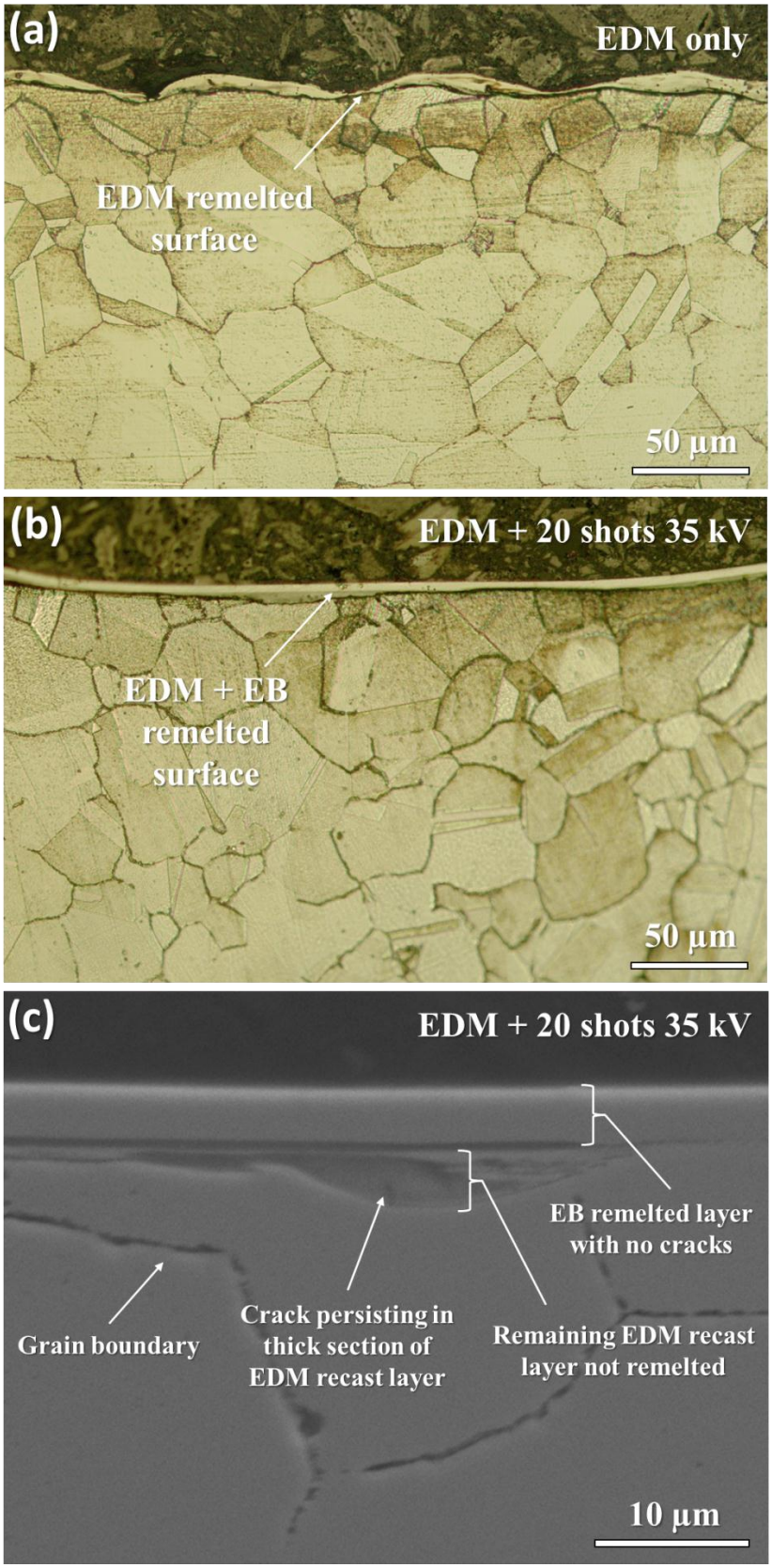


**Fig. 6.12 Cross-sectioned and etched optical images of 310 stainless steel (a) surface subject to EDM at 30 µs on-time, (b) surface irradiated by 20 shots at 35kV and (c) SEM image of cross-section.**

Fig. 6.12 (b) and (c) show cross-sectional optical and SEM images respectively of the uniform remelted layer of the sample subject to 20 shots at a 35 kV cathode voltage. These can be compared to the EDM'd only surface in (a) which exhibited a variation in thickness. This is explained by the randomness of spark location which occurs in EDM, combined with the principle of sparks taking place only one at a time, resulting in an uneven recast layer which is dependent on spark frequency and discharge parameters.

Porosity was also seen in the EDM'd recast layer not subject to pulsed electron beam irradiation (Fig. 6.12 (a)). This phenomenon is known to occur in EDM due to the embedding of gas bubbles the surface of the workpiece before solidification of the melted layer. The prevalence of porosity at the sub-micron scale was also revealed in Chapter 4. Under SEM imaging, the remelted layer produced by pulsed electron beam irradiation showed no indication of porosity, and was entirely homogenous in all images. However, this does not take into account sub-micron scale porosity invisible to SEM imaging.

Fig. 6.12 (c) shows the remelted layer at a particularly thick section of EDM recast layer. After irradiation no cracks were observed in the EB remelted layer itself at this cathode voltage and number of shots. However, it should be noted that although much of the layer is remelted with a smooth surface, a small crack remaining in the unmelted EDM recast layer, terminating at the bulk can be seen. This was one of only few examples of cracks observed to remain in cross-section. It is logical that with increasing depth of penetration with increased voltages as presented in Fig. 6.11, continued development of the irradiation process will permit larger thicknesses of EDM recast layers to be entirely remelted, and cracks spanning the whole depth of the

layer would be eliminated. However, there must be a fundamental limit related to the penetration depth of electrons. Despite the microstructure of the bulk material being clearly visible, it is not possible to resolve any microstructure in the remelted layer under optical or scanning electron microscopy. No discernible difference in microstructure just below the remelted layer compared to the bulk was observed. This suggests any heating beyond the visibly remelted layer is not sufficient to cause any microstructural change in this material.

Determining the homogeneity of the remelted layer in terms of crack repair and porosity is limited by the resolution of SEM imaging. TEM analysis was therefore also required to confirm the cross-sectional morphology of the layer at the sub-micron scale.

### 6.3.6 TEM analysis of grain size and grain orientation

Results presented thus far have demonstrated the crack repair phenomenon and the ability of the pulsed electron beam irradiation process to produce a crack free layer with reduced surface roughness. However, the metallurgical changes accompanying these morphological improvements have not yet been presented. TEM analysis was therefore conducted to determine the exact metallurgical structures present in the crack-free surface layer.

Two lamellae were prepared to cover the entire depth of the remelted layer, the near-surface lamella was first analysed using TEM in order to determine the grain size, grain orientation as well as depths of sub-layers associated with the phase transformations induced by the pulsed electron beam irradiation process. Fig. 6.13 shows bright-field and dark-field TEM cross-sectional images of the irradiated sample from the surface to a depth of 3 µm.

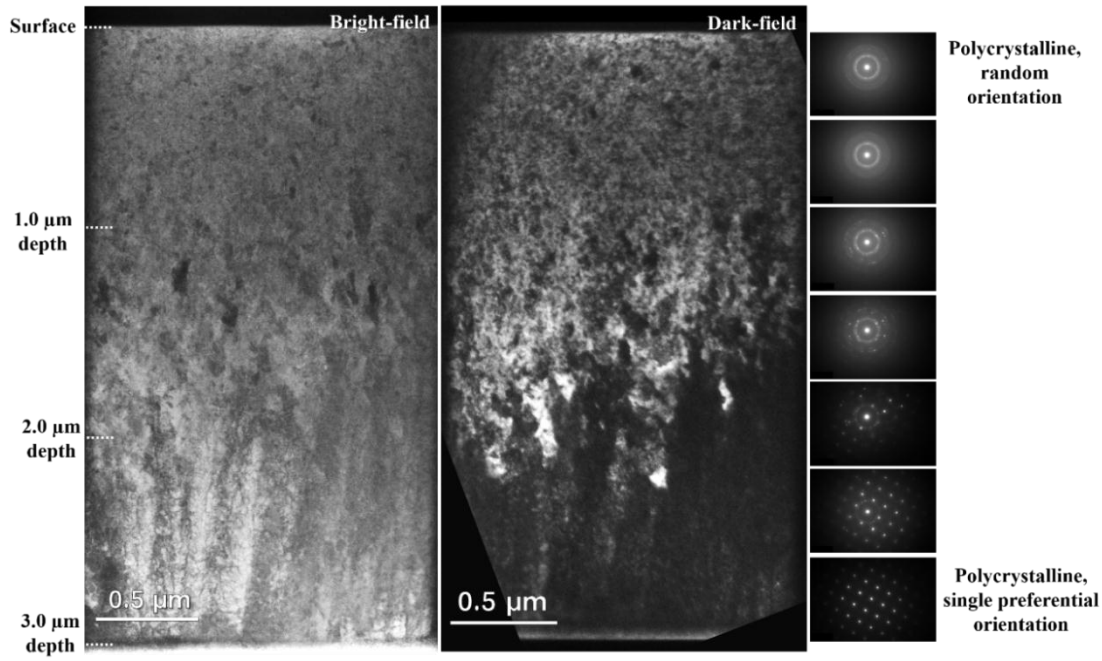


**Fig. 6.13 Bright-field and dark-field TEM images of a cross-section from the surface to 3 µm depth. SAED patterns expose random orientation close to the surface, and a single orientation beneath this. The interface between these regions is clearly exposed in DF mode.**

A graded grain structure can be seen upon initial observation of the both the BF and DF images, with the finest grain sizes existing at the top surface, and increasing in size until approximately 2.0 µm depth. Selected-area diffraction patterns (SAED) patterns accompany the images in Fig. 6.13 to reveal a fine polycrystalline structure. The ringed pattern in which individual rings can be clearly distinguished indicates a polycrystalline structure with no preferential orientation. In the dark-field image, this structure can be observed particularly clearly as the image is composed of a fine mixture of dark contrast and light contrast regions, suggesting a random distribution of orientations of grains. This polycrystalline structure is maintained between the top surface and approximately 1 µm depth. In the TEM images, between 1 and 2 µm depth, grains are noticeably coarser. A randomised grain structure in terms of orientation is also still indicated by SAED patterns, however the polycrystalline rings are composed of fewer individual spots compared to the patterns at the very top

surface, meaning fewer grains are contributing to the whole pattern over the same total area comprising the pattern, suggesting a larger grain size.

To quantify grain sizes within the two randomly oriented polycrystalline regions; between 0 and 1 µm, and between 1 and 2 µm depth, the diameters of 100 individual grains were measured in each region and were plotted, as shown in Fig. 6.14.

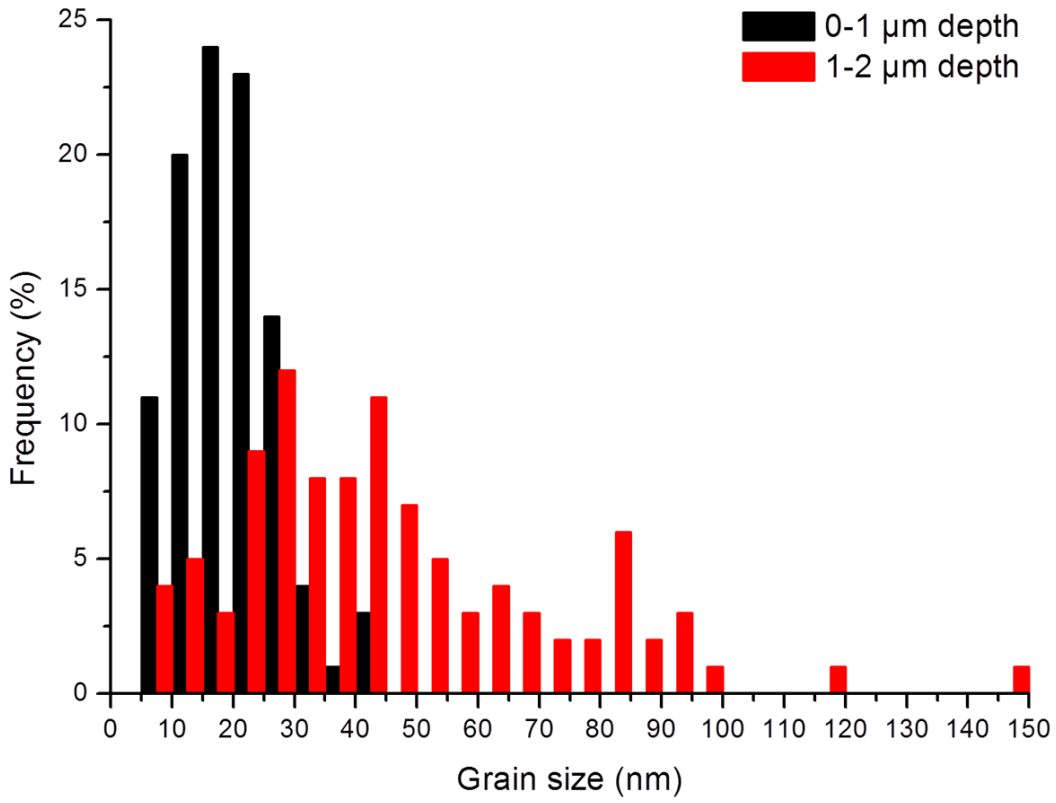


**Fig. 6.14 Histogram plots of grain sizes between the surface and 1 µm depth, and between 1 and 2 µm depth**

Within the first 1 µm depth, the modal (most frequent) grain size was between 15 and 20 nm. This can be compared with the region between 1 and 2 µm depth, in which the modal grain size was between 25 and 30 nm. Interestingly, the finest grain sizes of between 5 and 10 nm were seen in both regions, although this size range was three times more frequent in the top region of the lamella. The largest grain size observed in the top region was 43 nm, whereas a single 145 nm grain was seen in the deeper region. The median grain size between 0 and 1 µm depth was 18 nm, and the mean

value was 19 nm. Between 1 and 2 μm depth, the median value was 42 nm, with a mean of 46 nm.

Despite larger grain sizes only being observed in the region between 1 and 2 μm depth, the finest grain sizes of between 6 and 10 nm (6 nm was the smallest grain size measured) were seen in both the near surface region and as deep as 2 μm.

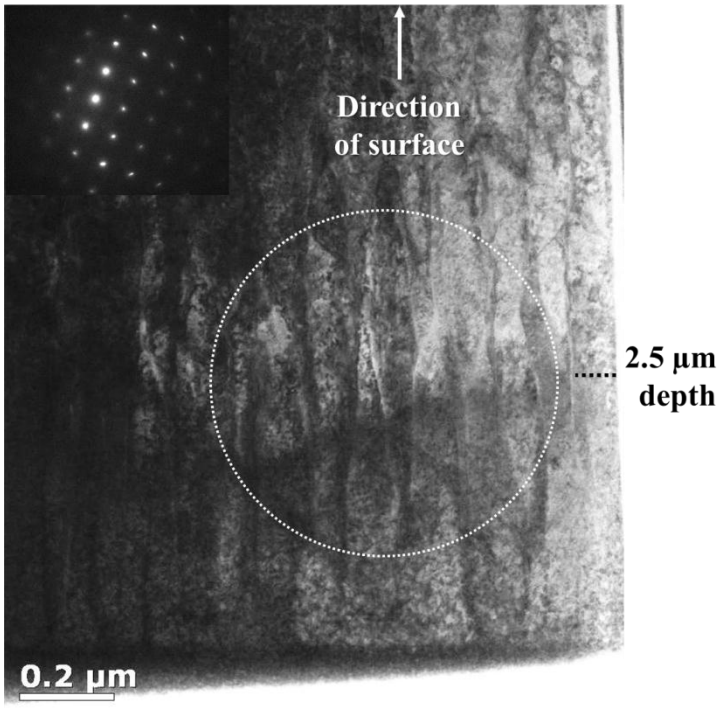


**Fig. 6.15 Bright-field image and associated SAED pattern of columnar grains with single preferential orientation between 2 and 3 μm beneath the top surface**

After the regions of the cross-section between 0 and 2 μm depth, a single-orientation region was observed. This is shown particularly clearly in the DF image in Fig. 6.13, where a sudden change from the randomly oriented polycrystalline region can be seen. The single orientation region is the uniform, dark contrast region, beneath the polycrystalline region in the dark field image, beginning at between 1.8 and 2.0 μm depth, and extending until the end of this sample, at 3.0 μm depth. In Fig. 6.15 a higher magnification image of this single-orientation region can be seen. Columnar grains between 50 and 100 nm width can be seen, aligned in a direction perpendicular

to the surface, from a depth of approximately 2 µm to 3 µm. An SAED pattern with a diameter of 1µm, incorporating several grains yields a single phase pattern with single orientation.

To analyse the grain structures seen in the region near to the interface between the layer remelted by the irradiation process and the remaining EDM recast layer, a second, deeper lamella was analysed. This lamella is a cross-section of the sample from a depth of between 1.0 µm and 6.0 µm. Between the top surface and 1.0 µm depth, the lamella was overly thinned and some of the sample within this top region was lost.

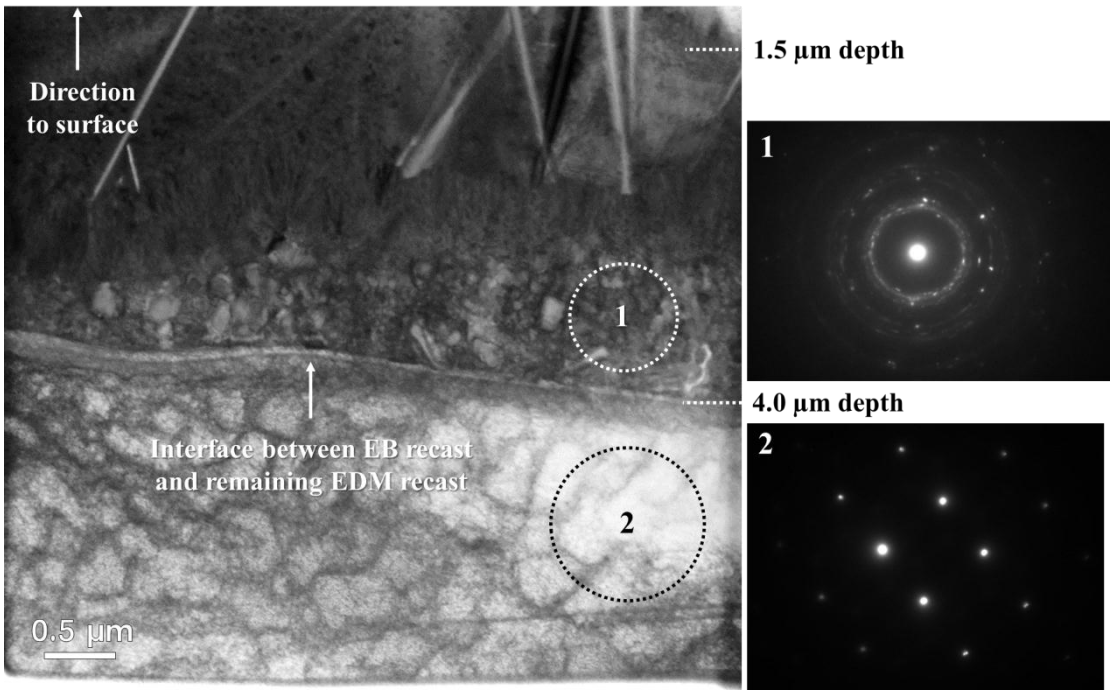


**Fig. 6.16 Bright-field image showing complex sub-layers, including the EB/EDM interface.**

A BF image of the lamella can be seen in Fig. 6.16. Several distinct regions can be observed, with a horizontal interface existing at approximately 4.0 µm depth. The region beneath this interface is characterised by one set of similar structures of a regular grain size, while the area above it contains a number of different structures of

varying sizes. Two SAED patterns are included in the figure; one of the region immediately above the interface between 3 and 4 µm depth from the surface, and one immediately beneath the interface, representing the structures between 4 and 5 µm into the surface.

In contrast with the previous TEM lamella imaged in Fig. 6.13 and Fig. 6.14, extending from the top of the sample (~1 µm depth) to approximately 2.5 µm depth, a number of needle structures were observed. These structures can be seen ending at the boundary between the polycrystalline region and the columnar region beneath. Beneath the sub-layer of columnar grains is a polycrystalline region with a random orientation, this is evidenced by both the varying dark and light contrast of grains in this layer, and the dominant polycrystalline rings of SAED pattern 1. Variation in grain size can be seen in this region, with grains in the size range of 40-250 nm diameter. Beneath this is the interface between the remelted layer due to pulsed electron beam irradiation, and the layer beneath, which is assumed to be created predominantly by the EDM process and not as a result of electron beam irradiation. It is possible that heating caused by the melted region above caused transformation in the region created by EDM. The interface is present at a depth of approximately 4.0 µm from the top surface, and this is consistent with the average measurement made in the layer thickness analysis conducted earlier in the chapter via SEM imaging and presented in Fig. 6.11. Beyond this interface, from a depth of 4.0 µm to the end of the lamella at 6.0 µm depth, a more regular grain structure, consisting of grains between 200 and 400 nm diameter can be seen. An SAED pattern incorporating multiple grains in this region yields a purely single phase pattern with a single preferential orientation. The uniform contrast of these grains in the bright-field imaging mode also highlights their single orientation.

### 6.3.7 Phase identification

In order to determine the phases present, indexing of SAED patterns taken during TEM imaging was performed. Fig. 6.17 shows indexed SAED patterns from the top surface in the region of finest grain size, from the region of columnar grains seen in Fig. 6.15, as well as the single orientation region seen below the EB/EDM interface. For convenience, the schematic in Fig. 6.21 should be referred to for ease of locating the SAED patterns.

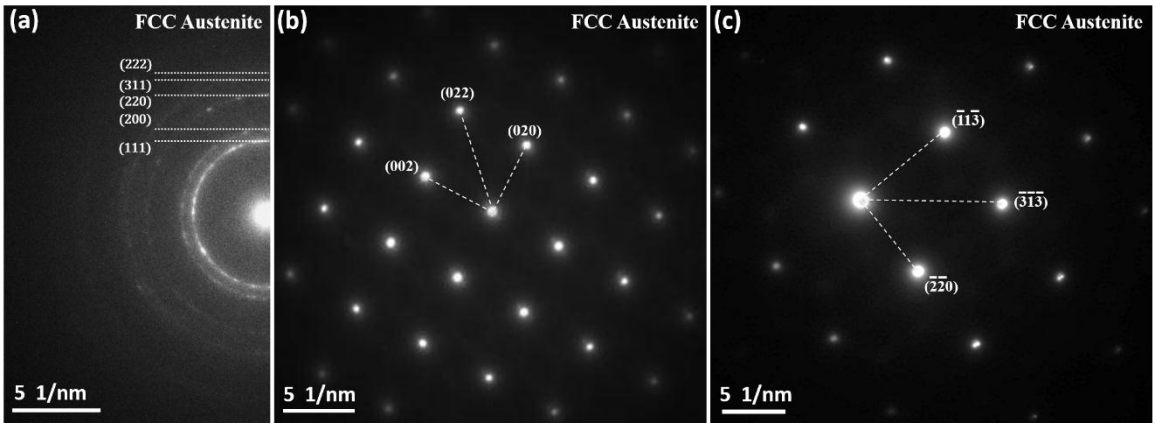


**Fig. 6.17 Refer to Fig. 6.21 for the location of patterns - (a) FCC polycrystalline SAED pattern taken 100 nm from the top surface, (b) FCC SAED single orientation pattern taken from multiple grains approximately 2.5 µm from the top surface and (c) FCC austenite pattern yielded from grains at 4.5 µm depth.**

A number of SAED patterns were taken from the fine polycrystalline region on the first (top) lamella, and all yielded a pattern belonging to FCC austenite with no preferential orientation. This can be seen in Fig. 6.17 (a). The polycrystalline pattern in location 1 in Fig. 6.16 was also identified as austenite, sharing the same pattern as seen in Fig. 6.17 (a). Despite this, the pattern was expectedly composed of fewer dots, given the larger grain size and therefore fewer different grain orientations contributing to the pattern. The pattern in Fig. 6.17 (b) is from the columnar grain region at the bottom of the top lamella, beneath the randomly oriented polycrystalline region. This crystalline pattern was also identified as belonging to FCC austenite with one single

orientation. A number of grains were used to produce an SAED pattern corresponding to location 2 in Fig. 6.16. The resultant pattern, seen in Fig. 6.17 (c), despite consisting of multiple grains, is a crystalline pattern of a single orientation, also corresponding to FCC austenite. This region of austenite continues until the bottom of the lamella, approximately 6 μm from the top surface.

From the second, deeper lamella imaged in Fig. 6.16, identification of the needle structures at the top of the image was difficult given the small area available for yielding diffraction patterns, resulting in surrounding structures contributing the majority to patterns, and the fact that little diffraction was being caused by these structures, as evidenced by their bright contrast in bright field imaging. Therefore, to summarise based on the SAED patterns, excluding the needle structures observed in the second TEM lamella, all areas of the TEM samples were composed of austenite.

### 6.3.8 XRD analysis

TEM is the most useful method for characterising small regions of a sample containing material structures with sub-micron scale dimensions. Despite this, the technique is inherently locational and not necessarily representative of the entire region of the 6x6 mm machined sample. In the TEM analysis in this chapter, two lamellae were prepared by FIB from the initial 6x6 mm machined and surface treated sample, and although the same phases were seen in the equivalent regions of both samples, a phase not seen in one was prevalent in the other. For this reason, XRD was used in order to determine the phases from an area of several $mm^2$, and therefore clarify the TEM results. XRD analysis is also more useful than TEM in order to determine the level of crystallographic texturing of certain phases in the sample, given the contribution of a much larger number of grains to the patterns. In this section,

glancing-angle XRD was also used to distinguish between phases detected within the first 1 µm from the top surface, as well as several µm deep. In particular, GAXRD was useful in order to identify the needle-like phase observed in TEM imaging within the first 2 µm depth into the sample, seen in Fig. 6.16.

XRD analysis was performed on the sample machined with EDM using 30 µs on-time and subject to 35 kV cathode voltage and 20 shots, i.e. the crack-repaired sample used in the TEM analysis in this chapter. It was also performed on the 5 µs machined sample subject to the same irradiation parameters, in order to identify any dependence of any final material characteristics on EDM settings. The analysis was repeated for the EDM only surfaces using both on-time settings, as well as for the EDM surfaces subject to only 1 shot at 35 kV, in order to reveal if multiple irradiation shots are required to induce the observed metallurgical changes. The raw material was also analysed for comparison. Fig. 6.18 presents the results of this analysis.

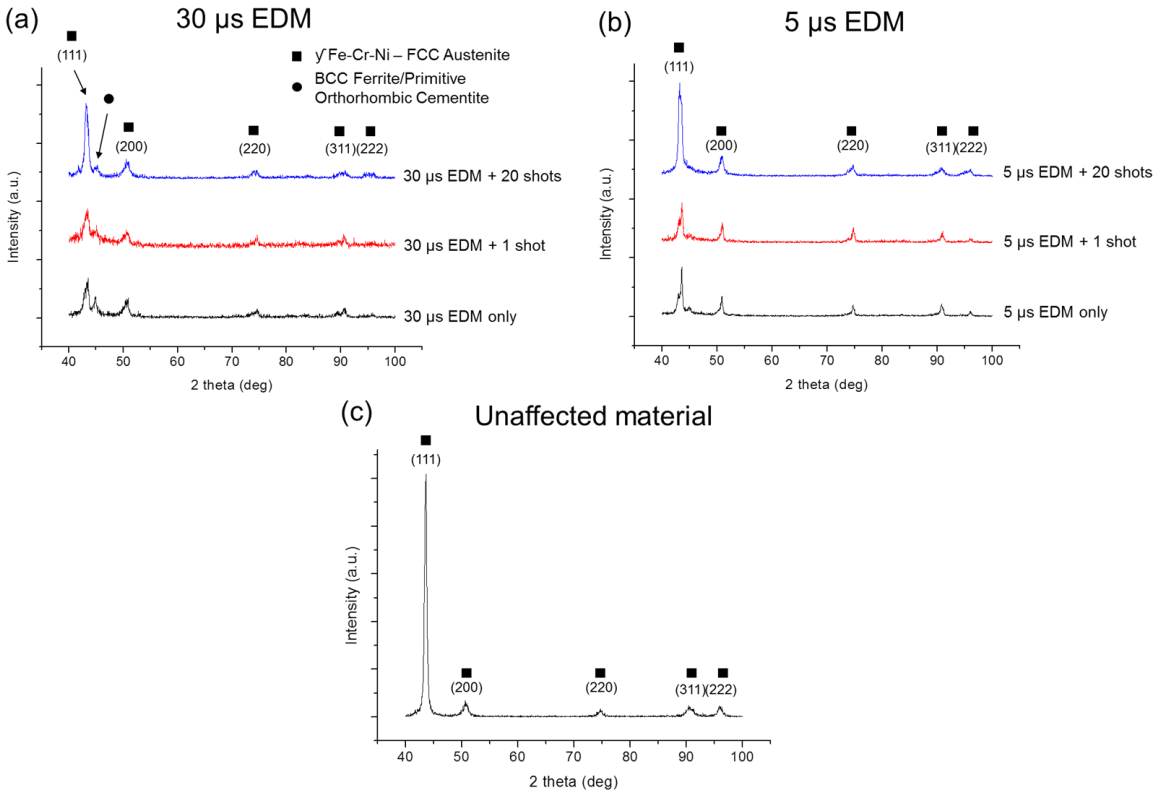


**Fig. 6.18 XRD analysis of (a) 30 µs EDM'd surfaces and (b) 5 µs EDM'd surfaces subject to irradiation at 35 kV by 1 and 20 shots and (c) unaffected steel.**

After EDM with both 5 µs and 30 µs on-times, there was a significant drop in the ratio of the austenite (111) to (200) peaks compared to the ratio of 14.8:1 for the unaffected material. For 5 µs EDM the ratio dropped to 2.45:1, and to 1.98:1 with the longer on-times of 30 µs indicating a significant loss of crystalline texture by the process, compared to the initially textured bulk material. After irradiation, crystalline texture was reintroduced for surfaces machined using both EDM parameters. Both surfaces showed similar changes in crystalline texture after EB irradiation at 35 kV. Fig. 6.18 (a) and (b) show the effect of 1 shot and 20 shots on the XRD of both EDM'd surfaces. The narrowing and increased ratio of intensity of the (111) peak relative to the (200) peak to 4.41:1 for the higher on-time, and to 4.60:1 with the lower on-time indicates the reintroduction of crystalline texture with the (111) planes orientating parallel to the surface. After 1 shot however this texture was not

introduced, indicating the process is taking place incrementally with each shot, and full texturing requires multiple shots.

Under all irradiation conditions the dominant phase was FCC austenite, and this is consistent with the TEM phase analysis. The peak to the right of the (111) austenite peak was not present in the initial raw austenitic stainless steel, however it appeared after EDM, and particularly strongly under the longer discharge on-time of 30 µs. This small peak reduced somewhat in intensity relative to the other peaks after 20 shots of irradiation. Since this is the only non-austenite peak in the XRD pattern, it is thought the phase or phases responsible for this peak is/are also responsible for the needle structures seen in the TEM image in Fig. 6.16.

Next, GAXRD was performed on the surface subject to 35 kV and 20 shots, as well as the EDM'd only surface using 30 µs discharge on-time. Standard XRD and GAXRD have quite different penetration depths and these depths are also dependent on material composition. The penetration depths using these two variations of the process are ideal for clarifying the structures present within the remelted layer induced by electron irradiation, seen by TEM imaging. Table 10 summarises example X-ray penetration depths from which 90% of the X-ray signal arises for both standard XRD and GAXRD. These depths were calculated using the composition of the initial raw material, and therefore it should be noted that chemical changes induced by the EDM process may therefore influence the penetration of X-rays into the sample to some degree.

**Table 10 XRD Penetration depths for 90% of signal in µm, at different 2 theta values**

| | 100° | 60° | 40° | 30° |
|---|---|---|---|---|
| Standard XRD | 4.69 | 3.06 | 2.09 | 1.58 |
| Glancing Angle | 0.41 | 0.41 | 0.40 | 0.40 |

In the standard XRD analysis, 2 theta values between 40° and 100° were used, and in the GAXRD analysis, 2 theta values between 40° and 60° were used, since the most relevant peaks were within this range. Based on these penetration depths, standard XRD alone typically penetrates to a depth which tells us the phases which dominate the EB remelted layer, however the shallower depths penetrated using GAXRD can further reveal whether these phases are present in the same ratios within the uppermost 400 nm. Fig. 6.19 shows X-ray spectra using GAXRD. GAXRD was performed on the EDM'd surface and the treated surface using 35 kV and 20 shots.

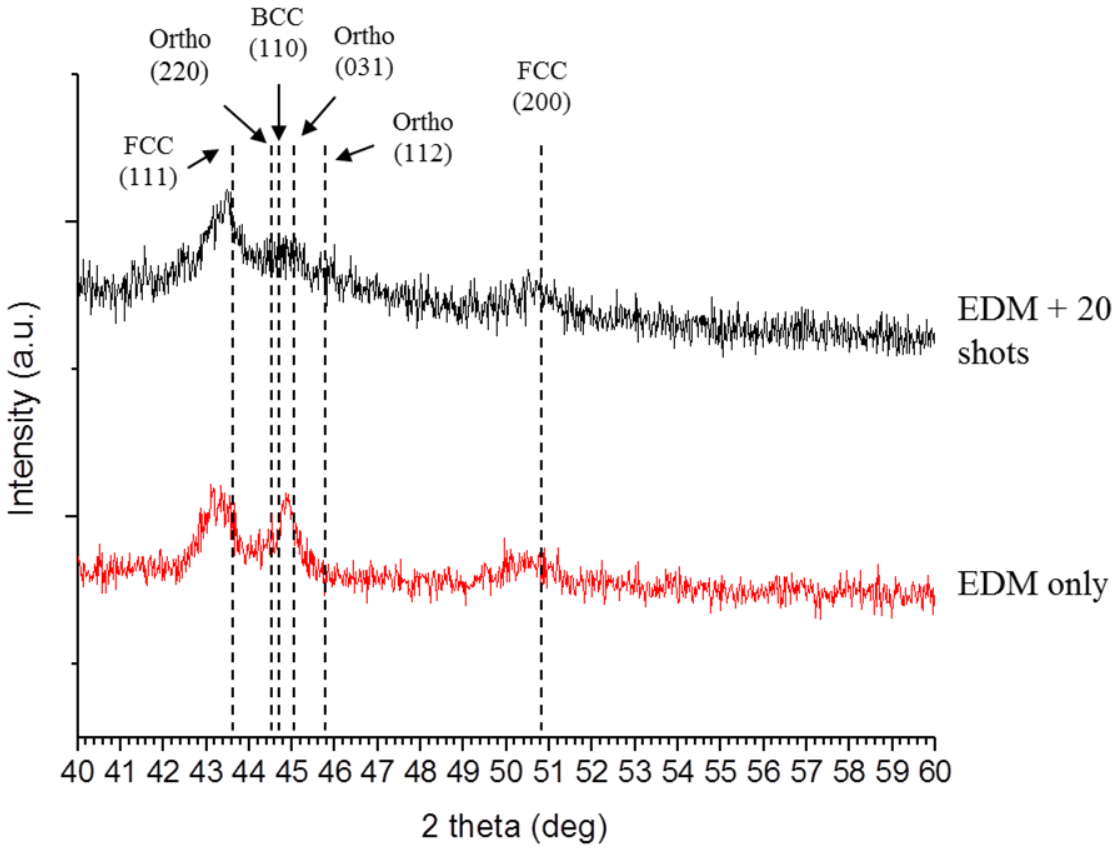


**Fig. 6.19 Glancing angle XRD patterns of the EDM'd surface and the irradiated EDM'd surface with 20 shots at 35kV**

GAXRD gives a peak to the right of the (111) austenite peak which is larger, compared to standard XRD, relative to the austenite peaks, indicating the corresponding phase is more prevalent withi the first 400 nm from the surface compared to beneath this. Between 44.5° and 45° 2 theta values, planes of both orthorhombic cementite and ferrite are expected in this region, therefore it is difficult to identify the phase with confidence. This is particularly the case for the broadened peak under GAXRD of the irradiated sample. However, if we compare this result with the needle structures which extend towards the surface in Fig. 6.16, the location of this peak is likely to correspond to orthorhombic cementite, indicating the needle structures are of this phase. This is reasonable given cementite is known to form as lath-shaped precipitates when viewed in cross-section [163, 164]. Under EDM only, this proposed cementite peak is stronger. This is consistent with the TEM analysis

conducted on an EDM'd steel by Cusanelli et al. [62], whereby needle-shaped cementite was seen in the first few hundred microns of the surface. The greater sharpness of the peak on the EDM'd only surface compared with the irradiated surface is consistent with larger crystallite size [165]. To summarise, the XRD results have confirmed the dominance of austenite both within the first 400 nm of the surface, and in the entire remelted layer. There is also evidence that the needle structures present in the polycrystalline, randomly oriented matrix within the first 2 μm, are cementite needles.

## 6.4 Discussion

### 6.4.1 Crack repair and surface morphology

In this chapter, surface cracks which are characteristic of EDM surfaces have for the first time been repaired by a novel mechanism using pulsed electron beam irradiation. No similar mechanism causing the homogenisation of cracks on a metal surface by a large-area beam or otherwise has been demonstrated before, and the ability to retain the dimensions of the intended workpiece shape after surface treatment while improving the morphological properties is a significant contribution. The technique is practically applicable given the rapid cycle time and the ability of the process to modify surfaces at high tilt angles, which is particularly relevant for the surface modification of micro-scale complex shaped parts. The mechanism which causes the crack repair process is illustrated in the schematic in Fig. 6.20, where the crack repair process under low voltage (15 kV) irradiation can be seen.

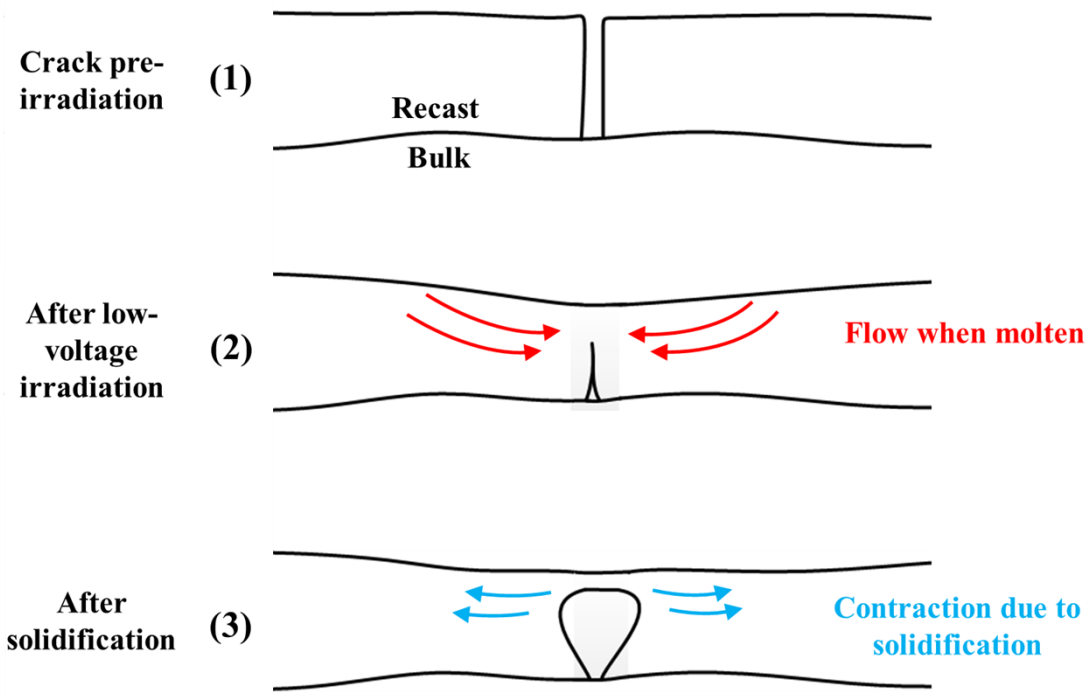


**Fig. 6.20 Schematic of crack resealing process in cross-section under low voltage irradiation**

In stage (1), before irradiation, there is a crack penetrating from the surface to the interface between the bulk and the recast layer created by EDM. In this schematic, in stage (2), upon low-voltage EB irradiation for example using 15 kV cathode voltage, some of the EDM recast layer becomes molten. During this time, it is thought that the molten material will flow due to cohesive surface tension effects. This is where the intermolecular forces cause attraction between similar molecules. The greater volume due to reduced density in the liquid state may also encourage material from both sides of the crack to move together. It is thought that other forces such as convection currents as well as gravity are not relevant here due to the rapid cooling rates ($10^8$ – $10^9$ K/s). Upon solidification, in stage (3), contraction due to volume reduction is expected, causing the crack to partially re-open. It is thought that under higher voltage irradiation, and more shots, the larger volume of material made molten, results in the movement of a larger volume of material, and the gradual homogenization of the

material around the crack. Since cooling rates are rapid, only a limited amount of material can be transferred under the action of a single shot.

Under the EDM parameters used which caused cracks to be generated, and under the range of irradiation parameters chosen in this study, AISI 310 stainless steel showed the most marked improvement in surface morphology out of the three materials subject to initial investigation, given a fully crack repaired surface could be produced using 20 shots of irradiation at a cathode voltage of 35 kV – a cycle time of only about 4 minutes once the initial 10 minute vacuum cycle was complete. Only partial crack repair could be achieved on the surface of 304 steel and Inconel 718 using the same machining conditions. Although with the parameters used in this study, 310 steel responded best in terms of crack repair, all the materials were able to undergo at least partial crack repair, indicating that pulsed electron beam irradiation under further parametric investigation as well as future increases in acceleration voltage and energy density, is likely to be able to crack repair a large range of materials. For this study, the expense and technical difficulty in preparing a TEM sample limited the investigation to the most successfully treated material, in order to yield the most useful conclusions on the effect of the irradiation process on the surface of machined materials. The surface of Inconel 718 for example using 20 shots at the highest voltage of 40 kV contained many cracks which were mostly repaired, with the same characteristics as for example 310 steel using the same parameters. The difference in behaviour of crack repair for the different materials is not surprising given their different thermal properties. 310 steel contains approximately 5% more Cr than 304 steel does, and its thermal conductivity at 100°C is 14.2 W/m.K compared to 16.2 W/m.K for 304 steel. The thermal conductivity of Inconel 718 is 11.4 W/m.K at 100°C. The melting ranges for the materials are quite similar however; Inconel melts

at 1260-1336°C, 304 at 1398-1421°C, and 310 at 1354 – 1402°C. Since the surfaces of the materials have also been modified chemically and metallurgically by the EDM process prior to irradiation, its effect is likely to be different for each material given their different compositions, and therefore the thermal properties of their surfaces are not exactly known. Another factor influencing the ability of the irradiation process to cause crack repair is the proportion of the energy applied to the surface which contributes to smoothing of the surface through melting of asperities. The surfaces of the materials after EDM with the same 30 μs on-time parameters exhibited slightly different characteristics, also caused by differences in thermal properties. Rougher surfaces with a higher frequency and sharper surface asperities would require a greater proportion of the applied beam energy to surface melt, and so asperities would be melted first.

In further work a more in depth parametric study on a larger range of materials would be insightful in understanding the exact properties of a material which influence its susceptibility to the crack repair phenomenon. This thesis however has demonstrated the principle of crack repair and its dependence on both material and electron beam irradiation parameters.

A significant change in surface morphology also accompanied the homogenisation of surface cracks on stainless steel. The high roughness of the initial machined surface typical after EDM was substantially reduced post irradiation. A mean Sa roughness of more than 3 μm was reduced to below 0.9 μm after irradiation. A reduction in asperity frequency and trough depth is particularly important with regards to sites for crack initiation due to stress concentration as well as sites which promote corrosion. The reduced roughness of the EDM'd surface may explain, in part, the improved corrosion

behaviour of EDM surfaces after pulsed electron beam irradiation as reported by Uno et al. [75].

After irradiation by 5 shots at 25 kV (see Fig. 6.6), craters, well known to be associated with the electron beam irradiation process, began to appear. The cracks previously in these regions are eliminated by the surface flow due to crater formation. The phenomenon of crater formation associated with pulsed electron beam irradiation has been reported in a variety of alloys. For example by Gao et al. [166] in magnesium alloy, as well as in aluminium-silicon alloys by Walker et al. [122] and tool steel by Zou et al. [114]. Craters are thought to form due to melting which starts just below the surface. Due to the expansion of the volume of melted matter and when the thickness of the solid layer which confines this melt pool can no longer sustain the expansion force, eruption occurs at the surface. It is also understood that heterogeneities such as intermetallic precipitates and carbides can serve as nucleation sites for sub-surface melting and subsequent eruptions given differences in density, coefficient of thermal expansion and melt temperatures. In particular for steels, craters have been shown by Zou et al. to form at the location of $Cr_7C_3$ carbides in tool steel [167] and at MnS inclusions in 316L stainless steel [115]. For Al-Si based alloys they have been shown to occur at sites of primary silicon particles [122]. For MnS inclusions the occurrence of craters at these regions has been explained by "weak points" associated with the presence of these MnS particles in the solid layer, above the melted layer which begins beneath the surface [115]. This concept may explain the cratering at these locations, in spite of the relatively high melting point of MnS – approximately 1600 °C. The occurrence of craters is important to understand since work by Zhang et al has shown that they are sensitive to corrosion pitting, particularly if they contain holes or cracks at the surface [168]. In this case, craters began to

appear after 5 shots with 25kV, and 1 shot with 35kV cathode voltage. The craters however did not contain any holes or cracks, and in fact craters appearing in the centre of a crack eliminated the crack which was previously present.

The production of a highly uniform layer (see Fig. 6.12) after 20 shots at 35kV with no cracks suggests the process has potential for extension of fatigue life, reducing area for corrosive attack as well as elimination of notches which would hinder mechanical wear behaviour. Fig. 6.11 is an important figure with regards to the direction future development of the technology should take. The depth of the remelted layer for the purpose of eliminating cracks on a surface is a critical parameter, and this figure demonstrates the dependence of depth on irradiation parameters. It suggests that with further increased acceleration voltages it may be possible to treat the largest thicknesses of recast layers typical of very aggressive machining strategies by EDM as well as other thermal based machining processes. The tendency of EDM and other thermal based machining processes to yield cracks under the most useful machining conditions may no longer be a factor in the choice of machining parameters, since they can be easily repaired under rapid surface treatment. This would present significant economic benefits for cutting of components that would have otherwise required slow machining strategies.

### 6.4.2 Phases and grain structure

The nature of the EDM process involves melting and resolidying of material of the workpiece surface in a carbon rich environment. Movement of carbon into the recast layer is expected when using oil based dielectrics, however the detection of carbon is difficult using EDX given the low energy K line of the X-ray, meaning it is easily absorbed by surrounding material. In terms of phase transformations in steels, carbon

levels are critical to the likely phases to be formed upon quenching. Therefore the material subject to electron beam irradiation in this study is highly modified from the initial composition of the 310 steel. Despite this some clear conclusions and explanations for the structures observed by TEM and XRD can be made.

The near-surface structure of the EDM'd 310 steel sample subject to 20 irradiation shots at 35 kV is characterised by nanograined austenite. Austenite is known to form after rapid quenching and this is known as retained austenite. Staehli et al. [169] showed this effect by the production of thin boundary layers of homogenous austenite after laser-pulse irradiation. The presence of very fine retained austenite in steel after pulsed electron irradiation has also been reported elsewhere [170, 171]. It is thought that the high cooling rate prevents further growth in size of the austenite grains. Since it was observed that after 1 μm depth from the surface, austenite grains are clearly larger, it is thought that the cooling rate in this location is reduced compared to immediately next to the surface. It has been shown by calculation that after pulsed electron beam irradiation the temperature is always the highest at the very top surface [162]. The highest rate of quenching from the melt and the highest velocity of the crystallisation front are expected at the surface (10 K/s and 5 m/s respectively) [172] and therefore such a grading of nanostructures is also expected.

Given the complex nature of the sub-layers observed in TEM imaging of the irradiated surface, a schematic detailing the structures identified can be seen in Fig. 6.21. Phases, approximate depth into the sample, grain size and grain orientation are summarised here.

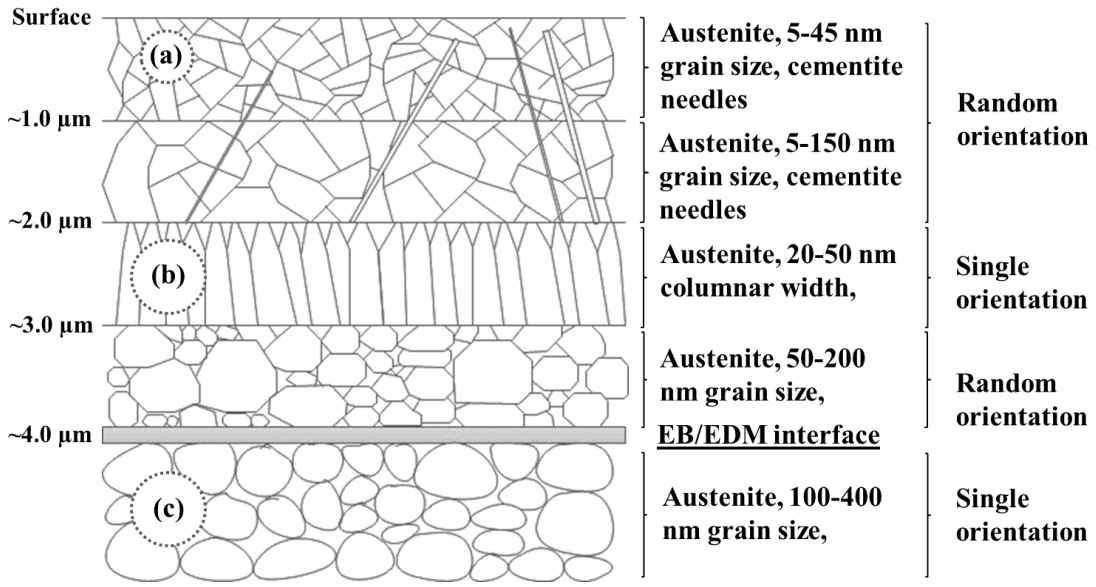


**Fig. 6.21 Schematic of sub-layers of electron beam irradiated EDM'd steel. Indexed patterns of labelled areas can be seen in Fig. 6.17.**

Fine plate structures (a needle–like shape in cross-section) within the top 2.5 µm were also observed. These structures appear to have grown from the interface between the randomly oriented austenite and the columnar austenite beneath this, at approximately 2.0 µm depth from the surface. GAXRD patterns suggest these may be cementite needles in a nanocrystalline austenite matrix, however, further TEM analysis would be required to confirm the identity of this phase. It should be noted that such needle structures were only observed in one of the two lamellae. This may be related to the inhomogeneity of the level of carbon absorption during the EDM process from the oil based dielectric, effectively resulting in a slightly different composition in the locations of the two lamellae. It is also known that both tool species and carbon contamination in the recast layer during EDM is not completely uniform at the nanometre scale, as was shown in Chapter 4. The expected absorption of carbon into the EDM recast layer during machining increases the stability of the cementite phase. The absence of martensite in the remelted layer would also be consistent with the

results of Proskurovsky et al. [172] when using a carbon steel treated by EB irradiation.

A solely austenite region was also observed beneath what is thought to be the EDM-EB interface. It is assumed that the phases present beneath this interface were also present before irradiation, given that they appear to be beneath the melt zone induced by irradiation. An austenitic microstructure in the EDM'd surface of C35 carbon steel, mold steel Impax, as well as pure Iron, has been shown to form when machining in an oil dielectric, as was the case in the study by Kruth et al. [173], who also observed significant cementite dendritic structures were formed even in the pure iron, inferring that the uptake of carbon from the dielectric is significant enough to cause carbides of iron to be formed, given it was that the found carbon content in the surface increased four-fold during machining in oil. There has also been evidence of cementite seen in the TEM/XRD study of carbon steel subject to EDM by Cusanelli et al. [62]. This may support the identification of a strong cementite XRD peak for the EDM'd only surface.

It has been shown that a nanostructured layer at the surface of carbon steel can improve its surface hardness and fatigue strength [124]. Similarly, a nanocrystallised surface on 316L stainless steel was shown to improve its surface hardness by almost three times [126]. In the former study, surface mechanical attrition treatment was used, utilising the vibration of steel balls, typically 1-10 mm diameter [125], larger than those used in shot peening, to induce significant plastic deformation and effective grain sub-division. The latter study used fast multiple rolling rotation, a plastic deformation process using static pressure to introduce a nanocrystalline surface on a large sample. Both of these processes are limited from application on components with a small surface or with delicate surface structures, whereas pulsed

electron beam irradiation is a more suitable process for the surface treatment, modification and introduction of fine nanostructures on highly intricate surfaces.

In the TEM analysis, oriented austenite grains were observed after approximately 2 μm from the top surface. XRD analysis also confirmed that the austenite phase became textured compared to the austenite phase in the EDM'd only sample. Crystallographic texturing can be an important material parameter since mechanical and chemical properties vary depending on the orientation of grains within the material.

XRD spectra of both EDM'd surfaces subject to irradiation by 20 shots at a cathode voltage of 35 kV indicated aligning of the (111) austenite planes parallel to the surface. After 1 shot at this voltage however, any induced texturing is not indicated by the XRD patterns on either sample, suggesting orientation is an incremental process and requires multiple shots. It has been shown that with electron beam irradiation under conditions which do not melt the surface of the workpiece, incremental crystal orientation of the austenite (111) planes aligning parallel to the surface can still take place [174]. This is explained by plastic deformation induced by an intense thermal stress wave produced by irradiation. However since melting of the surface was evident given the crack repair process explained by joining of material in the liquid state, the observed orientation shown, as shown in Fig. 6.18 is likely caused by grain growth in a single preferential direction, as suggested by the columnar nature of the oriented grains seen in the TEM images. The same preferred orientation has been observed in austenitic 316L stainless steel after irradiation with both pulsed electron beams [175] and pulsed ion beams, whereby the ratio of (111) to (200) austenite peaks increases with shot number as well as both energy density and shot number in the case of ion beams [176]. It has been shown by Shahryari et al. [177] that

crystallographic orientation of 316 stainless steel, in particularly with (111) and (100) planar orientation, improves resistance to pitting corrosion. The introduction of such a preferred orientation at the surface as shown in this study could therefore be another advantage for the application of these treated surfaces.

## 6.5 Conclusions

The aim of this chapter was to improve the properties of the EDM'd surface through a novel and convenient surface modification technique. The study has shown that a homogenised crack-free layer can be produced in the surface of EDM'd 310 steel which exhibited a large number of surface cracks after machining. For the first time a novel crack repair mechanism by an incident large area pulsed electron beam has been demonstrated. Surface cracking is a critical problem for EDM'd components since it is highly detrimental to fatigue performance. A detailed TEM and XRD metallurgical analysis was performed showing that an extremely fine graded nano-structure composes the crack-free layer. The rapidity, technical simplicity and large area of application of the surface treatment process makes the results in this chapter particularly significant for post-processing of machined components of a range of sizes and shape complexities, and for delicate micro parts whereby precise dimensions must be maintained. The specific conclusions made in this chapter are summarised below:

- A pulsed electron beam irradiation technique, using a range of acceleration voltages and number of pulses, was used to improve the surfaces of electrical discharge machined stainless steel with a cycle-time of between 11 and 15 minutes, including the initial 10 minute vacuum cycle.

- The Sa and Sz surface roughness values of EDM'd 310 steel machined by EDM with 30 µs on-time and 4.5 A can be improved from 3.1 µm and 28.7 µm to under 0.9 µm and 7 µm respectively, using 20 shots at 35 kV cathode voltage.
- Cracks induced by the EDM process can be entirely eliminated from the surface, and up to 4.0 µm depth of the new remelted surface when using a cathode voltage of 35 kV. When machining with 4.5 A and 30 µs on-time, this represents the majority of the depth of the recast layer, with only small sections of the recast layer remaining unaffected.
- The ability of the surface treatment process to repair surface cracks varies depending on the material used.
- The crack repair mechanism, the morphology of which could be observed clearly using low acceleration voltages of irradiation, appears to occur due to flow of both sides of the crack, followed by contraction upon cooling, leaving only some of the crack repaired under low voltages or few shots. Under 35 kV cathode voltage and 20 shots, cracks remain fully repaired with in the EB remelted layer.
- Using a low cathode voltage of 15 kV, surface crack density is increased; this may be due to surface evaporation revealing previously hidden sub-surface cracks. However with an increased voltage of 25 kV and 35 kV, crack density is generally reduced, and eliminated entirely after 20 shots at 25 kV and 35 kV.
- The thickness of the EB remelted layer depends mostly on acceleration voltage, and reaches up to 4.0 µm with 35 kV. A slight reduction in thickness

after 20 shots compared to 10 shots for all voltages suggests partial evaporation and mass loss from the surface.

- In a TEM study of the cross-section of the crack-repaired surface, a graded nanostructure was formed in the first 4.0 μm of the surface of austenitic stainless steel subject to pulsed electron beam irradiation after electrical discharge machining, with a grain size of below 10 nm present at the very top surface. Nanostructured coatings are desirable for their improved mechanical properties caused by grain boundary strengthening.
- A random orientation of austenite grains is seen within the first 2.0 μm from the free surface, with a needle-like phase thought to be cementite present within this matrix, below which is a single orientation region of columnar austenite grains, followed by a region of randomly oriented austenite grains beneath this.
- A sharp interface can be seen between the EB remelted layer and the remaining EDM recast layer beneath, which is composed of solely single-orientation polycrystalline austenite until at least 6.0 μm depth.
- XRD analysis suggests the textured austenite grains with (111) planes parallel to the surface within the remelted layer become oriented incrementally and this depends on the number of irradiation shots. Such an orientation has been correlated with improved corrosion behaviour.

In section 7.2, the future work which has emerged as a result of this study will be discussed.

# 7 Conclusions

## 7.1 General conclusions

The EDM process has unique characteristics which see to its continued usage in the manufacturing sector. Its ability to drill and cut the hardest and most brittle materials means it is a critical technology in the processing of high-value components. Concurrent with the adoption of EDM by industry since the 1950s, a significant academic effort has been made to understand the fundamental mechanisms behind material removal and the properties of parts produced by the process. This work has utilized a range of characterisation techniques to help complete the picture of the complicated phenomena which take place in the machining gap. This study has also recognised that new surface modification technologies will become essential for the post-processing of components machined by necessary processes such as EDM. It has been shown that pulsed electron surface treatment can be unified with EDM to produce a process chain which can solve a critical issue of the process by taking advantage of the novel properties of the irradiation technology.

This thesis reports investigations from a fundamental perspective on the damage and contamination occurring in the surface of materials machined by EDM. Pulsed electron beam irradiation surface modification was used to provide a solution to the most critical surface damage property which is caused by EDM; surface cracking. From this work, previously unobserved phenomena at the nano-scale of EDM'd surfaces have been revealed. The conditions under which material migrates between electrodes have also been explained. An understanding and prediction of damage and contamination occurring during the process are critical to the progress of EDM as a micro and nano-scale machining process. In the final research chapter, the repair of

surface cracks by pulsed electron beam irradiation was demonstrated. Surface cracking is detrimental to components since it leads to a reduction in the material's fatigue life and corrosion resistance. The rapidity and simplicity of pulsed electron irradiation mean that the generation of a crack-free surface layer on EDM'd materials by this method has substantial industrial implications, as deleterious surface properties caused by aggressive and economically useful machining parameters can be quickly eliminated.

Chapter 4 used a pure material machinable by EDM; single-crystal silicon, as a highly characterisable workpiece for the TEM investigation of damage occurring at the nano-scale by EDM. Several phenomena were observed at the nano-scale created by the EDM process not discussed before in literature. These are; nano-scale pores of sizes down to 10 nm; nano-crystals of embedded tool material of sizes down to 3 nm; and a crack with a diameter of 20 nm. Understanding of these is important because they are critical to the properties of the workpiece, but difficult to detect. Epitaxial regrowth of the crystal lattice was also observed in the recast layer, with a twinned crystalline structure remaining, suggesting EDM may be a viable method of maintaining the crystal structure of semiconductors during cutting. The study suggested that conventional microscopic techniques such as SEM and optical microscopy are not sufficient to characterise recast layers created by EDM, and the properties of materials machined by the process are in fact determined by phenomena occurring at the nano-scale. This knowledge is essential to the furthering of EDM as a process which can machine at the micro and sub-micron scale.

Chapter 5 revealed the material migration mechanism occurring during the complex discharge process. This mechanism allows material to transfer between electrodes, despite the cool dielectric medium existing in the discharge gap, which solidifies and

flushes the majority of machined material. The transfer of material between electrodes is thought to be a two-stage process, whereby material ejected at the end of discharge on-time is remelted in the discharge gap by a successive discharge, causing its fusion into the opposite electrode surface. A contaminated layer is created by the gradual buildup of material through discrete concentrated deposits at the locations of discharge. The thickness of the contaminated layer increases with increasing both discharge current and discharge on-time. Understanding this mechanism of transfer, and the conditions under which material is modified in this manner is essential to the avoidance of contamination, as well deliberate deposition, during EDM.

In Chapter 6, the damaging surface property of surface cracks characteristic of materials machined by EDM, was investigated. A crack repair process using a large area beam to remelt the surface was used to eliminate surface cracks through a novel rapid melting mechanism. Pulsed electron beam irradiation under the parameter of 20 irradiation shots at an acceleration voltage of 35 kV was capable of eliminating cracks within a 4 μm depth of the surface of EDM'd 310 stainless steel. Only a small section of the unaffected EDM recast layer remained beneath the homogenous remelted layer. A significant reduction in surface roughness parameters accompanied the repair of surface cracks. The thickness of this layer can be controlled through the choice of cathode voltage parameter, suggesting that increased voltages of new machines will be able to repair the surfaces of aggressively machined components. An ultra-fine graded nanostructure of austenite was shown to comprise the crack-free surface, with implications for improved hardness and wear behaviour due to grain boundary strengthening.

This thesis has made important contributions to the fundamental understanding of damage which occurs as a result of the complex phenomena which take place within

the EDM process. The µs time-scale at which machining occurs, and the µm dimension-scale of individual discharges mean that direct observation of phenomena taking place during discharge is extremely difficult. The use of TEM analysis and single-discharge characterisation has revealed previously unknown phenomena critical to the advancement of EDM as a precision machining tool. An industrially practical solution based on large-area pulsed electron beam irradiation which was demonstrated to repair surface cracks has significant implications for the machining of components which would have required removal of the recast layer, or for complex parts not possible to surface treat by other means. EDM will continue to be a necessary machining process well into the future given its indispensable niche advantages of machining of very hard/brittle materials, and its ability to create high-aspect ratio holes and complex shapes in hard as well as delicate components. This thesis is a step towards ensuring EDM continues to be utilised while dimensions of parts continue to decrease and component and material specifications become ever more stringent.

## 7.2 Future work

Several areas of suggested further work have been identified by the work in this thesis.

The nano-scale characterisation of EDM phenomena in Chapter 4 was performed on low-resistivity single-crystal silicon given its chemical purity, crystal simplicity and machinability by EDM. The material is however extremely brittle, and therefore the crack which was observed in the TEM image in Fig. 4.18 may be characteristic of this property under EDM. It may not necessarily be representative of the nano-scale morphology of other more ductile materials machined using the same parameters.

Since surface cracking is a critical property of EDM'd surfaces, it is particularly important to know if cracks invisible to optical and SEM imaging are dominant within the surface of most materials machined by the process. TEM analysis of metals machined by EDM under a variety of parameters would therefore be a valuable study.

The phenomenon of contamination of material suspended in the dielectric onto workpieces machined by EDM has been subject to much research in recent years, and a commercial machine capable of coating a workpiece with a chosen powder based material is now manufactured by Mitsubishi Electric. Although a number of materials have been used as coatings by this method, the fundamentals of this process have seen little academic interest, and the mechanism of attachment of material between electrodes investigated in Chapter 5 has contributed to this knowledge. Fundamental metallurgical analysis of a coating layer created by EDM has not been performed according to the literature review, and therefore a TEM analysis of the structure of the coatings would be a significant contribution to the understanding of coatings created by EDM, and would explain improved mechanical properties which have been reported by several authors. Continuation work to conduct this analysis is planned. Under precise control of the contamination process, a machining process combining material removal and deliberate attachment could also be conceived.

The work in this thesis using surface treatment aimed to show the potential for the pulsed electron beam irradiation process to be applied to EDM'd surfaces. Some characterisation work therefore remains before commercial application of the process. Cracking associated with EDM'd surfaces is correlated with reduced fatigue resistance since the crack initiation stage of fatigue failure has already occurred. It is also related to worsened corrosion behaviour given the increased area for chemical attack. Therefore fatigue and corrosion testing should be performed on treated EDM

surfaces. A nanostructured surface layer is a desirable characteristic of materials since improved mechanical behaviour is expected due to grain-boundary strengthening. Nano-hardness and nano-scratch testing should therefore be performed on irradiated EDM'd surfaces to identify improved tribological characteristics. To accompany the characterisation study in Chapter 6, a detailed residual stress analysis of the recast layer should be conducted, since the correlation between fatigue properties and residual stress is well documented. Such a stress analysis could be conducted both through XRD analysis and through direct measurement of strain in SAED pattern in TEM. Stress analysis through TEM may be necessary to characterise the less dominant phases present in the remelted layer. The complexity of the steel machined and surface treated, and in particular its composition and numerous possible phases, mean definitive conclusions on the microstructures produced in a larger range of materials are difficult to make. Therefore a TEM study of a commercially pure material undergoing EDM and EB irradiation would be useful to determine the applicability of the process chain.

The pulsed electron beam irradiation process is a recent addition to the range of surface modification techniques. The novelty and practical usefulness of the process given its large area and rapid cycle time have resulted in a large number of research papers being published in the area. This research is conducted by a few select groups around the world with access to the technology, and at an increasingly high rate each year. Since the majority of publications in the field deal with fundamental materials characterisation, the practical application of the process to an established and essential machining process such as EDM is a highly novel direction of research, and therefore it is recommended that work immediately following on from this thesis should be in this area.

# References

[1] Altan T, Lilly B, Yen YC. Manufacturing of dies and molds. CIRP Annals - Manufacturing Technology. 2001;50:405-23.

[2] Coldwell H, Woods R, Paul M, Koshy P, Dewes R, Aspinwall D. Rapid machining of hardened AISI H13 and D2 moulds, dies and press tools. Journal of Materials Processing Technology. 2003;135:301-11.

[3] Diver C, Atkinson J, Helml HJ, Li L. Micro-EDM drilling of tapered holes for industrial applications. Journal of Materials Processing Technology. 2004;149:296-303.

[4] Ho KH, Newman ST. State of the art electrical discharge machining (EDM). International Journal of Machine Tools and Manufacture. 2003;43:1287-300.

[5] Simao J, Lee HG, Aspinwall DK, Dewes RC, Aspinwall EM. Workpiece surface modification using electrical discharge machining. International Journal of Machine Tools and Manufacture. 2003;43:121-8.

[6] Aspinwall DK, Soo SL, Berrisford AE, Walder G. Workpiece surface roughness and integrity after WEDM of Ti–6Al–4V and Inconel 718 using minimum damage generator technology. CIRP Annals - Manufacturing Technology. 2008;57:187-90.

[7] Mohd Abbas N, Solomon DG, Fuad Bahari M. A review on current research trends in electrical discharge machining (EDM). International Journal of Machine Tools and Manufacture. 2007;47:1214-28.

[8] Wire Cut Company, Inc. **http://www.wirecutcompany.com/tooling.html**.

[9] Hi-Tek Manufacturing. **http://www.hitekmfg.com/photo-gallery-processes-turbine-industry.html**.

[10] Quality, cost, delivery drive EDM investment. **http://www.advancedmanufacturing.co.uk/features/quality-cost-delivery-drive-edm-investment**.

[11] Wire EDM: Things a Rotary Axis Can Do. **http://implant-mechanix.com/?cat=33**.

[12] Bojorquez B, Marloth RT, Es-Said OS. Formation of a crater in the workpiece on an electrical discharge machine. Engineering Failure Analysis. 2002;9:93-7.

[13] Kunieda M, Lauwers B, Rajurkar KP, Schumacher BM. Advancing EDM through fundamental insight into the process. CIRP Annals - Manufacturing Technology. 2005;54:599-622.
[14] Kojima A, Natsu W, Kunieda M. Spectroscopic measurement of arc plasma diameter in EDM. CIRP Annals - Manufacturing Technology. 2008;57:203-7.
[15] Kazimierz Albinski KM, Adam Miernikiewicz, Stefan Labuz and Marek Malota. The temperature of a plasma used in electrical discharge machining. Plasma Sources Science and Technology. 1996;5:736.
[16] Shervani-Tabar MT, Abdullah A, Shabgard MR. Numerical study on the dynamics of an electrical discharge generated bubble in EDM. Engineering Analysis with Boundary Elements. 2006;30:503-14.
[17] Li L, Diver C, Atkinson J, Giedl-Wagner R, Helml HJ. Sequential Laser and EDM Micro-drilling for Next Generation Fuel Injection Nozzle Manufacture. CIRP Annals - Manufacturing Technology. 2006;55:179-82.
[18] Altan T, Lilly B, Yen YC. Manufacturing of Dies and Molds. CIRP Annals - Manufacturing Technology. 2001;50:404-22.
[19] Chang Y-F, Hong R-C. Parametric curve machining of a CNC milling EDM. International Journal of Machine Tools and Manufacture. 2005;45:941-8.
[20] Han F, Wang Y, Zhou M. High-speed EDM milling with moving electric arcs. International Journal of Machine Tools and Manufacture. 2009;49:20-4.
[21] Kunleda M, Miyoshi Y, Takaya T, Nakajima N, ZhanBo Y, Yoshida M. High Speed 3D Milling by Dry EDM. CIRP Annals - Manufacturing Technology. 2003;52:147-50.
[22] Ho KH, Newman ST, Rahimifard S, Allen RD. State of the art in wire electrical discharge machining (WEDM). International Journal of Machine Tools and Manufacture. 2004;44:1247-59.
[23] Klocke F, Lung D, Thomaidis D, Antonoglou G. Using ultra thin electrodes to produce micro-parts with wire-EDM. Journal of Materials Processing Technology. 2004;149:579-84.
[24] Chen ST, Yang HY, Du CW. Study of an ultrafine w-EDM technique. Journal of Micromechanics and Microengineering. 2009;19.
[25] Meek J. M. CJD. Electrical Breakdown of Gases: John Wiley & Sons, 1953.
[26] Liu S, Huang Y, Li Y. A plate capacitor model of the EDM process based on the field emission theory. International Journal of Machine Tools and Manufacture. 2011.

[27] Bogaerts A, Neyts E, Gijbels R, van der Mullen J. Gas discharge plasmas and their applications. Spectrochimica Acta Part B: Atomic Spectroscopy. 2002;57:609-58.

[28] Luo YF. The dependence of interspace discharge transitivity upon the gap debris in precision electrodischarge machining. Journal of Materials Processing Technology. 1997;68:121-31.

[29] Natsu W, Shimoyamada M, Kunieda M. Study on expansion process of EDM arc plasma. JSME International Journal, Series C: Mechanical Systems, Machine Elements and Manufacturing. 2006;49:600-5.

[30] Nagahanumaiah, Ramkumar J, Glumac N, Kapoor SG, DeVor RE. Characterization of plasma in micro-EDM discharge using optical spectroscopy. Journal of Manufacturing Processes. 2009;11:82-7.

[31] Schumacher BM. After 60 years of EDM the discharge process remains still disputed. Journal of Materials Processing Technology. 2004;149:376-81.

[32] Lazarenko BR. To invert the effect of wear on electric power contacts 1943.

[33] Singh A, Ghosh A. A thermo-electric model of material removal during electric discharge machining. International Journal of Machine Tools and Manufacture. 1999;39:669-82.

[34] DiBitonto DD, Eubank PT, Patel MR, Barrufet MA. Theoretical models of the electrical discharge machining process. I. A simple cathode erosion model. Journal of Applied Physics. 1989;66:4095-103.

[35] Schumacher BM. About the Role of Debris in the Gap During Electrical Discharge Machining. CIRP Annals - Manufacturing Technology. 1990;39:197-9.

[36] Curodeau A, Richard M, Frohn-Villeneuve L. Molds surface finishing with new EDM process in air with thermoplastic composite electrodes. Journal of Materials Processing Technology. 2004;149:278-83.

[37] Kunieda M, Nakashima T. Factors Determining Discharge Location in EDM. IJEM. 1997;3:53=8.

[38] Mohri N, Suzuki M, Furuya M, Saito N, Kobayashi A. Electrode Wear Process in Electrical Discharge Machining. CIRP Annals - Manufacturing Technology. 1995;44:165-8.

[39] Marafona J. Black layer characterisation and electrode wear ratio in electrical discharge machining (EDM). Journal of Materials Processing Technology. 2007;184:27-31.

[40] Kunieda M, Kobayashi T. Clarifying mechanism of determining tool electrode wear ratio in EDM using spectroscopic measurement of vapor density. Journal of Materials Processing Technology. 2004;149:284-8.
[41] Soni JS, Chakraverti G. Experimental investigation on migration of material during EDM of die steel (T215 Cr12). Journal of Materials Processing Technology. 1996;56:439-51.
[42] Shue KY, Tsai YY, Chang YM. An investigation of attachment on electrode surface in Dry EDM. Advanced Materials Research2010. p. 407-12.
[43] Wang ZL, Fang Y, Wu PN, Zhao WS, Cheng K. Surface modification process by electrical discharge machining with a Ti powder green compact electrode. Journal of Materials Processing Technology. 2002;129:139-42.
[44] Furutani K, Saneto A, Takezawa H, Mohri N, Miyake H. Accretion of titanium carbide by electrical discharge machining with powder suspended in working fluid. Precision Engineering. 2001;25:138-44.
[45] Yang X, Guo J, Chen X, Kunieda M. Molecular dynamics simulation of the material removal mechanism in micro-EDM. Precision Engineering. 2010;35:51-7.
[46] Tsai Y-Y, Masuzawa T. An index to evaluate the wear resistance of the electrode in micro-EDM. Journal of Materials Processing Technology. 2004;149:304-9.
[47] Yuangang W, Fuling Z, Jin W. Wear-resist Electrodes for Micro-EDM. Chinese Journal of Aeronautics. 2009;22:339-42.
[48] Uhlmann E, Roehner M. Investigations on reduction of tool electrode wear in micro-EDM using novel electrode materials. CIRP Journal of Manufacturing Science and Technology. 2008;1:92-6.
[49] Jahan MP, Wong YS, Rahman M. A study on the fine-finish die-sinking micro-EDM of tungsten carbide using different electrode materials. Journal of Materials Processing Technology. 2009;209:3956-67.
[50] Han F, Yamada Y, Kawakami T, Kunieda M. Experimental attempts of sub-micrometer order size machining using micro-EDM. Precision Engineering. 2006;30:123-31.
[51] Egashira K, Morita Y, Hattori Y. Electrical discharge machining of submicron holes using ultrasmall-diameter electrodes. Precision Engineering. 2010;34:139-44.
[52] Kawakami T, Kunieda M. Study on factors determining limits of minimum machinable size in micro EDM. CIRP Annals - Manufacturing Technology. 2005;54:167-70.

[53] Song X, Reynaerts D, Meeusen W, Van Brussel H. A study on the elimination of micro-cracks in a sparked silicon surface. Sensors and Actuators, A: Physical. 2001;92:286-91.

[54] Takino H, Ichinohe T, Tanimoto K, Yamaguchi S, Nomura K, Kunieda M. Cutting of polished single-crystal silicon by wire electrical discharge machining. Precision Engineering. 2004;28:314-9.

[55] Takino H, Ichinohe T, Tanimoto K, Yamaguchi S, Nomura K, Kunieda M. High-quality cutting of polished single-crystal silicon by wire electrical discharge machining. Precision Engineering. 2005;29:423-30.

[56] Kunieda M, Ojima S. Improvement of EDM efficiency of silicon single crystal through ohmic contact. Precision Engineering. 2000;24:185-90.

[57] Yan J, Asami T, Harada H, Kuriyagawa T. Fundamental investigation of subsurface damage in single crystalline silicon caused by diamond machining. Precision Engineering. 2009;33:378-86.

[58] Chao CL, Ma KJ, Liu DS, Bai CY, Shy TL. Ductile behaviour in single-point diamond-turning of single-crystal silicon. Journal of Materials Processing Technology. 2002;127:187-90.

[59] Newton TR, Melkote SN, Watkins TR, Trejo RM, Reister L. Investigation of the effect of process parameters on the formation and characteristics of recast layer in wire-EDM of Inconel 718. Materials Science and Engineering A. 2009;513-514:208-15.

[60] Izquierdo B, Plaza S, Sánchez JA, Pombo I, Ortega N. Numerical prediction of heat affected layer in the EDM of aeronautical alloys. Applied Surface Science. 2012;259:780-90.

[61] Ramasawmy H, Blunt L, Rajurkar KP. Investigation of the relationship between the white layer thickness and 3D surface texture parameters in the die sinking EDM process. Precision Engineering. 2005;29:479-90.

[62] Cusanelli G, Hessler-Wyser A, Bobard F, Demellayer R, Perez R, Flükiger R. Microstructure at submicron scale of the white layer produced by EDM technique. Journal of Materials Processing Technology. 2004;149:289-95.

[63] Lee HT, Tai TY. Relationship between EDM parameters and surface crack formation. Journal of Materials Processing Technology. 2003;142:676-83.

[64] Wang CC, Chow HM, Yang LD, Lu CT. Recast layer removal after electrical discharge machining via Taguchi analysis: A feasibility study. Journal of Materials Processing Technology. 2009;209:4134-40.
[65] Ramulu M, Jenkins MG, Daigneault JA. Spark-Erosion Process Effects on the Properties and Performance of a Tib2 Particulate-Reinforced/SiC Matrix Ceramic Composite: John Wiley & Sons, Inc., 2008.
[66] Zeid OAA. On the effect of electrodischarge machining parameters on the fatigue life of AISI D6 tool steel. Journal of Materials Processing Technology. 1997;68:27-32.
[67] Tai TY, Lu SJ. Improving the fatigue life of electro-discharge-machined SDK11 tool steel via the suppression of surface cracks. International Journal of Fatigue. 2009;31:433-8.
[68] Patel KM, Pandey PM, Venkateswara Rao P. Surface integrity and material removal mechanisms associated with the EDM of Al2O3 ceramic composite. International Journal of Refractory Metals and Hard Materials. 2009;27:892-9.
[69] Alting L, Kimura F, Hansen HN, Bissacco G. Micro engineering. CIRP Annals - Manufacturing Technology. 2003;52:635-57.
[70] Kubiak KJ, Liskiewicz TW, Mathia TG. Surface morphology in engineering applications: Influence of roughness on sliding and wear in dry fretting. Tribology International. 2011;44:1427-32.
[71] Sedlaček M, Podgornik B, Vižintin J. Influence of surface preparation on roughness parameters, friction and wear. Wear. 2009;266:482-7.
[72] Silva FJG, Martinho RP, Alexandre RJD, Baptista APM. Increasing the wear resistance of molds for injection of glass fiber reinforced plastics. Wear. 2011;271:2494-9.
[73] Martínez-Mateo I, Carrión-Vilches FJ, Sanes J, Bermúdez MD. Surface damage of mold steel and its influence on surface roughness of injection molded plastic parts. Wear. 2011;271:2512-6.
[74] Firrao D, Matteis P, Scavino G, Ubertalli G, Ienco MG, Pinasco MR, et al. Relationships between tensile and fracture mechanics properties and fatigue properties of large plastic mould steel blocks. Materials Science and Engineering: A. 2007;468–470:193-200.

[75] Uno Y, Okada A, Uemura K, Raharjo P, Furukawa T, Karato K. High-efficiency finishing process for metal mold by large-area electron beam irradiation. Precision Engineering. 2005;29:449-55.
[76] Navas C, Conde A, Fernández BJ, Zubiri F, de Damborenea J. Laser coatings to improve wear resistance of mould steel. Surface and Coatings Technology. 2005;194:136-42.
[77] Laguna-Camacho JR, Cruz-Mendoza LA, Anzelmetti-Zaragoza JC, Marquina-Chávez A, Vite-Torres M, Martínez-Trinidad J. Solid particle erosion on coatings employed to protect die casting molds. Progress in Organic Coatings. 2012;74:750-7.
[78] Firrao D, Gerosa R, Ghidini A, Matteis P, Mortarino G, Pinasco MR, et al. Relation between fatigue crack initiation and propagation, toughness and microstructure in large steel blooms for automotive plastic molds. International Journal of Fatigue. 2007;29:1880-4.
[79] Brochu M, Verreman Y, Ajersch F, Bouchard D. High cycle fatigue strength of permanent mold and rheocast aluminum 357 alloy. International Journal of Fatigue. 2010;32:1233-42.
[80] Lai LC, Chiou WA, Earthman JC. Influence of electrical discharged machining and surface defects on the fatigue strength of electrodeposited nanocrystalline Ni. International Journal of Fatigue. 2010;32:584-91.
[81] Andrews S, Sehitoglu H. A computer model for fatigue crack growth from rough surfaces. International Journal of Fatigue. 2000;22:619-30.
[82] Rokhlin SI, Kim JY. In situ ultrasonic monitoring of surface fatigue crack initiation and growth from surface cavity. International Journal of Fatigue. 2003;25:41-9.
[83] Maradia U, Scuderi M, Knaak R, Boccadoro M, Beltrami I, Stirnimann J, et al. Super-finished Surfaces using Meso-micro EDM. Procedia CIRP. 2013;6:157-63.
[84] Yan BH, Lin YC, Huang FY. Surface modification of Al–Zn–Mg alloy by combined electrical discharge machining with ball burnish machining. International Journal of Machine Tools and Manufacture. 2002;42:925-34.
[85] Tsai HC, Yan BH, Huang FY. EDM performance of Cr/Cu-based composite electrodes. International Journal of Machine Tools and Manufacture. 2003;43:245-52.
[86] Ekmekci B. Residual stresses and white layer in electric discharge machining (EDM). Applied Surface Science. 2007;253:9234-40.

[87] Ghanem F, Braham C, Sidhom H. Influence of steel type on electrical discharge machined surface integrity. Journal of Materials Processing Technology. 2003;142:163-73.

[88] Ekmekci B, Tekkaya AE, Erden A. A semi-empirical approach for residual stresses in electric discharge machining (EDM). International Journal of Machine Tools and Manufacture. 2006;46:858-68.

[89] Das S, Klotz M, Klocke F. EDM simulation: finite element-based calculation of deformation, microstructure and residual stresses. Journal of Materials Processing Technology. 2003;142:434-51.

[90] Karacs A, Joob Fancsaly A, Divinyi T, Pető G, Kovách G. Morphological and animal study of titanium dental implant surface induced by blasting and high intensity pulsed Nd-glass laser. Materials Science and Engineering: C. 2003;23:431-5.

[91] Rahman MM. Optimization of process parameters on Ti-6Al-4V using central composite design method. Advanced Materials Research. p. 1393-400.

[92] Li C, Han Z, Li L, Liu G. Theoretical and experimental investigation into the surface roughness of small-hole EDM. Key Engineering Materials2011. p. 656-61.

[93] Kang XL, Yu DM, Guo H, Shang CP. Relationship between Electrical Parameters in combined EDM and surface quality. Applied Mechanics and Materials2011. p. 436-9.

[94] Yan BH, Wang CC, Chow HM, Lin YC. Feasibility study of rotary electrical discharge machining with ball burnishing for Al2O3/6061Al composite. International Journal of Machine Tools and Manufacture. 2000;40:1403-21.

[95] Menzies I, Koshy P. Assessment of abrasion-assisted material removal in wire EDM. CIRP Annals - Manufacturing Technology. 2008;57:195-8.

[96] Qu J, Shih AJ, Scattergood RO, Luo J. Abrasive micro-blasting to improve surface integrity of electrical discharge machined WC–Co composite. Journal of Materials Processing Technology. 2005;166:440-8.

[97] Guilemany JM, Llorca-Isern N, Szabo PJ. Residual stress characterisation of grit blasted steel surfaces. Surface Engineering. 1996;12:77-9.

[98] Arola D, Alade AE, Weber W. Improving fatigue strength of metals using abrasive waterjet peening. Machining Science and Technology. 2006;10:197-218.

[99] Mohri N, Saito N, Tsunekawa Y, Kinoshita N. Metal Surface Modification by Electrical Discharge Machining with Composite Electrode. CIRP Annals - Manufacturing Technology. 1993;42:219-22.

[100] Moro T, Mohri N, Otsubo H, Goto A, Saito N. Study on the surface modification system with electrical discharge machine in the practical usage. Journal of Materials Processing Technology. 2004;149:65-70.
[101] Hwang Y-L, Kuo C-L, Hwang S-F. The coating of TiC layer on the surface of nickel by electric discharge coating (EDC) with a multi-layer electrode. Journal of Materials Processing Technology. 2010;210:642-52.
[102] Simão J, Aspinwall D, El-Menshawy F, Meadows K. Surface alloying using PM composite electrode materials when electrical discharge texturing hardened AISI D2. Journal of Materials Processing Technology. 2002;127:211-6.
[103] Janmanee P, Muttamara A. Surface modification of tungsten carbide by electrical discharge coating (EDC) using a titanium powder suspension. Applied Surface Science. 2012.
[104] Kumar S, Batra U. Surface modification of die steel materials by EDM method using tungsten powder-mixed dielectric. Journal of Manufacturing Processes. 2012;14:35-40.
[105] Uno Y, Okada A, Uemura K, Raharjo P, Sano S, Yu Z, et al. A new polishing method of metal mold with large-area electron beam irradiation. Journal of Materials Processing Technology. 2007;187-188:77-80.
[106] OZUR GE, PROSKUROVSKY DI, ROTSHTEIN VP, MARKOV AB. Production and application of low-energy, high-current electron beams. Laser and Particle Beams. 2003;21:157-74.
[107] Proskurovsky DI, Rotshtein VP, Ozur GE. Use of low-energy, high-current electron beams for surface treatment of materials. Surface and Coatings Technology. 1997;96:117-22.
[108] Welsh DS. Current density limitations in a fast-pulsed high-voltage vacuum diode. Naval Postgraduate School ;: Monterey, Calif., 1992.
[109] Nazarov DS, Ozur GE, Proskurovsky DI. Production of low-energy, high-current electron beams in a gun with plasma anode. Izv Vyssh Uchebn Zaved, Fiz. 1994;3.
[110] Batrakov AV, Markov AB, Ozur GE, Proskurovsky DI, Rotshtein VP. Surface alloying of metallic substrates with pre-deposited films through a pulsed electron-beam mixing. The European Physical Journal - Applied Physics. 2008;43:283-8.
[111] Ivanov YF, Rotshtein VP, Proskurovsky DI, Orlov PV, Polestchenko KN, Ozur GE, et al. Pulsed electron-beam treatment of WC–TiC–Co hard-alloy cutting tools:

wear resistance and microstructural evolution. Surface and Coatings Technology. 2000;125:251-6.

[112] Markov AB, Rotshtein VP. Calculation and experimental determination of dimensions of hardening and tempering zones in quenched U7A steel irradiated with a pulsed electron beam. Nuclear Instruments and Methods in Physics Research Section B: Beam Interactions with Materials and Atoms. 1997;132:79-86.

[113] Rotshtein VP, Proskurovsky DI, Ozur GE, Ivanov YF, Markov AB. Surface modification and alloying of metallic materials with low-energy high-current electron beams. Surface and Coatings Technology. 2004;180-181:377-81.

[114] Zou JX, Grosdidier T, Zhang KM, Gao B, Hao SZ, Dong C. Microstructures and phase formations in the surface layer of an AISI D2 steel treated with pulsed electron beam. Journal of Alloys and Compounds. 2007;434-435:707-9.

[115] Zou JX, Zhang KM, Hao SZ, Dong C, Grosdidier T. Mechanisms of hardening, wear and corrosion improvement of 316 L stainless steel by low energy high current pulsed electron beam surface treatment. Thin Solid Films. 2010;519:1404-15.

[116] Gnyusov S, Tarasov S, Ivanov Y, Rothstein V. The effect of pulsed electron beam melting on microstructure, friction and wear of WC–Hadfield steel hard metal. Wear. 2004;257:97-103.

[117] Franke R, Haase I, Klemm M, Zenker R. Friction and wear behaviour of electron beam surface treated aluminium alloys AlSi10Mg(Cu) and AlSi35. Wear. 2010;269:921-9.

[118] Hao S, Xu Y, Zhang Y, Zhao L. Improvement of surface microhardness and wear resistance of WC/Co hard alloy by high current pulsed electron beam irradiation. International Journal of Refractory Metals and Hard Materials. 2013;41:553-7.

[119] Xu Y, Zhang Y, Hao SZ, Perroud O, Li MC, Wang HH, et al. Surface microstructure and mechanical property of WC-6% Co hard alloy irradiated by high current pulsed electron beam. Applied Surface Science. 2013;279:137-41.

[120] Hao Y, Gao B, Tu GF, Li SW, Hao SZ, Dong C. Surface modification of Al–20Si alloy by high current pulsed electron beam. Applied Surface Science. 2011;257:3913-9.

[121] Hao Y, Gao B, Tu GF, Li SW, Dong C, Zhang ZG. Improved wear resistance of Al-15Si alloy with a high current pulsed electron beam treatment. Nuclear Instruments and Methods in Physics Research Section B: Beam Interactions with Materials and Atoms. 2011;269:1499-505.

[122] Walker J, Murray J, Narania S, Clare A. Dry Sliding Friction and Wear Behaviour of an Electron Beam Melted Hypereutectic Al–Si Alloy. Tribology Letters. 2011:1-10.
[123] Zhang KM, Zou JX, Bolle B, Grosdidier T. Evolution of residual stress states in surface layers of an AISI D2 steel treated by low energy high current pulsed electron beam. Vacuum. 2013;87:60-8.
[124] Li D, Chen HN, Xu H. The effect of nanostructured surface layer on the fatigue behaviors of a carbon steel. Applied Surface Science. 2009;255:3811-6.
[125] Lu K, Lu J. Nanostructured surface layer on metallic materials induced by surface mechanical attrition treatment. Materials Science and Engineering: A. 2004;375–377:38-45.
[126] Chui P, Sun K, Sun C, Yang X, Shan T. Effect of surface nanocrystallization induced by fast multiple rotation rolling on hardness and corrosion behavior of 316L stainless steel. Applied Surface Science. 2011;257:6787-91.
[127] Zhang XD, Hao SZ, Li XN, Dong C, Grosdidier T. Surface modification of pure titanium by pulsed electron beam. Applied Surface Science. 2011;257:5899-902.
[128] Xu F, Tang G, Guo G, Ma X, Ozur GE. Influence of irradiation number of high current pulsed electron beam on the structure and properties of M50 steel. Nuclear Instruments and Methods in Physics Research Section B: Beam Interactions with Materials and Atoms. 2010;268:2395-9.
[129] Xu F, Guo G, Tang G, Ma X, Wang L, Ozur GE, et al. Microstructure modifications and corrosion behaviors of Cr4Mo4V steel treated by high current pulsed electron beam. Materials Chemistry and Physics. 2011;126:904-8.
[130] Mei X, Liu X, Wang C, Wang Y, Dong C. Improving oxidation resistance and thermal insulation of thermal barrier coatings by intense pulsed electron beam irradiation. Applied Surface Science. 2012;263:810-5.
[131] Okada A, Uno Y, Yabushita N, Uemura K, Raharjo P. High efficient surface finishing of bio-titanium alloy by large-area electron beam irradiation. Journal of Materials Processing Technology. 2004;149:506-11.
[132] Okada A, Kitada R, Okamoto Y, Uno Y. Surface modification of cemented carbide by EB polishing. CIRP Annals - Manufacturing Technology. 2011;60:575-8.
[133] Okada A, Uno Y, McGeough JA, Fujiwara K, Doi K, Uemura K, et al. Surface finishing of stainless steels for orthopedic surgical tools by large-area electron beam irradiation. CIRP Annals - Manufacturing Technology. 2008;57:223-6.

[134] Brinksmeier E, Riemer O, Gessenharter A, Autschbach L. Polishing of Structured Molds. CIRP Annals - Manufacturing Technology. 2004;53:247-50.
[135] Pouzada AS, Ferreira EC, Pontes AJ. Friction properties of moulding thermoplastics. Polymer Testing. 2006;25:1017-23.
[136] Murray JW, Kinnell PK, Cannon AH, Bailey B, Clare AT. Surface finishing of intricate metal mould structures by large-area electron beam irradiation. Precision Engineering. 2013;37:443-50.
[137] Williams DB, Carter CB. Transmission Electron Microscopy: A Textbook for Materials Science. Springer US, 1996.
[138] Okada A, Uno Y, Okamoto Y. A New Slicing Method of Monocrystalline Silicon Ingot by Wire EDM. 1998. p. 417-24.
[139] Qian J, Steegen S, Vander Poorten E, Reynaerts D, Van Brussel H. EDM texturing of multicrystalline silicon wafer and EFG ribbon for solar cell application. International Journal of Machine Tools and Manufacture. 2002;42:1657-64.
[140] Masuzawa T, Fujino M, Kobayashi K, Suzuki T, Kinoshita N. Wire Electro-Discharge Grinding for Micro-Machining. CIRP Annals - Manufacturing Technology. 1985;34:431-4.
[141] Shibahara K, Matsuno A, Takii E, Eto T. Green laser annealing with light absorber. 13th IEEE International Conference on Advanced Thermal Processing of Semiconductors, RTP 2005 , art no 1613689 , pp 101-1042005. p. 101-4.
[142] Zwick A, Carles R. Multiple-order Raman scattering in crystalline and amorphous silicon. Physical Review B. 1993;48:6024-32.
[143] Yan J. Laser micro-Raman spectroscopy of single-point diamond machined silicon substrates. Journal of Applied Physics. 2004;95:2094-101.
[144] Fang FZ, Wu H, Zhou W, Hu XT. A study on mechanism of nano-cutting single crystal silicon. Journal of Materials Processing Technology. 2007;184:407-10.
[145] Yan J, Asami T, Harada H, Kuriyagawa T. Crystallographic effect on subsurface damage formation in silicon microcutting. CIRP Annals - Manufacturing Technology. 2012;61:131-4.
[146] Jasinevicius RG. Influence of cutting conditions scaling in the machining of semiconductors crystals with single point diamond tool. Journal of Materials Processing Technology. 2006;179:111-6.

[147] Sarney WL. Understanding transmission electron microscopy diffraction patterns obtained from infrared semiconductor materials. Army Research Laboratory: Adelphi, MD, 2003.
[148] Duffar T, Nadri A. On the twinning occurrence in bulk semiconductor crystal growth. Scripta Materialia. 2010;62:955-60.
[149] Yan J, Asami T, Kuriyagawa T. Response of machining-damaged single-crystalline silicon wafers to nanosecond pulsed laser irradiation. Semiconductor Science and Technology. 2007;22:392-5.
[150] Ho SK, Aspinwall DK, Voice W. Use of powder metallurgy (PM) compacted electrodes for electrical discharge surface alloying/modification of Ti–6Al–4V alloy. Journal of Materials Processing Technology. 2007;191:123-6.
[151] Hackert-Oschätzchen M, Martin A, Meichsner G, Zinecker M, Schubert A. Microstructuring of carbide metals applying Jet Electrochemical Machining. Precision Engineering. 2013;37:621-34.
[152] Brånemark R, Emanuelsson L, Palmquist A, Thomsen P. Bone response to laser-induced micro- and nano-size titanium surface features. Nanomedicine: Nanotechnology, Biology and Medicine. 2011;7:220-7.
[153] Zhang Y, Liu Y, Ji R, Cai B. Study of the recast layer of a surface machined by sinking electrical discharge machining using water-in-oil emulsion as dielectric. Applied Surface Science. 2011;257:5989-97.
[154] Kanaya K, Okayama S. Penetration and energy-loss theory of electrons in solid targets. Journal of Physics D: Applied Physics. 1972;5:43-58.
[155] Liu H-S, Yan B-H, Huang F-Y, Qiu K-H. A study on the characterization of high nickel alloy micro-holes using micro-EDM and their applications. Journal of Materials Processing Technology. 2005;169:418-26.
[156] Yoshiyuki, Okada A, Okamoto Y, Yamazaki K, Risbud SH, Yamada Y. High efficiency fine boring of monocrystalline silicon ingot by electrical discharge machining. Precision Engineering. 1999;23:126-33.
[157] Wang D, Zhao WS, Gu L, Kang XM. A study on micro-hole machining of polycrystalline diamond by micro-electrical discharge machining. Journal of Materials Processing Technology. 2011;211:3-11.
[158] Cetin S, Okada A, Uno Y. Effect of debris distribution on wall concavity in deep-hole EDM. JSME International Journal, Series C: Mechanical Systems, Machine Elements and Manufacturing. 2004;47:553-9.

[159] Mohri N, Fukusima Y, Fukuzawa Y, Tani T, Saito N. Layer Generation Process on Work-piece in Electrical Discharge Machining. CIRP Annals - Manufacturing Technology. 2003;52:157-60.
[160] Liao YS, Wu PS, Liang FY. Study of Debris Exclusion Effect in Linear Motor Equipped Die-sinking EDM Process. Procedia CIRP. 2013;6:123-8.
[161] Lascoe ODASMI. Handbook of fabrication processes. Ohio: ASM International, 1988.
[162] Qin Y, Zou J, Dong C, Wang X, Wu A, Liu Y, et al. Temperature-stress fields and related phenomena induced by a high current pulsed electron beam. Nuclear Instruments and Methods in Physics Research, Section B: Beam Interactions with Materials and Atoms. 2004;225:544-54.
[163] Huang X, Pryds NH. Crystallography and morpholgy of cementite precipitates formed during rapid solidification of a ferritic stainless steel. Acta Materialia. 2000;48:4073-82.
[164] Kral MV, Fonda RW. The primary growth direction of Widmanstatten cementite laths. Scripta Materialia. 2000;43:193-8.
[165] Ungár T. The Meaning of Size Obtained from Broadened X-ray Diffraction Peaks. Advanced Engineering Materials. 2003;5:323-9.
[166] Gao B, Hao S, Zou J, Wu W, Tu G, Dong C. Effect of high current pulsed electron beam treatment on surface microstructure and wear and corrosion resistance of an AZ91HP magnesium alloy. Surface and Coatings Technology. 2007;201:6297-303.
[167] Zou JX, Grosdidier T, Zhang KM, Dong C. Cross-sectional analysis of the graded microstructure in an AISI D2-steel treated with low energy high-current pulsed electron beam. Applied Surface Science. 2009;255:4758-64.
[168] Zhang K, Zou J, Grosdidier T, Dong C, Yang D. Improved pitting corrosion resistance of AISI 316L stainless steel treated by high current pulsed electron beam. Surface and Coatings Technology. 2006;201:1393-400.
[169] Stähli G, Sturzenegger C. On the formation of austentic boundary layers by short laser-pulse reaction with steel. Scripta Metallurgica. 1978;12:617-22.
[170] Guan QF, Zou H, Zou GT, Wu AM, Hao SZ, Zou JX, et al. Surface nanostructure and amorphous state of a low carbon steel induced by high-current pulsed electron beam. Surface and Coatings Technology. 2005;196:145-9.

[171] Ivanov Y, Matz W, Rotshtein V, Günzel R, Shevchenko N. Pulsed electron-beam melting of high-speed steel: structural phase transformations and wear resistance. Surface and Coatings Technology. 2002;150:188-98.
[172] Proskurovsky DI, Rotshtein VP, Ozur GE, Ivanov YF, Markov AB. Physical foundations for surface treatment of materials with low energy, high current electron beams. Surface and Coatings Technology. 2000;125:49-56.
[173] Kruth JP, Stevens L, Froyen L, Lauwers B. Study of the White Layer of a Surface Machined by Die-Sinking Electro-Discharge Machining. CIRP Annals - Manufacturing Technology. 1995;44:169-72.
[174] Grosdidier T, Zou JX, Stein N, Boulanger C, Hao SZ, Dong C. Texture modification, grain refinement and improved hardness/corrosion balance of a FeAl alloy by pulsed electron beam surface treatment in the "heating mode". Scripta Materialia. 2008;58:1058-61.
[175] Hao S, Wu P, Zou J, Grosdidier T, Dong C. Microstructure evolution occurring in the modified surface of 316L stainless steel under high current pulsed electron beam treatment. Applied Surface Science. 2007;253:5349-54.
[176] Wang X, Zhu XP, Lei MK, Zhang JS. Influence of high-intensity pulsed ion beam irradiation on the creep property of 316 L stainless steel. Nuclear Instruments and Methods in Physics Research Section B: Beam Interactions with Materials and Atoms. 2007;259:937-42.
[177] Shahryari A, Szpunar JA, Omanovic S. The influence of crystallographic orientation distribution on 316LVM stainless steel pitting behavior. Corrosion Science. 2009;51:677-82.

# Appendix

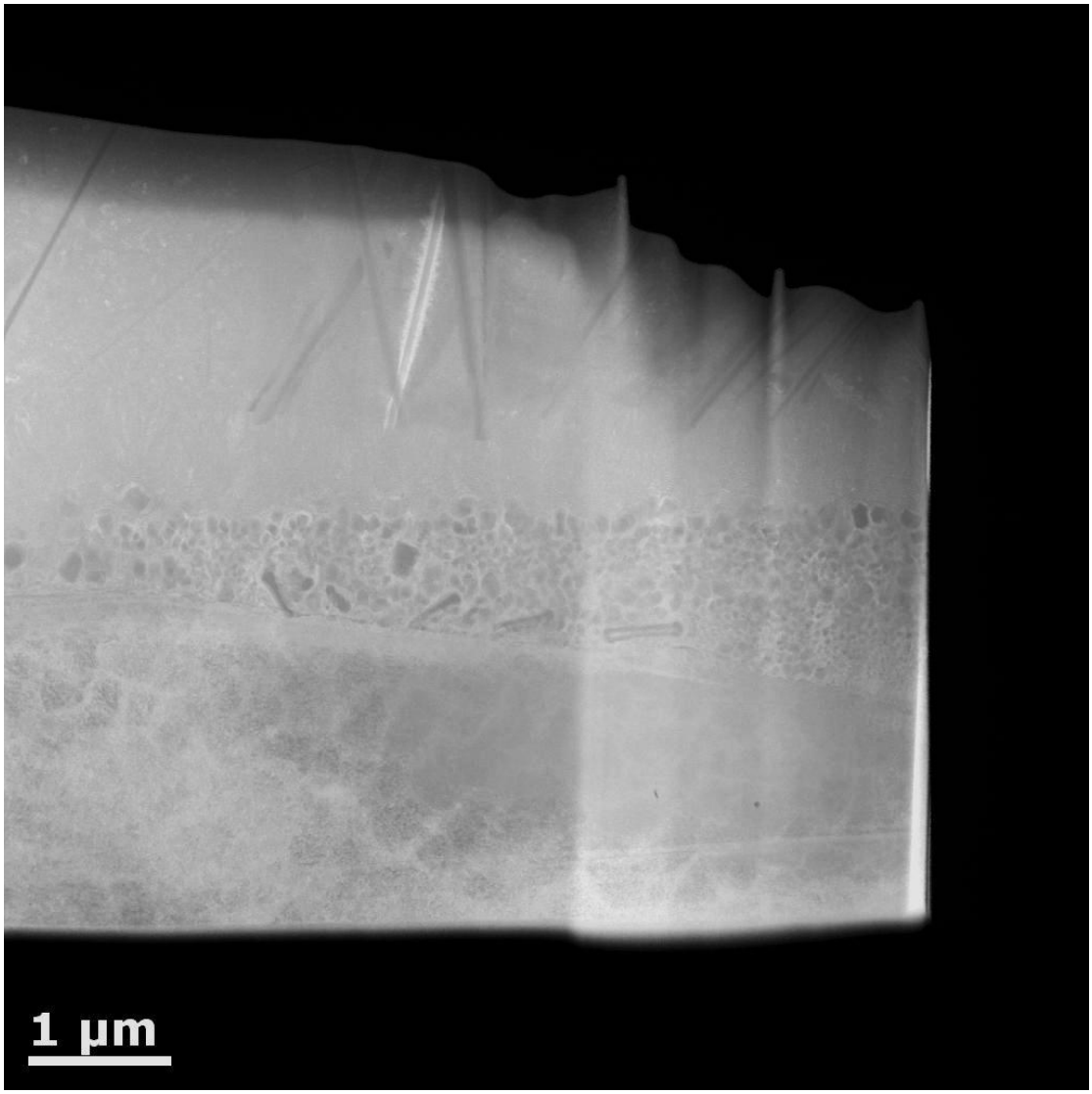


**Appendix Fig 1 Image of full lamella from deeper region of EB irradiated EDM'd 310 steel. FIB damage can be seen at the top right.**

In Appendix Fig 1, the entire bottom lamella used in Fig. 6.16 can be seen. The sample is noticeably damaged from FIB at the top right, where curtaining and over milling can be seen. In order to thin this large sample fully to over its entire area, maintaining the original top surface was very difficult, and so two TEM sample were used in this chapter. However, despite damage, the structures reported can be seen continued in the right region of the sample, including needles, the EB-EDM interface and austenite structures.

| Current | Layer thickness | Error | | Error | | Error |
|---|---|---|---|---|---|---|
| (A) | (µm) | | | | | |
| | 3µs ON, 2µs OFF | | 3µs ON, 10µs OFF | | 15µs ON, 10µs OFF | |
| 2.3 | 1.18776 | 0.17397 | 1.24367 | 0.23674 | 1.77159 | 0.25612 |
| 3.4 | 1.97989 | 0.3022 | -- | -- | -- | -- |
| 4.5 | 2.15557 | 0.3023 | 1.98877 | 0.32698 | 2.57679 | 0.59176 |

**Appendix Fig 2 Average thicknesses of EDM deposited layers used for graph in Fig. 5.12**

| Number of shots | Crack density | | | | | |
|---|---|---|---|---|---|---|
| | (crack length in mm per mm2) | | | | | |
| | 15kV | Error | 25kV | Error | 35kV | Error |
| 0 | 15.50953 | 0.5338 | 15.50953 | 0 | 15.50953 | 0 |
| 1 | 15.02788 | 1.31001 | 10.49696 | 0.78117 | 9.73665 | 0.46524 |
| 5 | 30.11956 | 0.97103 | 14.1335 | 0.66956 | 6.41404 | 0.62995 |
| 10 | 16.01155 | 1.02922 | 3.45487 | 0.36105 | 2.25419 | 0.60011 |
| 20 | 36.45117 | 1.79107 | 0 | 0 | 0 | 0 |

**Appendix Fig 3 Crack density of EB treated samples used to produce graph in Fig. 6.4**

| Number of shots | Mean crack length | | | | | |
|---|---|---|---|---|---|---|
| | (µm) | | | | | |
| | 15kV | Error | 25kV | Error | 35kV | Error |
| 0 | 45.55569 | 2.61196 | 45.55569 | 0 | 45.55569 | 0 |
| 1 | 45.66958 | 2.33768 | 20.47816 | 2.30553 | 34.90455 | 1.81699 |
| 5 | 45.75807 | 1.65205 | 50.29543 | 2.41124 | 74.39092 | 10.60528 |
| 10 | 30.92392 | 1.69547 | 18.27638 | 1.15257 | 128.1889 | 13.27114 |
| 20 | 47.72905 | 1.49011 | 0 | 0 | 0 | 0 |

**Appendix Fig 4 Average crack length of EB treated samples used to produce graph in Fig. 6.4**

| No. of shots (5 µs EDM) | Sa Roughness (µm) | Error | | | | |
|---|---|---|---|---|---|---|
| | 15kV | | 25kV | | 35kV | |
| 1 | 2.09 | 0.109 | 1.93 | 0.078 | 2.13 | 0.067 |
| 5 | 2.33 | 0.098 | 1.66 | 0.068 | 1.51 | 0.069 |
| 10 | 2.3 | 0.107 | 1.36 | 0.084 | 1.03 | 0.076 |
| 20 | 2.23 | 0.092 | 1.17 | 0.077 | 0.935 | 0.078 |
| | | | | | | |
| No. of shots (30 µs EDM) | Sa Roughness (µm) | Error | | | | |
| | 15kV | | 25kV | | 35kV | |
| 1 | 2.7 | 0.124 | 3.27 | 0.114 | 2.97 | 0.10943 |
| 5 | 3.3 | 0.10859 | 2.51 | 0.105 | 1.71 | 0.085 |
| 10 | 3.11 | 0.118 | 2.79 | 0.087 | 1.34 | 0.076 |
| 20 | 3.14 | 0.109 | 2.18 | 0.078 | 0.893 | 0.074 |

**Appendix Fig 5 Mean roughness and standard deviation of EDM'd surface subject to EB irradiation used to produce graph in Fig. 6.9**

| Number of shots | Mean layer thickness (µm) | | | | | |
|---|---|---|---|---|---|---|
| | 15kV (30µs EDM) | Error | 15kV (5µs EDM) | Error | 25kV (30µs EDM) | Error |
| 1 | 0.91495 | 0.05349 | 1.01678 | 0.08378 | 1.46393 | 0.07593 |
| 5 | 1.02785 | 0.0694 | 1.0212 | 0.06958 | 2.55609 | 0.10175 |
| 10 | 1.17071 | 0.09655 | 1.03357 | 0.08468 | 1.37324 | 0.09347 |
| 20 | 0.76062 | 0.05591 | 0.86238 | 0.05897 | 1.01637 | 0.06482 |
| 1 | 25kV (5µs EDM) | Error | 35kV (30µs EDM) | Error | 35kV (5µs EDM) | Error |
| 5 | 1.0872 | 0.12762 | 2.76348 | 0.17515 | 1.87508 | 0.1648 |
| 10 | 1.5051 | 0.07113 | 4.15886 | 0.17985 | 3.0503 | 0.13343 |
| 20 | 1.11582 | 0.07868 | 4.52332 | 0.20703 | 3.51079 | 0.14105 |
| | 1.04634 | 0.11005 | 3.86742 | 0.20483 | 3.3603 | 0.10593 |

**Appendix Fig 6 Mean thicknesses and standard deviations of measurements of EB remelted layers used to produce graph**